U.S. Department of Energy
Energy Efficiency and Renewable Energy
Bringing you a prosperous future where energy is clean, abundant, reliable, and affordable

HEAVY VEHICLE PROPULSION MATERIALS

Less dependence on foreign oil, and eventual transition to an emissions-free, petroleum-free vehicle

FreedomCAR and Vehicle Technologies Program

2004 ANNUAL PROGRESS REPORT

21ST CENTURY TRUCK PARTNERSHIP
FreedomCAR & Fuel Partnership

U.S. Department of Energy
Office of FreedomCAR and Vehicle Technologies
1000 Independence Avenue S.W.
Washington, DC 20585-0121

FY 2004

Progress Report for Heavy Vehicle Propulsion Materials

Energy Efficiency and Renewable Energy
Office of FreedomCAR and Vehicle Technologies
Advanced Materials Technologies

Edward Wall **Program Manager, OFCVT**
Rogelio Sullivan **Advanced Materials Technologies Team Leader**
Sidney Diamond **Technology Development Area Specialist**

May 2005

CONTENTS

1. HEAVY VEHICLE PROPULSION MATERIALS

Advanced materials are an enabling technology for fuel-efficient heavy-vehicle truck engines. The Heavy Vehicle Propulsion Materials Project is organized around the following technology issues: fuel systems; exhaust aftertreatment; air handling, hot section, and structural components; and standards.

Materials for Fuel Systems

The fuel systems for diesel engines are complex, expensive systems that are critically important to meeting the efficiency and emissions targets of the Office of FreedomCAR and Vehicle Technologies (OFCVT). Virtually every path to improving control of the combustion process in order to improve efficiency and reduce emissions depends on improvements in the fuel injection system.

Fuel injectors are highly precise. The individual components must fit together with clearances that are sometimes less than 1×10^{-6} meters. Control of the combustion process requires precise control of the size, shape, and surface finish of the injector components.

The current systems for reliably controlling multiple injections are limited by the ability of mechanical and electronic systems to respond precisely and quickly enough to provide additional injection control. Smart materials, such as piezoelectric materials, offer the potential for better control of fuel injection and have been recently introduced for automobiles. However, a number of improvements in materials and manufacturing methods for the materials are yet required for heavy vehicles.

Presently, the fuel system represents a significant portion of the cost of a heavy-duty diesel engine. Enabling materials and cost-effective, precision manufacturing processes are instrumental in developing improved fuel injection systems. In addition to new and improved materials, improved manufacturing and inspection methods for the injector components are being developed.

Manufacturing technology for nickel aluminide–titanium carbide cermet fuel system components continued this year in coordinated efforts at Oak Ridge National Laboratory (ORNL), Southern Illinois University–Carbondale (SIUC), CoorsTek, Inc. and Cummins, Inc. ORNL prepared a large batch of processed powder, which was provided to CoorsTek for injection molding of test components. The injection-molded components were then sintered at ORNL and provided to Cummins for testing in fuel injection systems. In a parallel effort, SIUC evaluated a low-cost, high-throughput process, continuous belt sintering, for manufacturing the cermet components. SIUC determined that rapid heating, at rates up to 750°C/minute, resulted in higher densities and more uniform microstructures and offers the potential to reduce sintering costs by as much as 50% by increasing part throughput.

Materials for Exhaust Aftertreatment

The reduction of nitrogen oxides (NO_x) and particulate emissions is critically important to OFCVT's program and is highly materials dependent. The U.S. Department of Energy (DOE) goals for improved efficiency of heavy vehicles are greatly complicated by engine design and exhaust aftertreatment technologies designed to meet the mandatory U.S. Environmental Protection Agency (EPA) emission regulations for 2007 and 2010. Materials and systems research is being conducted to minimize the potentially negative effects of emission-reduction technologies on fuel economy and to result in cleaner and more efficient engines.

Durability of exhaust aftertreatment systems in heavy vehicles is a concern. A lifetime of at least 500,000 miles is expected, and a 1,000,000-mile lifetime is desired (compared with 100,000 miles for automobiles). Exposure of the aftertreatment systems to high temperatures, vibration, erosion, and chemical attack by species in the oil and fuel results in degradation of performance. The effects of exposure in service on the microstructure and microchemistry of the aftertreatment systems are being characterized, and this research may lead to development of more durable systems. The development of advanced NO_x sensors is being conducted to facilitate optimal engine and aftertreatment control strategies.

Accomplishments this year included significant progress in a collaborative Ford–ORNL program intended to facilitate deployment of a NO_x trap for lean diesel or gasoline exhaust by (1) investigating materials issues related to deterioration of NO_x trap performance upon aging as a result of thermal and sulfation-desulfation cycles and (2) investigating materials that are robust under the lean NO_x trap operating conditions. The latter objective includes the synthesis of new materials. Accomplishments of this effort include completing a study of microstructural changes in a series of model catalysts during aging under lean and rich conditions at 500°C; beginning the updating of the ex-situ reactor to enable transmission electron microscopy (TEM) sampling under lean, rich, or stoichiometric conditions as well as lean-rich cycles; and equipping a new synthesis laboratory for the preparation of NO_x trap materials.

Research conducted at the High Temperature Materials Laboratory at ORNL is focused on the development and utilization of new capabilities and techniques for ultra-high-resolution TEM to characterize the microstructures of catalytic materials of interest for reducing NO_x emissions in diesel and automotive exhaust systems. This research aims to relate the effects of reaction conditions on the changes in morphology of heavy metal species on "real" catalyst support materials, typically oxides. Accomplishments included the characterization via high-resolution annular dark-field scanning TEM (STEM) that imaged the structure of a model NO_x trap material of near-atomic clusters and rafts of platinum atoms 1–3 atomic layers thick; characterization via TEM and STEM of core samples taken from catalyst monoliths removed from vehicles after up to 82,000 km of driving; and taking delivery of the new aberration-corrected electron microscope (ACEM), which will enable imaging of ultra-fine clusters of catalyst species on real catalyst samples of interest.

Exhaust aftertreatment materials projects are ongoing at both Caterpillar and Cummins. These projects are significant in that they represent a departure from an earlier culture in which the diesel engine companies relied heavily on catalyst manufacturers to provide the needed technologies and did not actively participate in the development of catalyst materials. These diesel engine manufacturers are actively collaborating with catalyst suppliers in the development of improved catalyst materials and are contributing to the development of a fundamental understanding of catalyst performance that is important to both suppliers and users of catalyst systems. In addition to the in-house efforts at Caterpillar and Cummins, Cummins and ORNL collaborated, via cooperative research and development agreements, in characterizing lab and engine-tested catalysts via X-ray diffraction, spectroscopy, and microscopy; and in characterizing diesel particulate filters and developing probabilistic design tools to predict the useful lifetime of the filters.

Ford Motor Co. and ORNL are collaborating on the development of a NO_x sensor that can be used in systems for on-board remediation of diesel engine exhaust. The sensor should have an operating temperature of 600–700° C and be able to measure NO_x concentrations from 1 to 1500 ppm at oxygen levels from 5 to 20 vol %. Prototype sensing elements are fabricated by patterning electronically conductive and catalytic layers onto oxygen-ion–conducting substrates. The sensing elements are characterized for NO_x response, oxygen sensitivity, and response time. Accomplishments this year included demonstrating NO_2 sensing elements with extremely high sensitivity; demonstrating biased NO-selective sensing elements; and constructing both types of elements to consist of co-planar electrodes, one of oxide and the other of a noble metal.

Materials for Air Handling, Hot Section, and Structural Applications

Engine design strategies for meeting EPA emission requirements have resulted in the need for significantly higher turbocharger boost. The higher boost requirements result in higher heat of compression and greater thermal and fatigue loads on turbocharger components.

Caterpillar began a new project in 2003 to design and fabricate a cost-competitive diesel engine turbocharger, using lightweight titanium materials, that provides a reduction in both fuel consumption and transient emissions. Caterpillar has designed a series turbocharger for use on the C15 engine platform. This turbocharger consists of one turbo wheel and two compressor wheels that are attached to a single rotating drive shaft. This compact design will replace the two-turbocharger system that is presently installed in the C15 engine. Titanium aluminide will be used for the turbo wheel, and one of the compressor wheels will be

made from a titanium alloy. Accomplishments this year included procuring cast TiAl turbine wheels, developing friction welding technology for joining the turbine wheels to shafts and for realizing a higher joint strength than in the base TiAl wheel, and conducting preliminary turbocharger bench tests.

In a related project, Dynamet Technologies is conducting a research and development project to develop low-cost Ti-6Al-4V billet feedstock using a blend of titanium and alloy powders and inexpensive Ti-6Al-4V machine turnings. Dynamet has evaluated this low-cost titanium alloy feedstock as starting billet material for casting, forging, and extrusion operations and has produced high-density material in each case.

Caterpillar and ORNL won a 2003 R&D 100 Award for the development of CF8C-Plus cast stainless steel. The new high-temperature stainless steel may have near-term applications in diesel engine exhaust manifolds and turbocharger housings. Thermal-mechanical fatigue (TMF) of the initial commercial heats was completed this year, together with aging of various specimens. There was a significant advantage for CF8C-Plus relative to CN-12 or high-SiMo cast iron in TMF testing to 760°C. This year, MetalTek International produced additional static sand-cast and centrifugally-cast heats of CF8C-Plus for testing at Caterpillar and ORNL. That testing began this year and will be completed next year.

Caterpillar, in collaboration with Argonne National Laboratory and ORNL, has a project to design and fabricate prototype engine valves from silicon nitride and titanium aluminide materials that are 30% lighter than steel valves, provide a 200% increase in service lifetime, and potentially increase fuel efficiency in advanced engines by 10%. A probabilistic design approach was developed for the high-hardness valve materials. The friction welding of TiAl valve heads and Ti-6V-4Al valve stems was successfully optimized. The effects of surface finish on the performance of silicon nitride valves was evaluated and indicated that valves with good surface finish performed well in bench tests.

Caterpillar is also developing innovative approaches to thermal barrier and wear-resistant coatings for engines. Durability issues for thermal sprayed coatings, particularly thermal barrier coatings, remain the major technical challenge to their implementation in new engine designs. New approaches to coating design and fabrication are being developed to aid in overcoming this technical hurdle. Specific objectives are (1) to develop laser technology for surface dimpling, cleaning, and laser-assisted spraying to enhance adherence and increase coating strength; (2) to develop phosphate-bonded composites for thermal management coatings; and (3) to evaluate quasicrystalline materials as potential thermal barrier and wear coatings. This year, a cost analysis of laser pre- and post-treatments was conducted, and post-laser tacking was selected as the method for treating coatings to increase adherence. Phosphate-bonded composite coatings survived thermal cycling to 650°C with good residual adherence to the substrate. Quasicrystalline coatings were sprayed using the high-velocity oxygen-fueled technique, and evaluation began. In a collaborative effort, ORNL demonstrated the use of high-density infrared surface treatment as a means of producing hard-metal coatings with low porosity.

The feasibility of reducing the weight of a heavy-duty engine by substituting a lighter material for the cast iron engine block and cylinder head was evaluated by ORNL and Ricardo, Inc. Finite element analysis was used to compute the stresses, temperatures, and fatigue safety factors of a 5.9-L diesel engine, run at the maximum design power, for three lightweight casting alloy systems: titanium, aluminum, and magnesium. The analysis indicated the feasibility of simple material substitutions in all cases, with the exception that the titanium alloy cylinder head will require inserts to reduce the temperature in the valve bridge area. Reducing the weight of the entire engine by up to 33% for the magnesium alloy and 20% for the aluminum alloy, and up-rating the power of the engine by 50% while reducing the weight by 15% for the titanium alloy, were predicted to be feasible.

Efforts in cost-effective manufacturing were carried out by ORNL, the University of Michigan, and Purdue University. Technology for machining difficult materials, such as titanium alloys, was developed in the ORNL/University of Michigan collaboration. ORNL investigated surface modification of lubricated ceramic parts for applications in fuel systems and related applications. Purdue University is investigating the consolidation of low-cost machining chips to produce nanocrystalline components with high strength and hardness.

In a new effort this year, ORNL is investigating the plastic deformation behavior of industrial ceramics and the potential for low-temperature forming of components. In collaboration with Pennsylvania State University, a novel sintering method was developed to fabricate nanocrystalline (less than 100-nm grain size)

zirconia ceramics. Enhancement of the plastic deformation of sub-micron zirconia in applied electric fields was observed in collaborative work with North Carolina State University. ORNL also established dynamic indentation and instrumented scratch testing facilities and associated finite-element analysis models to characterize and model contact-induced damage and its links to wear performance and to the optimization of machining and rolling contact fatigue.

Materials and Testing Standards

OFCVT has an International Energy Agency (IEA) "Implementing Agreement for a Programme of Research and Development on Advanced Materials for Transportation Applications" (IA-AMT). The objectives of the IA-AMT are as follows:

1. to identify and evaluate promising new processing and surface engineering technologies capable of improving materials performance in transportation systems and
2. to promote and implement pre-competitive development and verification of advanced characterization methods appropriate for advanced materials for transportation applications.

Annex III, which was approved in July 2002, consists of two subtasks on contact reliability of advanced engine materials including structural ceramics, composites, and nanostructured friction/wear coatings. Subtask 1 is an information exchange, and Subtask 2 focuses on the development of standard test methods and procedures for determining the rolling contact fatigue resistance of advanced materials. At present, the active contracting parties for the IA-AMT are Germany (Bundesanstalt für Materialforschung und–prüfung), Canada (CANMET), United Kingdom (Department of Trade and Industry), and the United States (DOE).

A new activity to be conducted under the IEA program was initiated last year by the National Institute of Standards and Technology (NIST). The objectives of this new effort are as follows:

1. organize an international cooperative research program on an integrated surface modification technology under the auspices of the IEA
2. design and identify surface features and patterns that can achieve friction reduction and enhanced durability for heavy-duty diesel engine components
3. develop understanding and appropriate models to explain texturing effects on frictional characteristics
4. develop appropriate thin films and coatings to achieve a synergistic and complementary relationship with texturing to enhance performance
5. discover and develop surface chemistry for protecting the films and coatings that work in synergy with the textures

Accomplishments this year include the development of a new design principle for surface texture design to enable friction reduction under boundary lubrication conditions.

NIST also leads a project to develop standard testing methods for advanced materials, primarily ceramics. Step by step, we are building a national and international standards infrastructure to facilitate the commercial utilization of new advanced materials in engine applications. The generic test method standards developed to date have proved to be so practical, reliable, and versatile that they are now being used to support a wide range of applications, including surgical implants in humans and even ceramic military body armor. In FY 2004, the pre-standardization work on the flexural strength of split cylinders was completed, a NIST *Guide to Practice on Fractographic Analysis of Brittle Materials* was 50% completed, and several standards from the American Society for Testing and Materials and the International Organization for Standards were revised.

The rolling contact fatigue (RCF) effort is led by ORNL. Its objectives include the characterization of the RCF performance of ceramics and tribological coatings; determination of the effects of subsurface damage, microstructure, material properties, and contact stress on RCF performance; and correlation of RCF performance measured by different internationally-used RCF test techniques. In FY 2004, a three-ball-on-rod

test facility was established and informal collaboration was initiated with Bournemouth University in the United Kingdom.

Rogelio Sullivan
Team Leader, Materials Technologies
Office of FreedomCAR and Vehicle Technologies
Energy Efficiency and Renewable Energy

Sidney Diamond
Technology Development Area Specialist
Office of FreedomCAR and Vehicle Technologies
Energy Efficiency and Renewable Energy

2. MATERIALS FOR FUEL SYSTEMS

A. Low-Cost, High-Toughness Ceramics

T. N. Tiegs, F. C. Montgomery, and P. A. Menchhofer
Oak Ridge National Laboratory
P.O. Box 2008, MS-6087
Oak Ridge, TN 37831-6087
(865) 574-5173; fax: (865) 574-4357; e-mail: tiegstn@ornl.gov

DOE Technology Development Area Specialist: Dr. Sidney Diamond
(202) 586-8032; fax: (202) 586-2476; e-mail: sid.diamond@ee.doe.gov
ORNL Technical Advisor: D. Ray Johnson
(865) 576-6832; fax: (865) 574-6098; e-mail: johnsondr@ornl.gov

Contractor: Oak Ridge National Laboratory, Oak Ridge, Tennessee
Prime Contract No: DE-AC05-00OR22725

Objectives

- Develop high-toughness materials that are also low in cost.

Approach

- Develop TiC-based composites with 40–60 vol % Ni_3Al to take advantage of their expansion characteristics, which are very close to those for steel.
- Conduct a development effort in collaboration with CoorsTek, Inc., and Cummins Engine on processing scale-up and engine testing.

Accomplishments

- Supplied a large batch of processed powder mixtures to CoorsTek for injection molding of test components.
- Sintered injection-molded components for engine testing in fuel injection systems.

Future Direction

- Complete work with CoorsTek (a parts supplier) to scale up the processing and to supply CoorsTek with pilot-plant–scale quantities of powder mixtures for injection molding trials.
- Supply sintered parts produced in conjunction with CoorsTek to Cummins Engine Co. for rig testing of machined components.

Introduction

TiC-Ni_3Al composites are under development for application in diesel engines because of desirable physical and mechanical properties. For these applications, the Ni_3Al volume content is on the order of 30 to 50 vol % in order to match the thermal expansion of steel. Typically, flexural strengths greater than 1000 MPa up to 800°C and fracture toughnesses higher than 15 MPa$\sqrt{m}$ are obtained for the composites. The composites are densified by liquid-phase sintering, and most of the early work used gas-atomized Ni_3Al particles with fine TiC powders.

Later work was done using Ni and NiAl powders (along with the TiC) to form Ni_3Al by an in-situ reaction during sintering. Over the last few years, the in-situ reaction process was developed significantly because it produced high mechanical properties and developed a fine TiC grain size. The finer grain sizes were favored because of better wear resistance.

The fabrication techniques and equipment employed in production are very similar to those for the fabrication of WC-Co hard metals, and thus the processing costs are well established. However, when the economics of producing the TiC-Ni_3Al composites were examined, a significant cost was associated with the use of the NiAl precursor powder (about 55% of the total raw material cost). Because the costs of the starting raw materials can be a significant fraction of the total cost of a component, alternative materials for fabricating the cermets are of interest. Part of the reason for the high cost of the NiAl is that it is produced only as a specialty powder at the present time. The development effort is being done in collaboration with CoorsTek.

Results

Large-Batch Processing of TiC-Ni_3Al Composites

Several large batches (>3 kg each) of a 50% TiC-Ni3Al (with 2% molybdenum) composition have been milled and blended together to produce ~13 kg of powder. Approximately 10 kg was sent to CoorsTek for injection molding testing. A large batch (>3 kg) was also produced that used a cheaper NiAl powder from the same manufacturer that was coarser than that previously used. Much of the earlier work used powder that had particle sizes ≤20 μm. The batch produced recently used NiAl powder with particle sizes ≤150 μm (−100 mesh).

The sintering furnace used for processing studies was out of service for many months because of a bad controller and was repaired during the last quarter of the fiscal year. However, sintering runs were completed on injection-molded test components from CoorsTek. These parts were sintered and sent to Coors-Tek and Cummins Engine Company for final component finishing and engine testing.

Alternate Precursors for Ni_3Al Formation

All previous work used a combination of Ni and NiAl for an in-situ reaction to form the Ni_3Al. Because the costs of the starting raw materials can be a significant fraction of the total cost of a component, alternative materials for fabricating the cermets are of interest. Several new batches were milled and pressed into discs and billets. The compositions are described in Table 1.

As shown, several different compositions are being examined. The new batch of Al-30 Ni from the catalyst manufacturer will determine if these materials can be made without the impurities, as observed previously. Earlier work demonstrated that these precursors produced high-density parts but had low strengths because of impurity contamination. One of the other samples will re-examine the use of pre-alloyed Ni_3Al (made by gas atomization). Earlier work at high TiC contents (70–90 vol %) showed these Ni_3Al powders produced non-homogeneous microstructures with large "pools" of Ni_3Al surrounded by the finer TiC grains. However, with the TiC content of interest now at 50 vol %, the presence of the Ni_3Al pools may not be significant to the performance of the cermets. Samples were also fabricated using a commercial Hastelloy X powder. This is a Ni-Cr-Fe-Mo alloy with good oxidation and corrosion resistance.

An attempt was made to make a pre-reacted Al-Ni precursor that could be milled to fine sizes during the normal processing of the cermets (Sample DC-3-10). Thermodynamic calculations indicated that the lowest heat of formation per gram was associated with making Al_3Ni. Appropriate amounts of aluminum and nickel were dry-milled and then fired (at a slow heating rate) to 700°C, which is sufficient to melt the aluminum. The resulting reacted product was very hard and non-friable. Consequently, this route to producing an Al-Ni precursor did not appear to be one with significant potential.

Table 1. Summary of TiC-Ni_3Al compositions fabricated

Batch no.	TiC content (vol %)	Ni_3Al source
DC-3-7	50	NiAl + Ni (milling done with larger WC media)
DC-3-8	50	Al-30 Ni Catalyst (new batch from manufacturer)
DC-3-9	50	Pre-alloyed Ni_3Al (-325 mesh)
DC-3-10	50	Reacted Al_3Ni
DC-3-11	50	Hastelloy X

Conclusions

Pilot scale batches of TiC-Ni_3Al composite mixtures were produced. In collaboration with Coors-Tek, injection-molded components were fabricated and sintered to high density. The parts will be used for engine testing by Cummins Engine Company.

Publications/Presentations

T. N. Tiegs, F. C. Montgomery, and D. A. Menchhofer, "Effect of NiAl Precursor Type on Fabrication and Properties of Ni_3Al-Bonded Carbide Composites," presented at the American Ceramic Society Conference on Ceramics and Composites, Cocoa Beach, FL, Jan. 25–28, 2004.

T. N. Tiegs, F. C. Montgomery, and P. A. Menchhofer, "Effect of Ni-Al Precursor Type on Fabrication and Properties of TiC-Ni_3Al Composites," to be published in *Ceram. Eng. Sci. Proc.*

B. Low-Cost Manufacturing Processes for Ceramic and Cermet Diesel Engine Components

Dale E. Wittmer, Professor
Southern Illinois University,
Carbondale, IL 62901
(618) 453-7006; fax: (618) 453-5847; e-mail: wittmer@engr.siu.edu

DOE Technology Development Area Specialist: Dr. Sidney Diamond
(202) 586-8032; fax: (202) 586-1600; e-mail: sid.diamond@ee.doe.gov
ORNL Technical Advisor: D. Ray Johnson
(865) 576-6832; fax: (865) 574-6098; e-mail: johnsondr@ornl.gov

Contractor: Oak Ridge National Laboratory, Oak Ridge, Tennessee
Prime Contract No.: DE-AC05-00OR22725
Subcontractor: Southern Illinois University, Carbondale, Illinois

Objective

- Investigate higher continuous sintering rates as a more cost-effective manufacturing process for ceramic and cermet diesel engine components.

Approach

- Process cermet compositions containing titanium carbide (TiC) and nickel aluminide intermetallic matrix phase into cylindrical shapes by standard dry pressing techniques.
- Sinter the cermets by continuous sintering at much higher sintering rates than previously investigated.
- Measure physical properties and compared them with previously processed materials.

Accomplishments

- Modified the continuous furnace at Southern Illinois University–Carbondale (SIUC) to allow for the investigation of higher sintering rates, which appear to produce more uniform microstructures in nickel aluminide bonded TiC cermets. Higher sintering rates could lead to improved economics of production, while more uniform microstructures give inherently more uniform properties and performance.
- Continued interaction with Oak Ridge National Laboratory (ORNL) and CoorsTek to promote commercialization of cermet diesel engine components.

Future Direction

- The past year was the final year of funding for this project. However, exploration of the use of higher sintering rates for other potential cermet formulations should be continued.

Introduction

All manufactured parts can potentially benefit from improved manufacturing processes and the incorporation of advanced materials. Injection molding has been previously shown to be a very cost-effective method for producing precision parts with minimal labor cost, and continuous sintering has been proven industrially to provide an economic advantage for sintering many advanced ceramics. More recently, continuous sintering has been used as

a means of rapid sintering of cermets composed of TiC in an intermetallic matrix.

To reduce costs, it is essential to minimize material waste while maximizing the yield of finished parts that are within specifications. A potential means of maximizing the furnace yield of parts that are in-specification while minimizing material losses due to furnace-related problems, thereby reducing part cost, is the use of continuous sintering. The continuous furnace at SIUC has been used to sinter a wide range of pre-alloyed intermetallic-TiC formulations and similar formulations where the intermetallic is formed by reaction sintering of the individual elements. Based on this work, the most promising intermetallics contained 30–50 vol % of NiA, NiC, or NiCrFe added to a fine-grained commercial TiC. These formulations were found to have high strength, hardness, toughness, and corrosion resistance. In addition, their thermal expansion can be engineered to be very close to that of cast iron and steel, which will reduce thermal expansion mismatch in several key diesel engine applications.

The present work was focused on modifying the continuous furnace to allow for higher transport rates through the furnace without causing damage to the furnace structure. Once modified, cermets were sintered at much higher sintering rates than previously investigated. Also, interactions were continued with ORNL and CoorsTek to promote commercialization of these cermets for diesel engine components.

Approach

Continuous Furnace Modification

The continuous furnace was constructed using an ultra-high molecular weight polyethylene (UHMW-PE) gear on the exit end of the furnace. This was done to give some flexibility to the ceramic link belt and to avoid stresses that might cause the ceramic pins in the belt to fracture. Attempting to run the continuous furnace at high transport speeds, in excess of about 1.5 in./min (4.31 cm/min), when the furnace temperature exceeded 1400°C, caused overheating of the UHMW-PE gear. It was believed that running for extended periods of time at these rates or higher would eventually cause damage to the ceramic link belt. Figure 1 shows the continuous furnace and Figure 2 shows the original

Figure 1. Continuous furnace at SIUC showing location of original polymer gear.

Figure 2. Original ultra-high molecular weight polyethylene gear.

polymer gear. To eliminate this problem, an aluminum alloy, 6061-T6, gear was designed and machined at SIUC. Figure 3 shows the new aluminum alloy gear installed on the continuous furnace exit drive. As seen, several holes were machined in the gear to improve heat transfer, which allows the gear to run cooler.

Investigation of High Heating Rates

Previous continuous sintering of cermets at SIUC was accomplished at sintering rates less than or equal to 125°C/min. This task investigated the use of continuous sintering as a means of obtaining high heating rates (>125°C/min) in the liquid-phase sintering of Ni_3Al-TiC cermets. Since the continuous furnace uses a ceramic belt to transport the load through the hot zone, the heating rate is dependent on the belt speed. The modification of the furnace allowed the investigation of much higher heating rates than previously investigated. The cermets investigated are sintered by liquid-phase sintering; therefore, employing high heating rates could enhance particle rearrangement and solution precipita-

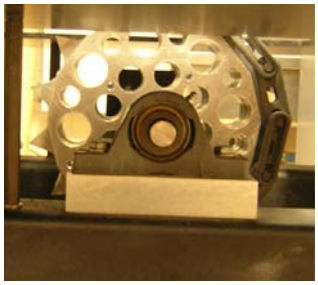

Figure 3. Aluminum alloy gear installed.

tion during the formation of the liquid. In the Ni_3Al-TiC system, TiC is known to be soluble in the intermetallic, with about 4% Ti remaining in solution in the Ni_3Al. It was hoped that the high heating rates would lead to enhanced solution and precipitation of the TiC, thereby producing finer TiC in the microstructure. Ni_3Al-TiC cermets containing 50 vol % intermetallic were sintered in flowing argon at 1450°C, using four different belt speeds that corresponded to heating rates of 125, 250, 500 and 750°C/min. Soak time at peak temperature was held constant at 30 min. Following sintering, density and microhardness were determined and the microstructure investigated by scanning electron microscopy (SEM).

Industrial Collaboration

Collaboration between SIUC, ORNL, and CoorsTek has continued since the start of this project. Cermets processed by low-pressure injection molding and continuous sintering were submitted to ORNL for wear testing, and materials have been submitted to CoorsTek for evaluation. During this project period, CoorsTek submitted materials to SIUC for sintering and evaluation.

Results

Furnace Modification

The furnace was modified as planned by the addition of the aluminum alloy gear, as shown in Figure 3. This modification allowed the belt speed to be increased from 0.75 to 4.5 in./min (1.9 to 11.43 cm/min), which is equivalent to 125 and 750°C/min, respectively. This is assuming a maximum hot-zone temperature of 1450°C and all three zones being at temperature. Obviously, higher hot-zone temperatures would lead to higher heating rates. This is significant in that traditional production furnaces usually do not exceed heating rates of over 50°C/min, and usually operate at much lower temperatures.

Investigation of High-Heating Rates

As reported, four different heating rates were investigated. Figure 4 shows the equivalent heating rate as a function of belt speed.

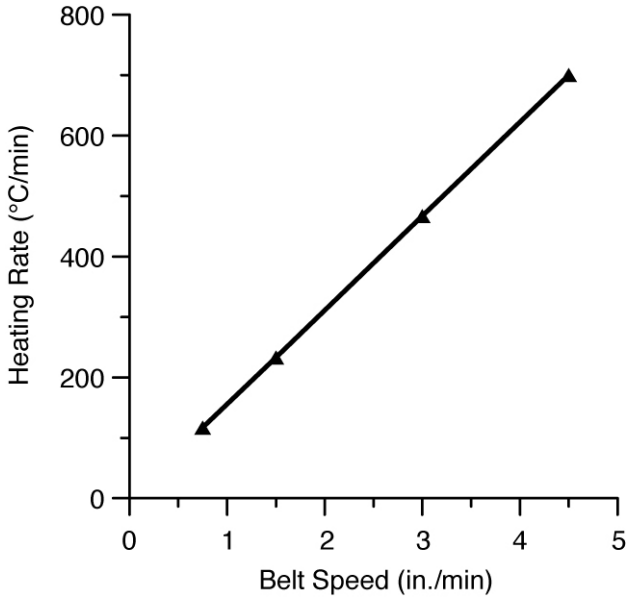

Figure 4. Heating rate as a function of belt speed.

The resulting density results are shown in Figure 5. The relative density achieved was higher at the higher heating rates, with the belt speed of 3.0 in./min (7.62 cm/min) or heating rate of 500°C/min giving the highest density results.

As seen in Figure 6, the lower sintering rates produced microstructures in which the intermetallic appears as large pools. The bright phase is the intermetallic, and the dark phase is the TiC or, in some cases, porosity. These intermetallic pools were found to be reduced in size at the higher heating rates. At the highest heating rate, 750°C/min, the pools appear to have been eliminated. In addition, there appears to be more rounding of the TiC particles at the higher heating rates.

Some potential advantages of the higher heating rates appear to be obvious. The use of the continuous furnace has been found previously to offer a reduction of as much as 50% in the sintering costs for advanced ceramics. A similar saving could be anticipated for cermets if the properties obtained are acceptable. The higher heating rates obviously

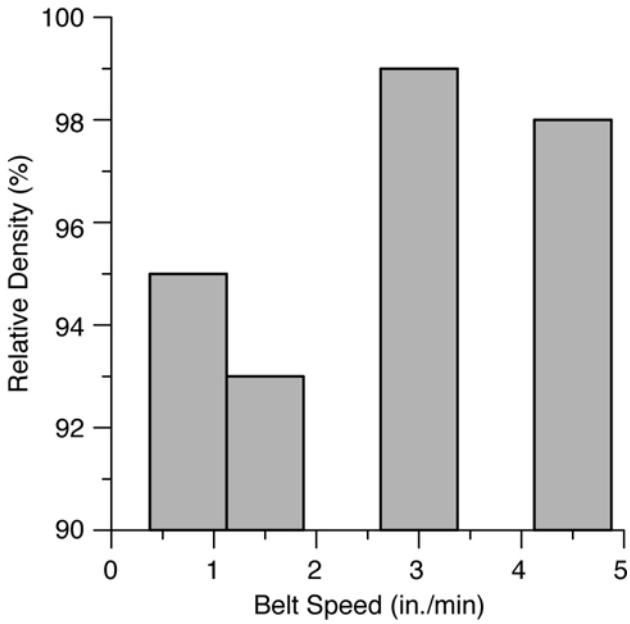

Figure 5. Relative density as a function of belt speed.

would allow for the production of more parts per shift, which would further reduce the overall manufacturing cost. An additional advantage of the high heating rate appears to be more uniform microstructures, which should in turn produce more uniform properties for the cermets.

Industrial Collaboration

SIUC, ORNL, CoorsTek, and Cummins have been involved in a confidential collaboration, and all data related to this project have been the responsibility of the individual contributors. During this reporting period, SIUC received four test bars from CoorsTek for continuous sintering and evaluation. None of the test bars was sintered without warping, and the densities obtained were well below the benchmark set by CoorsTek

The results of wear testing at ORNL have been very favorable for many of the cermets investigated. The hardness, toughness, and strength of the cermets investigated are responsible for the very high wear resistance. The effects of wear resistance of the intermetallic and of particle size of the TiC in the cermet are not very well understood. Several of the simple cylindrical shapes produced at SIUC were previously submitted to Peter Blau at ORNL for sliding wear evaluation. The results continue to be encouraging.

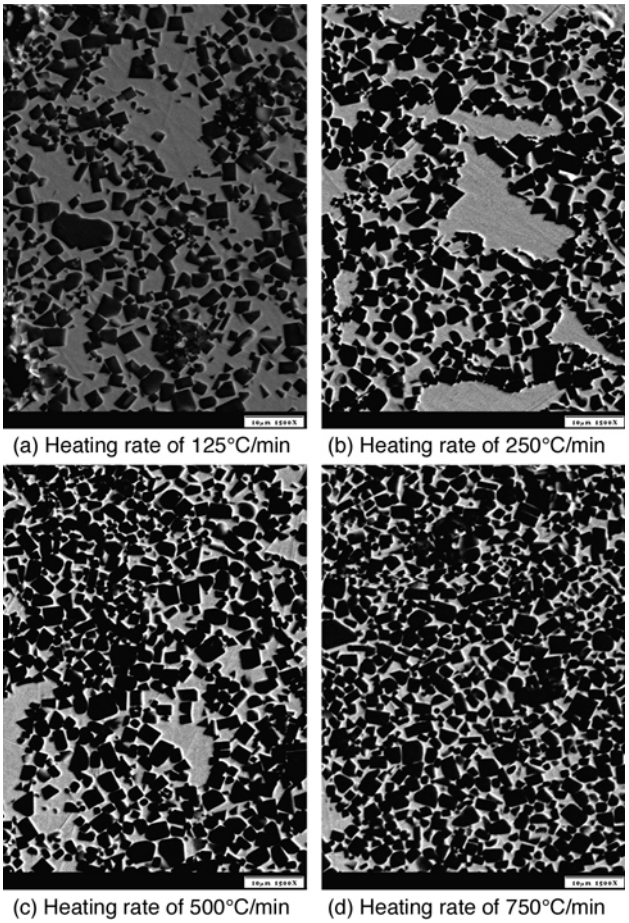

Figure 6. SEM microstructures for the four heating rates investigated.

Conclusions

The continuous furnace was modified to allow for higher heating rates. Ni_3Al-TiC cermets containing 50 vol % intermetallic were sintered in flowing argon at 1450°C using four different belt speeds corresponding to heating rates of 125, 250, 500 and 750°C/min. Higher heating rates produced higher densities and more uniform microstructures than the lower heating rates. Higher heating rates could lead to improved production costs by increasing part throughput.

Presentation

Dale E. Wittmer and Joshua W. Steffen, "Effect of High Sintering Rates on Microstructure of Ni_3al-Tic Cermets," (poster presentation at PM2TEC 2004, Chicago, IL, June 13–17, 2004), pp. 38–43 in *Advances in Powder Metallurgy and Particulate Materials*, Part 9, 2004.

C. Cermet Composites for Wear Applications

M. Anderson, T .M. Yonushonis, R. J. Stafford, M. Henrichsen, D. J. Gust, B. Seegmiller, and J. Stephan**
Cummins, Inc.
Columbus, IN 47202-3005
(812) 377-7678; fax: (812) 377-2041; e-mail: matt.anderson@cummins.com
**CoorsTek, Golden, CO*

DOE Technology Development Area Specialist: Dr. Sidney Diamond
(202) 586-8032; fax: (202) 586-1600; e-mail: sid.diamond@ee.doe.gov
ORNL Technical Advisor: D. Ray Johnson
(865) 576-6832; fax: (865) 574-6098; e-mail: johnsondr@ornl.gov

Contractor: Oak Ridge National Laboratory, Oak Ridge, Tennessee
Prime Contract No.: DE-AC05-00OR22725
Subcontractor: Cummins, Inc., Columbus, Indiana

Objectives

- Optimize injection molding binder composition and sintering cycles to achieve 99+% density. This will include determination of the shrink rate during sintering for prototype tool construction and demonstration.
- Test prototype components in an intended application on Cummins Fuel System test rigs to show the viability of the material in an application.

Approach

- Make a prototype injection molding tool of a proposed Cummins Fuel Systems component and produce test pieces of the TiC/Ni_3Al cermet to near-net shape for evaluation of shrinkage, microstructure uniformity, and density.
- Conduct abuse tests of prototypes machined from isostatically pressed rods of the TiC/Ni_3Al cermet at Cummins Fuel Systems.

Accomplishments

- Achieved a 99+% dense structure with the injection molding process. The TiC distribution within the Ni_3Al matrix was uniform, and there was good wetting of the TiC particles. The shrink rate was also determined.
- Successfully tested prototypes at Cummins Fuel Systems. The components are required to withstand both sliding and impact wear. No adverse wear was observed after the testing.

Future Direction

- Finalize the design and test the injection-molded materials on Cummins Fuel Systems test rigs.
- Determine and/or develop a supply base for raw material constituents.

Introduction

Increasingly stricter diesel engine combustion emission standards and the desire of buyers for maintained or improved fuel economy require that fuel injection systems become more advanced. Higher fuel injection pressures (to aid emissions control) and more precise control of when and how much fuel is injected (for both emissions control and fuel economy) are required. New materials that exhibit excellent wear properties against steel components are needed for applications where components slide and impact against each other. One material that Cummins is interested in was developed under a DOE cooperative agreement: TiC/Ni_3Al.

TiC/Ni_3Al is a composite of TiC powder in a Ni_3Al matrix that was developed in collaboration with Oak Ridge National Laboratory (ORNL) and CoorsTek. Its composition was established to match the unique properties required for Cummins Fuel Systems applications. CoorsTek and ORNL have developed the processing methods to make the material, while Cummins has been responsible for finding an application for it, testing the material in fuel system components, and evaluating its performance against that of other materials.

Approach

The established composition of TiC/Ni_3Al cermet will be processed using the powder injection molding process to create a near-net shape component. Its microstructure, density, and shrinkage rate will be evaluated to determine the effectiveness of the manufacturing process. Coinciding with this work, fuel system rig testing of some prototype components will be conducted to evaluate the performance and wear resistance of the cermet material in a potential application in the next-generation fuel system at Cummins.

Results

The first injection-molded batch was successfully completed. It achieved over 99% density when sintered in a non-overpressure argon atmosphere. The microstructure (see Figure 1) shows the porosity and TiC particles are well distributed throughout the structure. The high- magnification scanning electron microscope (SEM) image in Figure 2 shows good wetting of the TiC particles. This first batch had a higher shrinkage rate than expected; therefore,

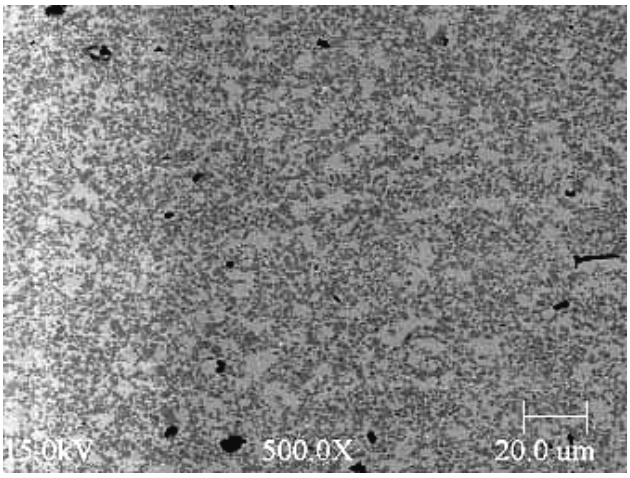

Figure 1. SEM backscattered image of polished cross-section of injection-molded TiC/Ni_3Al cermet. The black spots are porosity, the dark gray phase is the TiC, and the light phase is the Ni_3Al matrix.

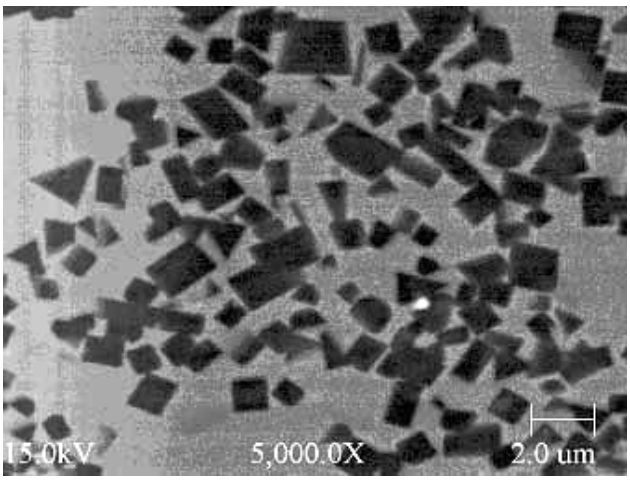

Figure 2. SEM backscattered image of the sample shown in Figure 1. No delamination between the TiC particles and the Ni_3Al particles is observed.

a second sintering run was performed after some slight tooling changes to accommodate the new shrinkage rate. This run produced similar results to the first.

The application testing at Cummins Fuel Systems commenced with parts machined from isostatically pressed rods of the TiC/Ni_3Al material. The application experiences both sliding and impact loading, and 350 hours of abusive testing was conducted between two tests. No observable damage was present on the impact surface, and the sliding wear surface was pristine, as was the mating steel component.

Conclusions

Process optimization work at CoorsTek has progressed well, and CoorsTek is able to create functional test pieces for component evaluation at Cummins. Cummins has shown that the material has a viable application in its next-generation fuel system.

3. MATERIALS FOR EXHAUST AFTERTREATMENT

A. Materials for Exhaust Aftertreatment

Paul W. Park, Herbert DaCosta, Svetlana M. Zemskova, Alex Panov, Jill R. Akers, Christie S. Ragle and Craig F. Habeger
Caterpillar Inc.
P.O. Box 1875
Peoria, IL 61656
(309) 578-4065; fax (309) 578-2953; e-mail: park_paul_w@cat.com

DOE Technology Development Area Specialist: Dr. Sidney Diamond
(202) 586-8032; fax: (202) 586-1600; e-mail: sid.diamond@ee.doe.gov
ORNL Technical Advisor: D. Ray Johnson
(865) 576-6832; fax (865) 574-6098; e-mail: johnsondr@ornl.gov

---

Contractor: Oak Ridge National Laboratory, Oak Ridge, Tennessee
Prime Contract No: DE-AC05-00OR22725
Subcontractor: Caterpillar Inc., Peoria, Illinois

Objectives

- Develop advanced materials applied for diesel engine aftertreatment systems that will comply with future emission regulations.
- Develop a prototype lean-NO_x (nitrogen oxides) catalyst system to demonstrate >50% NO_x conversion with <5% fuel penalty.
- Evaluate capabilities of commercial and near-commercial NO_x sensor technologies to meet future Environmental Protection Agency (EPA) requirement for on-board NO_x monitoring.
- Develop novel NO_x sensor materials and concepts functioning at low NO_x concentrations (<100 ppm).
- Evaluate filtration properties of various sintered metal media for application in diesel particulate filters (DPFs).

Approach

- Identify a reformer technology to provide desirable reductants for selected lean-NO_x catalyst materials, which will maximize NO_x reduction performance.
- Develop catalyst durability test protocols for sulfur and phosphorus poisoning.
- Develop test protocols and evaluate various prototype NO_x sensor technologies.
- Synthesize perovskite-type materials for NO_x sensor application.
- Develop novel NO_x sensor materials based on semiconductors functionalized with organic sensitizers.
- Use our modified test bench and new test protocols to evaluate the capability of various particulate matter trap materials.
- Identify the critical parameters for soot oxidation in catalyzed particulate filters.

Accomplishments

- Identified a promising reformer technology, "reformer-assisted lean-NO_x catalyst system" to achieve high NO_x conversion.
- Performed steady state engine tests and achieved 44% NO_x conversion with 5.6% fuel penalty.
- Identified the challenges of NO_x sensor application, including poor accuracy at low NO_x concentrations (<200 ppm) and cross-sensitivity to other gas components.
- Among prototype NO_x sensors tested, determined that a mixed-potential NO_x sensor showed better performance at low NO concentration below 100 ppm.
- Fabricated perovskite materials in-house that showed the best sensitivity to NO reported in the literature among electrochemical-type NO_x sensor materials.
- Identified semiconductor materials functionalized with organic sensitizers to show pronounced response to low NO concentrations (10 ppm).
- Found a combination of sintered metal materials that provided competitive filtration efficiency and backpressure with substantially lower volume compared with a conventional wall-flow filter material.
- Developed a test protocol that provides reliable soot loading (amount and type of soot) on cordierite, SiC, and sintered metal DPF samples, as well as regenerative capabilities of cordierite filters.

Future Direction

- Assess sulfur and phosphorus poisoning behavior on the lean-NO_x catalysts.
- Document intellectual properties resulting from the lean-NO_x project and transfer the invention to a strategic partner.
- Study the effect of a "rich" exhaust environment and cross-sensitivity of NH_3, H_2S, H_2 and hydrocarbons on NO_x sensor technologies.
- Perform durability and rapid aging tests to assess the lifetime of the selected NO_x sensors.
- Conduct a fundamental study of NO_x -sensing mechanism using a computational modeling technique.
- Catalyze sintered metal materials and evaluate their DPF regeneration features.
- Investigate the effects of temperature, space velocity, and gas composition on the soot oxidation rates in DPF samples.
- Evaluate particulate-matter regeneration and material durability of various DPF materials.

Introduction

The objective of this effort is to develop and evaluate materials that will be used in aftertreatment systems for diesel engine applications to comply with future government emission regulations. The materials include catalysts for NO_x abatement, filtration media for particulate control, and novel materials to improve NO_x sensing capabilities in the exhaust system. This year's focus is on

- development of a prototype reformer-assisted lean-NO_x catalyst system to improve NO_x reduction (>50%) and to minimize fuel penalty (<5%)
- identification of the critical parameters for soot oxidation in a catalyzed particulate filter
- further evaluation of particulate filtration characteristics of sintered metal materials, evaluation of the current state-of-the-art NO_x sensor technologies
- development of novel NO_x sensor materials to improve sensing capabilities at low NO_x concentrations (<100 ppm)

Approach

Lean NO_x. This effort focused on identifying new lean- NO_x catalyst formulations that effectively

utilize selected reductants, including H_2, CO, alkane, oxygenated hydrocarbons, or mixtures of these. The concept of reformer-assisted lean- NO_x catalysis has been assessed with various reformer technologies to identify the right reformer technology that is able to provide the desirable reductants to the catalyst materials. A prototype system consisting of a promising catalyst and a selected reformer was developed to conduct engine tests in order to demonstrate the proof of concept.

NO_x sensor. A commercially available NO_x sensor does not demonstrate adequate sensitivity and selectivity to measure the 0.2 g NO_x/bhp*h level proposed for 2010 and OBDII regulations. The objective of this project is to develop a promising NO_x sensor technology capable of meeting or exceeding EPA's 2010 standard for OBDII monitoring systems for diesel engine exhaust emissions. The approach is aimed at thorough evaluation of commercial or nearly-commercial electrochemical NO_x sensors in order to guide sensor developers to further improvements. The development of novel sensor concepts was pursued as an alternative NO_x sensor technology.

Particulate matter trap. Our modified test bench used to evaluate particulate filter materials includes a diesel fuel burner, a chemical reactor, a bench of Horiba analyzers, and a scanning mobility particle sizer (SMPS). The amount of particulate matter captured is determined using the pressure change across the sample, while the efficiency of the filter is determined using SMPS data. The composition of the exhaust from the burner is measured with the Horiba analyzers. The capability of various particulate matter trap materials, including sintered metals, was evaluated using the bench system. The system can easily be adapted to test other materials, such as cordierite and SiC particulate filters.

Results

Lean NO_x

Lean-NO_x catalyst material. A synergy effect was identified when alumina and zeolite-based materials were combined in a specific order. The combination catalyst significantly improves lean-NO_x performance with a liquid hydrocarbon reductant. (Figure 1) The kinetic parameters and the influence of fuel components on NO_x reduction performance over the selected catalyst were obtained using in-house bench test systems to further understand the efficiency of the catalysts and to provide insight into optimization strategies for a reformer technology.

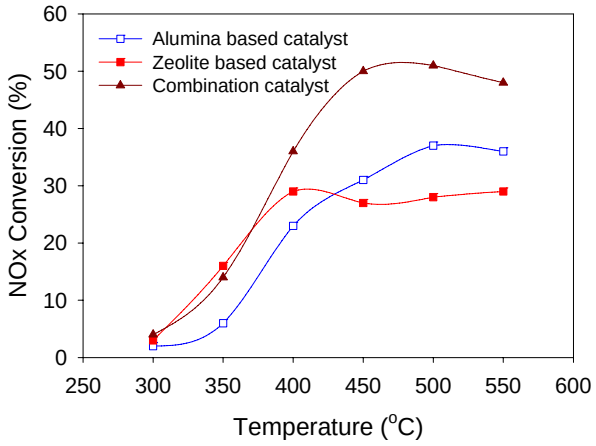

Figure 1. Comparison of NO reduction over individual catalysts and a combination catalyst tested with a liquid hydrocarbon (0.05% NO, C_1/ NO_x =3, 9% O_2, 7% H_2O, 35,000 h^{-1}).

Engine test. The engine tests were performed using two different levels of horsepower (275 and 500 hp) and two different NO_x emission-compliant engines (years 1998 and 2004) with catalysts of two different sizes (17 and 34 L), respectively. The effects of space velocity, catalyst temperature, reductant species, catalyst formulation, and reductant-to-NO_x ratios were studied. The results showed 44% NO_x conversion was achieved with a 5.6% fuel penalty from weighted OICA steady state cycles (nine selected modes). The test results showed that the reformer significantly enhanced NO_x reduction performance and reduced the fuel penalty (Figure 2).

NO_x Sensor

Commercial and nearly-commercial NO_x sensor technologies. Evaluation of state-of-the-art NO_x sensor technology in the presence of 0–1000 ppm ammonia showed that the sensor output increases with increasing NH_3 concentration, while the NO_x analyzer reading (used for control purposes) remained constant (Figure 3). This cross-sensitivity substantially limits sensor applications under "fuel-rich" environments or in the presence of reductants such as NH_3 (ammonia/urea selective catalytic reduction), H_2 (reformer technology), and C_xH_y (hydrocarbons selective catalytic reduction). In addition, the sensor showed poor resolution at low

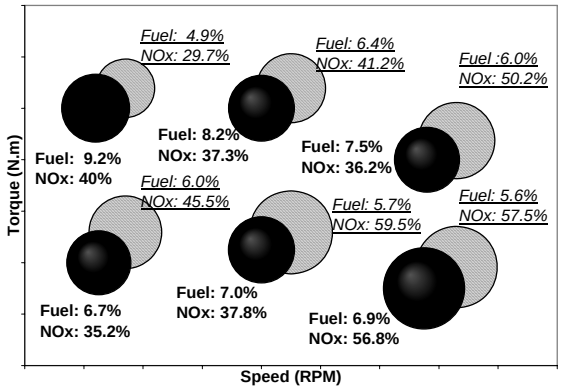

Figure 2. NO_x reduction performance and fuel penalty data obtained from selected OICA steady state cycles of a diesel engine equipped with a prototype reformer-assisted lean- NO_x catalyst system. Black circles: without reformer, Shaded circles: with reformer.

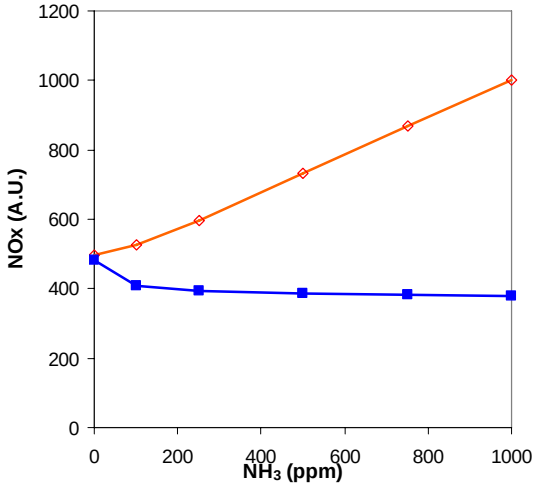

Figure 3. Output from a commercial sensor (diamonds) and a NO_x analyzer (squares) as a function of ammonia concentration.

NO_x concentrations. Evaluation of nearly-commercial NO_x sensor technologies in low NO_x concentrations has been completed. One sensor has been identified as exhibiting a good linear response to low NO concentrations, specifically in the range of 0–20 ppm. Reproducibility tests showed that the sensor response can vary by up to 4.5% and needs further improvement

Perovskite-type NO_x sensor materials. Novel amperometric-type electrodes on yttria-stabilized zirconia (YSZ) as solid electrolyte and La/Fe perovskites (ABO_3 composition) as chemically interactive material (CIM) were prepared in-house by screen-printing and tape-casting techniques (Figure 4). Materials were tested at low NO concentrations (<100 ppm) in the presence of 0–20% O_2 in N_2 at 700–800ºC. Materials exhibited much higher conductivity (up to 400 mA) in comparison with other mixed metal oxides described in the literature and showed better NO_x sensitivity. The CIM cited in literature[1] exhibited an amperometric NO_x sensor output that yielded Δ47 mA for the increment of 500 ppm NO, while the La/Fe materials prepared in our study showed a Δ5–25mA output increase for the increment of 15–50 ppm NO at applied voltages greater than 0.8V (Figure 5). These are the best results reported in the literature for electrochemical type NO_x sensor materials.

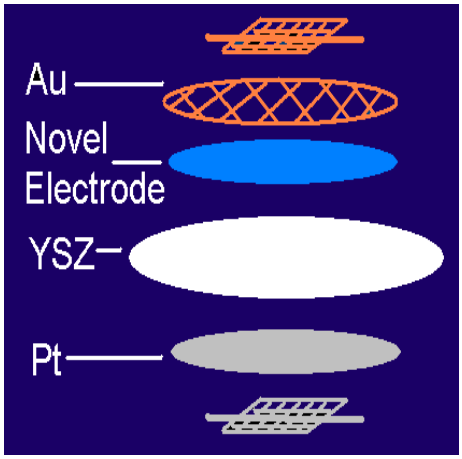

Figure 4. Schematic of a novel electrode fabrication for a NO_x sensor.

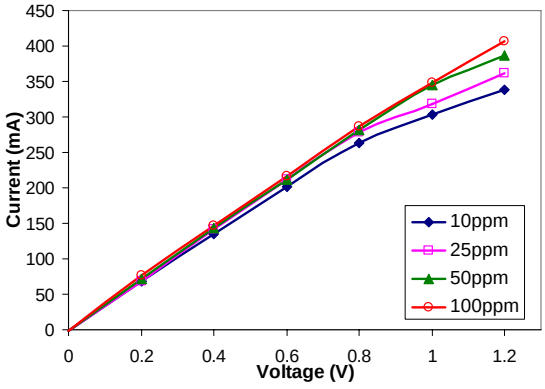

Figure 5. I(V) response curves of an amperometric La/Fe sensor at various NO concentrations (ppm).

Semiconductors functionalized with organic sensitizer NO_x sensor materials. Functionalized semiconductor materials were evaluated for optical detection of NO. Semiconductor-coated quartz sub-

strates were provided by a supplier or prepared in-house by the spray-pyrolysis method using organometallic precursors. The dip-coating method was used to prepare sensitized semiconductor materials. The UV-VIS tests at ambient conditions showed that pronounced response to 10 and 100 ppm NO was exhibited. Therefore, a novel NO_x sensor concept employing functionalized semiconductor materials can be developed. This concept offers many advantages over traditional electrochemical sensor technologies such as direct NO measurement, including no requirement for a catalyst or a heater.

Particulate Matter Trap

We have completed and submitted for publication a work in collaboration with Jinyu Zhu and Kyeong Lee from Argonne National Laboratory on the characterization of particulates produced in our diesel fuel burner, focusing on morphology, microstructures, and fractal geometry. This work revealed that diesel particulate matter produced using the newly developed test protocol shows morphological characteristics similar to those of the particulates produced in diesel engines.

The first and second generations of test protocols were developed for soot oxidation studies on DPFs that provide consistent soot loading on the DPF samples. The protocol was used with our bench to evaluate new DPF filtration media based on sintered metal technology. Preliminary results indicated that a combination of new sintered metal materials yielded competitive filtration efficiency (Figure 6) and backpressure (Figure 7) with substantially lower volume compared with a commercial wall-flow cordierite DPF tested under the same conditions. Further work is in progress to validate the tests described in this report and to apply this approach to regenerate particulate matter accumulated on various filtration materials.

Conclusions

The research has demonstrated a prototype reformer-assisted lean-NO_x system that has the potential to achieve >50% NO_x conversion with a <5% fuel penalty with the optimization of catalyst materials as well as fuel injection strategy. The comercialization plan has been being developed through the collaboration of strategic partners. The current

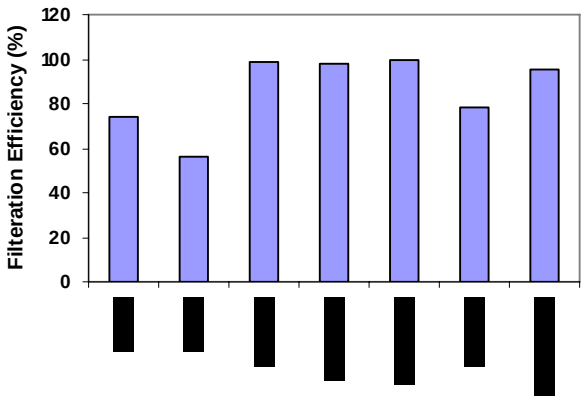

Figure 6. Comparison of filtration efficiencies of various sintered metal media (SM series) and an un-catalyzed wall flow cordierite particulate filter.

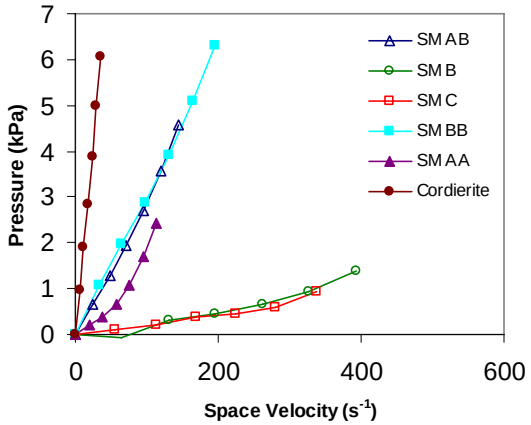

Figure 7. Comparison of backpressure as a function of space velocity for various sintered metal media (SM series) and an un-catalyzed wall flow cordierite particulate filter.

electrochemical NO_x sensor concept has limitations owing to poor accuracy at low NO_x concentrations and cross-sensitivity to ammonia. The novel NO_x sensor concepts studied in this program showed promising results and warrant further development. The testing performed with sintered metal filtration media indicates that this material has competitive filtration efficiency and backpressure compared with a traditional wall-flow cordierite filter and provides a significant reduction in volume. This material, therefore, deserves further testing to confirm these results and examine its regenerative properties.

Reference

1. F. Menil et al., "Critical Review of Nitrogen Monoxide Sensors for Exhaust Gases of Lean Burn Engines," *Sensors and Actuators B67*, 1–23, 2000.

Publications/Presentations

Carrie L. Boyer and Paul W. Park,"Effect of SO_2 on the Activity over $Ag/\gamma\text{-}Al_2O_3$ Catalysts for the Reduction of NO_x in Lean Conditions," submitted to *Appl. Catal. B.*

Svetlana Zemskova, Paul W. Park, J. S. Lin, J. Wen, and I. Petrov, "Study of High Surface Area Alumina and Ga-alumina Materials for deNO_x Catalyst Applications," presented at the 28th International Conference and Exposition on Advanced Ceramics and Composites, Cocoa Beach, FL, January 25–30, 2004.

Craig F. Habeger, "Requirements for NO_x Sensors in Heavy Duty Diesel Exhaust Environments," presented at the 28th International Conference and Exposition on Advanced Ceramics and Composites, Cocoa Beach, FL, January 25–30, 2004.

Jinyu Zhu, Kyeong Lee, Alexander Panov, and Jill Akers, "An Investigation of Particulate Morphology, Microstructures, and Fractal Geometry for a Diesel Engine-Simulating Combustor," SAE paper 2004-01-3044, Society of Automotive Engineers, 2004.

Patents Issued

Paul W. Park, "Metal/Metal Oxide Doped Oxide Catalysts Having High deNO_x Selectivity for Lean NO_x Exhaust Aftertreatment Systems," U.S. Patent 6,706,660, March 16, 2004.

Paul W. Park, "Method of Preparing Doped Oxide Catalysts for Lean-NO_x Exhaust," U.S. Patent 6,703,343, March 9, 2004.

B. Development of Materials Analysis Tools for Studying NO_x Adsorber Catalysts

Thomas Watkins, Larry Allard, Doug Blom, Michael Lance, Harry Meyer, and Chaitanya Narula
Oak Ridge National Laboratory
P.O. Box 2008,
Oak Ridge, TN 37831-6064
(865) 574-2046; fax: (865) 574-3940; e-mail: watkinstr@ornl.gov

DOE Technology Development Area Specialist: Dr. Sidney Diamond
(202) 586-8032; fax: (202) 586-1600; e-mail: sid.diamond@ee.doe.gov
ORNL Technical Advisor: D. Ray Johnson
(865) 576-6832; fax: (865) 574-6098; e-mail: johnsondr@ornl.gov

Contractor: Oak Ridge National Laboratory, Oak Ridge, Tennessee
Contract No.: DE-AC05-00OR22725

Objective

- Produce a quantitative understanding of the process/product interdependence leading to catalyst systems with improved final product quality, resulting in diesel emission levels that meet the 2007 emission requirements.

Approach

- Characterize lab-engine tested samples with X-ray diffraction (XRD), spectroscopy, and microscopy. Correlate findings with Cummins data and experience.

Accomplishments

- Supported continued characterization of new materials from various stages of the catalyst's life cycle.
- Obtained rates of desulfation and activation energies for various catalytic compositions after different periods of aging.
- Continued ex-situ microstructural, microchemical, and crystallographic studies of these new materials in simulated engine environments.

Future Direction

- Evaluate gradient formation on a macro scale of active elements on a catalyst as a function of catalyst history and operating conditions.
- Evaluate thermal degradation of a No_x stoichiometric reduction (NSR) catalyst as a function of macroscopic position within the catalyst support brick.
- Determine the soot and ash distribution as a function of macroscopic position within the NSR catalyst support brick.

Introduction

To meet the 2007 emission requirements for diesel exhaust, aftertreatment in diesel engines may be necessary. The technology for 2007 will need to integrate aftertreatment with engine control systems. Currently, no commercial off-the-shelf technologies are available to meet these standards. Consequently, Cummins, Inc., is working to understand the basic science necessary to effectively use these catalyst systems. ORNL is assisting with the materials characterization effort.

Base-metal oxides (BMOs) are major components in current nitrogen oxides (NO_x) adsorber catalysts that Cummins seeks to use in aftertreatment systems that contain NO_x adsorber catalysts. Although the function of these adsorbers is to collect surface nitrite/nitrate (NO_x) species, they also collect oxy-sulfur (SO_x) species. Both species are to be released from these surface sites during different regenerations, during which the adsorber BMO is either heated to some critical temperature and/or exposed to a reducing or reactant atmosphere. Sulfur adsorption is unfortunately a form of poisoning of adsorber catalysts and is a major problem that must be resolved for BMO-based emission reduction technologies to become commercially viable.

Approach

In general, the crystal structure, morphology, phase distribution, particle size, and surface species of catalytically active materials supplied by Cummins will be characterized using XRD, Raman spectroscopy, and electron microscopy. These materials will come from all stages of the catalyst's life cycle: raw materials, as-calcined, sulfated, regenerated, etc. Both ORNL and Cummins personnel have participated in this work.

Samples

Briefly, a Cummins catalyst supplier provided "core" samples taken from cordierite "bricks" containing the catalyst along the exhaust path for the following conditions: fresh (unused), degreened (zero desulfation hours), and engine-aged catalysts (>zero desulfation hours). Three main variables were considered with these samples: platinum (Pt) loading (1 or 2 wt %), brick position (1, 2, 3 or 4; 1 most upstream), and desulfation hours (the number of hours the catalyst system is at the desulfation temperature of ~500°C; actual engine time ~150% of desulfation time). The X-ray and spectroscopy work on these samples was discussed previously.[1] The remainder of the microscopy work for these samples is presented in this report.

New engine-tested brick/core and powder samples were examined in FY 2004. These samples consisted of a series of cores with varied amounts of Pt loading, a sample that had lost performance after numerous desulfations, and a sample loaded with sulfur. The powder samples contained Pt, γ-alumina, and BMOs, such as $BaCO_3$.

Results

X-ray

XRD and neutron powder diffraction (NPD) were employed to aid understanding of the crystalline nature of the samples. For the unfamiliar, the following analogy can be applied: As a fingerprint identifies a person, so a diffraction pattern identifies a crystalline material.

Preliminary NPD was attempted with the idea that phases containing lighter elements, namely the target BMO, could be observed. The washcoat components, cordierite ($Mg_2Al_2Si_5O_{18}$) and possibly Pt, were identified in brick 3, 2 wt % Pt, 1000 desulfation hours. However, no BMO-containing phases were identified/observed. Given the circumstances under which the data were taken, NPD should be revisited in the future when a more appropriate and optimized instrument is available.

Three phases were observed in the E270-3 samples (composition differs from the sample described in the preceding paragraph) with synchrotron radiation: Pt, γ-alumina (washcoat), and cordierite. The samples varied in Pt content and were run for months at 500°C, cycled in with hydrogen and no sulfur. XRD indicated that the order of decreasing Pt content was E271 (most), E272, 273, and E270 (least); while the chemisorption indicated E270 (most), E271, 272, and E273 (200, 100, 50, 25 g/ft^3, respectively). The crystallite size was effectively ~34 nm for all four samples. Two other core samples ("commercial samples") were examined with laboratory XRD: one that lost performance after numerous desulfations (Exp6&7) and one that was "loaded" with sulfur (E358-03).

Washcoat components, cordierite, and Pt were identified in both samples. No sulfur-containing compounds were observed. The crystallite size was 10 and 4 nm for samples Exp6&7 and E358-03, respectively, which is in agreement with the observed loss in catalytic performance. Comparison with prior data[1] suggests that sample Exp6&7 has undergone the equivalent of 150 hours of desulfation at 500°C.

A set of FRESH powders was examined with high-temperature XRD. Samples E362a, E363a, and E364a contain a series of BMOs, respectively, which are reported to be stabilizers for Pt. Pt and γ-alumina were identified by XRD in all of these samples. The high-temperature XRD data for all samples showed Pt coalescence/sintering occurring at temperatures in excess of 450°C (e.g., Figure 1), as evidenced by the breadth narrowing and intensity increase of the (111) and (200) Pt peaks. The high-temperature XRD data for sample E364a (FRESH, $BaCO_3$) showed the $BaCO_3$ decomposing/reacting with the Al_2O_3 to form a spinel, $BaAl_2O_3$ (see Figure 2).

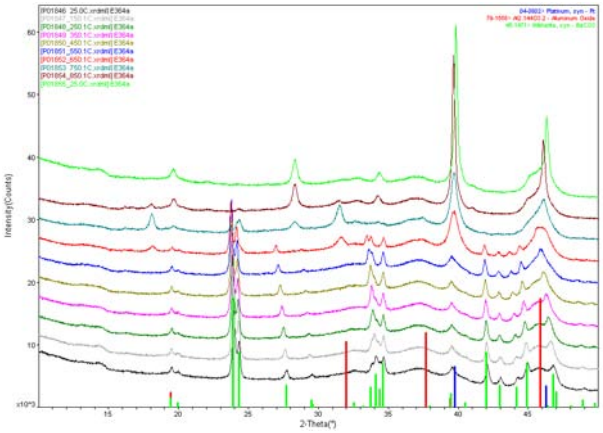

Figure 1. The diffraction patterns for E364a as a function of temperature.

Spectroscopy

Spectroscopic techniques provide important information about the chemical state of and identification of adsorbed surface species. Two complementary spectroscopic techniques are Raman spectroscopy and X-ray photoelectron spectroscopy (XPS), which provide molecular and low-frequency vibrational information, respectively.

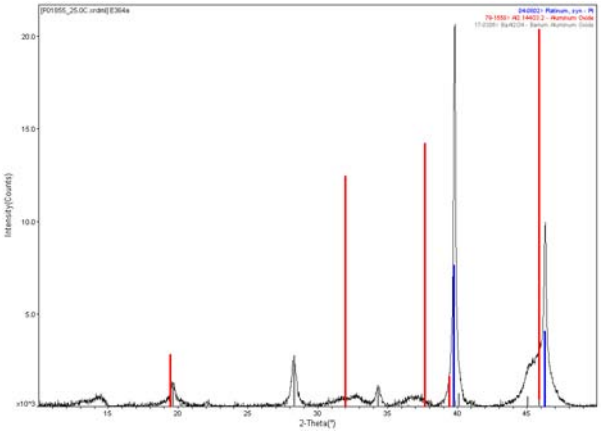

Figure 2. The diffraction pattern for E364a after exposure to elevated temperatures.

Raman

Raman spectroscopy measures the characteristic vibrational energy levels of molecules and crystals and so is very sensitive to any changes in bonding, stoichiometry, and phase/symmetry. In this case, frequency changes of a washcoat component vibration were monitored with desulfation time. Previously, we discovered a decrease in peak width and the increase in peak position of a washcoat-attributed Raman band, which occurs as a result of the growth of the Pt particle size. Although Raman spectroscopy could not directly measure the Pt particle size in these samples, the changes in the Raman spectra with Pt size were calibrated for this specific catalyst formulation so that Raman could nondestructively measure Pt particle coarsening. The origin of the change in Raman spectrum was determined using molecular simulations, as shown in Figure 3. When a Pt atom is adsorbed onto a washcoat particle, the Pt will change the electron charge density by forming a metallic bond with one of the washcoat atoms. This in turn increases the force constants of the washcoat components (see Table 1). Since the bonds are getting stronger, they vibrate at a higher frequency, which explains why the Raman bands increase in frequency with Pt.

Raman spectroscopy is also very sensitive to adsorbed sulfur on the support. The vibration of the SO_4^{-2} species has a band at ~960 cm^{-1}. Using a high-temperature stage, the amount of sulfur present on a BaO support was monitored in situ in a reducing atmosphere. By monitoring the relative peak heights of $BaSO_4$, $BaCO_3$, and BaO with

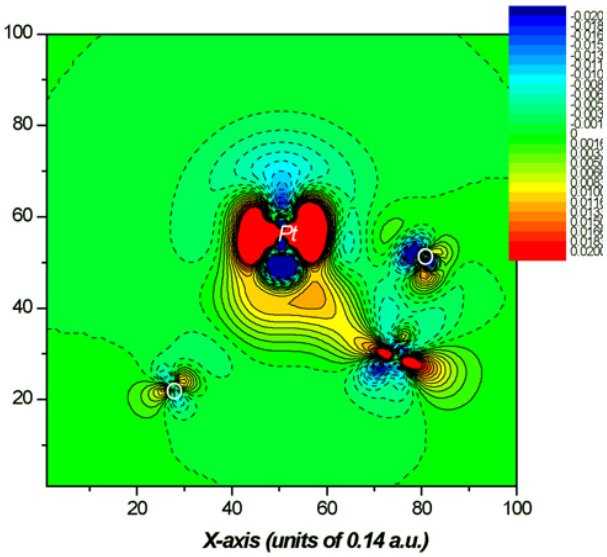

Figure 3. The *change* in electron charge distribution that originates from chemical bonding between Pt and the washcoat material. Regions where electrons are withdrawn (blue), and where the charge density is increased (red). The predicted change in force constant describes the observed shift in the Raman spectrum.

Table 1. The force constants of a washcoat component before and after Pt adsorption. The K value (in mdyne/Å) generally increases, causing the Raman peaks to shift to higher frequency with Pt concentration

K1(host)	K2(w.Pt)	Site
0.032	0.086	O^1 x
0.093	0.112	O^1 z
0.033	0.038	WC x
0.077	0.113	WC z
0.003	0.005	O^2 x
0.017	0.009	O^2 z

time at different temperatures, the activation energies for sulfation were directly measured. Table 2 shows activation energies for sulfation with and without Pt present and with and without oxygen present. The activation energies for both BaO and $BaCO_3$ were measured simultaneously since these two phases had peaks in different positions. Three main observations were taken from these results. First, Pt reduces the activation energy in all cases, which is expected. Second, the presence of oxygen reduces the activation energy for sulfation. This suggests that O_2 participates in the formation of $BaSO_4$ by donating an oxygen atom by the following equations:

Table 2. The activation energy of sulfation (kcal/mole) in four conditions, with and without Pt and O_2. The presence of Pt reduces the activation energy, as does an oxidizing environment

O_2 present?	Pt present?	BaO	$BaCO_3$
No	No	17.8	25.4
No	Yes	11.0	17.9
Yes	No	11.6	15.9
Yes	Yes	7.4	13.1

$$BaCO_3 + SO_2 + ½\ O_2 \rightarrow BaSO_4 + CO_2$$

and

$$BaO + SO_2 + ½\ O_2 \rightarrow BaSO_4.$$

However, this means that the reaction can proceed only with O_2 present. Since we have measured sulfation in an anaerobic environment, we believe that the extra oxygen must therefore come from the bulk lattice of the BaO and $BaSO_4$. Third, the sulfation of BaO is easier than that of $BaCO_3$. These results show the power of Raman spectroscopy for monitoring surface reactions in situ on these catalyst materials. By changing the gaseous environment, we can infer what chemical reactions are taking place and then take steps to improve the catalyst system based on this new information.

X-ray Photoelectron

XPS was used to analyze chemistry along the length (~5 cm) of individual "troughs" or channels of several "as run" brick/core samples. Figure 4 shows the S 2p, Cl 2p, and Pt 4f core level intensities as a function of position along the catalyst trough of sample E358-03. The sulfur concentration was highest on one end and fell to near-zero intensity by the midpoint of the core. As the sulfur intensity diminished, the chlorine signal grew, reaching a maximum of >1 at. %. Measurements of the Pt 4f core level show a slight decrease at the high-sulfur end, but the overall signal intensity is weak, making the significance of this decrease uncertain. In contrast, the results for sample Exp6&7 showed significant sulfur at only one end of the core, at the position of the first measurement (see Figure 5). Figure 5 also shows that the chlorine intensity was higher in this sample overall and showed an increase from its lowest value at the high-sulfur end of ~2 at. % to a maximum of 5–6

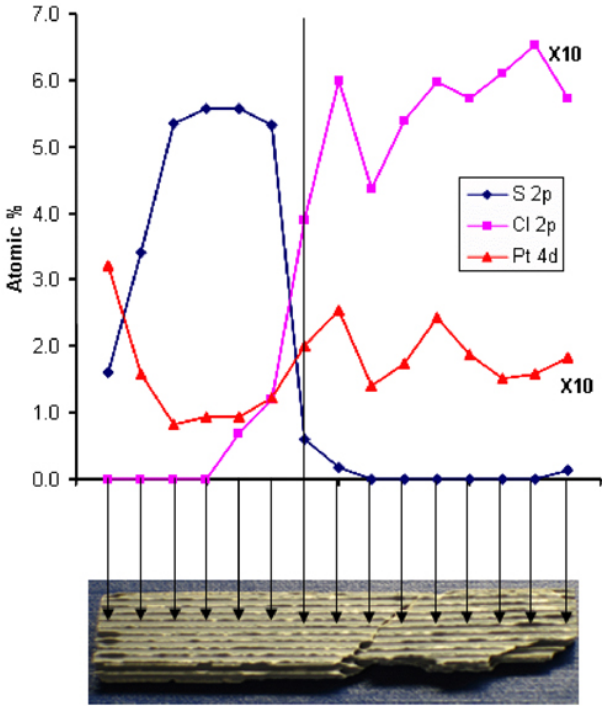

Figure 4. S 2p, Cl 2p, and Pt 4f signals as a function of position along a single catalyst trough/channel of sample E358-03. These signal intensities, along with other minor and major component intensities, were used to calculate the at % of each constituent. Measurements were made every ~5 mm, as indicated on the photo.

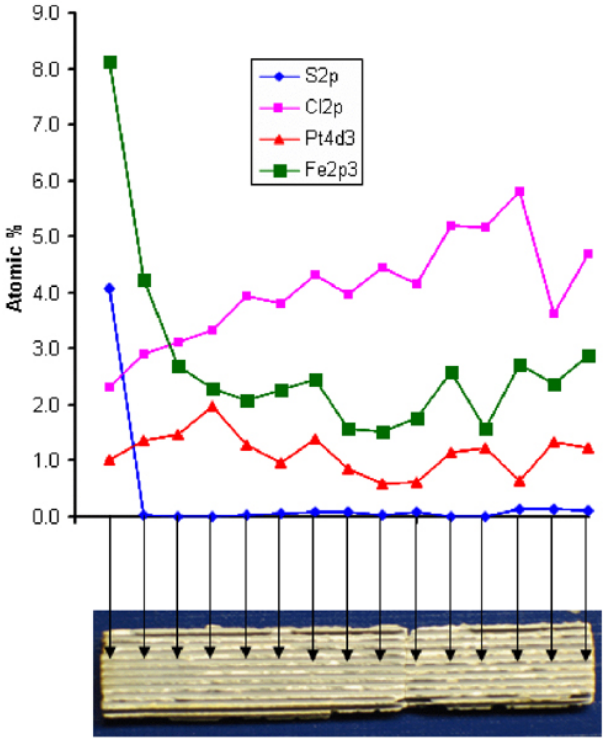

Figure 5. S 2p, Cl 2p, Fe 2p and Pt 4f signals as a function of position along a single trough/channel of sample Exp6&7. These signal intensities, along with other minor and major component intensities, were used to calculate the atom % of each constituent. Measurements were made every ~5 mm, as indicated on the photo.

at. % at the opposite end. As with sample E358-03, the Pt showed little variation from one end to the other. A small but significant amount of iron, ~8 at. %, was detected on this sample at the sulfur-end of the core. This rapidly decreased to ~2 at. % by the third measurement location and remained near this level for all other measurements. Taken together, these measurements demonstrated that this measurement technique was helpful in understanding sulfur distribution. The value of this technique was that the measurements were done on real monolith core samples, not samples that were handled or treated specially for ultra-high vacuum surface analytical techniques.

Four brick/core engine-aged samples were desulfated at temperatures of 450, 500, 550 and 600°C and examined using XPS. Figure 6 shows the S 2p core level intensity as a function of position along an individual catalyst channel/ trough for each. There is a definite trend going from 450 to 550 to 600°C. All samples show similar (1.5–2 at. %) and high sulfur at one end versus the other. Each also shows a drop from this initial

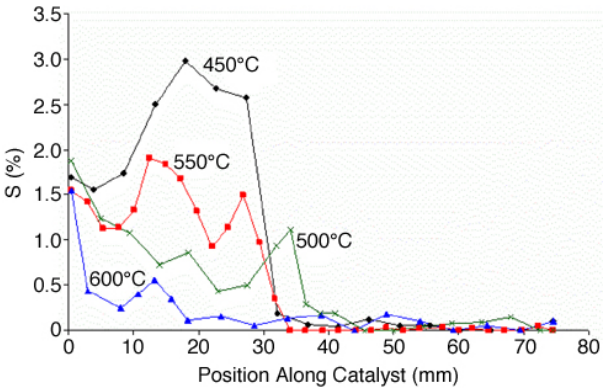

Figure 6. Sulfur concentration, as determined by XPS measurements, as a function of position along individual catalyst troughs for samples desulfated at 450, 500, 550, and 600°C. Measurements of the S 2p signal intensity were made every 3–5 mm.

value along the first centimeter of the core. After the initial decrease, all samples show an increase. The length over which the increase occurs varies from 450°C (~1.5 cm) to 550°C (~1 cm) to 600°C (~0.5 cm). The sulfur concentration then de-

creases, reaching near-zero levels by the midpoint of the core. There also appears to be a second, smaller rise for the 450 and 550°C samples at ~3 cm. The 500°C sample showed a similar initial high sulfur level (in fact, the highest of all the samples) but then exhibited a general decrease over the first half of the core before reaching near-zero levels. Two separate trials on two different (but nearly adjacent) troughs showed the 500°C was self-consistent. Further studies should be attempted to determine the reason that this sample did not follow the trend of the others. No significant trends for other minor components were noted. Chlorine levels for the four samples were generally low and did not correlate with the sulfur signal as noted above for sample E358-03. This study showed that tracking the sulfur on real catalyst cores was feasible and showed trends versus desulfation temperature.

Microscopy

Transmission electron microscopy (TEM), scanning transmission electron microscopy (STEM), and electron probe microanalysis (EPMA) techniques were used to continue characterization of the microstructure of the NO_x trap catalysts. In the previous report, the microstructure and chemistry of samples with 1 wt % Pt loading at different positions along the reactor were studied; and the changes in morphology of Pt particles, as well as the distribution of elements such as the trapping component within the washcoat, were elucidated. In subsequent work, a series of samples with 2 wt % Pt loading were studied in like fashion. Some example results and main conclusions from the microscopy and microprobe experiments are given below.

In contrast to the 1 wt % Pt loading results, high-resolution bright-field TEM images of the 2 wt % Pt fresh catalyst did in fact clearly reveal discrete Pt catalyst particles (see Figure 7). Similar results were obtained with high-angle annular dark-field (HA-ADF) images taken in the Hitachi HD-2000 STEM instrument. The de-greened samples showed discrete fine particles of Pt, on the order of 5 nm in diameter, using both TEM and STEM methods. HA-ADF images on the STEM provided a facile method for imaging the particles in high contrast and for measuring particle sizes. These measurements were made on all observed

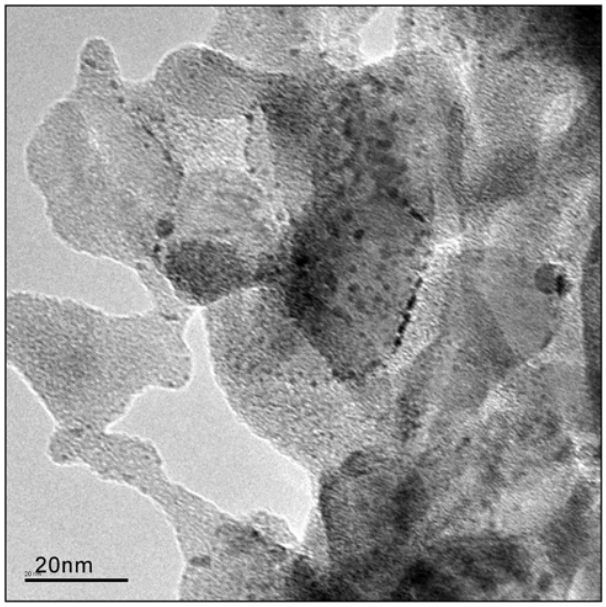

Figure 7. Bright-field TEM micrograph of fresh 2 wt % Pt catalyst sample with discrete Pt particles evident in brick 2, FRESH.\

samples (except the fresh specimen). Samples from the bricks with 2 wt % Pt loading with 150, 500, and 1000 desulfation hours displayed 8-, 10.5-, and 11.5-nm particles, respectively. Figure 8 shows the HA-ADF image of brick 2 with 150 desulfation hours, for example. The results were nearly identical, with respect to average particle size, to those obtained from the 1 wt % Pt samples, with only a slight increase of about 1 nm in the diameters of particles in the 500 and 1000 desulfation hour samples.

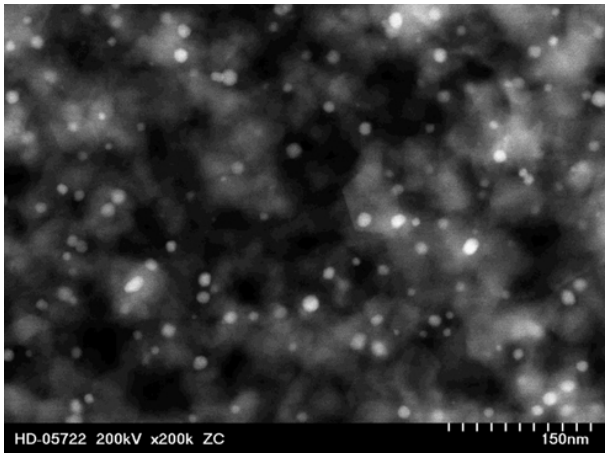

Figure 8. Z-contrast STEM image illustrating dispersion and size of 2 wt % Pt particles in brick 2 after 150 hours of deS.

EPMA was used to determine the bulk distributions and quantitative measurements of the Pt trapping component and sulfur species by acquiring X-ray counts from small regions from the outer surface of the washcoat layer into the cordierite framework. These measurements mapped Pt at the 2 wt % level, as expected. The trapping component initially was present also at about the 0.7–0.8 wt % level, and sulfur in all the 2 wt % Pt samples was less than 0.1 wt % in the bulk of the washcoat; but it seemed to concentrate in thin layers at the cordierite-washcoat interface. Unlike the 1 wt % Pt samples, where Pt showed concentrations primarily at free surfaces within and external to the two washcoat layers, Pt was very uniformly dispersed within the washcoats of the 2 wt % Pt samples (see Figure 9). The differences are likely due to different rates of drying employed in deposition of the washcoats on the cordierite support. In the fresh samples, the trapping component was sometimes observed to be strongly concentrated at the interface between the inner washcoat and the cordierite framework material. In most samples, however, the trapping component showed a uniform concentration, with occasional high concentrations in very small, widely scattered regions.

The trapping component concentration remained very uniform throughout the washcoat with engine aging, but the overall concentration decreased by 150 desulfation hours to about the 0.5 wt % level. As with 1 wt % Pt samples, this result is important because it shows the trapping component that is available for NO_x adsorption, whereas the XRD data showed only total trapping component. Thus the decrease in the total amount of trapping component coupled with the increase in Pt particle size could suggest a reduction in the total number and surface area of Pt-trapping component contact sites upon aging. This would also explain the reduced performance of the NO_x trap. Energy-dispersion spectroscopy spectra in the TEM showed small trapping component peaks, but no discrete trapping component phase was detected. Platinum particle sizes at brick positions 1 and 4 in 2 wt % Pt loaded samples were similar to those of brick 2, indicating that the particle growth behavior was similar regardless of sample position in the reactor.

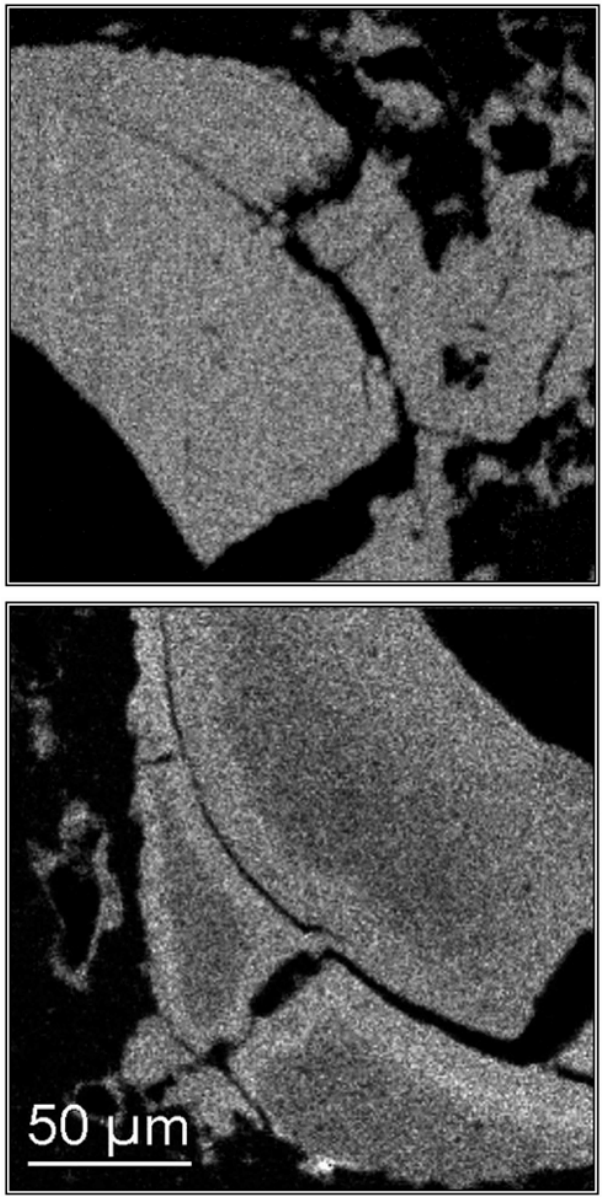

Figure 9. Two EPMA Pt X-ray maps demonstrating differences in dispersion of Pt between the (a) 1 wt % Pt and (b) 2 wt % Pt in both bricks after 150 hours of deS. Pt is uniformly distributed in the 2 wt % sample; in the 1 wt % sample, it is higher at the surface and free surfaces throughout the washcoat than in the bulk.

References

1. Thomas Watkins, Larry Allard, Doug Blom, Michael Lance, Chaitanya Narula, and Harry Meyer, "Development of Materials Analysis Tools for Studying NO_x Adsorber Catalysts," *Heavy Vehicle Propulsion Materials 2003 Annual Progress Report*, Energy Efficiency and Renew-

able Energy Office of FreedomCAR and Vehicle Technologies, March 2004.

Publications

H. L. Fang and M. J. Lance, "Influence of Soot Surface Changes on DPF Regeneration," accepted for publication in *J. Soc. Auto. Eng.* (2004).

J. Parks, A. Watson, B. Epling, L. Campbell, R. England, N. Currier, A. Yezerets, H. Fang, T. Yonushonis, T. Gallant, T. Watkins, D. Blom, L. Allard, M. Lance, H. Meyer and C. Narula, "NO_x Absorber Catalyst Durability: Light- and Heavy-Duty Perspectives," pp. 304–311 in *Proceedings of 2003 DEER Conference: 9th Diesel Engine Emission Reduction Conference*, August 24–28, 2003, Newport, RI.

Presentations

T. R. Watkins, L. Allard, D. Blom, M. J. Lance, C. Narula, H. Meyer, R. D. England, H. Fang, and T. Yonushonis, "Development of Materials Analysis Tools for Studying NO_x Adsorber Catalysts," presented at NLCat 2003, 4th DOE National Laboratory Catalysis Conference, Oak Ridge, Tennessee, October 23, 2003.

T. R. Watkins, L. Allard, D. Blom, M. J. Lance, C. Narula, H. Meyer, R. D. England, H. Fang, and T. Yonushonis, "Development of Materials Analysis Tools for Studying NO_x Adsorber Catalysts," presented at the 53th Annual Denver Conference, Steamboat Springs, Colorado, August 2, 2004.

T. R. Watkins, L. Allard, D. Blom, M. J. Lance, C. Narula, H. Meyer, R. D. England, H. Fang, and T. Yonushonis, "Development of Materials Analysis Tools for Studying NO_x Adsorber Catalysts," presented by D. R. Johnson at the 10^{th} Diesel Engine Emission Reduction (DEER) Conference, Coronado, California, August 30, 2004.

C. Development of NO_x Sensors for Heavy Vehicle Applications

David L. West, Fred C. Montgomery, Timothy R. Armstrong,
Jaco H. Visser and David J. Kubinski**
Oak Ridge National Laboratory
P. O. Box 2008, Mail Stop 6063
Oak Ridge, TN 37831-6063
(865) 574-5377; fax (865) 574-6918; blaupj@ornl.gov
**Scientific Research Laboratory, Ford Motor Co.*

DOE Technology Development Area Specialist: Dr. Sidney Diamond
(202) 586-8032; fax: (202) 586-1600; e-mail: sid.diamond@ee.doe.gov
ORNL Technical Advisor: D. Ray Johnson
(865) 576-6832; fax: (865) 574-6098; e-mail: johnsondr@ornl.gov

---

Contractor: Oak Ridge National Laboratory, Oak Ridge, TN
Prime DOE Contract Number DE-AC05-00OR22725;
Subcontractor: Ford Motor Company, Detroit, Michigan

Objectives

- Develop nitrogen oxides (NO_x) sensors for remediation and monitoring of diesel engine exhausts.
  - Sensors should have an operating temperature of 500–700°C and be able to measure NO_x concentrations from ~1 to 1500 ppm at oxygen levels from 5 to 20 vol %.
  - Since NO_x is a mixture of NO and NO_2, it would be useful to have sensors selective for either NO or NO_2 or able to measure "total NO_x" ([NO] + [NO_2]).

Approach

- Fabricate prototype sensing elements by screen printing electrode layers onto oxygen-ion-conducting substrates [typically yttria stabilized zirconia (YSZ)].
- Operate elements either in a non-Nernstian mode (where the output is a voltage) or under dc electrical bias.
- Characterize elements for NO_x response, sensitivity to varying O_2, and recovery/response kinetics.

Accomplishments

- Demonstrated NO_2 sensing elements with extremely high sensitivity (50 mV/decade at 700°C, 7 vol % O_2 over the concentration range 20–200 ppm_V NO_2).
- Demonstrated biased NO-selective sensing elements.
- Constructed both types of elements to consist of co-planar electrodes, one oxide electrode and the other a noble metal (usually platinum).

Future Direction

- Determine the effects of H_2O on sensing element performance and stability. (Diesel exhausts are rich in H_2O, typically 4–15 vol %).
- Characterize cross-sensitivity to other species often found in diesel exhausts (CO, hydrocarbons, CO_2).
- Evaluate long-term stability of these sensing elements in atmospheres simulating diesel exhaust.

- Investigate use of low-frequency ac biasing, especially the effect on drift of the baseline sensor response compared with dc-biased elements.

Introduction

The primary pollutants (excluding the greenhouse gas CO_2) from the combustion of low-sulfur fuels are CO, hydrocarbons, and NO_x. Spark-ignited, direct-injection (SIDI) auto and truck engines employ a three-way catalyst (TWC) that can remove all three of these pollutants. However, the TWC is only effective over a narrow range of O_2 in the exhaust, losing its effectiveness for NO_x removal at high partial pressures of O_2. This means that the currently employed TWC is not effective for NO_x remediation of the exhaust from compression-ignited (diesel) engines, as these are O_2-rich (typically 5–20 vol % O_2).

In the current absence of a "lean-NO_x" catalyst, three technologies have been proposed to meet the challenge of NO_x remediation of diesel exhausts: lean-NO_x traps (LNTs), selective catalytic reduction (SCR) with hydrocarbons, and SCR with urea. All of these technologies will require on-board NO_x sensors, to control trap regeneration (LNT) or reagent injection (SCR).

This project is developing NO_x sensing elements that can be used in diesel engine exhausts. The minimum requirement for this application is an operating temperature of 500–700°C and the ability to measure 1–1500 ppm NO_x. It should be emphasized that "NO_x" refers to mixtures of NO and NO_2; therefore, full NO_x characterization of the exhaust may require that two of the following three concentrations be measured: NO, NO_2, or NO_x (= NO + NO_2). This project is a cooperative research and development agreement with Ford Motor Company.

Approach

Some sample geometries for prototype sensing elements are shown in Figure 1. The YSZ substrate is manufactured in-house using Tosoh TZ8YS YSZ powder, and the electrodes (oxide and platinum) are screen-printed and fired. Inks for the platinum electrode are typically obtained commercially; for the oxide electrode, inks are formulated in-house

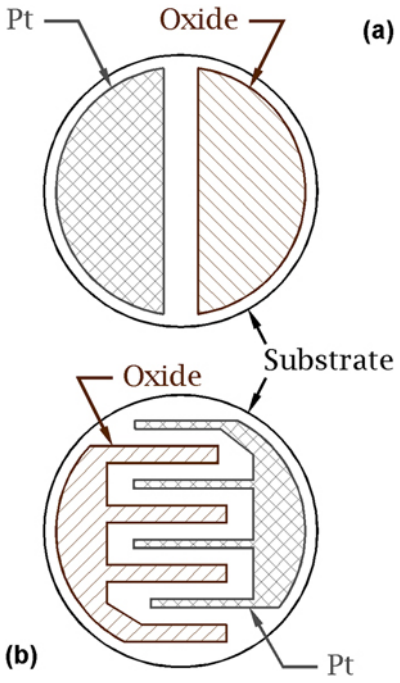

Figure 1. Schematic semicircular (a) and interdigitated (b) sensing element geometries.

using proprietary methods and materials. The precise composition of the oxide electrode is dictated by the target application of the sensing element. For non-Nernstian NO_2 sensing elements, a binary transition metal oxide electrode is sufficient. [The term "non-Nernstian" is used because in the presence of 10–100 ppmv of NO_2, these elements can produce large dc output voltages (on the order of 0.1 V), which far exceed the predictions of the Nernst equation.] For sensing elements that will be biased to yield NO-selective behavior, a more complex oxide electrode is required.

The sensing elements depicted schematically in Figure 1 can be operated in either non-Nernstian or biased mode. In non-Nernstian mode, the voltage between the oxide and platinum electrodes is monitored. In the biased mode, either a constant dc current or voltage is imposed across the electrode pair. The measured voltage (current biased) or current (voltage biased) is then monitored and is useful as a sensing signal for NO_x.

Prototype sensing elements are evaluated both microstructurally and for sensing performance. Isothermal sensing performance is characterized by exposing the sensing elements to varying concentrations of NO_x at a fixed O_2 level or varying O_2 levels at fixed concentrations of NO_x. Because NO_x is a mixture primarily of NO and NO_2, in our characterization we typically expose the sensing element to either NO or NO_2.

Results

Representative electrode and substrate microstructures are shown in Figure 2. The screen-printed and fired (1200°C) ZnO electrode is relatively open and porous compared with the YSZ substrate. The typical electrode thickness after firing is 20–30 μm (determined by non-contact profilometry); this compares well with the predicted thickness given the mesh size and emulsion thickness of the screen used for printing the electrodes.

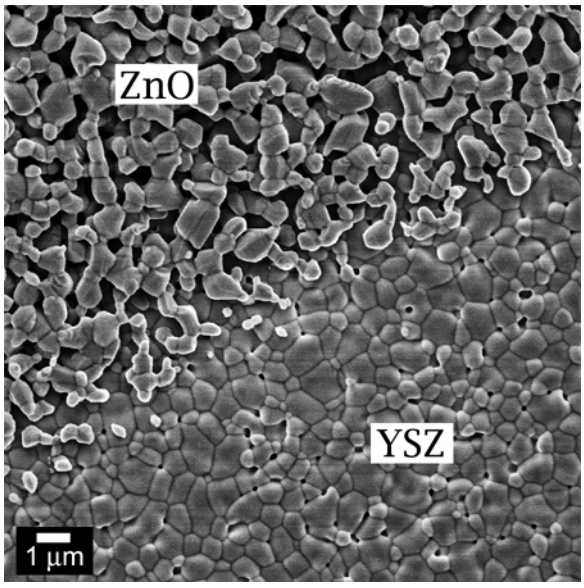

Figure 2. Plan view of a ZnO electrode on a YSZ substrate. Secondary electron image at 5 kV.

As Figure 3 shows, when paired with platinum in the geometry shown in Figure 1a, the binary oxides ZnO, Cr_2O_3, and NiO have yielded excellent non-Nernstian NO_2 sensing elements. For example, a ZnO/Pt sensing element, operating at 700°C in 7 vol % O_2, displayed an NO_2 sensitivity of ~50 mV/decade over the concentration range 20–200

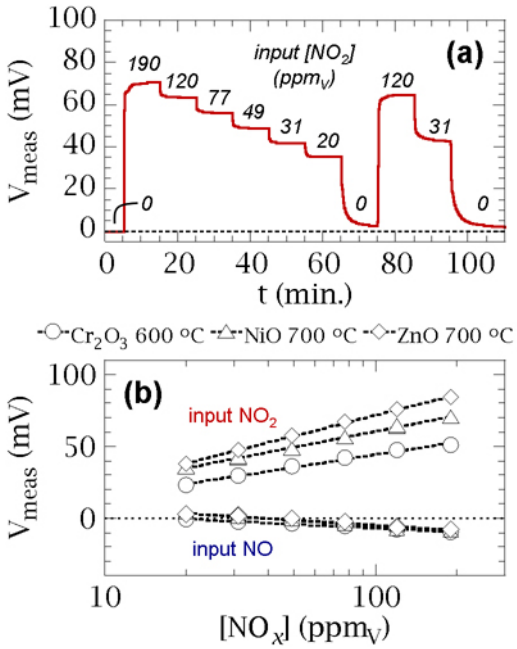

Figure 3. Response trace of an NiO/Pt sensing element as the input NO_2 is varied at 700°C in 7 vol % O_2 (a) and the variation in measured voltage with input NO_x for different binary oxide/Pt sensing elements in 7 vol % O_2 (b).

ppm_V NO_2, with 20 ppm_V NO_2 giving rise to a voltage of approximately 40 mV.

Diesel exhaust varies in O_2, typically ranging from 5 to 20 vol %.[1] Therefore, it is important to characterize the O_2 dependence of the sensing element response. Figure 4 shows that for these non-Nernstian NO_2 sensors, the measured voltage is a function of O_2 only in the presence of NO_2. We currently believe that this is observed because the voltage developed in the presence of NO_2 is related to the different behavior of the oxide and platinum electrodes with respect to the reduction of NO_2 and oxidation of oxygen ions (O^{2-}) in the YSZ solid electrolyte:

$$NO_2(g) + 2e^- \rightarrow NO(g) + O^{2-}, \text{ and} \quad (1)$$
$$O^{2-} \rightarrow 1/2O_2(g) + 2e^- \quad .(2)$$

The simultaneous occurrence of these reactions on both the oxide and platinum electrodes gives rise to a mixed potential on each electrode, the precise value of which will depend on the rate of Eqs. (1) and (2) on each electrode, the absorptive behavior of NO_2 and O_2 on each electrode, and the catalytic behavior of each electrode.[2] In the absence of NO_2, (Figure 4b), there is no gaseous species readily

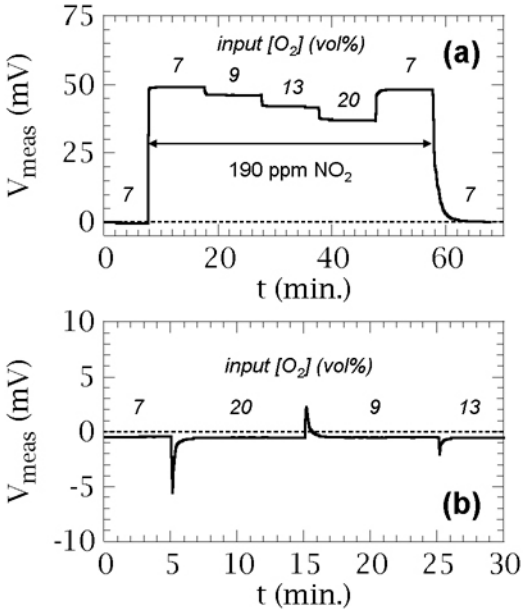

Figure 4. Measured voltage as O_2 is varied between 7 and 20 vol % with 190 ppm_V of NO_2 (a) and 0 ppm_V NO_2 (b) for an NiO/Pt sensing element operated in non-Nernstian mode.

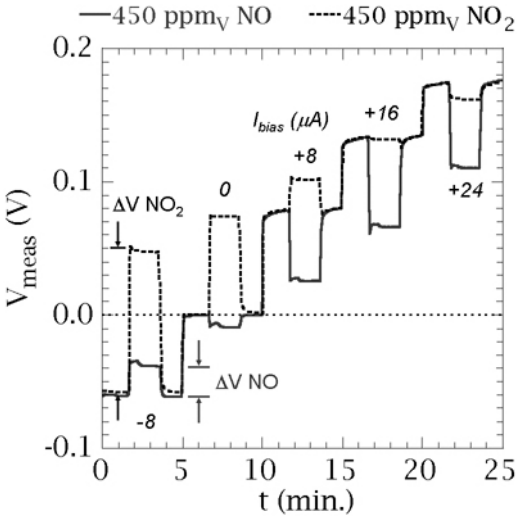

Figure 5. Voltage traces as 2-minute pulses of 450 ppm_V NO_x are applied at different current biases. Data collected at 600°C in 7 vol % O_2.

available for reduction, and a mixed potential cannot develop.

The dominant equilibrium NO_x species above 500°C is NO.[3] Therefore, although we cannot assume that the NO/NO_2 ratio in diesel exhaust is at equilibrium, it seems likely that NO would be more prevalent in the exhaust at the desired operating temperatures of 500–700°C. Thus sensor design may be simplified if sensing elements sensitive to NO could be developed. This can be done with the application of bias, as described below.

Equations (1) and (2) describe electrochemical reduction of NO_2 and oxidation of O^{2-}, respectively. A similar pair of equations can be written for the electrochemical oxidation of NO (to NO_2) and reduction of O_2 (to O^{2-}). Since these are electrochemical phenomena, it may be possible to adjust the rates of the various reactions by applying electrical bias to the sensing element (as is done in non-Faradaic electrochemical modification of catalytic activity).[4] To demonstrate this with biased sensing elements, a dc current bias was stepped at discrete levels (e.g., −16, −8, 0, 8, 16 μA for 5 min each), and a brief (2-min) 450-ppm_V pulse of either NO or NO_2 was applied at each bias level. The result is shown in Figure 5, where it can be seen that at negative biases (oxide electrode biased negatively with respect to the platinum electrode), the change in voltage induced by NO_2 is much larger than that induced by NO. However, as the bias is increased to positive values, the changes induced by NO are larger relative to those due to NO_2, and at a certain positive bias (~+16 μA for the sensing element in Figure 5) the introduction of 450 ppm_V NO gives a large signal while the same amount of NO_2 gives only a small response.

This asymmetry (stronger response to NO than NO_2) to was displayed over a wide concentration range (~50–1500 ppm_V NO_x) as shown in Figure 6. Although the mechanism of the enhanced NO response with bias is still under investigation, it seems clear that the oxide electrode must promote the oxidation of NO in order for the effect to be seen. Under conditions of positive bias, for current to flow through the YSZ electrolyte, oxygen ions must flow through the YSZ to the oxide electrode (the anode), and the external electrical circuit must supply electrons to the platinum electrode (the cathode). Therefore, it would appear that the electrochemical reactions occurring in the presence of NO are the reverse of Eq. (1) (oxidation of NO) at the oxide electrode and the reverse of Eq. (2) (reduction of O_2) at the platinum electrode.

Less clear is the mechanism underlying the weak response to NO_2 seen in Figure 6. One possible explanation is that the oxide electrode strongly promotes the reduction of NO_2 via Eq. (1),

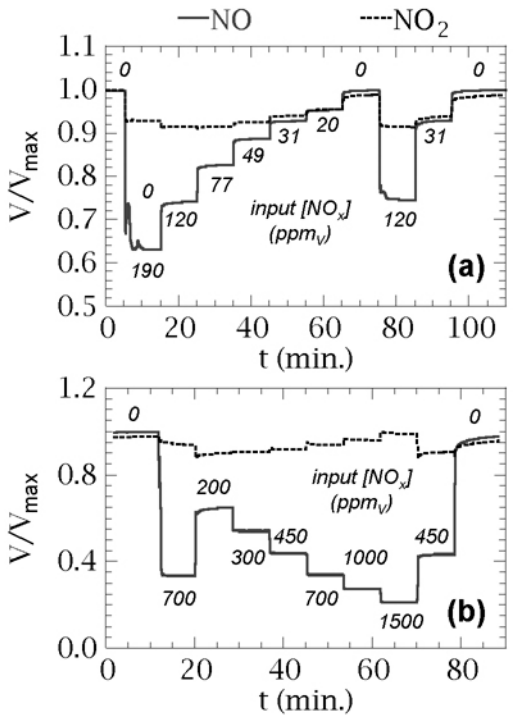

Figure 6. Response (600°C, 7 vol % O_2) of a current-biased sensing element to input NO and NO_2. The concentration variations of the two NO_x species were nominally identical.

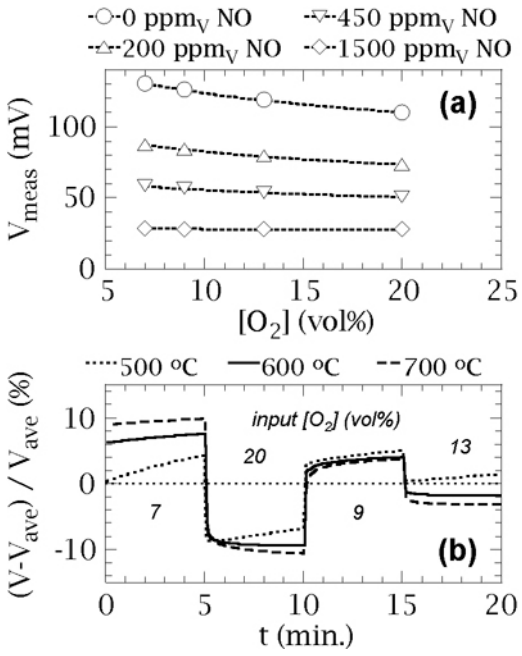

Figure 7. Variation of current-biased sensing element signal (at 600°C) with O_2 with different input NO (a) and response trace measured while varying O_2 with no input NO_x (b).

and this interferes with the expected anodic reaction [Eq. (2)] at the oxide electrode with positive bias and only NO_2 and O_2 present. Lending credence to this is the observation that at sufficiently large positive biases, as seen in Figure 5, the introduction of either NO or NO_2 decreases the measured voltage.

The O_2 dependence of these biased sensing elements is quite different from the reaction of the non-Nernstian elements discussed earlier. As Figure 7 shows, these elements show an O_2 dependence that is a decreasing function of NO. In the absence of NO, the measured voltage of a current-biased element can vary ~20% as O_2 is varied from 7 to 20 vol % (Figure 7b). However, in the presence of 1500 ppm_V NO, variation of O_2 over this range has little effect (Figure 7a). This behavior points to the presence of NO as having an anomalously strong effect on the electrode/ electrolyte interfacial resistance.

An important concern as sensor development progresses is the role of electrode geometry, as rigid space constraints will apply to the final sensor design. As an initial step in addressing these concerns, semicircular and interdigitated sensing elements (Figure 1) have been fabricated and characterized. Figure 8 indicates that the geometry variation had little impact on the magnitude and functional form of the NO response. It is also seen in Figure 8 that for these biased sensing elements, an almost linear response is obtained at low input NO, and that the extent of this linear regime increased with the element operating temperature. This is in contrast to the logarithmic behavior exhibited by the non-Nernstian elements in Figure 3. The linear behavior at low NO_x, combined with the observation that the NO-selectivity of the biased elements seemed to decrease with NO_x (Figure 6), indicates that careful sensor design will be necessary to use these biased sensing elements for low NO_x levels. Finally, temperature was much more important than electrode geometry in governing the recovery time from NO exposure, as shown in Figure 9.

Conclusions

Progress in NO_x sensor development has proceeded along two main fronts. In the first approach, non-Nernstian sensing elements using binary oxides and platinum have been developed. These elements respond strongly to NO_2 and produce an output voltage that is proportional to the

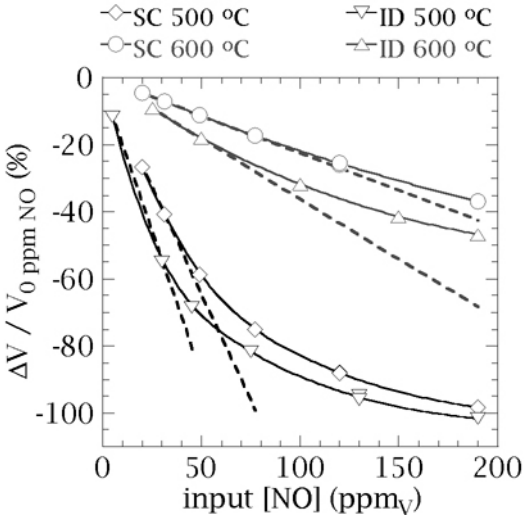

Figure 8. Response to input NO for biased sensing elements with the two different geometries (semicircular (SC) and interdigitated (ID)) of Figure 1. Data collected in 7 vol % O_2.

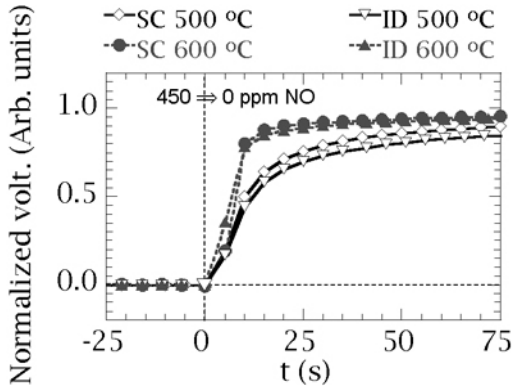

Figure 9. Recovery from NO exposure for biased sensing elements with the two different geometries of Figure 1, semicircular (SC) and interdigitated (ID).

logarithm of NO_2. Use of a more complex oxide electrode and a dc electrical bias enables selective detection of NO, the stable form of NO_x at high temperature. Pending evaluation of selectivity and stability, these two types of sensing elements are candidates for incorporation into NO_x sensors for heavy vehicle applications.

Publications

D. L. West, F. C. Montgomery, and T. R. Armstrong, "Electrically Biased NO_x Sensing Elements with Co-Planar Electrodes," in *205th Meeting of the Electrochemical Society*, San Antonio, TX, May 2004.

D. L. West, F. C. Montgomery, and T. R. Armstrong, "NO-Selective NO_x Sensing Elements for Combustion Exhausts," accepted by *Eurosensors XVIII*, Rome, Italy, September 2004.

D. L. West, F. C. Montgomery, and T. R. Armstrong, "High-T NO_x Sensing Elements Using Conductive Oxides and Pt," *Proceedings of ICEF: Engines for Mobile, Marine, Rail, Power Generation and Stationary Applications*, Long Beach, CA, November 2004.

D. L. West, F. C. Montgomery, and T. R. Armstrong, "Electrode Materials for Mixed-Potential NO_x Sensors," in *Proceedings of the 28th International Cocoa Beach Conference on Advanced Ceramics and Composites*, Cocoa Beach, FL, January 2004.

Patent

D. L. West, F. C. Montgomery, C. Maxey and T. R. Armstrong, "Sensing Devices Having CoPlanar Electrodes," filed with the U.S. Patent Office.

References

1. J. Kaspar, P. Fornasiero, and N. Hickey, "Automotive Catalytic Converters: Current Status and Some Perspectives," *Catalysis Today* **77**, 419–49 (2003).

2. A. A. Arias de Velasco, P. T. Moseley, R. Peat, and J. G. Peláez, "Atmosphere-dependent Potentials at Oxide Interfaces," *Sensors and Actuators B*, **15–16**, 55–62 (1993).

3. K. B. J. Schnelle and C. A. Brown, "NO_x Control," in *Air Pollution Control Technology Handbook*, CRC Press, Boca Raton, 2001.

4. C. G. Vayenas, S. Bebekis, I. V. Yentekakis, and S. Neophytids, "Non-Faradaic Electrochemical Modification of Catalytic Activity: The Work Function of Metal Electrodes in Solid Electrolyte Cells," *Solid State Ionics* **53–56**, 97–110 (1992).

D. Ultra-High-Resolution Electron Microscopy for Characterization of Catalyst Microstructures and Deactivation Mechanisms

*L. F. Allard, D. A. Blom, D.W. Coffey, C. K. Narula, and M. A. O'Keefe**
Oak Ridge National Laboratory
P.O. Box 2008
Oak Ridge, TN 37831-6064
(865) 574-4981; fax: (865) 576-5413; e-mail: allardlfjr@ornl.gov
**Dept. of Materials Science and Engineering, Lawrence Berkeley National Laboratory, Berkeley, CA*

DOE Technology Development Area Specialist: Dr. Sidney Diamond
(202) 586-8032; fax: (202) 586-1600; e-mail: sid.diamond@ee.doe.gov
ORNL Technical Advisor: D. Ray Johnson
(865) 576-6832; fax: (865) 574-6098; e-mail: johnsondr@ornl.gov

Contractor: Oak Ridge National Laboratory, Oak Ridge, Tennessee
Prime Contract No.: DE-AC05-00OR22725

Objectives

- Develop and utilize new capabilities and techniques for ultra-high resolution transmission electron microscopy (UHR-TEM) to characterize the microstructures of catalytic materials of interest for reducing emissions of nitrogen oxides (NO_x) in diesel and automotive exhaust systems.
- Relate the effects of reaction conditions on the changes in morphology of heavy metal species on "real" catalyst support materials (typically oxides).

Approach

- Use new field emission microscope at the High Temperature Materials Laboratory to image catalyst particles at near-atomic level to characterize systematic series of model NO_x trap catalyst materials (composed of 2% platinum by weight on a mixed CeO_2-ZrO_2-La_2O_3-BaO-Al_2O_3 support material) and to develop techniques applicable for imaging future catalysts at sub-Ångstrom levels with the new Aberration-Corrected Electron Microscope (ACEM).
- Conduct studies of a series of NO_x trap catalyst specimens, provided by Ford Research Laboratory colleague Dr. G. Graham, that had been field-tested by running in vehicles with spark-ignition direct-injection (SIDI) engines, rather than by simulating exhaust compositions and cycles using bench-top reactors.

Accomplishments

- Characterized via high-resolution annular dark-field scanning TEM (STEM) imaging the structure of a model NO_x trap catalyst composed of 2% platinum by weight on a mixed CeO_2-ZrO_2-La_2O_3-BaO-Al_2O_3 support material. The imaging showed, for example, that initial dispersions of platinum species consisted of near-atomic clusters and "rafts" of platinum atoms one to 3 atomic layers thick.
- Characterized the progression of changes in the microstructure of NO_x trap catalysts as a result of vehicle aging, by TEM and STEM analysis of core samples taken from the centers of catalyst monoliths removed from the vehicles after 30,000, 53,000 and 82,000 km of driving.
- Successfully factory tested and subsequently accepted delivery of the ACEM, funded by the Office of Energy Efficiency and Renewable Energy. Achieved an Oak Ridge National Laboratory (ORNL) PEP milestone for

beneficial operation of all critical imaging systems and demonstrated the capabilities of the new microscope for imaging ultra-fine clusters of catalyst species on real catalyst samples of OFCVT interest.

Future Direction

- Use new high-resolution electron microscopy imaging techniques and energy-loss electron spectroscopy on the ACEM to characterize diesel particulate NO_x –reduction and lean NO_x trap samples in collaboration with Ford Research Laboratory colleagues.
- Develop new thrust capability for characterization of catalyst structures at the atomic level using the ACEM, using techniques of electron tomography. This will involve constructing a new specimen holder to allow high tilts (up to ±75 degrees), and assessing the ability of annular dark-field STEM imaging to provide unambiguous information on the shapes of fine catalyst particles and the shape changes that occur on aging.

Technical Progress

Microstructure of Pt/Mixed-Oxide Model Catalysts

A model NO_x trap catalyst composed of 2% platinum by weight on a mixed CeO_2-ZrO_2-La_2O_3-BaO-Al_2O_3 support material (or more formally, 2%Pt-98%[10%CeO_2-ZrO_2-90%(2%La_2O_3-98%$BaO.6Al_2O_3$)]) is being studied (in a separate task) to determine the effects of exposure to lean–rich exhaust mixtures on the microstructure of the catalyst. In the present task, the model catalyst material was characterized using the high-resolution annular dark-field imaging capability of the JEOL 2010F field emission TEM on loan as part of the new ACEM project. This effort served as a precursor to imaging of the ultrastructure of our catalyst samples using similar (but aberration-corrected) STEM imaging techniques on the ACEM.

The STEM/TEM instrument provides both bright-field TEM and dark-field STEM imaging capabilities, and typical results at the resolution level of the 2010F allowed the imaging of “rafts” of platinum species on the alumina/baria and ceria/zirconia phases of the experimental catalysts (e.g., Figure 1). However, the significantly higher resolution expected from the ACEM should permit unambiguous and more quantitative characterization of the exact structure of the as-dispersed precious metal species on both experimental and “real” catalyst samples. This will provide a better understanding of the initial stages of growth of catalyst particles under aging conditions, so that advances can be made in controlling heavy metal particle size changes with exposure to temperature and exhaust gas conditions.

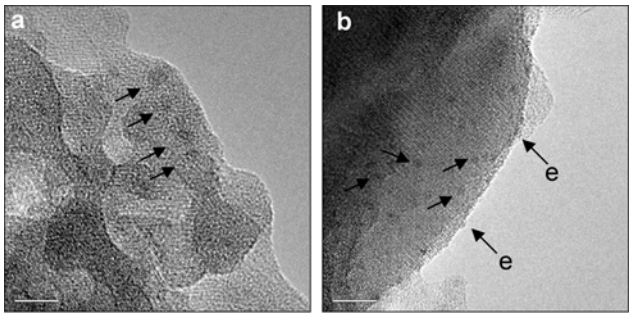

Figure 1. (a) Alumina phase with platinum rafts (arrows). (b) Ce-Zr phase with platinum rafts (arrows). Possible edge-on rafts are also shown (arrows labeled “e”). Scale = 5 nm

Microstructure of SIDI Vehicle-Tested Catalysts

In collaboration with Dr. George Graham of Ford Research Laboratory, we characterized a series of NO_x trap catalyst specimens that were field-tested by running in vehicles with SIDI engines. These catalysts comprised a double washcoat configuration on standard cordierite brick monoliths. The initial washcoat is composed of a baria-alumina composition on which platinum is dispersed at the 1 wt % level as the heavy-metal catalytic species. The second washcoat is composed of ceria-zirconia with rhodium dispersed at about the 0.2 wt % level. Catalyst core samples were taken from the centers of catalyst monoliths removed from the vehicles after 30,000, 53,000, and 82,000 km of driving, and their microstructures were compared with the microstructure of a fresh catalyst sample that had seen no vehicle aging.

The technique of “spectrum imaging” was used extensively to obtain quantitative information on the microstructural and chemistry changes on aging.

With this technique, an annular dark-field image is acquired from a chosen sample area. Then the same sample area is scanned point by point over a long time (up to hours, with drift correction implemented during the scan), with an energy-dispersive spectroscopy (EDS) spectrum acquired and saved at each point, to make the so-called spectrum image. In the present work, spectrum images of 512 × 384 pixel count (about 20 K spectra) were acquired, providing the ability to perform "principal component analysis" (PCA) with the data processing capabilities of the acquisition software. It is a way of identifying patterns in data and expressing the data in such a way as to highlight their similarities and differences. Patterns in data can be hard to find in data of high dimensions (i.e., a large number of points, each with an EDS spectrum), and PCA is a powerful tool for analyzing such data (details are beyond the scope of this report). A straightforward application is to extract "maps" of elements and phases from the spectrum image.

For example, an annular dark-field image from the 30,000-km catalyst sample is shown in Figure 2a. The EDS spectrum represented by the entire area of the image is shown in Figure 2c. The majority component is alumina, with cerium and zirconium also clearly present. The platinum component is essentially in the noise at this full scale, but the platinum L family is clearly present, as indicated in Figure 2d, with no overlaps of other elements. When a window is applied to show only the counts from the platinum L family, as shown in Figure 2b, the one-to-one correspondence between the bright-contrast particles in the annular dark-field image and the high-density platinum concentrations in the platinum image (as marked by arrows) clearly confirm the location and size distribution of platinum in the specimen area.

A similar result from the 82,000 km sample is shown in Figure 3a, which shows platinum particle growth as a result of aging phenomena during the extended driving cycle. A benefit of the spectrum imaging process is that the presence of any minor components in an image area can be determined. In the case of these SIDI catalysts, rhodium is supposed to be present at about 10% of the level of the platinum (i.e., at the 0.1 wt % level), but in the images acquired to date, no rhodium was identified (all the bright contrast particles in any image acquired corresponded to platinum). It is likely that either

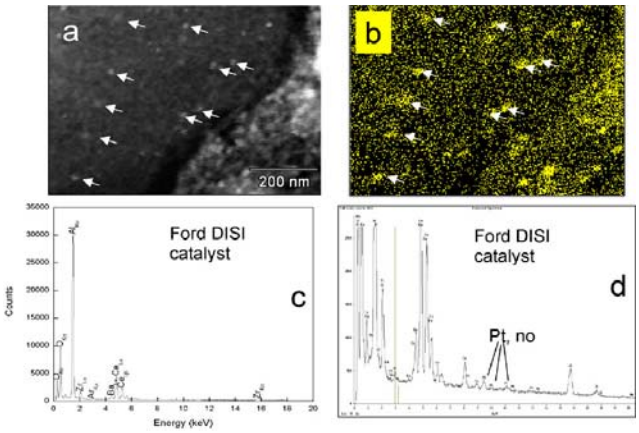

Figure 2. (a) Annular dark-field image of 30,000-km SIDI catalyst. (b) Platinum map extracted from sum spectrum of Fig. 2c. (c) Sum spectrum from spectrum image collection. (d) Expanded sum spectrum showing clear platinum peaks.

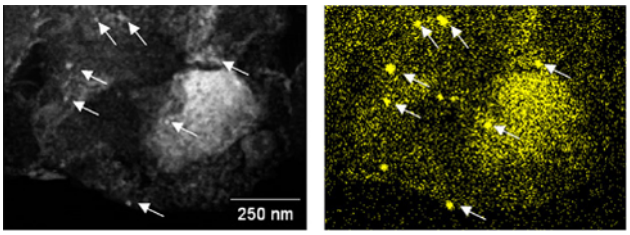

Figure 3. (a) Annular dark-field image of catalyst area in 82,000-km SIDI sample. (b) Platinum map extracted from spectrum image. Note the ability to locate the platinum particles unambiguously, even in the presence of a large bright-contrast aggregate of Ce-Zr in the center of the image (the increased contrast in this area in the platinum map is due to an increase in the background from the high-atomic-number material).

rhodium is atomically dispersed even after significant aging in the test vehicles, or it is present in widely isolated particles that will require further analysis to locate. Data such as these are providing a significant input to the understanding of the effects of vehicle aging of NO_x trap catalysts.

Ultra-High Resolution Imaging of Catalyst Clusters Using the ACEM

ORNL's ACEM (Figure 4) was delivered in May 2004 and installed in the newly constructed Advanced Materials Characterization Laboratory. The instrument is one of the first two combination STEM/TEM instruments in the country that are

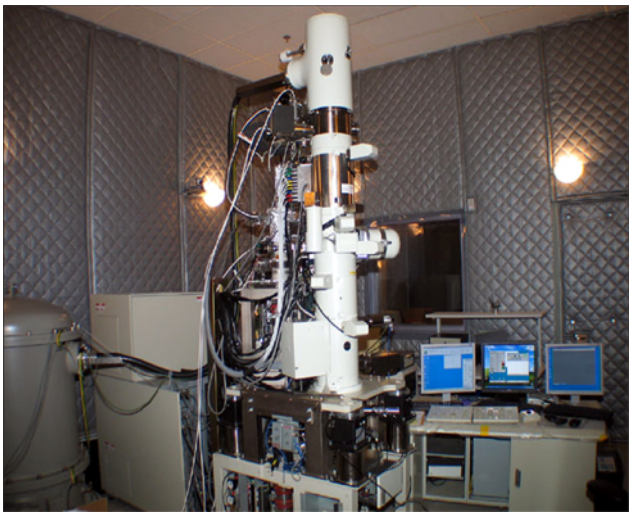

Figure 4. ORNL's ACEM, the JEOL 2200FS-AC, during final assembly and test-out. The instrument will ultimately be operated from the adjacent control room (seen through window behind the instrument).

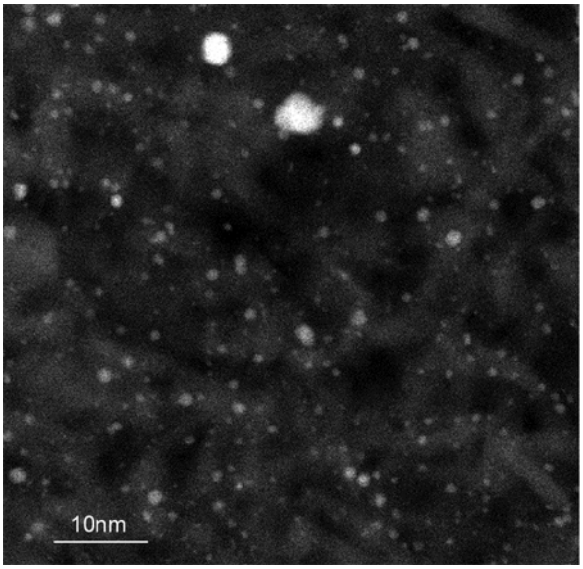

Figure 5. Example of an early very high-resolution annular dark-field image of platinum species on alumina support. The finest bright spots represent platinum clusters of a few atoms, with perhaps single atoms also seen.

equipped with a special corrector element on the illumination to enable a probe size of 0.7Å (compared with a 1.4-Å probe in the uncorrected instrument). This increase in probe resolution results in a 10-fold improvement in contrast in STEM dark-field imaging mode and should enable resolution of heavy metal species such as platinum on light oxide support materials at the single-atom level. An early result from the ACEM is the annular dark-field image shown in Figure 5, which is from a sample of as-deposited platinum on alumina. The platinum particles show in bright contrast; the two large particles are in the 2.5–4 nm size range (and are the only two particles visible unambiguously in standard bright-field images). The finest spots may be single atoms of platinum, or at most clusters of two or three atoms. The image illustrates the advanced capability the ACEM will provide for future catalyst characterization.

Analysis of catalyst materials at ultra-high resolution provides the potential to characterize directly the shapes of nanometer-sized particles and their changes with aging. The ultimate goal is to obtain a full understanding of the mechanisms of catalyst activity, selectivity, and aging. In parallel work to the development of advanced imaging techniques in the laboratory, we are collaborating with Lawrence Berkeley National Laboratory in a computational component of the work that involves modeling catalyst particles and calculating the images expected from them (conventional TEM images have been simulated so far, with STEM images to be done in the future). It is of great interest to determine, with very small particles comprising only a relatively few atoms, what crystal facets are exposed at the surface from the initial fine particle dispersions to larger particles as the catalyst ages. A typical model is shown in Figure 6, along with the corresponding computed TEM image and a chosen line profile that illustrates that, in the ideal case, there is a one-to-one correspondence between image intensity and the number of atoms in a column. This suggests that real atomic structure images of a particle taken from different directions (i.e., in a tomography application) might allow unambiguous characterization of the exact particle shape, with the specific crystal planes exposed on the surface thereby analyzed. A new research thrust area is being developed to implement the capability and techniques for nanoparticle shape determination with sub-Ångstrom imaging in the ACEM.

Conclusions

The acquisition and imminent beneficial operation of the ACEM will provide OFCVT programs with the top capability in the nation for characterization of catalyst materials and other materials of in-

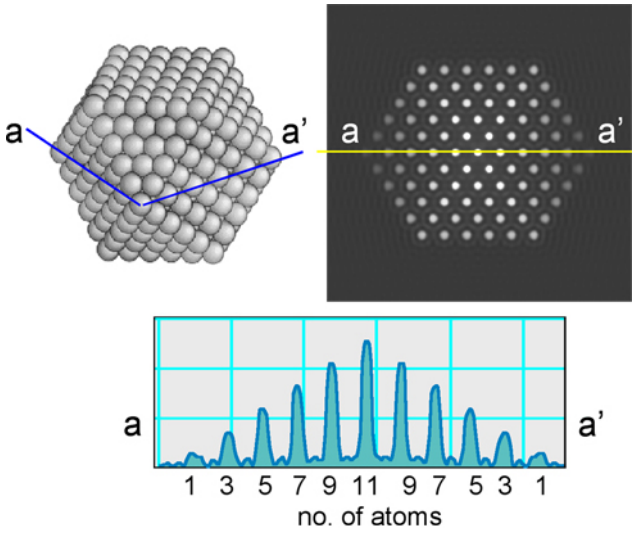

Figure 6. Example of model catalyst particle imaging computation. A cuboctohedron particle geometry is shown, with the image of the particle looking down the plane of a-a'. A line trace thru the image shows a direct relationship between atom column intensity and the number of atoms in each column.

terest to the program. Imaging at the single-atom level of heavy catalyst species on oxide substrates—coupled with electron spectroscopy to obtain, for example, chemical binding information—will add a new dimension to our understanding of the behavior of these complex materials. The present work using ORNL's current TEM and STEM instruments, with techniques such as annular dark-field imaging and especially spectrum imaging, has paved the way for rapid implementation of the next level of imaging and analysis capabilities. Both model NO_x trap catalysts and catalysts run in vehicles for known times have been characterized. Changes in platinum particle sizes and the relationship between the various oxide support species upon aging have supplied information on the mechanisms of catalyst degradation. Finally, initial work on modeling of catalyst particle shapes and the resulting images has shown promise for allowing the determination of particle morphologies (exposed crystal facets) with high-resolution electron tomography using the ACEM.

Publications/Presentations

L. F. Allard, D. A. Blom, M. A. O'Keefe, C. Kiely, M. Watanabe, M. Kawasaki, T. Kaneyama, and H. Sawada, "First Results from the Aberration-Corrected JEOL 2200FS-AC STEM/TEM, pp. 110–111 in *Proceeding M&M 2004*, San Francisco Press, San Francisco.

M. A. O'Keefe and L. F. Allard, "A Standard for Sub-Ångstrom Metrology of Resolution in Aberration-Corrected Electron Microscopes." *Microscopy & Microanalysis* **10** 1002–1003 (2004).

M. A. O'Keefe and L. F. Allard, "Sub-Ångstrom Microscopy for Materials Science," abstract for Nanometrology Workshop, National Institute of Standards and Technology, Gaithersburg, MD, May 2004.

M. A. O'Keefe and L. F. Allard, "Sub-Ångstrom Electron Microscopy for Sub-Ångstrom Nano-Metrology," pp. 52–53 in *Proceedings of National Nanotechnology Initiative Grand Challenge Workshop on Instrumentation and Metrology for Nanotechnology*, National Institute of Standards and Technology, Gaithersburg, MD, 2004.

L. F. Allard and M. A. O,Keefe, "Sub-Angstrom Metrology of Resolution in Aberration-Corrected Transmission Electron Microscopes using the A-OK Standard Test," p. 9 in *Proceedings of the 1st Aberration-Corrected MSA Meeting*, 2004. location of meeting?

M. A. O,Keefe, L. F. Allard, and K. H. Downing, "Atomic-Resolution Tomography," presented at the Center for Nanophase Materials Sciences Workshop on Microscopy, Metrology and Manipulations using Electrons, Ions, and Photons, Oak Ridge, Tennessee, September 15–16, 2004.

E. Microstructural Changes In NO_x Trap Materials under Lean and Rich Conditions at High Temperatures

C. K. Narula, K. Lester, H. Meyer, L. Allard
Oak Ridge National Laboratory
P.O. Box 2008, MS 6116
Oak Ridge, TN 37831-6116
(865) 574-8445; fax: (865) 576-6298; e-mail: narulack@ornl.gov

DOE Technology Development Area Specialist: Dr. Sidney Diamond
(202) 586-8032; fax: (202) 586-1600; e-mail: sid.diamond@ee.doe.gov
ORNL Technical Advisor: D. Ray Johnson
(865) 576-6832; fax: (865) 574-6098; e-mail: johnsondr@ornl.gov

Contractor: Oak Ridge National Laboratory, Oak Ridge, Tennessee
Prime Contract No.: DE-AC05-00OR22725

Objective

- Facilitate deployment of a nitrogen oxides (NO_x) trap for lean diesel or gasoline exhaust by
  - — investigating materials issues related to deterioration of the performance of NO_x traps upon aging as a result of thermal and sulfation-desulfation cycles
  - — investigating materials that are robust under the lean NO_x trap operating conditions

Approach

- Synthesize new model catalyst systems containing platinum (Pt): Pt/$BaO.6Al_2O_3$, [10%CeO_2-ZrO_2, 90%(2%La_2O_3, 98%$BaO.6Al_2O_3$)], and 2%Pt, 5%MnO_2, 93%[10%CeO_2-ZrO_2, 90%(2%La_2O_3, 98% $BaO.6Al_2O_3$)].
- Treat them under thermal, lean-diesel, and rich-diesel conditions at 500ºC for 4 h and monitor changes in microstructure. The next step involves evaluation under lean-rich cycles and aging under laboratory aging cycles.
- Evaluate the performance of the selected systems on a bench-top flow reactor.

Accomplishments

- Completed the microstructural evaluation of model catalysts Pt/$BaO.6Al_2O_3$, [10%CeO_2-ZrO_2, 90%(2%La_2O_3, 98%$BaO.6Al_2O_3$)] and 2%Pt, 5%MnO_2, 93%[10%CeO_2-ZrO_2, 90%(2%La_2O_3, 98% $BaO.6Al_2O_3$)]. The latter is a better representative of this class of NO_x trap systems.
  - — Completed and reproduced the study of microstructural changes on aging under diesel lean and rich conditions at 500ºC.
  - — Completed microstructural changes under thermal aging studies of these samples for comparison.
  - — Completed microstructural changes in thermally aged samples after extended exposure to lean and rich conditions.
- Began updating the ex-situ reactor to enhance its capabilities to enable treatment of transmission electron microscopy (TEM) samples under lean, rich, or, stoichiometric conditions, as well as lean-rich cycles. This reactor will be capable of rapid screening of the model catalyst powders for their durability in exhaust under the operating conditions for diesel and gasoline engines.
- Equipped the synthesis laboratory to enable preparation of NO_x trap materials. The bench-top-flow reactor is being set up.

Future Direction

- Evaluate model catalyst systems on a bench-top flow reactor for their efficiency and durability as NO_x traps under simulated diesel and gasoline conditions [with or without sulfur oxides (SO_x) in the simulated exhaust]. These results will provide a benchmark for evaluation of new materials.
- Carry out microstructural characterization of model NO_x trap powders after aging under lean, rich, or stoichiometric conditions on the bench-top flow reactor and TEM samples on an ex-situ microreactor.
- Investigate new materials that can withstand NO_x trap operating conditions without detrimental structural changes.

Introduction

NO_x traps are at the forefront of various strategies under investigation to treat NO_x from diesel and lean-gasoline engines.[1] NO_x traps collect engine-out NO_x during lean operation and treat it during short rich-operation cycles.[2] Fresh NO_x traps work very well but cannot sustain their high efficiency over the lifetime of a vehicle. The efficiency loss is believed to be caused by aging due to high-temperature operation and sulfation-desulfation cycles necessitated by the SO_x in the emissions from the oxidation of sulfur in fuel. In order to design a thermally durable NO_x trap, there is a need to understand the changes in the microstructures of materials that occur during various modes of operation (lean, rich, and lean-rich cycles). This information can form the basis for selection and design of new NO_x trap materials that can resist deterioration under normal operation.

NO_x traps are derived from commercial three-way catalysts installed to treat emissions from engines operating at stoichiometric air-fuel ratios. Therefore, the basic components of NO_x traps are identical to three-way catalysts. The advanced version of a three-way catalyst is a two-layer system on a honeycomb substrate with the inner layer based on Pt-alumina and the outer layer on rhodium-ceria-zirconia. The NO_x traps derived from advanced three-way catalysts are identical to the catalysts except for a high baria content (the upper limit being close to 20%) in the alumina layer. Thus aging can lead to intermixing of layers, crystallization of baria-containing phases that are not good NO_x absorbers, and sintering of precious metals. The first goal of this project is to determine if one or all of the microstructural changes take place and if these changes occur during lean, rich, or lean-rich cycles. The tasks to achieve this goal are as follows:

- Complete microstructural characterization of fresh and thermally aged NO_x trap materials to determine the species formed as a result of aging.
- Complete microstructural characterization of fresh NO_x trap materials after exposure to lean conditions to determine the species formed during lean cycles.
- Complete microstructural characterization of fresh NO_x trap materials after exposure to rich conditions to determine the species formed during rich cycles.

The second goal of the project is to investigate and design new materials that can withstand NO_x trap operating conditions without undergoing detrimental structural changes. The results from the first goal will provide insights into changes that occur in NO_x trap materials at a microstructural level upon extended exposure to NO_x trap operating conditions, enabling selection and design of materials for the second goal.

Approach

Our approach involves synthesizing new model catalyst systems; treating them under thermal, lean, and rich conditions; and monitoring microstructural changes to understand the deterioration mechanism. In order to rapidly screen model catalyst systems, we have designed an ex-situ reactor system that is being further upgraded to enhance its capabilities. The updated system will operate in the 25–1000°C range and will have the ability to introduce periodic rich pulses while the catalyst is being treated under lean or stoichiometric conditions.

The information from this study will be used to design thermally durable catalyst systems and will be tested on a bench-top flow reactor system.

Results

Over the last 2 years, we determined the microstructural changes that occurred in a supplier lean NO_x trap system (based on Pt/BaO-Al_2O_3 and CeO_2-ZrO_2 materials) upon being aged on (1) a pulsator at Ford Motor Company, (2) a dynamometer at Ford, and (3) vehicles with gasoline direct-injection, spark-ignition (DISI) engines in Europe.

- After pulsator aging, lean and rich aged samples showed that the sintering of Pt particles occurs during aging, and barium migrates into the ceria-zirconia layer. Both of these factors reduce the Pt-barium oxide surface area where NO_x adsorption and reduction take place during lean and rich cycles, respectively. The stoichiometric aging also leads to the migration of barium into the ceria-zirconia layer, but the sintering of Pt is less severe.
- The dyno-aged samples showed extensive sintering of Pt and its migration into the ceria-zirconia layer. The sintering of rhodium was also observed. The migration of barium into ceria-zirconia and the sintering of the precious metal component could explain the deterioration of performance
- The analysis of the samples evaluated on-vehicle after 32,000 km and 80 km showed that the bulk of the sintering of precious metals occurred in the stages of on-vehicle aging.

These results primarily show precious metal sintering and barium migration to be the cause of performance deterioration in NO_x trap materials in gasoline engine exhaust conditions. While the laboratory aging protocols for diesel engines are in development, we have compiled data showing early-stage changes in model NO_x trap materials under diesel conditions. We assumed that lower-temperature simulated diesel exhaust would slow down the aging compared with gasoline engine exhaust. Thus we completed a series of thermal aging, diesel lean aging, and diesel rich aging cycles of a model NO_x trap and a model NO_x trap modified with manganese oxide, as well as Pt/Al2O3, for comparison purposes. The results are summarized in the following paragraphs.

Synthesis of New Model Catalysts

Pt/Al_2O_3: The Pt/alumina was prepared by the impregnation method using H_2PtCl_6 salt. X-ray powder diffraction (XRD) shows broad diffraction peaks for alumina and no peaks due to Pt, as expected because of the small particle size of Pt in the freshly prepared sample (Figure 1).

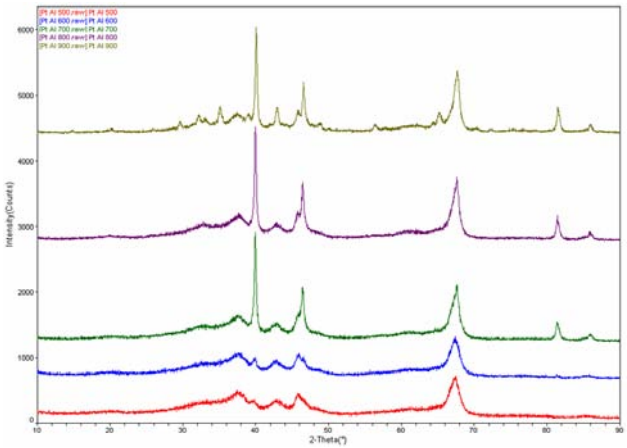

Figure 1. X-ray diffraction patterns of Pt/Al_2O_3.

2%Pt, 5%MnO2, 93%[10%CeO2-ZrO2, 90%(2%La2O3, 98% BaO.6Al2O3)]: The model catalyst was synthesized by impregnating 2%Pt, 97%[10%CeO_2-ZrO_2, 90%(2%La_2O_3, 98% BaO.6Al_2O_3)] with manganese nitrate and subsequent decomposition.

Microstructural Changes in Model Catalysts

The microstructural changes in model catalysts (Pt/Al_2O_3), (2%Pt, 98%[10%CeO_2-ZrO_2-90%(2%La_2O_3, 98%BaO.6Al_2O_3)]), and (2%Pt, 5%MnO_2, 93%[10%CeO_2-ZrO_2, 90%(2%La_2O_3, 98% BaO.6Al_2O_3)]) after thermal treatment at 500, 600, 700, 800, and 900ºC; lean treatment at 500ºC for 4 h; and rich treatment at 500ºC were followed with XRD and transmission electron microscopy (TEM). Here lean and rich treatment refers to exposure of sample in an ex-situ reactor (Figure 7a, described previously) to diesel lean and diesel rich conditions. A summary of changes in the precious metal (Pt) is presented in Table 1.

Table 1. Summary of Pt particles size changes under various treatment conditions in model catalysts I, II, and III

Sample	Treatment conditions				
	Fresh	Thermal treatment (XRD of powders)	Thermal treatment at 500°C on ex-situ reactor	Treatment under lean conditions on ex-situ reactor	Treatment under rich conditions on ex-situ reactor
Pt/Al_2O_3	1–1.2 nm	600ºC, 3.4 nm 700ºC, 17.1nm 800ºC, 26.1nm 900ºC, 39.5nm	2–4 nm	8–10nm	2–4 nm
Model NO_x trap catalyst I: 2%Pt-98%[10%CeO_2-ZrO_2-90%(2%La_2O_3-98%BaO.6Al_2O_3)]	1–2nm	600ºC, 2.6 nm 700ºC, 21.3nm 800ºC, 37.2nm 900ºC, 48.4nm	1–2 nm	1–2nm	1.5–3.5 nm
Model NO_x trap catalyst II: 2%Pt, 5%MnO_2–93%[10%CeO_2-ZrO_2-90%(2%La_2O_3-98% BaO.6Al_2O_3)]	1–2 nm	700ºC, 20.7nm 800ºC, 27.0nm 900ºC, 34.0nm	1–2 nm	2–3nm	1–2nm

Thermal Treatment

- Thermal treatment of samples was carried out at 500, 600, 700, 800, and 900ºC in a bench-top furnace in air.
- Pt/Al_2O_3: In XRD patterns (Figure 1) of Pt/Al_2O_3, diffraction peaks due to Pt particle size start to grow in 500–900ºC range. The calculated Pt particle sizes (using the Scherrer formula, assumes spherical particles) are 3.4, 17.1, 26.1, and 39.5 nm at 600, 700, 800, and 900ºC, respectively. At 500ºC, the alumina is a mixture of γ-alumina and hydrated γ–alumina. At 800ºC, a broad peak assignable to the alpha phase can be seen. At 900ºC, the diffraction peaks due to α– and γ – alumina are observed. TEM of the fresh sample shows that the Pt particle size is in the 1–1.2 nm range (Figure 2). This particle size grows to 2–4 nm on thermal treatment in a furnace at 500°C for 4 h.
- 2%Pt, 98%[10%CeO_2-ZrO_2, 90%(2%La_2O_3, 98%BaO.6Al_2O_3)]: In XRD patterns (Figure 3), diffraction peaks due to Pt particle size start to grow in the 500–900ºC range. The calculated Pt particle sizes (using the Scherrer formula, assumes spherical particles) are 2.6, 21.3, 37.2, and 48.4 nm at 600, 700, 800, and 900ºC, respectively. TEM of the fresh sample shows that the Pt particle size is ~1 nm (Figure 4). This

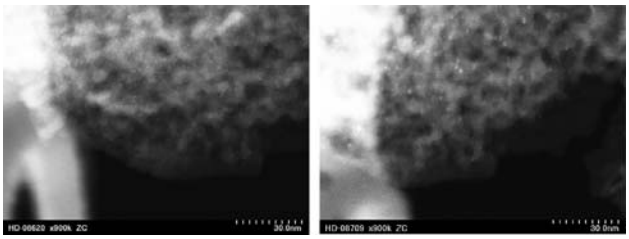

Figure 2. TEM of fresh and thermally aged (500ºC, 4 h) Pt/Al_2O_3.

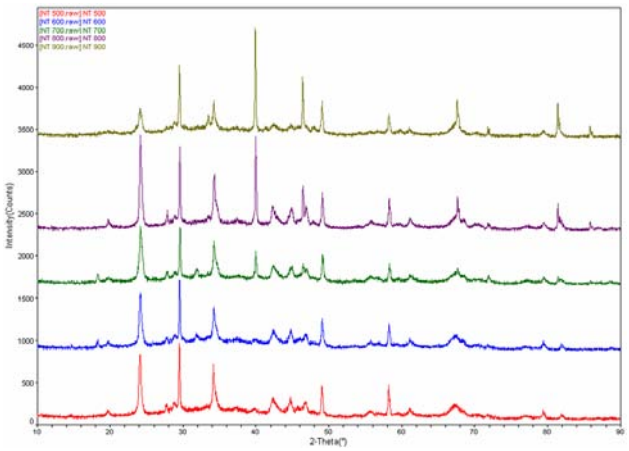

Figure 3. XRD patterns of 2%Pt-98%[10%CeO_2-ZrO_2-90%(2%La_2O_3-98%BaO.6Al_2O_3)].

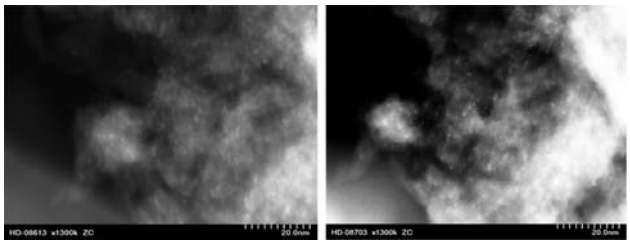

Figure 4. TEM of fresh and thermally aged (500ºC, 4 h) 2%Pt-98%[10%CeO_2-ZrO_2-90%(2%La_2O_3-98%$BaO.6Al_2O_3$)].

particle size grows to 1–2 nm upon thermal treatment in a furnace at 500ºC for 4 h.

- 2%Pt, 5%MnO_2, 93%[10%CeO_2-ZrO_2, 90%(2%La_2O_3, 98% $BaO.6Al_2O_3$)]: In XRD patterns (Figure 5), diffraction peaks due to Pt particle size start to grow in the 500–900ºC range. The calculated Pt particle sizes (using the Scherrer formula, assumes spherical particles) are 20.7, 27, and 34 nm at 700, 800, and 900ºC respectively. TEM of the fresh sample shows that the Pt particle size is ~1 nm (Figure 6). This particle size grows to 1–2 nm upon thermal treatment in a furnace at 500ºC for 4 h.

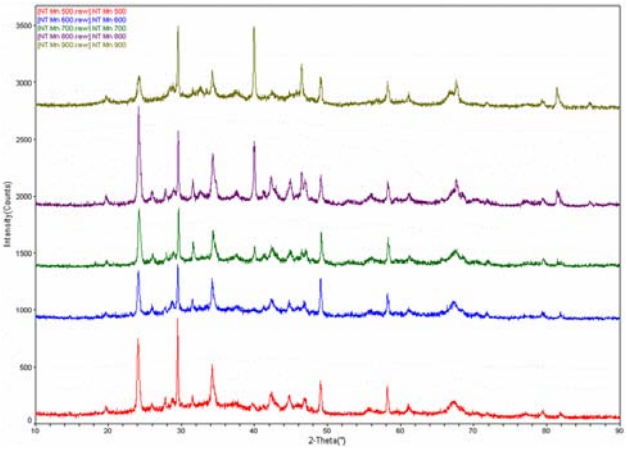

Figure 5. XRD patterns of 2%Pt, 5%MnO_2–93% [10%CeO_2-ZrO_2-90%(2%La_2O_3-98% $BaO.6Al_2O_3$)].

Lean and Rich Treatment in Ex-situ Reactor

The aging of model catalysts was carried out in our ex-situ reactor system (schematics in Figure 7) under lean or rich diesel exhaust conditions at 500°C for 4 h [CO, CO_2, H_2, HC, NO_x, H_2O, flow rate 100cc/min] showed some sintering of Pt particles,

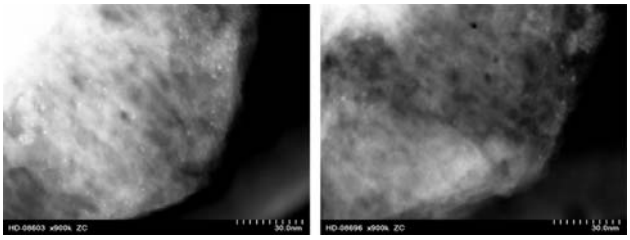

Figure 6. TEM of fresh and thermally aged (500ºC, 4 h) 2%Pt, 5%MnO_2–93%[10%CeO_2-ZrO_2-90%(2%La_2O_3-98% $BaO.6Al_2O_3$)].

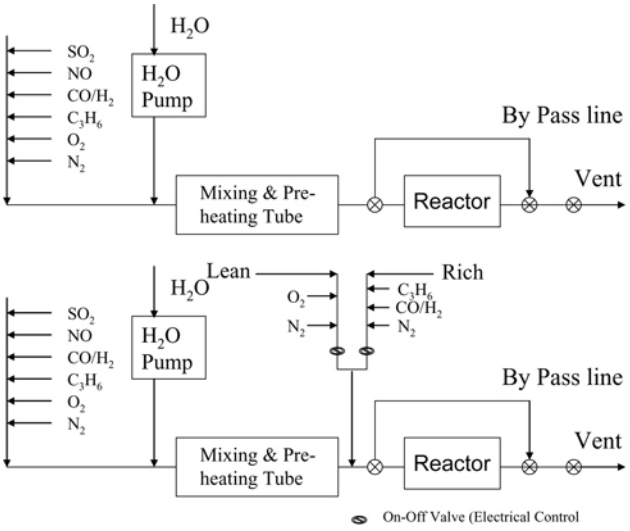

Figure 7. a. Schematics of current ex-situ reactor; b. Schematics of modified ex-situ reactor.

and the size grew to ~2.5nm. However, the sintering was significantly less than that observed upon thermal aging (~30–40nm) at 500°C in air.

It is important to note that the experiments in the ex-situ reactor system do not precisely duplicate the aging of NO_x traps during normal operation. The alternating lean/rich conditions are not present in our experiments; instead, our samples are exposed to lean conditions, and a lack of control of space velocity due to the very small amount of catalyst leads to NO_x absorber saturation conditions. The saturation condition persists throughout our treatment.

Lean Treatment

- Pt/Al_2O_3: TEM of the fresh sample shows that the Pt particle size is in the 1–1.2 nm range (Figure 8). This particle size grows to 8–10 nm in diesel lean simulated exhaust in the ex-situ reactor at 500ºC for 4 h.

- 2%Pt, 98%[10%CeO_2-ZrO_2, 90%(2%La_2O_3, 98%BaO.6Al_2O_3)]: TEM of the fresh sample shows that the Pt particle size is ~1 nm (Figure 9). This particle size grows to 1–2 nm upon lean treatment in the ex-sit reactor at 500ºC for 4 h.
- 2%Pt, 5%MnO_2, 93%[10%CeO_2-ZrO_2, 90%(2%La_2O_3, 98% BaO.6Al_2O_3)]: TEM of the fresh sample shows that the Pt particle size is ~1 nm (Figure 10). This particle size grows to 2–3 nm in diesel lean simulated exhaust in the ex-situ reactor at 500ºC for 4 h.

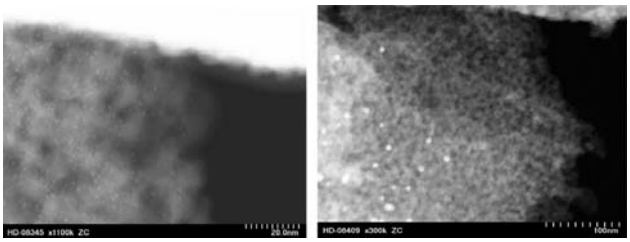

Figure 8. TEM of fresh and lean aged (500ºC, 4 h) Pt/Al_2O_3.

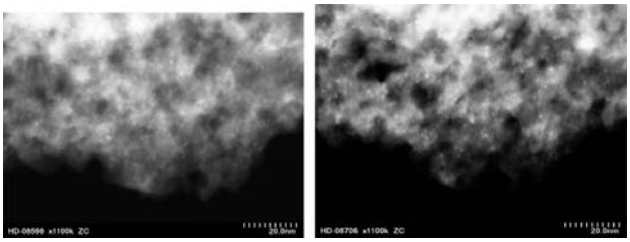

Figure 9. TEM of fresh and lean aged (500ºC, 4 h) 2%Pt-98%[10%CeO_2-ZrO_2-90%(2%La_2O_3-98%BaO.6Al_2O_3)].

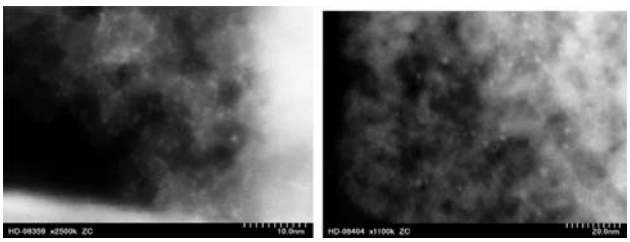

Figure 10. TEM of fresh and lean aged (500ºC, 4 h) 2%Pt, 5%MnO_2–93%[10%CeO_2-ZrO_2-90%(2%La_2O_3-98% BaO.6Al_2O_3)].

Rich Treatment

- Pt/Al_2O_3: TEM of the fresh sample shows that the Pt particle size is in the 1–1.2 nm range (Figure 11). This particle size grows to 2–4 nm in diesel rich simulated exhaust in the ex-situ reactor at 500ºC for 4 h.
- 2%Pt, 98%[10%CeO_2-ZrO_2, 90%(2%La_2O_3, 98%BaO.6Al_2O_3)]: TEM of the fresh sample shows that the Pt particle size is ~1–1.2 nm (Figure 12). This particle size grows to 1.5–3.5 nm in diesel rich simulated exhaust in the ex-situ reactor at 500ºC for 4 h.
- 2%Pt, 5%MnO_2, 93%[10%CeO_2-ZrO_2, 90%(2%La_2O_3, 98% BaO.6Al_2O_3)]: TEM of the fresh sample shows that the Pt particle size is ~1 nm (Figure 13). This particle size grows to 1–2 nm in diesel rich simulated exhaust in the ex-situ reactor at 500ºC for 4 h.

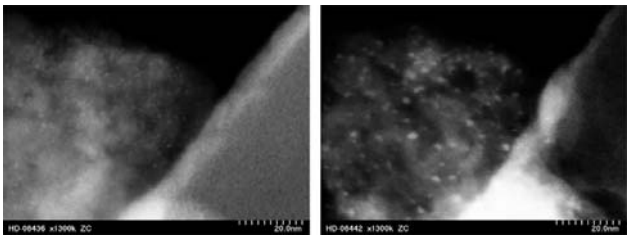

Figure 11. TEM off fresh and rich aged (500ºC, 4 h) Pt/Al_2O_3.

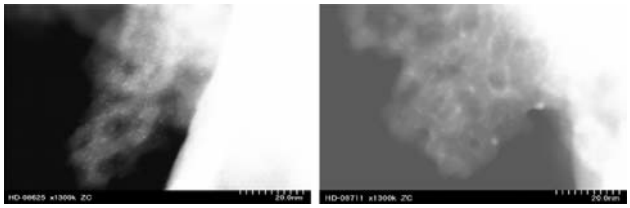

Figure 12. TEM of fresh and rich aged (500ºC, 4 h) 2%Pt-98%[10%CeO_2-ZrO_2-90%(2%La_2O_3-98%BaO.6Al_2O_3)].

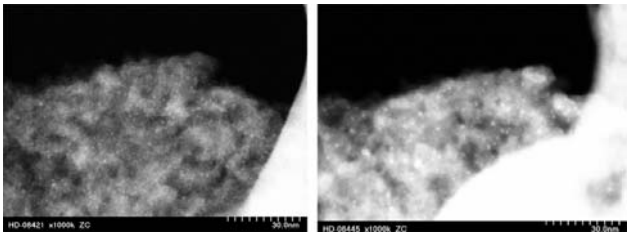

Figure 13. TEM of fresh and lean aged (500ºC, 4 h) 2%Pt, 5%MnO_2–93%[10%CeO_2-ZrO_2-90%(2%La_2O_3-98% BaO.6Al_2O_3)].

Modifications in Ex-situ Reactor

The ex-situ reaction is under modification to include the ability to cycle through lean and rich conditions. This involves the addition of a gas-flow controller and installation of solenoid valves that can be controlled through a computer using the Labview

software system. The installation of plumbing is complete, and the new ex-situ reactor should be in operation shortly. The schematics of the modified reactor are shown in Figure 7b.

Surface Studies of Fresh and Aged Model NO_x Trap Catalyst

The results of X-ray photoelectron spectroscopy analysis (XPS) of 2%Pt, 98%[10%CeO_2-ZrO_2, 90%(2%La_2O_3, 98%BaO.6Al_2O_3)] are presented in Table 2. Powder samples of the fresh, thermally aged (500ºC in air for 4h), and lean simulated exhaust-exposed (after thermal aging) catalysts were pressed onto an indium foil and then analyzed. The high concentration of Pt and lathanum in fresh samples is due to the migration of these elements to the surface. Thermally aged samples probably achieve a redistribution of elements, leading to a reduced concentration of these elements on the surface. When a thermally aged sample is exposed to simulated lean NO_x conditions for about 4 h at 500ºC, the surface composition does not change significantly. The lack of a significant increase in nitrogen or carbon after extended exposure to lean diesel exhaust is puzzling. Further experiments are in progress to determine if it is just a surface phenomenon, or if the bulk material loses nitrate during our cooling protocol.

Conclusions

Our results from the study of microstructural changes in a supplier lean NO_x trap system (based on Pt/BaO-Al_2O_3 and CeO_2-ZrO_2 materials) upon aging on (1) a pulsator at Ford, (2) a dynamometer at Ford, and (3) vehicles in gasoline DISI engines in Europe show that precious metal sintering and barium migration occurs. This could be a cause of performance deterioration in NO_x trap materials.

We have successfully employed an ex-situ reactor to study aging in model NO_x trap catalysts. This system has allowed us to study changes in samples in a selected area under thermal, lean diesel, or rich diesel conditions. We have updated the ex-situ reactor to a lean–rich cycle NO_x trap system. This protocol will allow us to rapidly screen catalyst systems without having to do start-and-stop experiments to understand aging.

Our next goal is to complete the bench-flow reactor and start evaluating new model catalyst systems for their performance and relate them to microstructural changes.

References

1. N. Miyoshi, S. Matsumoto, K. Katoh, T. Tanaka, J. Harada, N. Takahashi, K. Yokota, M. Sigiura., and K. Kasahra, "Development of New Concept Three-Way Catalyst for Automotive Lena-Burn Engines," SAE paper 95-0809, Society of Automotive Engineers..

2. N. Takahashi, H. Shinjoh, T. Iijima, T. Suzuki, K. Yamazaki, K. Yokota, H. Suzuki, N. Miyoshi, S. Matsumoto, T. Tanizawa, S. Tateishi, and K. Kasahara, "The New Concept 3-Way Catalyst for Automotive Lean-Burn Engine: NO_x Storage and Reduction Catalyst," *Catalysis Today* **27**, 63–69 (1996).

Table 2. XPS analysis of 2%Pt-98%[10%CeO_2-ZrO_2-90%(2%La_2O_3-98%BaO.6Al_2O_3)]

Element	Fresh		Thermally aged at 500ºC in air for 4 hours		Aging under simulated lean diesel exhaust at 500ºC for 4 hours	
	Atomic %	Wt %	Atomic %	Wt %	Atomic %	Wt %
O	57.8	33.5	59.3	34.9	61.7	37.7
Al	26.6	26.0	27.6	27.4	26	26.8
C	6.3	2.7	3.7	1.6	4.1	1.9
Ba	3.9	19.4	5.9	29.8	5.1	26.7
La	2.2	11.0	0.5	2.5	0.6	3.2
N	0.3	0.2	0.2	0.1	0	0
Pt	1	7.1	0.5	3.6	0.5	3.7

Presentations

C. K. Narula, "Recent Advances in Lean NO_x Treatment in Automotive Exhaust," invited seminar at Purdue University, West Lafayette, Indiana, April 22, 2004.

C. K. Narula, "Applied Catalysis Program," a presentation of results to the Science and Technology Technical Review Panel, National Transportation Research Center, Oak Ridge, TN, 2004.

F. Aftertreatment Catalysts Materials Research

Matthew Henrichsen and Randy Stafford
Cummins, Inc.
1900 McKinley Ave.
Columbus, IN 47203
(812) 377-418-0428; e-mail: matthew.henrichsen@cummins.com

ORNL Technology Development Area Specialist: Dr. Sidney Diamond
(202) 586-8032; fax: (202) 586-1600; e-mail: sid.diamond@ee.doe.gov
ORNL Technical Advisor: D. Ray Johnson
(865) 576-6832; fax: (865) 574-6098; e-mail: johnsondr@ornl.gov

Contractor: Oak Ridge National Laboratory, Oak Ridge, Tennessee
Prime Contract No: DE-AC05-00OR22725
Subcontractor: Cummins Inc., Columbus, Indiana

Objective

- Develop the knowledge and tools necessary to satisfy the U.S. Environmental Protection Agency (EPA) 2007 and 2010 diesel emissions regulations while minimizing the total cost of ownership.

Approach

- Develop reactors and test methods for understanding the fundamental behavior of catalysts.
- Evaluate novel base metal oxide catalysts for oxidation of diesel soot with conventional and microwave heating.
- Improve understanding of sulfation and desulfation of commercial nitrogen oxides (NO_x) reduction catalysts through reactor studies.

Accomplishments

- Evaluated the kinetics of desulfation on a commercial NO_x reduction catalyst.
- Demonstrated that microwave heating results in catalyzed soot oxidation rates substantially similar to those from conventional heating.

Future Direction

- Continue sulfation and desulfation studies with private funding.
- Continue the search for low-temperature soot oxidation catalysts.

Introduction

The 2007 and 2010 EPA regulations on particulate and NO_x emissions from diesel engines mandate significantly lower emissions than the current regulatory standards. These regulations are seen as aftertreatment-forcing by the diesel industry.

NO_x traps (also referred to as NO_x storage and release catalysts) are a primary path toward compliance with the 2007 and 2010 EPA regulations. However, the poisoning effects of sulfur reduce the efficiency of NO_x traps in capturing and destroying NO_x emitted from diesel engines. Even though sulfur levels will be reduced in future diesel fuels, any

amount of sulfur in fuel will be detrimental because the effect of sulfur on NO_x traps is cumulative. NO_x traps can be desulfated by high-temperature reduction. Desulfation, however, can require an extended time at high temperature. If the desulfation process requires 10 minutes for completion for light-duty applications, then desulfation will be impractical because the average time between engine start and stop for a light-duty vehicle is less than 10 minutes.

Catalysts commonly used for soot oxidation in catalyzed soot filters are based on platinum group metals and cerium oxides. The use of platinum group metals significantly increases the cost of catalyst systems. Base metal oxide catalysts, while typically less active than platinum group metal catalysts, are much less expensive. There have been reports in the literature that microwave heating accelerates soot oxidation in the presence of some base metal oxide catalysts more than conventional heating to a similar temperature accelerates oxidation. If true, this could allow very low-temperature regeneration of soot filters, significantly reducing the stress on the system and the cost of regeneration.

Approach

An Emerachem NO_x adsorber catalyst was selected for evaluation of sulfation and desulfation behavior. The impacts of desulfation temperature, reductant concentration, duration of exposure to reductant, and sulfur loading on desulfation rates and desorbed sulfur species were measured. The behavior of other NO_x adsorber catalysts will be similar to the behavior of this catalyst, although the temperature required for desulfation will likely be higher.

Using the microwave thermal gravimetric analysis (TGA) method developed under this program at Notre Dame University, microwave and conventional TGA was applied to several catalysts. Catalysts were selected based on other literature reports of accelerated activity in microwave heating and the principal investigators' knowledge of microwave heating and soot oxidation.

Results

Sulfation and Desulfation

A proprietary Emerachem catalyst was applied to a 3-in.-long 400-cpsi NGK extruded cordierite catalyst substrate. A core drill was used to separate 0.6-in.-diameter cores from the catalyzed substrate for use in a bench flow reactor. All cores were prepared for desulfation experiments using the degreening cycle detailed in Table 1. Before sulfation/desulfation testing, the performance of each catalyst core was evaluated at the conditions described in Table 2.

Table 1. Experimental conditions for degreening

Parameter	Lean	Rich
Time (sec)	300	300
Space velocity (1/h)	30,000	30,000
Temperature (°C)	575	575
NO (ppm)	300	0
SO_2 (ppm)	0	0
CO (%)	0	2.5
H_2O (%)	8	8
CO_2 (%)	8	8
O_2 (%)	8	0
N_2	Balance	Balance

Table 2. Experimental conditions for catalyst characterization before sulfation/desulfation.

Parameter	Lean	Rich
Time (sec)	56	4
Space velocity (1/h)	30,000	30,000
Temperature (°C)	Varied	Varied
NO (ppm)	300	0
SO_2 (ppm)	0	0
CO (%)	0	2.5
H_2O (%)	8	8
CO_2 (%)	8	8
O_2 (%)	8	0
N_2	Balance	Balance

For evaluation of temperature effects, a fresh core was used for each desulfation temperature. Conditions during sulfation and desulfation are listed in Table 3. It is important to note that no oxygen was included in the desulfation gas stream. This both aided in controlling the temperature of the cores during desulfation and eliminated the need to inject extra reductant to remove the oxygen.

The total sulfur release is shown in Figure 1. As shown in Figure 2, even a small portion of residual sulfur will adversely impact subsequent NO_x reduction performance. High-efficiency NO_x removal at lower temperatures in Figure 2 was due to the mildness of the NO_x performance cycle rather than to a lack of impact due to sulfur poisoning.

Table 3. Experimental conditions for sulfation/desulfation.

Parameter	Sulfation	Desulfation

Time (min)	37	15
Space velocity (1/h)	30,000	30,000
Temperature (°C)	550	Varied
NO (ppm)	0	0
SO_2 (ppm)	40	0
CO (%)	0	4.0
H_2O (%)	8	8
CO_2 (%)	8	8
O_2 (%)	8	0
N_2	Balance	Balance

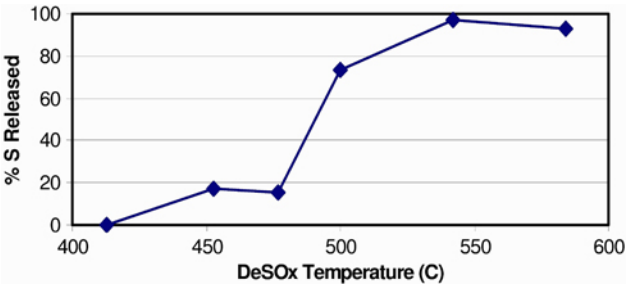

Figure 1. Total sulfur released during desulfation as a function of desulfation temperature.

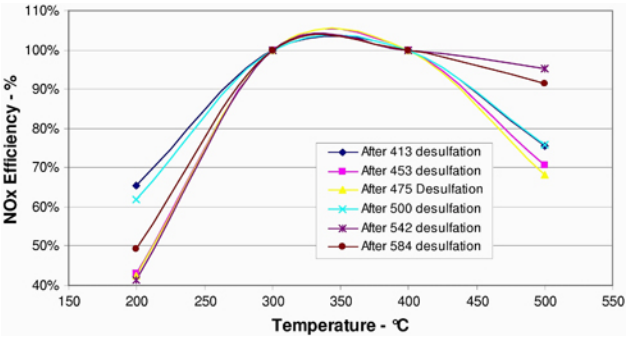

Figure 2. NOx performance after desulfation at various temperatures.

Similar degreening cycles and test methods were used in preparing fresh cores for evaluation of the impact of reductant concentration. The impact of reductant concentration on total sulfur release is shown in Figure 3. All cores were fresh except for the 0.25% CO core, which had been previously used for the 4% CO data. Temperature was 550°C for each of these experiments. The decrease in sulfur release with increasing reductant at low concentration was likely due to CO poisoning of the oxidation

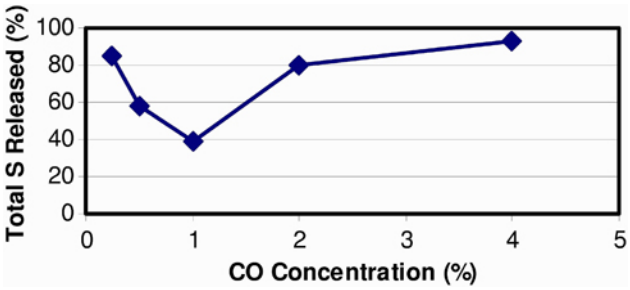

Figure 3. Total sulfur released during desulfation as a function of CO concentration at 550°C.

sites on the platinum catalyst. The high-temperature NO_x reduction performance of cores desulfated with 0.5% and 2% CO was similar, and both were better than the core desulfated at 1% CO.

The impact on desulfation of the sulfur quantity loaded on the catalyst was investigated at 550°C and at 2% CO. As total sulfur on the catalyst increased, sulfur released during desulfation increased nearly proportionally. Desulfation time effects were investigated at 550°C with 2% CO. As desulfation time increased, sulfur release increased and the release rate decreased (see Figure 4).

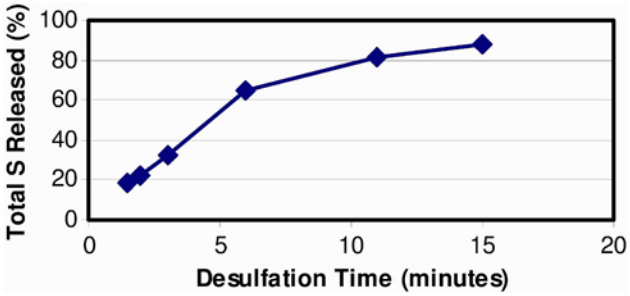

Figure 4. Total sulfur released during desulfation as a function of desulfation time at 550°C and 2% CO.

Microwave-heated Catalytic Soot Oxidation

As discussed in the previous annual report, a microwave TGA was constructed and calibrated so that microwave effects on catalyzed oxidation of soot could be investigated. Calibration to conventional TGA results was done with a microwave susceptor supporting the soot specimen so that heating of the soot was primarily though conduction and convection (see Figure 5). The presence of the susceptor allowed heating of the specimen without

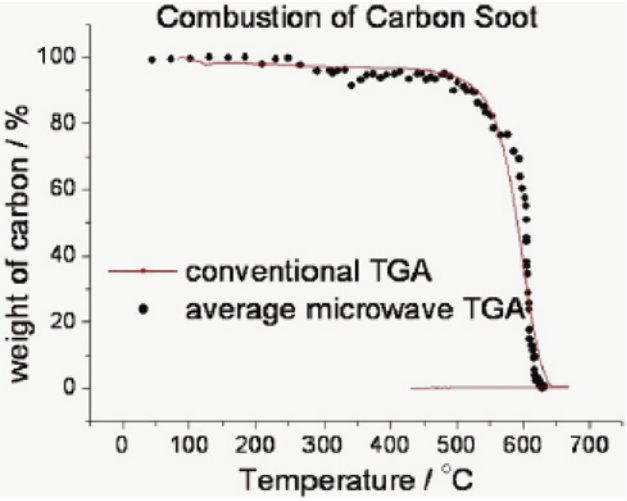

Figure 5. Comparison of microwave and conventional TGA results for uncatalyzed soot oxidation.

significant thermal gradients; but in the absence of a susceptor, thermal gradients were present.

Figure 6 shows the result of heating a mixture of CuO and carbon with microwaves on a quartz (non-suscepting) specimen support. Each specimen in the photograph was heated for a longer time than the specimen immediately to its left. The specimen on the left was not heated. The specimen in the middle has a mottled color, indicating that carbon has been oxidized. Note that the lighter colors are present toward the center of the pile of powder in the basket. (CuO alone is a red-brown color.) The specimen on the right is entirely red-brown in the middle of the pile, while the edges remain black. This indicates that the temperature gradients measured through infrared thermography (Figure 7) are indicative of where the soot is burning.

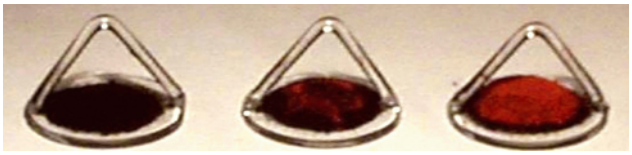

Figure 6. Mixtures of CuO and soot heated to various temperatures in microwave TGA.

It is not surprising that the edges of the specimens are cooler because of the higher surface area there relative to the mass available to absorb microwaves. Because of this effect, the fraction of soot burned (when no susceptor other than the soot is

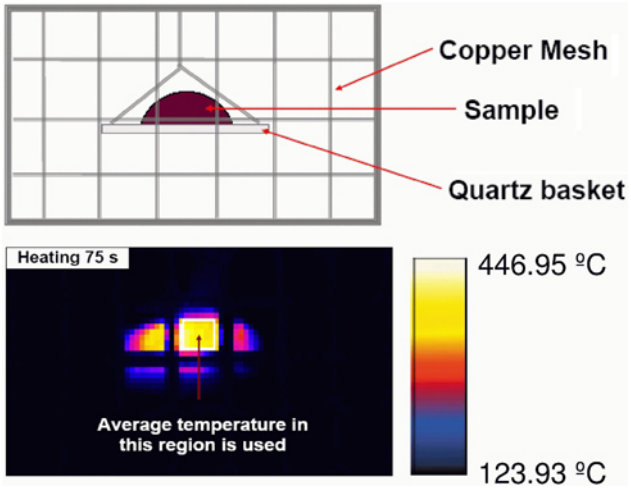

Figure 7. Thermography of specimen during heating in microwave TGA.

present) is a function of the soot present at the beginning of the experiment. (See Figure 8.)

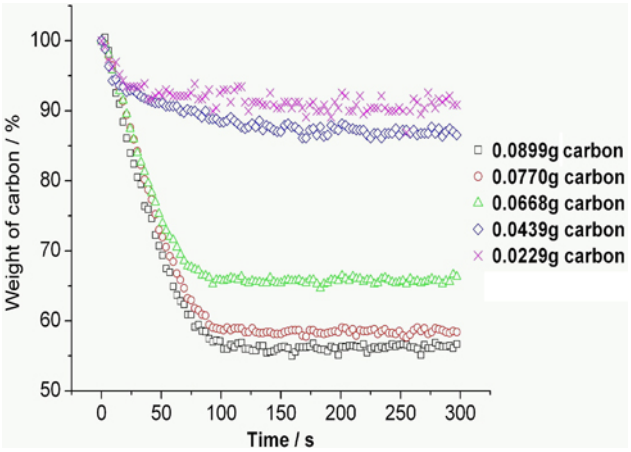

Figure 8. Soot oxidation vs. time for various soot loads in microwave TGA.

Despite this drawback of the microwave TGA system, it could be used for evaluating the usefulness of potential microwave catalysts because large effects were being looked for. Although a decrease in soot oxidation temperature of as little as 25 or 50°C would be useful in a real system, the added cost and complexity of microwave heating would be justified only by a much larger decrease in soot ignition temperature.

Figure 9 shows TGA results for mixtures of soot with CuO and $LiFe_5O_8$. Both oxides slightly

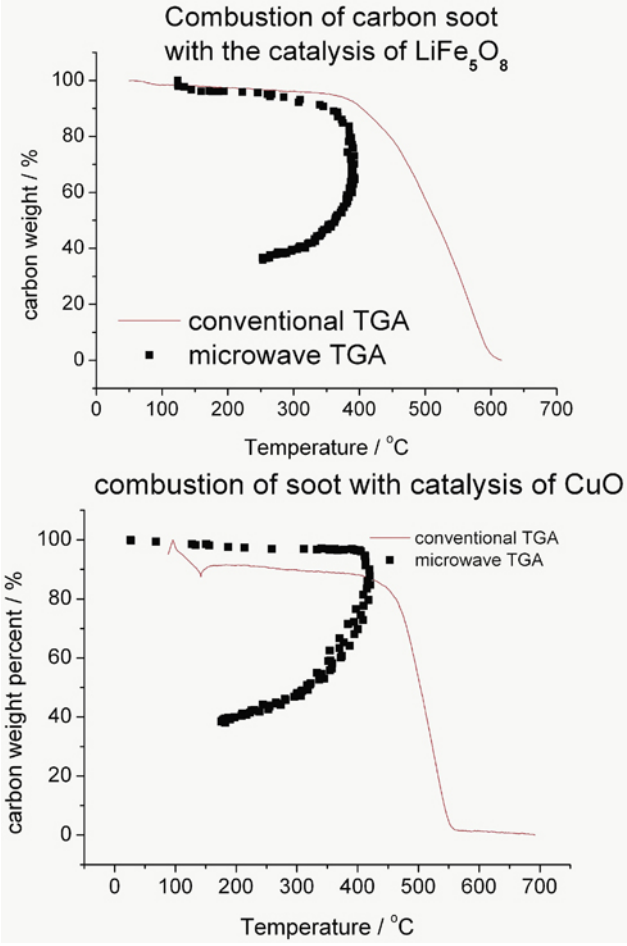

Figure 9. Catalyzed soot oxidation with microwave and conventional heating.

catalyze soot oxidation in conventional and microwave heating. It is important to note that in Figure 8, surface temperatures from microwave TGA are being compared with bulk temperatures from conventionally heated TGA. (Bulk temperatures in microwave heating can be substantially higher than surface temperatures.) The best point to compare the microwave and conventional results is at the beginning of oxidation. This best represents the temperature required for ignition.

While both CuO and $LiFe_5O_8$ lower soot oxidation temperatures relative to uncatalyzed oxidation, the difference between microwave and conventional temperatures required for ignition is less than 50°C. Taking into consideration the surface temperature measurement and temperature gradients likely present in the microwave TGA, these data provide no reasonable basis to believe that microwave heating significantly improves catalytic oxidation of soot.

Summary and Conclusions

An examination of the kinetics of desulfation on a commercial NO_x adsorber catalyst was begun. The information will be useful for designing desulfation control strategies. The impact of microwave heating on soot oxidation was investigated. Based on measurements made with microwave and conventionally heated TGA, it is not likely that microwave heating significantly lowers the temperature of catalyzed soot oxidation with the catalysts examined in this work.

Publications

Hongmei An, Caitlin Kilroy, and Paul J. McGinn, "An Examination of Microwave Heating to Enhance Diesel Soot Combustion," submitted to *Applied Catalysis B, Environmental*.

J. Kong, M. Henrichsen, and A. J. Shih, "Infrared Thermometry Measurement of Temperature Distribution in The Microwave Regeneration of Diesel Particulate Filters," *International Journal of Engine Research*, in press.

G. Durability of Diesel Particulate Filters

Edgar Lara-Curzio
Oak Ridge National Laboratory
P.O. Box 2008, MS-6069
Oak Ridge, TN 37831-6069
(865) 574-1749; fax: (865) 574-6098; e-mail: laracurzioe@ornl.gov

Technology Development Area Specialist: Dr. Sidney Diamond
(202) 586-8032; fax: (202) 586-1600; e-mail: sid.diamond@ee.doe.gov
Field Technical Manager: D. Ray Johnson
(865) 576-6832; fax: (865) 574-6098; e-mail: johnsondr@ornl.gov

Contractor: Oak Ridge National Laboratory, Oak Ridge, Tennessee
Prime Contract No.: DE-AC05-00OR22725

Objective

- Identify and implement test techniques to characterize the physical and mechanical properties of ceramic diesel particulate filters (DPFs) and to develop analysis tools for predicting their reliability and durability.

Approach

- Identify and implement test techniques to determine the physical and mechanical properties of DPF ceramic substrates.
- Investigate the applicability of probabilistic design tools to DPF ceramic substrates. In particular, the applicability of the Ceramic Analysis and Reliability Evaluation of Structures (CARES) code to predict the reliability of DPF ceramic substrates will be investigated.

Accomplishments

- Completed the stress analysis of DPF beams subjected to flexural loading. The importance of accounting for the cellular structure of the component has been identified.
- Obtained the elastic properties of DPFs using a dynamic mechanical analyzer.

Future Direction

- Organize a round-robin test program to assess the precision of four-point bending test methods to determine the flexural strength of DPF ceramic substrates.
- Assess the susceptibility of DPF ceramic substrates to slow-crack growth using dynamic fatigue and double-torsion test methods.
- Implement probabilistic design tools to predict the reliability and durability of DPF ceramic substrates subjected to arbitrary thermomechanical histories.

Introduction

The pollution emitted by diesel engines contributes greatly to the nation's air quality problems. Even with more stringent environmental regulations set to take effect in 2004 and 2007, existing trucks and buses will continue to emit nitrogen oxides (NO_x) and particulate matter (PM), both of which contribute to serious public health problems.[1] Fortunately, there are several technologies designed to reduce pollution from existing trucks and buses, such as DPFs. A DPF is a ceramic device that collects PM in the exhaust stream. The high temperature of the exhaust heats the ceramic structure and allows the particles inside to break down (or oxidize) into less harmful components. DPFs reduce emissions of PM by 60 to 90% and emissions of hydrocarbons and carbon monoxide by 60 to 90%.

A typical DPF consists of a ceramic honeycomb with hundreds of cell passages partitioned by walls (Figure 1). Each cell passage has a square cell opening at one end and is closed at the other end so that the cell passages are alternately closed at each end. This structure forces the exhaust gases through the porous, thin ceramic honeycomb walls. When the exhaust gases carrying carbon particles flow through the fine pores of the walls, the carbon particles are filtered out. Porosity values in the range of 60% heighten filtration efficiency to more than 90% while reducing gas-flow resistance so as not to affect the engine performance.

The process of diesel PM collection begins as soon as the engine is started and continues while the engine is operating. As carbon particles collect on the ceramic walls of the DPF, the backpressure of the system increases. This problem is alleviated by burning the trapped PM, through a catalytic reaction using exhaust gas heat at 400°C or more. The burning produces carbon dioxide and water vapor that pass through the filter. This process, called regeneration, results in a cleaner filter. The regeneration process depends upon exhaust temperature, oxygen, NO_x content, time, and PM levels.

The key to the successful use of DPFs is to reliably regenerate the filter (e.g., burn the PM that the filter traps or collects). Traditionally, combustion of soot is done in an oxygen atmosphere (air). In air, soot will burn at about 500°C. However, this is not a typical operating temperature for diesel engine exhaust. As a result, to burn soot in air, an active system is required, i.e., one that increases the temperature of the exhaust using some external heat source. But if an active system is not carefully controlled, or if the level of PM collected on the filter walls is too high, a filter may experience an uncontrolled burn where the temperature increases to 600°C or more, resulting in damage to the filter element.

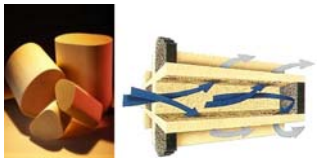

Figure 1. Corning's cordierite-based DPFs.

The objective of this project is to develop and implement methodologies to predict the reliability of DPFs. A useful conceptual model for this purpose is the reliability bathtub curve, which describes reliability-related phenomena of a component over its life cycle.[2] A schematic of the reliability bathtub curve is depicted in Figure 2. It consists of three stages: The infant mortality phase is characterized by premature failures due to improper manufacturing or assembly, poor workmanship, or defects introduced during processing. The second stage corresponds to the useful life of the component and is characterized by a constant failure rate. In this regime, failures are typically associated with random, excessive loads. If sufficiently high safety factors are used during the design process, the magnitude of this failure rate should be negligible. The third stage of the bathtub curve is known as the "wear-out" phase, in which the failure rate increases with time as a result of aging phenomena. Aging phenomena include thermal and mechanical fatigue, corrosion, and creep deformation, among others.

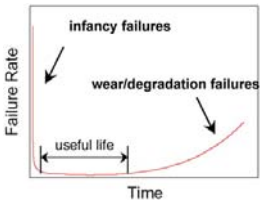

Figure 2. Reliability bathtub curve.

Because of accelerated wear-out, the time at the onset of wear-out is often regarded as the useful life of the component The reliability bathtub curve can

be used as a good descriptor of how the failure rate of DPFs evolves over time. Infancy failures of DPFs could be related to manufacturing or process defects (e.g., large pores, inclusions, cracking) or defects introduced during assembly. Failures of DPFs during their useful life will be dictated by the intersection between the spectrum of thermomechanical loads and the distribution of DPF strengths. Such failures could result from excessive vibration, for example, or unwanted thermal excursions during transients associated with regeneration. Wear-out and degradation failures of DPFs could be associated with the growth of microcracks assisted by thermal fatigue, the chemistry of the environment, and/or chemical and microstructural changes in the material due to long-term exposure to elevated temperatures in the exhaust environment and the presence of compounds used for aftertreatment processes.

The objective of this project is to develop life prediction methods for DPFs and, by using those methods, to design more durable and reliable DPFs.

Approach

Designing DPFs that are durable and reliable poses significant challenges. For example, the porosity of DPFs, which allows them to remove PM from the exhaust gas stream, has a deleterious effect on their mechanical strength. This is important because DPFs experience demanding thermomechanical conditions during service, including thermal shocks resulting from rapid heating/cooling and stresses that arise from temperature gradients. The approach to be followed in this project includes identifying and implementing test techniques for non-destructive evaluation of ceramic substrates to assess their integrity. Their physical and mechanical properties and the mechanisms responsible for their degradation in the various stages of the bathtub curve also will be determined and identified. The properties to be analyzed include thermal expansion, thermal conductivity, heat capacity, density, porosity, elastic properties, strength, fracture toughness, and resistance to crack growth at ambient and elevated temperatures in air and in relevant environments. The information generated will be used in turn to implement probabilistic design tools. In particular, the applicability of the CARES code[3] to predict the reliability of DPF ceramic substrates will be investigated. Such probabilistic design methodologies are based on a combination of experimentally-determined strength data, stress analyses of the component using finite-element analysis, and the selection of appropriate failure criteria. The durability (service life) of the component can also be predicted using this framework by considering the mechanisms responsible for the degradation of material strength, such as slow-crack growth or creep.

The implementation of these methodologies has been successful in considering dense structural ceramic components. However, there is limited work on their use to analyze non-structural, porous ceramic components.

Results

To use CARES to predict the reliability of porous ceramic structures, it is necessary, through thorough fractography, to identify the flaws that control the strength of the material. This often amounts to identifying strength-limiting flaws that reside in the volume of the material and on the surface of the component. Often, more than one population of flaws can be identified in the volume or on the surface. Although fractographic analyses are essential for identifying strength-limiting flaws as part of the probabilistic design methodologies, the porous nature of the material and the cellular structure of the component have made fractographic analysis effectively impossible. This is an important issue that will be researched further in the future.

One of the first tasks carried out was focused on analyzing the flexural behavior of beams of various sizes obtained from ceramic substrate DPFs. Special attention was given to determining flexural strength. The maximum tensile stress in a beam when it is subjected to bending is given by

$$\sigma_{max} = \frac{M\,c}{I} \qquad (1)$$

where I is the second moment of inertia of the cross-sectional area of the beam, M is the moment, and c is the distance from the neutral axis to the bottom of the beam, which is subjected to the maximum tensile stress. Figure 3 depicts a schematic of such a beam subjected to 4-point bending (dimensions are in inches), and Figure 4 illustrates the calculation of the maximum tensile stress when the cellular structure of the beam is either taken into account or

Figure 3. Schematic of DPF ceramic substrate 1×1 beam subjected to 4-point bending.

neglected. It was found that when the cross-sectional structure of the beam is neglected, the flexural strength is underestimated by 25%. These results were verified through a finite-element stress analysis (Figure 5).

The discrepancy in determining the flexural strength of beams when the cellular structure of the beam is neglected is further magnified when the cross-sectional area of the beam increases. Figures 6–8 depict the case for a 2×2 beam. In this case, the flexural strength is underestimated by 45% when the cellular structure of the beam is neglected. These

$\sigma = \frac{Mc}{I}$

$M = (0.5)(.15) = 0.075\ lbs \cdot in$

$c = 0.041\ in$

Moment of inertia and stress using beam theory

$I = \frac{1}{12}(.082)^4$ Assuming solid cross-section

$I = 3.77 \times 10^{-6}\ in^4$

$\sigma = 815.6\ psi$

Moment of inertia and stress using actual cross section

$I = \frac{1}{12}(.082)^4 - \left[\frac{1}{12}(.058)^4\right]$

$I = 2.82 \times 10^{-6}\ in^4$ Accounting for the cross-sectional area

$\sigma = 1{,}088.6\ psi$

Figure 4. Stress analysis for DPF ceramic substrate 1×1 beam subjected to 4-point bending.

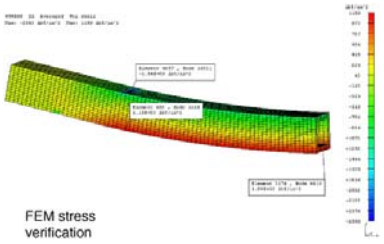

Figure 5. Results of stress analysis using finite elements for a 1×1 DPF ceramic substrate beam subjected to 4-point bending.

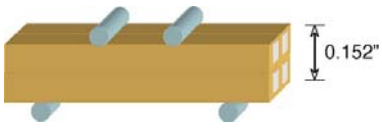

Figure 6. Schematic of DPF ceramic substrate 2×2 beam subjected to 4-point bending.

$\sigma = \frac{Mc}{I}$

$M = (0.5)(.15) = 0.075\ lbs \cdot in$

$c = 0.076\ in$

Moment of inertia and stress using beam theory

$I = \frac{1}{12}(.152)^4$ Assuming solid cross-section

$I = 4.448 \times 10^{-5}\ in^4$

$\sigma = 128.1\ psi$

Moment of inertia and stress using actual cross section

$I = \frac{1}{12}(.152)^4 - 4\left[\frac{1}{12}(.058)^4 + (.058)^2(.035)^2\right]$

$I = 2.423 \times 10^{-5}\ in^4$ Accounting for the cross-sectional area

$\sigma = 235.2\ psi$

Figure 7. Stress analysis for DPF ceramic substrate 2×2 beam subjected to 4-point bending.

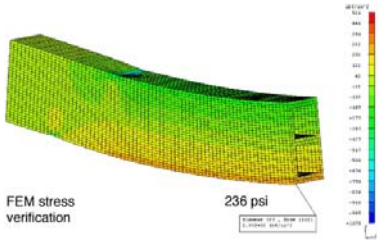

Figure 8. Results of stress analysis using finite elements for a 2×2 DPF ceramic substrate beam subjected to 4-point bending.

results were also verified using a finite-element stress analysis.

As indicated, one of the objectives of this project is to implement probabilistic design methodologies to analyze porous ceramic components with complex cellular structures. One of the questions that needs to be answered is to what extent the meso-structure of the component (cellular structure) can be accounted for, neglected, or simplified, in order to achieve accurate results with numerical expediency. These experimental results indicate that it is necessary to account for the cellular structure of the material, but in order to achieve numerical expediency, local-global techniques will be investigated.

Another important consideration in implementing probabilistic design methodologies requires accurate knowledge of the properties of the material, including their elastic properties. The elastic properties of porous DPF test specimens have been determined with a high degree of accuracy through the use of a dynamic mechanical analyzer. Figure 9 depicts the experimental set-up, which consists of a 3-point bending fixture in which the middle roller is attached to an actuator. A small, cyclic sinusoidal signal is used to stress the test specimen, and the response is recorded to determine the dynamic

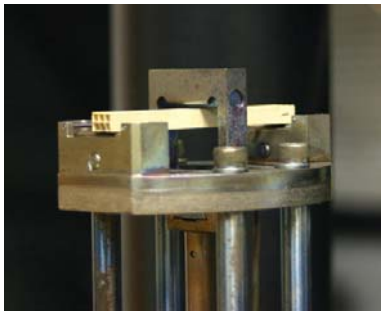

Figure 9. Three-point bending fixture for determining elastic properties of DPF ceramic substrates by using a dynamic mechanical analyzer.

modulus of the material. Figure 10 depicts the cross-sectional area of the beams evaluated, while Table 1 lists the values obtained for the storage and loss moduli of the material. The sensitivity of this test technique makes it ideal for monitoring damage evolution, as determined by changes in elastic properties.

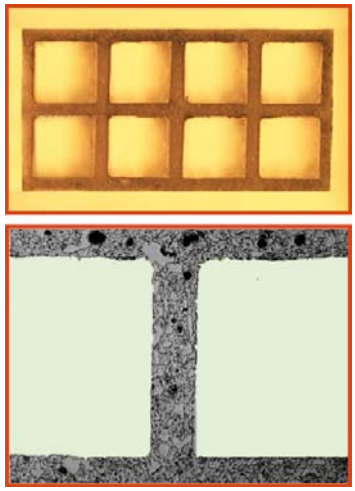

Figure 10. Cross-sectional area of 4×2 DPF ceramic substrate beam.

Table 1. Dynamic modulus properties of ceramic substrate DPF.

Sample	No. of tests	Storage modulus (GPa)	Loss modulus (GPa)	Tan δ
1	4	14.7 ±0.7	0.21±0.03	0.01±0.00
2	6	13.3 ±0.89	0.25±0.07	0.02±0.00
3	5	13.4 ±0.9	0.23±0.04	0.02±0.00
4	5	15.2 ±0.7	0.22±0.04	0.02±0.01
5	5	14.9 ±0.6	0.23±0.03	0.02±0.00
Average		14.2 ±1.1	0.23±0.05	0.02±0.00

Summary

Test techniques have been identified and implemented to determine the physical and mechanical properties of DPF ceramic substrates. Specifically, values for the elastic modulus and flexural strength have been determined by dynamic mechanical analysis and 4-point bending, respectively. A round-robin testing program involving Corning, Cummins, and Oak Ridge National Laboratory has been planned and will be carried out to assess the precision of test methods for determining strength and elastic properties. Work is under way to implement probabilistic design methodologies to predict the reliability and durability of DPFs when they are subjected to an arbitrary thermomechanical history.

References

1. United States Environmental Protection Agency, Office of Transportation and Air Quality, “Questions and Answers on Using a Diesel Particulate Matter Filter in Heavy-Duty Trucks and Buses,” EPA420-F-03-017, June 2003.

2. G. S. Wasserman, *Reliability Verification, Testing and Analysis in Engineering Design*, Marcel Dekker, New York, 2003

3. N. N. Nemeth, L. P. Powers, L. A. Janosik and J. P. Gyekenyesi, *Ceramics Analysis and Reliability Evaluation of Structures Life prediction program: Users and Programmers Manual*, National Aeronautics and Space Administration—Glen Research Center, Life Prediction Branch, 1993.

4. MATERIALS FOR AIR HANDLING, HOT SECTION, AND STRUCTURAL COMPONENTS

A. High-Temperature Advanced Materials for Lightweight Valve Train Components

Jeremy S. Trethewey, Principal Investigator
Mark Andrews, John Grassi, David Longanbach, and Matt Fletcher
Caterpillar Inc.
Tech Center 854-80 TC-E
14009 Old Galena Rd.
Mossville IL, 61552
(309) 578-0056; fax: (309) 578-2953; e-mail: trethewey_jeremy_s@cat.com

DOE Technology Development Area Specialist: Sidney Diamond
(202) 586-8032; fax: (202) 586-1600; e-mail: sid.diamond@ee.doe.gov
ORNL Technical Advisor: D. Ray Johnson
(865) 576-6832; fax: (865) 574-6098; e-mail: johnsondr@ornl.gov

---

Contractor: Oak Ridge National Laboratory, Oak Ridge, Tennessee
Prime Contract No: DE-AC05-00OR22725
Subcontractor: Caterpillar Inc., Peoria, IL

Objective

- Design and fabricate prototype engine valves from silicon nitride and titanium aluminide (TiAl) materials that are 30% lighter than steel valves and provide a 200% increase in service lifetime and a 10% increase in fuel efficiency.

Approach

- Select γ-TiAl and silicon nitride materials for this project because of their high corrosion resistance and ability to maintain superior strength at elevated temperatures.
- Use an optimization routine in conjunction with a probabilistic approach to design valves (although the traditional deterministic method is practical for traditional metals, a probabilistic approach is necessary for high-hardness materials).
- Develop welding techniques to join TiAl to a titanium alloy in the fabrication of TiAl valves.
- Perform bench tests and engine tests to verify the robustness of valve design.

Accomplishments

- Successfully optimized friction welding between TiAl valve heads and Ti-6V-4Al valve stems.
- Conducted bench tests on silicon nitride valves with varying quality of surface finish; valves with good surface finish performed well and valves with poor surface finish failed in an anticipated mode.
- Completed flexure testing of silicon nitride material specimens with different finish machining parameters; results yielded Weibull moduli between 10 and 25.

Future Direction

- Perform bench tests on finish-machined silicon nitride engine valves; then perform engine testing in collaboration with the National Transportation Research Center.
- Procure additional valve blanks and flexure specimens from a second supplier; finish-machine, bench test, and engine test to evaluate strength and durability.
- Continue developing ceramic valve life prediction model using results from bench tests as input.

Introduction

Valve train components in heavy-duty engines operate under high stresses and temperatures and in severely corrosive environments. Advanced ceramics and emerging intermetallic materials are highly resistant to corrosion and oxidation and possess high strength and hardness at elevated temperatures. These properties are expected to allow higher engine operating temperatures, lower wear, and enhanced reliability. In addition, the lighter weight of these materials (about 1/3 that of production alloys) will lead to lower reciprocating valve train mass that could improve fuel efficiency. This research and development program is an in-depth investigation of the potential for use of these materials in heavy-duty engine environments.

The overall valve train effort will provide the materials, design, manufacturing, and economic information necessary to bring these new materials and technologies to commercial realization. With this information, component designs will be optimized using computer-based lifetime prediction models and validated in rig bench tests and short- and long-term engine tests. After proof of concept is established with valves, this design approach will be applied to other components made from high-temperature materials.

Approach

In an effort to develop the tools necessary to design effectively with high-strength, lightweight, brittle materials, a three-pronged approach was adopted. First, computational analysis was performed to optimize thermal and mechanical stresses within the valve during operating conditions. This initial design was cast into silicon nitride and TiAl valve blanks by several suppliers. The second phase of this approach is a characterization effort intended to evaluate valve performance on rig tests and engine tests. Third, a parallel path of study investigating the effects of damage caused by various machining techniques is being pursued. In order to minimize the probability of a brittle failure caused by surface defects, optimal surface finish must be achieved.

Work reported in the FY 2003 report outlines the design process used to adapt the current baseline metallic valve design to a design more suited for a ceramic material. For example, the head dimensions were changed to reduce the stress concentration experienced in the fillet radius. Several silicon nitride valve blanks were procured and finish-machined to these specifications. Because of the high cost of TiAl, only the heads of the valves were cast and finish-machined. After rough machining, the TiAl heads were successfully friction-welded to cylindrical stock of a titanium alloy (Ti-6V-4Al). Subsequently, they will be finish-machined before rig and engine testing.

Results

The mechanics of a structural brittle material are inherently different from those of a traditional metal. Whereas a metal (current-production valve material) may be adequately modeled as a continuum material, a brittle material (proposed valve material) is susceptible to microscopic flaws or cracks. A primary failure mode of a structural ceramic is the propagation of a surface crack initiated during machining. Therefore, it is imperative to understand the influence of various machining parameters on material strength and reliability.

Two types of valves were bench tested with a motor-driven valve impact rig: valves with a good surface finish (NT551 material) and a valve with a poor surface finish (SN235P material). Several NT551 valves survived 1000-hour rig tests incurring minimal damage (Figure 1). However, there appear to be engine deposits on the fillet radius and on the contact regions (composition and nature of the deposits has not yet been determined).

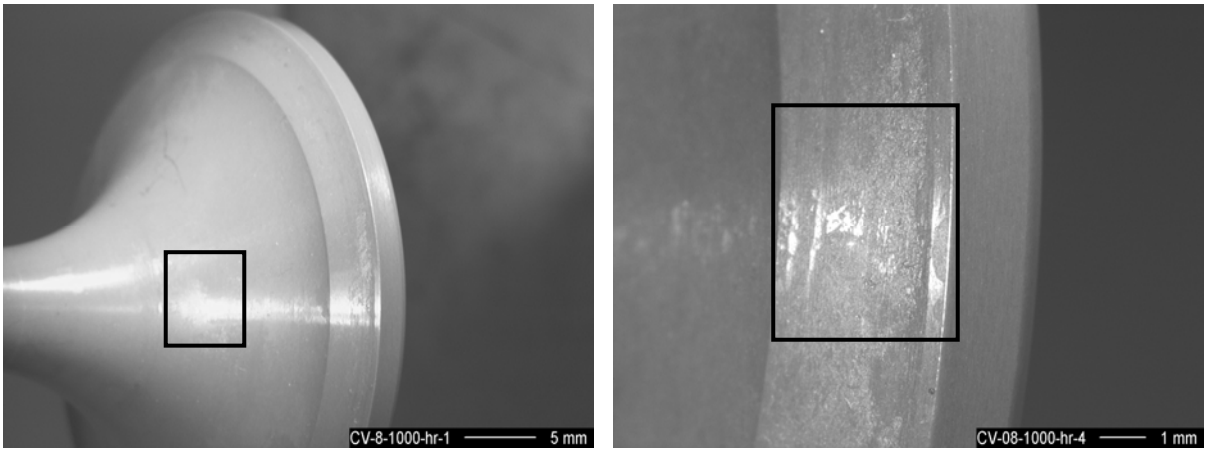

Figure 1. NT551 engine valves subject to 1000 hours of impact / wear tests. Note the deposits in the fillet radius and the contact regions (boxed regions)

In contrast to the good performance of the valves with acceptable surface finish, the performance of a poorly finished valve (SN235P material) was less than acceptable. This does not imply a difference in the quality of the materials but rather the importance of proper machining and surface finish. The keeper groove was not finished to specification, resulting in a rough surface with significant microcracking. Within one hour of rig testing, the valve fractured at the keeper groove. Microscopic analysis indicated that the fracture origin coincided with the region of severe machining damage (Figure 2). Nondestructive analysis performed by J. G. Sun at Argonne National Laboratory confirmed that the failure was a result of a pre-existing surface defect (Figure 3). Note that the white line corresponds to the location in the keeper groove where the flaw originated.

It was therefore decided to discontinue the bench rig testing until the appropriate surface finish was provided for all portions of the valve. The result of a subsequent investigation suggested that there may be an unacceptably low static friction coefficient between the valve and the keeper locks, resulting in a misapplication of the load from the valve spring. A study was launched to determine if the frictional force is inadequate for this application.

To further investigate the importance of surface finish to material strength, an optimization study was performed on cylindrical material (SN235P) flexure specimens with varying machining parameters. The test specimens (8 mm diam × 75 mm length) were subjected to three different finishing machining processes before they were strength-tested in four-point flexure. The tests were conducted at the Oak Ridge National Laboratory (ORNL) through a facility user agreement. A specialized four-point test fixture was designed and built for the cylindrical test specimens by A. Wereszczak of ORNL. All tests were conducted at ambient temperature conditions at the displacement rate of 0.5 mm/min, as specified in the ASTM C-1161 standard.

Figure 4 shows the characteristic strength and uncensored Weibull moduli of 12 different surface finish conditions. The characteristic strength shown in Figure 4 suggests that the inherent strength of the SN235P material is met regardless of machining condition. However, it is apparent that some of the finishing processes improve the data variance, as indicated by the high Weibull modulus values in Figure 4. A plausible explanation for the increase in the Weibull modulus values is that some finishing processes induce an appreciable compressive residual stress while others do not. The fractured samples will be examined using X-ray diffraction at ORNL to investigate the role of residual stress in the materials' strength behavior.

Conclusions

An investigation into the use of advanced materials for valve train applications is under way. The three-pronged approach combines probabilistic design techniques, rig and engine testing, and a systematic study of the effects of machining damage on reliability material. Rig testing exposed the importance of generating components with low-defect sur-

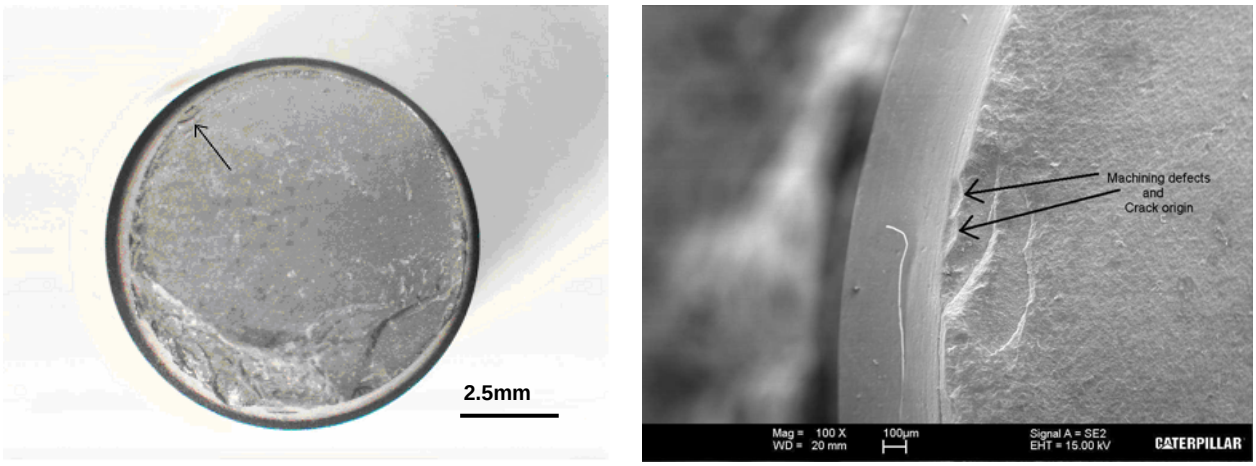

Figure 2. Fracture surface from fractured SN235P valve keeper groove observed from axial view: (left) optical micrograph, (right) scanning electron microscope image.

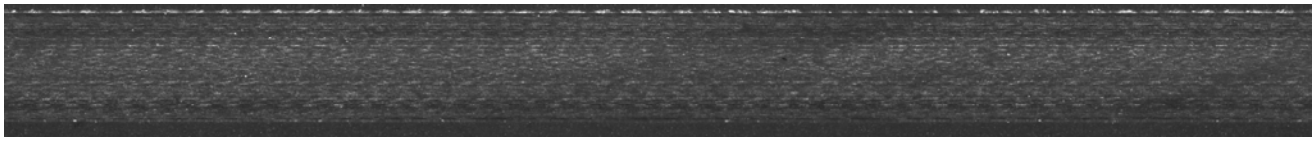

Figure 3. Laser scanning nondestructive evaluation image of the keeper notch of a poorly finished SN235P valve, showing a line of possible machining damage at the top of the image.

faces, and a study examining the effect of machining conditions on identical material specimens reached the same conclusion.

In addition to this fundamental study, several other steps will be taken to further examine the feasibility of fabricating a commercially viable ceramic or intermetallic valve. Arrangements are being made to engine test the silicon nitride valve prototypes near ORNL. Also, a new test rig will be rebuilt that will allow examination of both thermal and mechanical effects on experimental valves; and a more detailed life prediction model will be developed to examine the effect of accumulated damage on ceramic and intermetallic valves. Present and future efforts will help establish an understanding of how to design and manufacture nontraditional lightweight materials for valve train and other heavy-duty diesel engine applications.

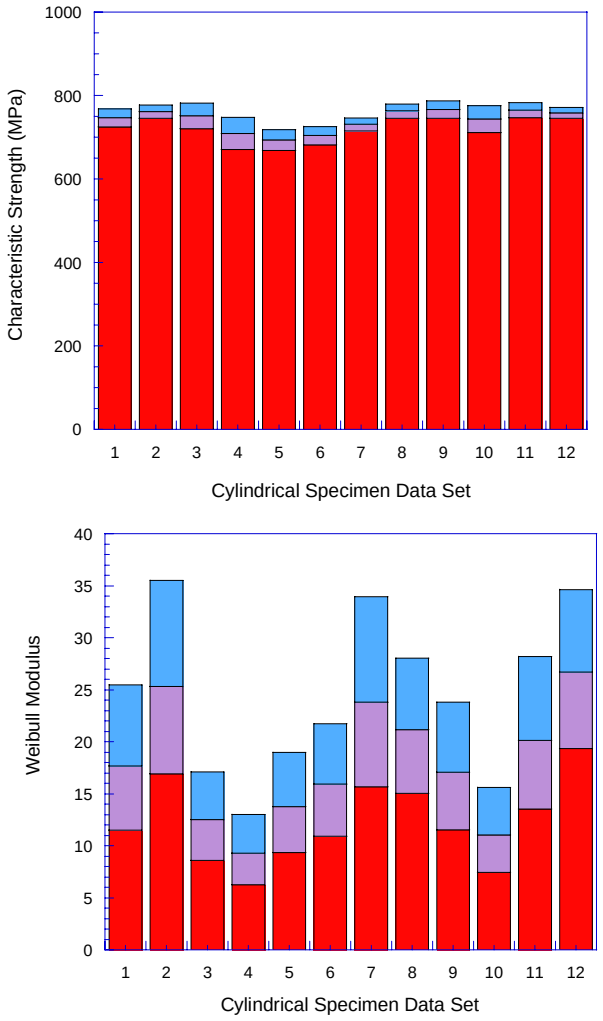

Figure 4. Results from four-point flexure test of SN235P cylindrical test specimens for various finish machining conditions: (top) uncensored Weibull characteristic strength; (bottom) uncensored Weibull moduli. Note that regions at the top of each column represent the 95% confidence interval of the data.

B. Engineered Surfaces for Diesel Engine Components

M. Brad Beardsley and Jesus Chapa-Cabrera
Caterpillar Inc.
Technical Center Bldg. E/854
P.O. Box 1875
Peoria, IL 61656-1875
(309) 578-8514, fax: (309) 578-2953, e-mail:beardsley_m_brad@cat.com

DOE Technology Development Area Specialist: Dr. Sidney Diamond
(202) 586-8032; fax: (202) 586-1600; e-mail: sid.diamond@ee.doe.gov
ORNL Technical Advisor: D. Ray Johnson
(865) 576-6832; fax: (865) 574-6098; e-mail: johnsondr@ornl.gov

Contractor: Oak Ridge National Laboratory, Oak Ridge, Tennessee
Prime Contract No: DE-AC05-00OR22725
Subcontractor: Caterpillar Inc., Peoria, Illinois

Objective

- Evaluate new laser technologies such as surface dimpling, cleaning, and laser-assisted spraying to enhance adherence and increase coating strength.
- Develop phosphate-bonded composites for internal thermal management coatings.
- Evaluate new quasicrystalline materials as potential thermal barrier and wear coatings.

Approach

- Evaluate laser treatment techniques by treatment of small samples.
- Examine the resulting sample microstructures to determine the potential of the treatment method.
- Measure the mechanical and physical properties of phosphate-bonded composites and use them to determine their potential for use as thermal barrier coatings (TBCs).
- Evaluate the thermal stability of quasicrystalline materials using diffusion couples to assess the stability of the aluminum-based quasicrystalline materials at engine operating temperatures.

Accomplishments

- Completed cost analysis of laser pre- and post-treatments and selected post-laser "tacking" as the method for treating coatings to increase adherence.
- Developed phosphate-bonded composite coatings that survived initial thermal cycling to 650ºC with good residual adherence to the substrate.
- Sprayed quasicrystalline coatings using the high-velocity oxygen fueled technique and began evaluating their thermal conductivities.

Future Direction

- Install a 2000-W Q-switched laser in Caterpillar's thermal spray facility to investigate the effects of laser surface ablation on the adherence and density of thermal-sprayed coatings.

- Prepared phosphate-bonded coatings with high surface adherence that have shown promise as high-temperature adhesives as well as TBCs. Additional formulations are under development.
- Conduct additional oxidation studies as well as limited in-cylinder engine testing for the aluminum-based quasicrystalline coating, which has shown limited stability at 900°C in diffusion couples. At temperatures below 500°C, the material shows promise to retain the low thermal conductivity of the quasicrystalline state..

Introduction

Engine testing of thermal sprayed coatings has demonstrated their potential benefit as thermal barriers and as wear coatings to reduce fuel consumption, reduce wear, and reduce component temperatures.[1,2,3] The durability of thermal sprayed coatings, particularly TBCs, remains the major technical challenge to their implementation in new engine designs. New approaches to coating design and fabrication will be developed to aid in overcoming this technical hurdle.

Three approaches to new TBCs have been pursued: (1) laser treatments applied to plasma-sprayed TBCs to modify their structures and adherence to enhance durability, (2) new quasicrystalline materials capable of being sprayed using a high-velocity oxygen-fuel (HVOF) process that produces denser coatings with higher bond strengths, and (3) new phosphate-bonded composites that allow for inner diameters to be coated and that have low thermal conductivity and high adherence.

Laser Treatments. Two types of laser treatments have been investigated. The laser-assisted plasma spray technique uses the power applied by the laser to completely melt the sprayed materials on the substrate to allow for metallurgical bonding and higher adherence of the coating. A second laser treatment, laser ablation, uses a high-power, short-pulsed laser to ablate the surface oxide on the substrate and interlayer of the sprayed material to increase the bonding of the coatings. Initial samples were produced using laser techniques that melted the sprayed materials to demonstrate the effect of the coating structure. Consultation with the Fraunhofer Institute in Dresden, Germany, provided sufficient confidence in the process to proceed with installation of a 4-kW YAG laser in Caterpillar's thermal spray laboratory for further process development. A review of the laser ablation technique with the University of Technology at Belfort-Montbeliard (UTBM) in France provided sufficient data to show that the technique has promise for improving the adherence of sprayed coatings. Caterpillar is acquiring a Q-switched laser capable of producing the energy needed for the ablation process to proceed with this evaluation.

Quasicrystalline Materials. This new class of metallic materials exhibit low thermal conductivity with high thermal expansion as a result of their unique, aperiodic crystal structure. The material chosen for evaluation is an aluminum-based quasicrystal, $Al_{71}Co_{13}Cr_8Fe_8$, shown previously to be capable of 1100°C operation in a turbine engine.[4] Initial diffusion couples have been run to aid understanding of the thermal stability of the alloy at operating temperatures.

Phosphate-bonded Composites. Phosphate-bonded composites consist of filler material bonded together by a phosphate. The compositions of both the filler and the phosphate binder can be widely varied and, for this reason, so can the properties of the composite. Phosphate-bonded composites are well known and have been in use for many years as refractory mortars and cements; high-temperature, corrosion-resistant coatings; temporary bone replacement; fast-cure paving cement; and dental cement.

Of the well-known phosphates, most are not suitable for high-temperature use. These include all of the hydrated crystal forms, such as those used for bio-replacement; low-temperature cements; and paving compounds, which simply decompose at elevated temperatures. Certain other non-hydrated alkali and alkaline phosphates are equally unsuitable because of their tendency to form low-melting-temperature eutectics in some environments. Metal phosphates have the highest potential for long-term chemical durability in high-temperature applications such as internal combustion and turbine engines.

Approach

Laser Treatments. Initial sprayed samples were treated using a key-hole laser beam to demonstrate the resulting coating structure. The samples were 10

mm in diameter with a substrate thickness of 3 mm. Coating thickness was approximately 0.5 mm with two types of coatings treated. One type of sample was the bond coating only with no ceramic top coat. The second coating type was a bi-layer bond coat/ceramic. The bond coating was a standard Ni-20%Cr-6%Al-0.5%Y, and the ceramic was 8% yttria-zirconia. The resulting laser-treated coating microstructures were analyzed for depth of penetration and cracking.

The laser ablation treatment was evaluated by reviewing the prior work preformed by UTBM in France. This work demonstrated good adherence for coatings applied to aluminum and titanium substrates. As these materials are highly reactive, the laser ablation done just prior to the coating application would remove the inherent surface oxide, allowing for better substrate wetting. Limited work has been done on steel and cast iron materials, but sufficient technical promise was shown for Caterpillar to invest in the Q-switch laser required for further process evaluation. The lasers will be delivered to Caterpillar in December 2004.

Quasicrystalline Materials. Owing to the metallic nature of the $Al_{71}Co_{13}Cr_8Fe_8$ quasicrystal, HVOF spraying techniques can be used to produce coatings with this material. The HVOF process produces higher density and better bonding of the coating than the plasma spray process by using high particle velocities at relatively low particle temperatures to "peen" or "forge" the particles onto the substrate surface. The low temperature of the process prevents ceramics from being sprayed using this technique.

HVOF coatings of $Al_{71}Co_{13}Cr_8Fe_8$ were produced for diffusion couple testing. Four diffusion couples were produced: (1) the quasicrystal and a steel substrate; (2) the quasicrystal, a Ni-17Cr-6Al-0.5Y bond coat, and a steel substrate; (3) the quasicrystal, a Ni-31Cr-11Al-0.6Y bond coat, and a steel substrate; and (4) the quasicrystal, a Fe-26Cr-8Al-0.4Y bond coat, and a steel substrate. The diffusion couples were produced by spraying a 12.5-mm-diam by 19-mm steel substrate with 0.5-mm-thick layers of the bond coatings and quasicrystal. The bond coatings were applied first, followed by the diffusion couple.

The diffusion experiments were conducted by sealing each type of sample in evacuated quartz tubes. Temperatures of 500, 700 and 900°C with times of 25, 100 and 500 hours were used. The samples were water-quenched after annealing. Samples were then mounted and polished for examination by optical microscopy, scanning electron microscopy, and microprobe analysis.

Phosphate-bonded Composites. Research efforts on metal-phosphate composites at Caterpillar have been aimed at developing seal coatings, corrosion resistant coatings, and, more recently, thermal insulating coatings. Thin, corrosion-resistant coatings have been applied on various surfaces and have been successfully tested in various applications. Metal-phosphate adhesives have been used at Caterpillar for assembling prototype aftertreatment components for testing at temperatures around 800°C. Qualitative testing between phosphate-based and commercially available adhesives has shown the superior adhesive strength of the phosphate-based adhesives; however, quantitative characterization of the strength of phosphate-based adhesives was deemed necessary to assess their potential for high-temperature adhesive applications and as an intermediate step for the development of robust coatings.

Binder preparation and characterization. The basic stoichiometry of the phosphate material under consideration is 1.4 Al_2O_3: 0.25 Cr_20_3: 3 P_2O_5. The binder preparation consists of continuously stirring orthophosphoric acid at 110°C and dissolving chromium trioxide, which is later reduced by adding sucrose; finally, alumina is added to the desired stoichiometry until it is fully dissolved. Additional chemistries, including the use of different chemical species and different proportions, are being explored.

Adhesive preparation and characterization. Adhesive composites consisting of 68% packed alumina with average particles of 0.7 μm were produced, filling the interstitial space with different phosphate binders. For lap shear testing, 1 × 1 × 0.5 blocks of 90% pure alumina were used to make bonded, stepped specimens. The mixtures had a thick slurry consistency and were applied by brush on a section of the surface of the blocks. The brushed halves of two blocks were then aligned to form a step, obtaining a consistent alignment with an aluminum fixture that was built to produce five specimens at a time. Next, the fixture containing the samples was introduced to a curing oven at 300°C. A small amount of pressure perpendicular to the joint was applied at this stage.

Results

Laser Treatments. Laser tacking of the zirconia ceramic induces high amounts of cracking and void formation (Figure 1). Laser tacking of the bond coating material was more successful, in that cracking was suppressed during solidification of the material because of the higher ductility of the metal (Figure 2). This indicates that the laser-assisted plasma processing will need to be applied to thinner layers of the ceramic coating as it is built up during spraying to reduce the residual stress induced. Layer buildup during spraying usually proceeds at 0.025 mm or less for the ceramic layers. If the laser beam interaction time can be adjusted to provide sufficient heat input during coating application, it should be possible to build the ceramic layer without detrimental cracking.

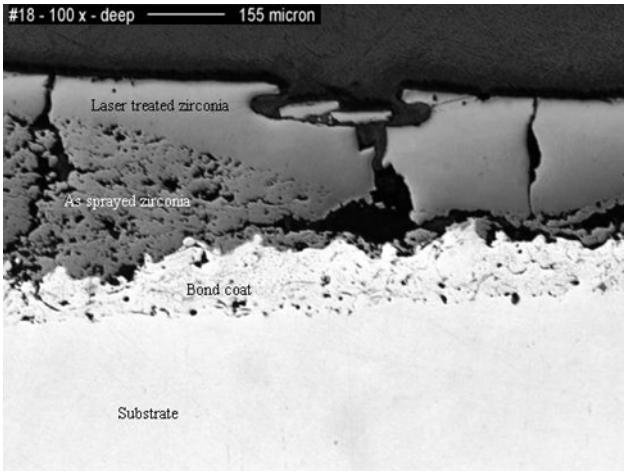

Figure 1. Laser tacked ceramic using medium laser power showing melting of the zirconia layer with crack and void formation.

Quasicrystalline Materials. HVOF spraying of the quasicrystalline material produced a dense, well-bonded structure (Figure 3). The stability of the quasicrystalline material at 700°C when in contact with the steel substrate material was fair, and a minor interaction zone was created after 500 hours (Figure 4). Cracking in the diffusion couple samples is due to the high stress state caused during water

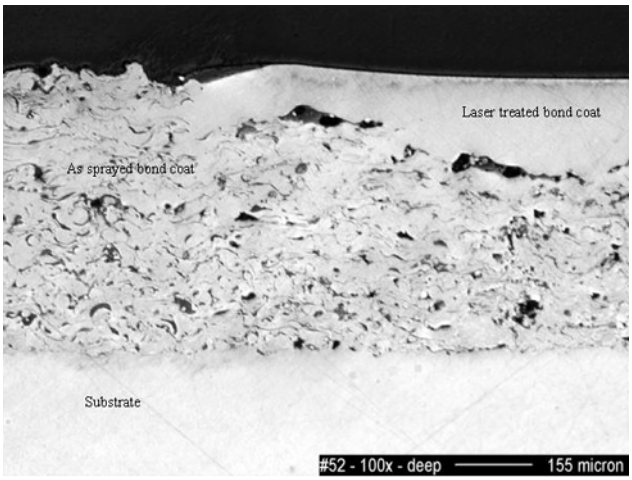

Figure 2. Laser tacked bond coating at medium laser power showing melting of the bond coat material with fusing into the coating and oxide formation under melt pool.

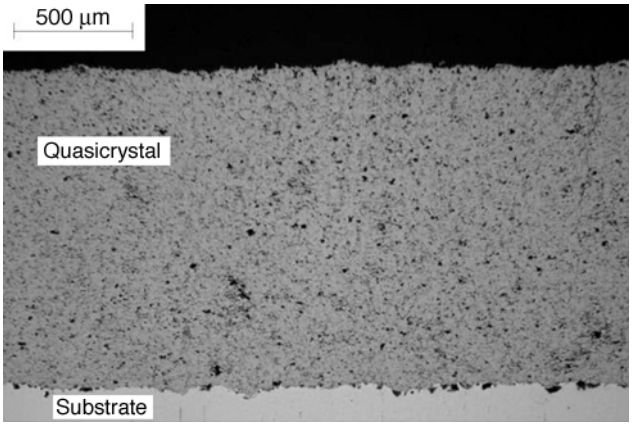

Figure 3. HVOF quasicrystalline material showing dense, well bonded coating structure.

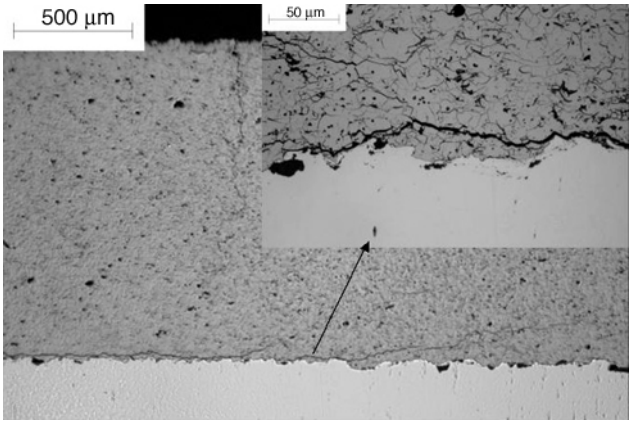

Figure 4. Quasicrystal/substrate diffusion couple after 500 hours at 700ºC showing small reaction zone at interface.

quenching of the samples after exposure. At the higher 900°C temperature, the reaction zone with the substrate increased substantially, as expected (Figure 5). When coupled with the nickel-based bond coatings, large reaction zones were developed at the 700°C temperature (Figure 6), probably as a result of the higher reactivity of the aluminum with the nickel. As with the steel substrate, a smaller reaction zone was found with the iron-based bond coat (Figure 7). Microprobe analysis of the diffusion couple samples is under way to better understand the interaction of the materials at temperature. Oxidation samples will be made and exposed at similar temperatures to determine the effect of oxidation on the material stability.

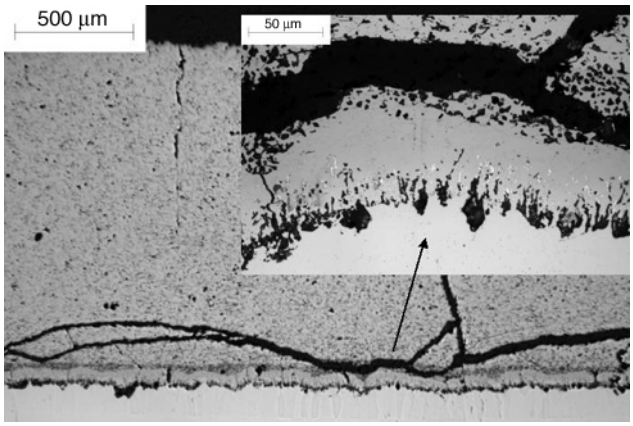

Figure 5. Quasicrystal/sbustrate diffusion couple after 25 hours at 900ºC showing small reaction zone at interface.

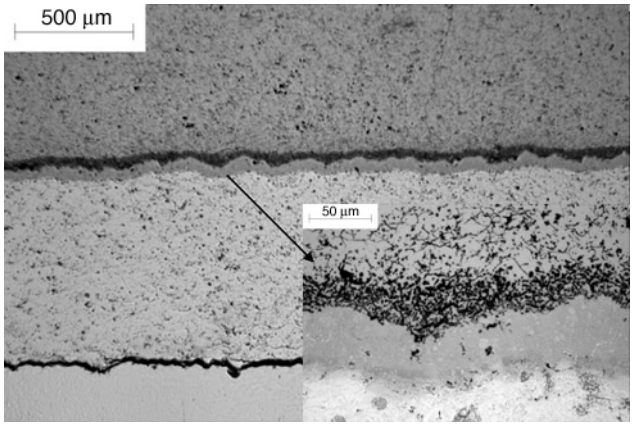

Figure 6. Quasicrystal Ni-31Cr-11A1-0.6Y diffusion couple after 500 hours at 700ºC showing large reaction zone at interface.

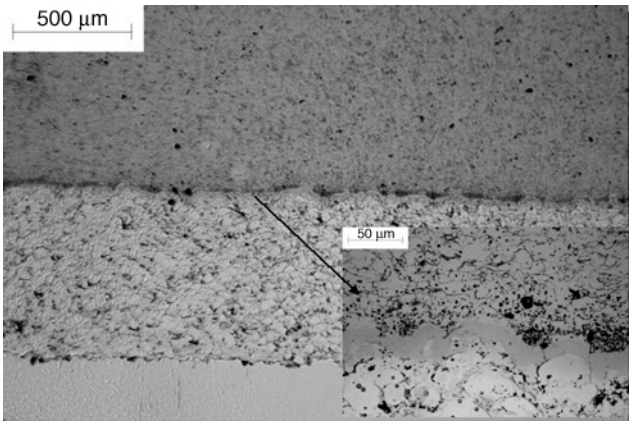

Figure 7 Quasicrystal/Fe-26Cr-8A1-0.4Y diffusion couple after 500 hours at 700ºC showing a large reaction zone at interface.

Phosphate-bonded Composites. Evaluation of the shear strength of the different metal-phosphate-based adhesives and two commercial adhesives was conducted following the ASTM D401 standard. The fixture used for this test is shown in Figure 8.

Figure 8. Fixture used for measuring the shear strength of the adhesives as per ASTM D401.

Data obtained from the shear lap testing are shown in Figure 9. Results are presented for the phosphate adhesive Ad7, which is the phosphate adhesive that yielded the highest strengths on the first round of experiments. Strength data of two

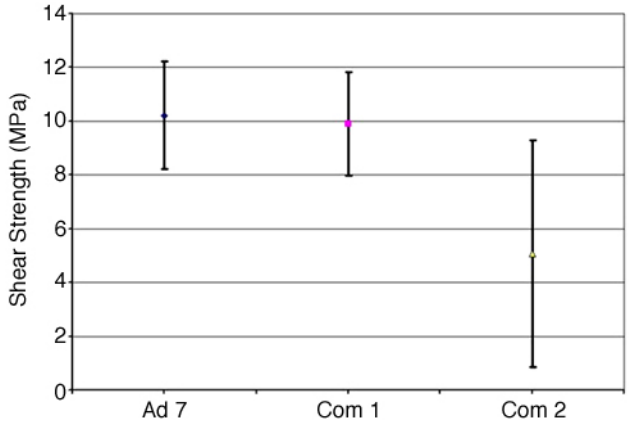

Figure 9. Measured strengths of adhesive produced in-house, Ad7, compared with commercially available adhesives Com-1, Com-2.

commercial adhesives, designated as Com1 and-Com2, are shown for comparison. The error bars represent the standard deviation. These preliminary results suggest that phosphate adhesives can be produced with strengths of at least the same level as commercial adhesives. Testing with other phosphate formulations is continuing. Selected formulations showing the highest shear strengths will be used for continuing coating development.

Conclusions

Laser Treatments. Sufficient promise has been demonstrated for laser surface treatments to proceed with moving a 4-kW YAG laser into Caterpillar's thermal spray laboratory for further evaluation of the laser-assisted plasma spray process and to procure a Q-switched laser system for evaluation of the laser ablation method. Moving the YAG laser and procuring the Q-switched laser are being done independently of the current program funding.

Quasicrystalline Materials. The reaction zones of the substrate/quasicrystalline and Fe-26Cr-8Al-0.4Y/quasicrystalline diffusion couple samples indicate some promise for limiting the interdiffusion of the materials in a TBC structure by designing the coatings to have interface temperatures of below 500°C. The ability to use a graded design may be limited by the reactivity of the quasicrystalline material with the bond coating materials used for grading. Further evaluation will be necessary to understand what types of graded designs can be made.

Phosphate-bonded Composites. The current phosphate-bonded composite shows much promise as a high-temperature adhesive, and commercialization of the material for this use will be pursued.

References

1. R. A. Miller, *Assessment of Fundamental Materials Needs for Thick Thermal Barrier Coatings (TTBC's) for Truck Diesel Engines*, Department of Energy/National Aeronautics and Space Administration/21749-1, NASA TM-103130, 1990.

2. M. B. Beardsley, and H. J. Larson, *Thick Thermal Barrier Coatings for Diesel Components*, DOE/NASA/0332-1, National Aeronautics and Space Administration CR-190759, 1992.

3. M. B. Beardsley, P. G. Happoldt, K. C. Kelley, E. F. Rejda, and D. F. Socie, "Thermal Barrier Coatings for Low Emission, High Efficiency Diesel Engine Applications," SAE Tech Paper Series, 1999-01-2255, Government/Industry Meeting, Washington, D.C., 1999.

4. A. Sanchez, F. J. Garcia, J. M. Algaba, J. Alvarez, P. Valles, M. C. Garcia-Poggio, and A. Aguero, "Application of Quasicrystalline Materials as Thermal Barriers in Aeronautics and Future Perspectives of Use for These Materials," *Mat. Res. Soc. Symp. Proc.* **553**, 447–458 (1999).

C. Processing and Characterization of Structural and Functional Materials for Heavy Vehicle Applications

J. Sankar, Z. Xu, and S. Yarmolenko
Department of Mechanical Engineering
North Carolina A & T State University
1601 East Market Street
Greensboro, NC 27411
(336) 256-1151, ext. 2282; fax: (336) 256-1153; e-mail: sankar@ncat.edu

DOE Technology Development Area Specialist: Dr. Sidney Diamond
(202) 586-8032; fax: (202) 586-1600; e-mail: sid.diamond@ee.doe.gov
ORNL Technical Advisor: D. Ray Johnson
(865) 576-6832; fax: (865) 574-6098; e-mail: johnsondr@ornl.gov

Contractor: Oak Ridge National Laboratory, Oak Ridge, Tennessee
Prime Contract No: DE-AC05-00OR22725
Subcontractor: North Carolina A&T State University, Greensboro, North Carolina

Objectives

- Produce yttria-stabilized zirconia (YSZ) thin films using combustion chemical vapor deposition technique for solid oxide fuel cells.
- Investigate the nucleation of YSZ and its controlling parameters.
- Study the evolution of the thin film microstructure.
- Enhance the film deposition rate.

Approach

- Deposit YSZ thin films using combustion chemical vapor deposition (CCVD).
- Characterize the films using scanning electron microscopy (SEM) and X-ray diffraction.
- Study the effects of substrate temperature and metal concentration on the nucleation density.
- Examine the evolution of the thin film microstructure by experiments and stochastic simulation.
- Optimize the operation parameters of the CCVD system.

Accomplishments

- Enhanced the nucleation density
- Developed a stochastic model to simulate the evolution of the thin film microstructure.
- Established a set of conditions for high film growth rates.

Future Direction

- Study YSZ film deposition on porous electrodes.

Introduction

YSZ is an oxygen-ion-conductive material that has conventionally been used as an electrolyte in solid oxide fuel cells (SOFCs) and in oxygen sensors for pollution and safety monitoring, control, and automation of industrial processes, and energy conservation.[1] Because of the relatively low electrical conductivity of YSZ (about 0.1 $S \cdot cm^{-1}$ at 1000°C), most of the ohmic loss is due to the resistance of the electrolyte. To reduce the ohmic loss and increase the power generating efficiency of the fuel cell, it is desirable to use a thin film electrolyte. On the other hand, a temperature of as high as 1000°C is usually employed to obtain reasonable ion conductivity for YSZ material. This high temperature makes material selection difficult and increases the product cost greatly. Reducing the thickness of the electrolyte would increase the conductivity at lower temperatures.

YSZ thin films usually have been synthesized by CCVD or electrochemical vapor deposition (EVD).[2,5] [Should this ref callout be 2–5? No callouts found for refs. 3 and 4.] The vacuum systems used by these techniques limit the sizes of the parts and increase the cost of the products. Liquid fuel CCVD is a promising technique to produce YSZ thin films for industrial applications because CCVD works in an open atmosphere and offers the potential for conformal deposition of films on non-flat surfaces. Moreover, because no vacuum chamber is needed for the process, there is no size restriction on parts on which the film can be deposited. Because of the relatively high precursor concentration in liquid fuel compared with the fuel usually used for low-pressure CVD processes, CCVD is expected to have a higher deposition rate. Therefore, CCVD is a promising technique for producing YSZ thin films for industrial SOFC applications at a lower cost than any other CVD/EVD technique.

Electrolytes for SOFCs must be highly dense to avoid any cross flow of oxygen or fuel. The main purpose of this research is to produce dense YSZ thin films through the study of nucleation and microstructure evolution. Reducing the cost of fuel cell manufacturing by using thin film technology and a high film growth rate is of great interest. Methods to enhance the growth rate of YSZ have been studied.

Approach

Thin films of YSZ to be used as electrolytes for SOFCs have been deposited using CCVD. The deposition system was developed at North Carolina A&T State University. Metal-organic reagents were dissolved in an organic solvent (toluene). The solution was atomized into small aerosols with a nebulizer, mixed with oxygen, and then ignited by a pilot flame. Thin films then were deposited on substrates placed downstream of the aerosol flame.

Nucleation study of YSZ was performed by varying the substrate temperature and metal concentration in the solvent. At design conditions, depositions were conducted for different lengths of time. The microstructures of these depositions were observed and analyzed, and the grain growth was studied with stochastic modeling. Efforts to enhance the film growth rate were carried out through study of the effects of thermophoresis and metal concentration. All the present depositions were performed on mirror-polished single-crystal silicon substrates. The phases of the deposited films were examined with X-ray diffraction, and their morphology was characterized by SEM.

Results

Nucleation

Effect of substrate temperature. The temperature of the substrate is an important factor that controls the nucleation density, defined as the number of aggregates created per unit area. To be able to use the image analysis software Image Pro to compute the nucleation density, the nucleation time of the YSZ particles was set for 130 s. The depositions were conducted at substrate temperatures of 800, 900, 1000, 1100, and 1200ºC and a metal concentration of 1.25E-03 M. The as-grown samples were characterized with SEM as shown in Figure 1.

Counting the particle number in the specific area with the application software showed that the nucleation rates ranged over an order of magnitude, from 10^{10} to 10^{11} cm^{-2}, in the tested temperature range. The nucleation rate variation versus the substrate temperature is illustrated in Figure 2. The variation of the nucleation rate with the substrate temperature is characterized by two tendencies: When the substrate temperature is between 1000 and 1200°C, the nucleation rate decreases with the

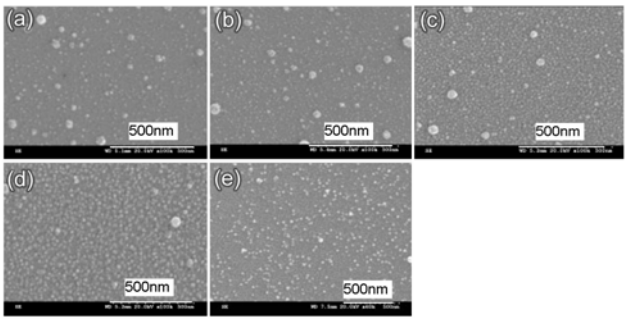

Figure 1. Micrographs of YSZ nuclei nucleated at various substrate temperatures: (a) 800°C, (b) 900°C, (c) 1000°C, (d) 1100°C, and (e) 1200°C under conditions of nucleation time of 130 sec and total metal concentration of 1.25×10^{-3} M.

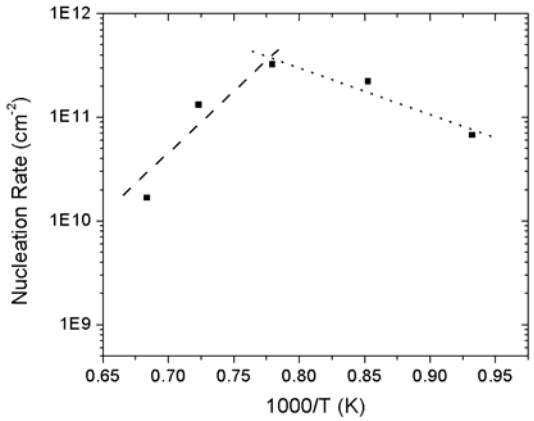

Figure 2. YSZ nucleation rate as a function of the substrate temperature according to the information in Figure 1.

substrate temperature; in the substrate temperature range of 800 to 1000°C, the nucleation rate increases with the substrate temperature. The former nucleation rate tendency was well accepted. As far as the author knows, the latter tendency has not been reported. It is proposed that at low substrate temperatures, the material species in the gas phase condense into a solid phase and coagulate into particles. They rebound from the surface instead of becoming adsorbed when they hit the substrate surface. This process also leads to depletion of species in the gas phase that is needed for CVD and then results in a decrease in the nucleation rate. The images in Figure 1 also reveal that on samples nucleated at low temperatures, there are many large nodular particles that support the above statement.

Effect of metal concentration. Another method used to enhance the nucleation rate was to increase the deposition flux, i.e., the metal concentration, for our experimental system. At low concentrations of 5×10^{-4} and 1.25×10^{-3}, only isolated particles presented on the substrate surface after depositions of 130 s, whereas almost continuous films were obtained when the concentration was increased to 3×10^{-3} M and up. At high total metal concentrations, the particle size reached 30–50 nm. From this set of experiments, it can be concluded that the lowest metal concentration, 5.5×10^{-4} M, is not suitable if a high nucleation rate is demanded.

Structural Evolution

Experimental study. To grasp the physics of the evolution process of the YSZ thin film, the grain sizes at various stages of the processing time were measured for statistical post-processing. Figure 3 shows the micrographs of YSZ particles/crystallites at different processing times. In Figure 3(a), the nuclei can hardly be seen after only 70 s of processing, except some large particles that are assumed to be contamination. From Figures 3(b) to (d), with the increase of processing time, the sizes of the particles increase; however, the number of particles is reduced. This phenomenon can be interpreted by the mechanisms of coarsening and coalescence of the growing particles. With increased processing time, the sizes of the particles increase. Some secondary nucleation and growth on the large particles can be noticed. It is also reasonable to assume that the secondary nucleation should take place on the substrate before all the surface of the substrate is covered with particles. The film consists of both (111) and (100) oriented crystals. The difference in orientation originated at the stage when the particles were very small.

According to the obtained mean particle radii, particle growth rate can be estimated by plotting the mean diameter versus the growing time, as shown in Figure 4. The particle growth rate is approximately linear during the time period studied (130 to 430 s). The intercept of the line on the time axis is about 33.3 s, which shows the incubation time for nucleation. With prolonged deposition time, continuous thin films can be obtained.

Stochastic simulation. The number and size of the particles were obtained with the image processing software. After statistical post-

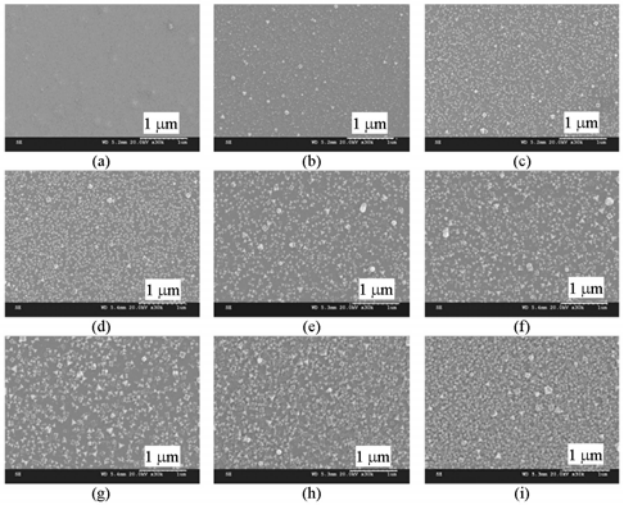

Figure 3. Microstructure of the YSZ particles/crystallites at different processing times: (a) 70 s, (b) 130 s, (c) 190 s, (d) 250 s, (e) 310 s, (f) 370 s, (g) 430 s, (h) 490 s, and (i) 550 s on Si(100) substrates, at a substrate temperature of about 1200°C, metal concentration of 1.25×10^{-3} M.

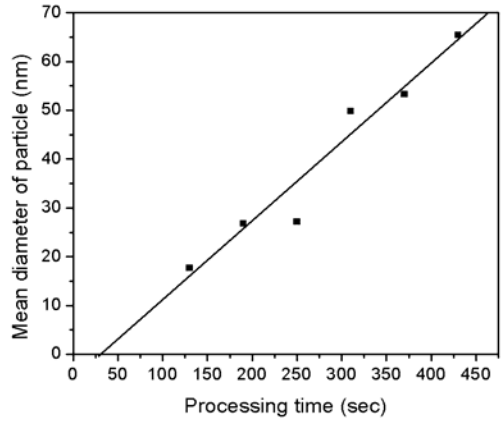

Figure 4. Particle growth rate vs. processing time from the data obtained from the micrographs as shown in Figure 3.

processing, a comparison of cumulative distribution functions (CDFs) of grain radius normalized by the mean radii is given in Figure 5. As can be seen from Figure 5, there is a distinct dispersion among these CDFs plotted in the normalized space. Thus the use of a normal grain growth model cannot accurately capture the evolution process of grains in YSZ thin films. The deviation from the normal grain growth model is mainly attributed to the orientation-dependent grain boundary energies and mobility.

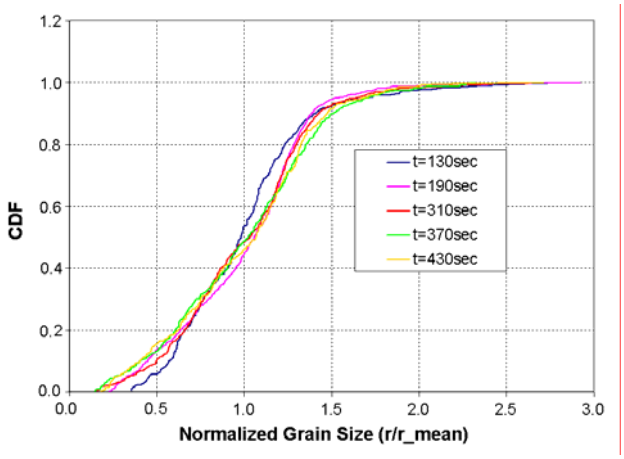

Figure 5. Comparison of CDFs of grain radius in normalized space.

The lognormal distribution has been used extensively as the initial distribution of grain size.[6,7] To validate the use of the lognormal model, a comparison of the initial CDF of grain radius at *t=130s* with its equivalent lognormal distribution is shown in Figure 6. As shown in Figure 6, the equivalent lognormal distribution can accurately capture the true initial grain size distribution. A stochastic model was developed by taking the radii of the neighboring grains and the orientation-dependent constants into consideration. The computational efforts were greatly reduced by dividing the entire population of grains into several sub-groups based on the level of their percentiles. It was assumed that all grains within each sub-group have identical grain growth behavior. The orientation-dependent grain growth constants were determined from curve fitting of the experimental data. An example of comparing model prediction with the experimental observations is shown in Figure 7.

Growth Rate

Thermophoresis is a thermal-gradient–directed flow of material from high-temperature to low-temperature regions. Thermophoresis has been found to be a strong factor in some CVD environments.[8] A temperature gradient across a diffusion boundary layer causes a thermophoresis effect. In this case, if the flame were hotter than the substrate, on average, the gas molecules from the substrate would have a smaller velocity than the gas molecules traveling toward the substrate. This creates a driving force for YSZ clusters formed in

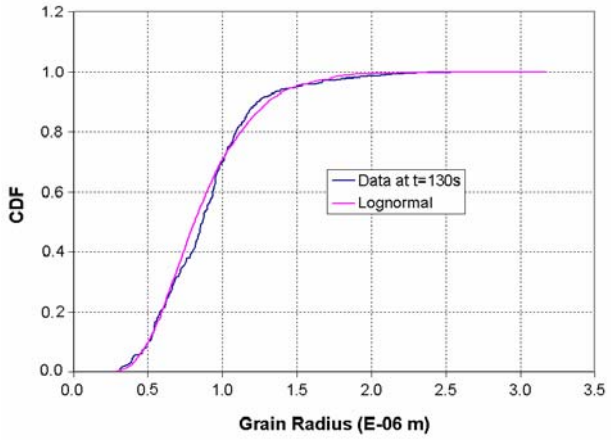

Figure 6. Illustration of accuracy of using an equivalent lognormal distribution for statistical characterization of initial grain size distribution.

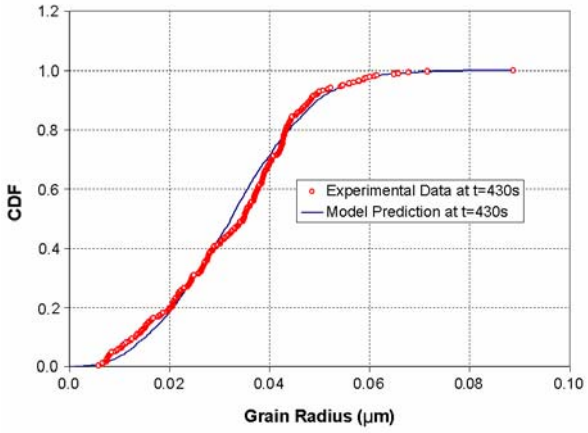

Figure 7. Comparison of model prediction with measured CDF data of grain radius at *t=430s*.

the direction toward the substrate. A larger temperature gradient adjacent to the substrate increases the thermophoresis effect. The study of the effect of thermophoresis was carried out by film depositions at different substrate-to-nuzzle distances from 51 mm (far into the flame) to 83 mm (out of the visible end of the flame). The film thickness measured on SEM images is plotted versus the substrate-to-nozzle distance in Figure 8 on a solid line. The data can be fit by an exponential equation. With an increase in the substrate-to-nozzle distance, precursor concentration in the flame will be attenuated because of the expansion of the flame. Normalization was done to eliminate the effect of concentration dilution on the film growth rate. The normalized thickness data were again plotted in the

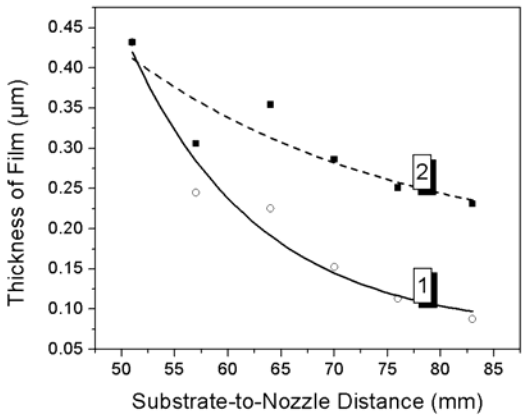

Figure 8. Film thickness as a function of the substrate-to-nozzle distance, line 1 for the original measured data, line 2 for the normalized data.

same graph of the originally measured data, as is shown in Figure 1 by curve 2 in the dashed line. It is apparently noticeable that after normalization, the growth rate of the film still follows the exponentially decaying mode with the substrate-to-nozzle distance. In other words, the parameter substrate-to-nozzle distance does play a role in film growth.

The effect of the metal concentration on the film growth rate is shown in Figure 9. Within the range of the concentration employed in our experiments, a linear relationship was obtained between the film growth rate and the concentration. By observing the morphologies of the samples, the films had well-crystallized and faceted particles as long as the metal concentration was less than 4.25×10^{-3} M. Beyond this limitation, the film was in a cauliflower-like structure.

Conclusions

According to the investigations we have performed, the CCVD technique has been demonstrated to be a promising method for film processing of YSZ electrolyte. Nucleation density can be improved by controlling the substrate temperature and the metal concentration appropriately. The analysis of the grain growth demonstrated that after the initial stage, the grain growth does not follow the lognormal mode. A stochastic model has been developed to predict the grain size in the film at any deposition time. The experiments confirmed the enhancement of the film

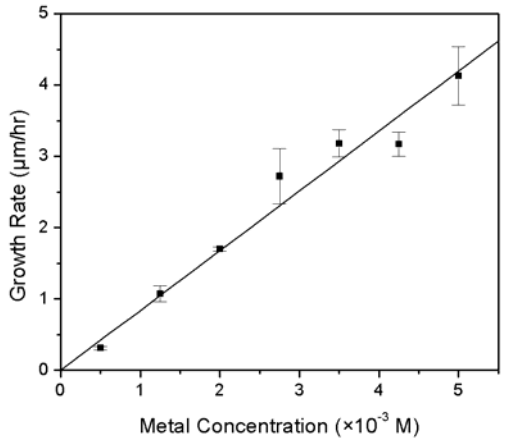

Figure 9. Film growth rate versus metal concentration in the liquid solution.

growth rates by employing the effect of thermophoresis and increasing the metal concentration.

References

1. S. P. S. Badwal, "Ceramic Superionic Conductors," p. 570 in *Materials Sciences and Technology, A Comprehensive Treatment*, R. W. Cahn, P. Haasen, and E. J. Kramer, eds., Vol. 11, 1994.

2. G. Garcia, J. Casado, J. Llibre, and A. Figueras, *J. Crystal Growth* **156**, 426 (1995).

3. S-C. Hwang and H-S. Shin, *J. Am. Ceram. Soc*. **82**(10), 2913 (1999).

4. U. B. Pal and S. C. Singhal, *J. Electrochem. Soc*. **137**, p. 937 (1990).

5. L. G. J. De Haart, Y. S. Lin, K. J. de Vries, and A. J.Burggraaf, *J. Eur. Ceram. Soc*. **8**(1), 59 (1991).

6. V. Y. Novikov, *Acta Mater*. **47**(18), 4507 (1999).

7. C. V. Thompson, *Annu. Rev. Mater. Sci*. **20**, 245 (1990).

8. W. Bai, K. L. Choy, N. H. J. Stelzer, and J. Schoonman, *Solid State Ionics* **116**, 225.

Publications

1. Z. Xu, J. Sankar, and S. Yarmorlenko, "Yttria-Stabilized Zirconia Coatings Produced Using Combustion Chemical Deposition," *Surface and Coating Tech.*, in print.

2. Z. Xu, C. Hilton, Bobby Watkins, Sergey Yarmolenko, and J. Sankar, "Thin YSZ Electrolyte Film Depositions on Dense and Porous Substrates", paper IMECE2003-43330, *2003 ASME International Mechanical Engineering Congress and RD&D Expo*, 2003.

3. Z. Xu, J. Sankar, S. Yarmolenko, and Q. Wei, "Nucleation And Growth of Yttria-Stabilized Zirconia Thin Films Using Combustion Chemical Vapor Deposition," pp. 509–514 in *Materials Research Society Symposium Proceedings*, Vol. 756, 2003.

4. Z. Xu, S. Yarmolenko, and J. Sankar, "Enhancement Of YSZ Thin Film Deposition Rate In CCVD," pp. 861–862 in *Proceedings of 10th International Conference on Composites Engineering*, New Orleans, July 20–26, 2003.

D. NDE Development for Ceramic Valves for Diesel Engines

Jiangang Sun
Argonne National Laboratory
9700 South Cass Avenue
Argonne, IL 60439
(630) 252-5169; fax: (630) 252-4798; e-mail: sun@anl.gov

DOE Technology Development Area Specialist: Dr. Sidney Diamond
(202) 586-8032; fax: (202) 586-1600; e-mail: sid.diamond@ee.doe.gov
ORNL Technical Advisor: D. Ray Johnson
(865) 576-6832; fax: (865) 574-6098; e-mail: johnsondr@ornl.gov

---

Contractor: Oak Ridge National Laboratory, Oak Ridge, Tennessee
Contract No.:DE-AC05-00OR22725
Subcontractor: Argonne National Laboratory, Argonne, Illinois

---

Objectives

- Develop a laser scattering nondestructive evaluation (NDE) method for detection and characterization of sub-surface defect/damage in silicon-nitride ceramic valves so NDE data can be used to determine cost-effectiveness and reliability of ceramics valves for diesel engines.
- Identify strength-limiting flaws and failure mechanisms in cylindrical silicon-nitride specimens due to inherent material defects or machining damage.

Approach

- Continue optimization of an automated laser scattering NDE system for fast scanning of entire valves.
- Inspect as-processed valves to determine the level of machining damage and evaluate bench-tested valves for accumulated damages.
- Correlate NDE data with fracture test results for machined cylindrical silicon nitride specimens to identify fracture initiation defects and defect type, depth, and severity.

Accomplishments

- Successfully tested a photomultiply tube (PMT) optical detector in a laser scattering system. The PMT detector is more sensitive and >6 times faster than the current semiconductor optical detector.
- Evaluated ten NT551 silicon-nitride valves that were bench tested for 100, 500, and 1000 hours. Analyzed processing and accumulated damages in the valve head sections.
- Inspected 48 as-processed SN235P silicon nitride valves. Determined levels of machining damage in various sections of the valves and identified severe damage that caused valve failure.
- Demonstrated laser scattering detection sensitivity for fracture initiation defects in machined cylindrical SN235P silicon nitride specimens.

Future Direction

- Implement the PMT detector in the automated NDE valve-scan system and use optical fibers for collecting and delivering scatter light to the detector. Further investigate other detectors that may have higher speed for this application.
- Inspect re-machined SN235P valves for initial damage level due to machining. Characterize accumulated damage by periodic inspection of these valves during planned rig/engine tests of various operating conditions and durations.
- Develop new theoretical, experimental, and quantitative image-processing methods for optimized characterization of strength-limiting subsurface defects/damage (size and depth) due to corrosion, fatigue, impact, and wear in silicon nitride ceramics.

Introduction

Advanced ceramics are leading candidates for high-temperature engine applications that offer improved fuel efficiency and engine performance. Among them, silicon nitrides are being evaluated as valve train materials for diesel and natural gas engines. However, material defects and process/operation-induced damage in the subsurface may significantly degrade the reliability and performance of these ceramics. These defects are typically less than 100 microns in size and within 200 microns under the surface. To detect and characterize these defects, Argonne National Laboratory (ANL) developed a laser scattering NDE method to measure detailed subsurface microstructures for ceramics. The objective of this research is to demonstrate that this method can be used to assess/evaluate the cost-effectiveness and reliability of ceramic valves for diesel engines. The primary effort in FY 2004 was to evaluate accumulated impact/wear damages in 10 NT551 silicon nitride valves tested in a bench rig for 100, 500, and 1000 hours and to inspect 48 as-processed (machined) SN235P silicon nitride valves for initial machining quality. Another effort was focused on NDE identification of fracture initiation defects in machined cylindrical SN235P silicon nitride specimens. This research is collaborated with Caterpillar, Inc.

Approach

The critical region of ceramic components for structural applications is near-surface (usually to a depth of <200 μm). The common types of defects in this region are mechanical ones, such as cracks, spalls, inclusions, and voids. Because ceramics are partially translucent to light, a laser scattering method based on cross-polarization detection of optical scattering originated from the subsurface can be used for noncontact, nondestructive measurement of subsurface microstructure in such materials. By scanning the entire surface (flat or curved) of a ceramic component and constructing a two-dimensional (2D) scatter image, subsurface defects can be readily identified, as they exhibit excessive scattering over the background, and their type and severity may be analyzed. To apply this technology for NDE of ceramic valves, an automated laser scattering system was developed by ANL for scanning entire valve surfaces. This system utilizes two rotation and two translation stages to align and focus the laser beam on the valve surface during the scan; and the resulting 2D scattering image data are used to identify the location, size, and relative severity of subsurface defects/damage. This system can therefore be used for inspection of the quality of as-processed valves and for evaluation of accumulated damage in ceramic valves from rig/engine tests.

Results

Evaluation of Bench-Tested NT551 Valves

Ten NT551 silicon nitride valves (Figure 1) were tested for 1000 h in a valve bench rig at Caterpillar. These valves were seated with metallic seat inserts at matched or mismatched angles, or with eccentric seat inserts. The bench test matrix is listed in Table 1.[1] These valves were examined by the automated laser scattering system at accumulated durations of 100, 500, and/or 1000 h as shown in Table 1. NDE data for each valve at different test durations were compared and analyzed to determine

Table 1. Bench test matrix and NDE evaluation intervals for NT551 valves

Valve number	100-h valve-seat	400-h valve-seat	500-h valve-seat	Total hours	NDE at accumulated bench-test hours
CV04, CV12	30-30	30-30	30-30	1000	500
CV19, CV20	45-45	45-45	45-45	1000	500, 1000
CV18, CV25	45-30	45-30	45-30	1000	500, 1000
CV08, CV15	30-45	30-ECC	30-ECC	1000	100, 500, 1000
CV14, CV16	30-ECC	30-ECC	30-ECC	1000	100

Notes: numbers for valve-seat are their respective angles; ECC = eccentric seat insert.

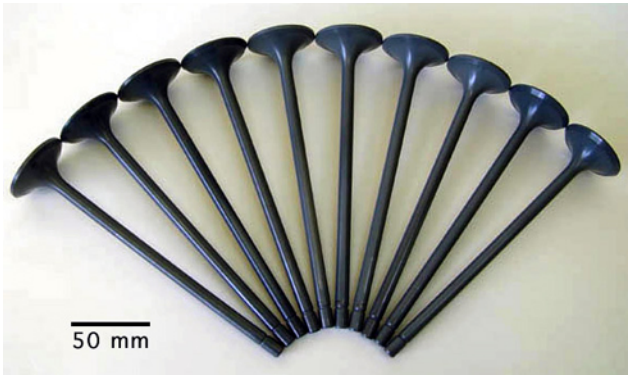

Figure 1. Ten NT551 silicon nitride valves.

any new damage or growth of existing defects in the contact and fillet radius surfaces.

Figure 2 shows the laser scattering image of the valve-head section of NT551 valve CV19 after a 1000-h bench test. The scanned axial length was 30 mm (the top 4-mm region is the contact area) and is aligned in the vertical direction. The scan resolution was 10 microns in the axial direction and 11 microns in the circumferential direction. Typical of all NT551 valves, NDE data for CV19 indicated no significant accumulated damage from the bench tests, except surface wear within the contact surface. Figure 3 shows the detailed image of the contact surface. The reduction of scattering intensity within the wear scars (two darker horizontal stripes) was due to surface damage of increased roughness and contamination (embedded metal particles from the metal seat insert). Several segmented subsurface flaws of high optical-scattering intensity near the top

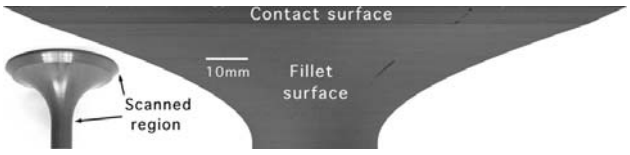

Figure 2. Laser scattering scan image for NT551 valve CV19 after 1000-h bench test.

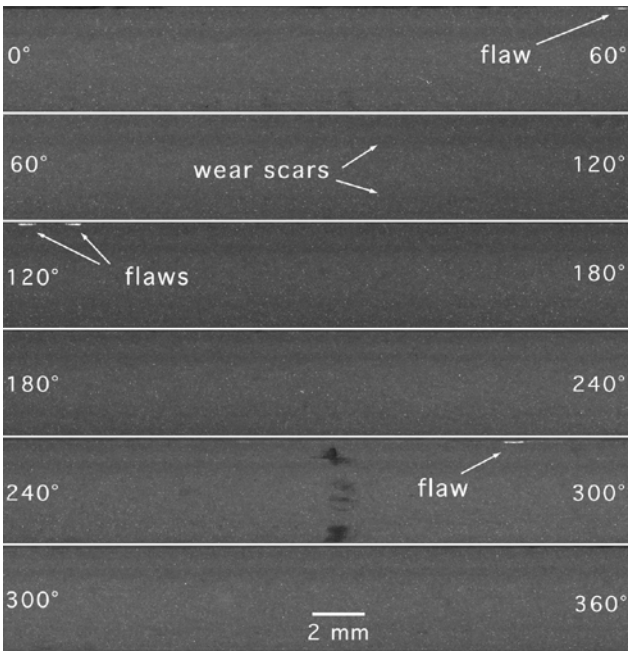

Figure 3. Laser scattering image of the contact surface of NT551 valve CV19.

edge are indicated in Figure 3. One of the detected edge flaws is shown in Figure 4 and compared with the surface photomicrograph. This flaw is pre-spall damage that was probably generated during valve processing. Other flaws within the subsurface are mostly material porosity of <80 μm in size. Valve CV19 also has several machining-damage marks in

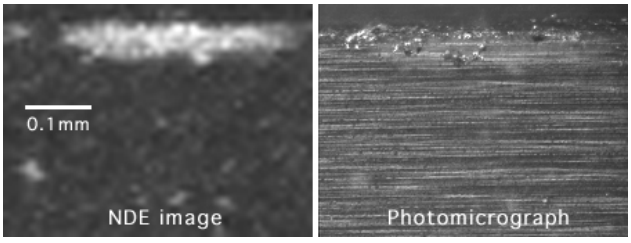

Figure 4. Detailed laser scattering image and photomicrograph of a subsurface edge flaw.

the fillet radius surface. In addition, subsurface damage, near a scratch, that was not present after a 500-h test was seen after a 1000-h test (Figure 5).

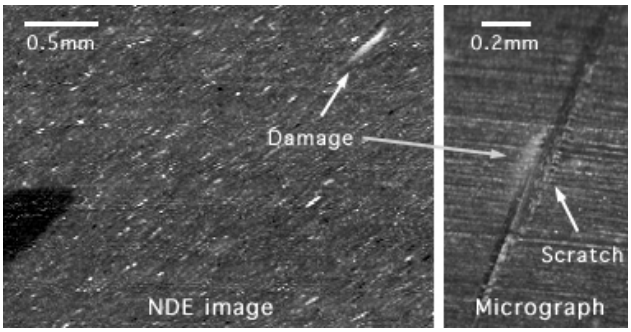

Figure 5. Detailed laser scattering image and photomicrograph of a subsurface scratch damage.

Inspection of As-Processed SN235P Valves

Forty-eight as-processed (machined) SN235P silicon nitride valves were inspected by the valve-scan NDE system. These were diesel and natural-gas intake and outlet valves, each with a slightly different axial profile. Figure 6 shows a laser scattering image of a typical SN235P diesel intake valve. Spatial resolution in both scan directions is ~10 micron. Significant machining damage was found in the fillet radius and nearby stem regions, as shown in detailed images in Figure 7. The damage is seen as lines of high optical-scattering intensities along the machining direction. This result is consistent with the machining conditions for these valves. As indicated in ref. 1, because of an error in the machining process, the valve fillet and keeper notch regions were only rough-machined, while the contact surface and the majority of the stem regions were fine-machined. The high damage level in the fillet region as detected by the NDE would likely reduce valve strength.

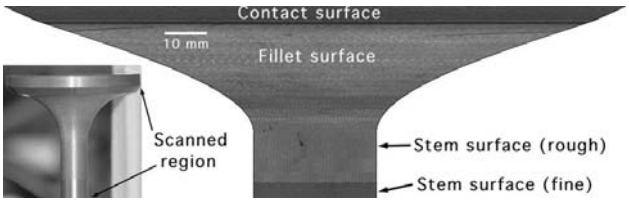

Figure 6. Laser scattering image of a typical SN235P diesel intake valve.

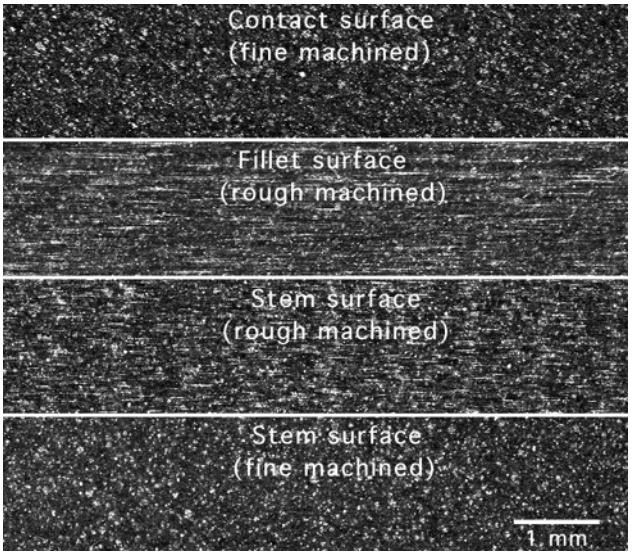

Figure 7. Detailed laser scattering images in various regions, as indicated in Figure 6.

Machining damage in the valve keeper notch region was not anticipated to be significant. However, when a diesel valve was tested in the bench rig at Caterpillar, it was soon broken near the upper edge of the keeper notch. In comparison, ten NT551 valves were tested in the same rig for 1000 h without a single failure. From scanning electron microscopy analysis, Caterpillar determined that the fracture origin was machining damage. NDE image data for a typical SN235P valve notch are shown in Figure 8. Very severe machining damage was found around the entire circumference of the upper edge, which is at the same location of the notch failure. The damage appears to be segmented; each segment is similar to the edge flaw of NT551 valve, as shown in Figure 4. The intensity of this damage is much higher than that within the notch which, however, is already considered to be more significant than typical rough machining damage. Because all machining damage is likely to be median cracks, these results indicate that laser scattering intensity may be correlated with crack depth and may predict failure.

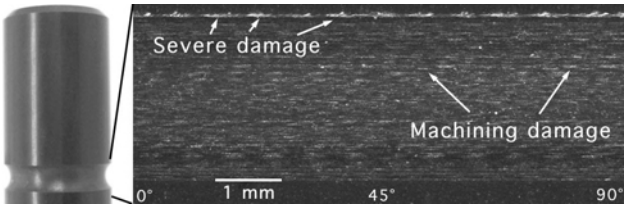

Figure 8. Laser scattering image in keeper notch region of a typical SN235P valve.

Detection of Machining Damage and Fracture Origins

Three sets of cylindrical SN235P silicon nitride specimens were examined by the laser scattering method to determine machining damage. Similar to the results for SN235P valves (Figures 6–7), NDE data showed damage level and distribution at different machining conditions. In addition, a color variation was observed on some rod surfaces, as seen in Figure 9. This coloration change is probably due to non-uniform mixing of powder materials during material processing, and it may have some effect on the mechanical property of the rods.

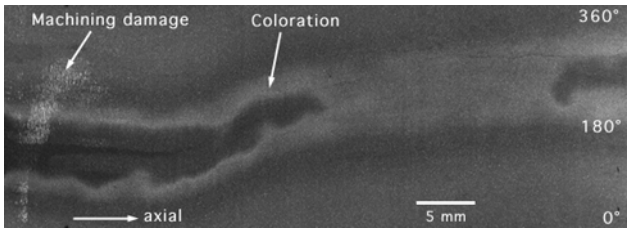

Figure 9. Color variation in a machined rod.

NDE data were correlated with destructive test results to determine the fracture initiation defect for these cylindrical SN235P specimens. The fracture surfaces were first examined to locate the fracture flaw site. This site was then mapped in the tensile (or cylinder) surface. By comparing the flaw location with a previously acquired laser scattering image for the surface, the fracture initiation defect can be identified in the NDE image. Figure 10 shows the fracture surfaces of a SN235P rod in which the fracture initiation defect can be easily observed. The correlation of the surface photomicrograph with the laser scattering image is seen in Figure 11. As indicated, the fracture initiation defect is not the largest in the region. This is because the strength test used a four-point bending fixture. The maximum stress is therefore localized within an axial line in a particular azimuth angle. Only those defects positioned within the maximum stress line will grow and cause fracture. The fracture initiation defect in this specimen appears to be a high-porosity material defect.

Conclusions

An automated laser scattering system developed by ANL was used to evaluate ten NT551 valves at accumulated bench-test durations of 100, 500,

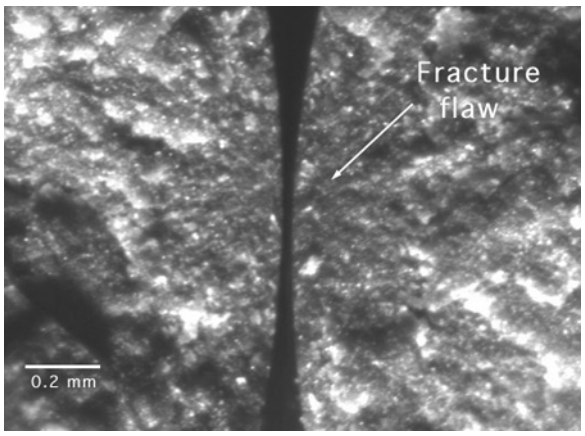

Figure 10. Fracture surfaces of a fractured SN235P rod.

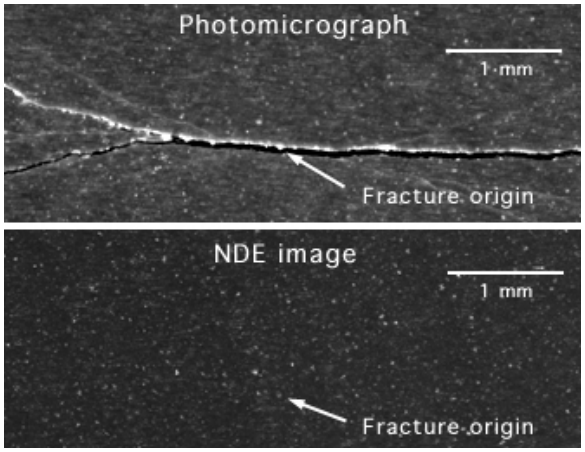

Figure 11. Photomicrograph and laser scattering image on tensile surface of a fractured SN235P rod.

and/or 1000 h. NDE data for each valve at different test durations were analyzed to determine any new damage or growth of existing defects. In general, no significant subsurface damage from the bench tests was detected. Existing flaws, such as machining damage and inherent material defects, did not grow under the various test conditions and durations. Damage from the bench tests was mainly in the valve contact surface, including wear scars and an unknown deposit for some valves.[1] The NDE data will be correlated with the retained strength from destructive tests of these valves.

Forty-eight as-processed (machined) SN235P valves were inspected by the valve-scan system. Because of an error in the machining process, the valve fillet and keeper notch regions were only rough-machined, while the contact and stem surfaces were fine-machined. The NDE data showed significant

machining damage in the rough-machined fillet radius and nearby stem regions. More severe damage was found at the upper edge of the keeper notch. The severe damage at the keeper notch was responsible for a valve failure, and the high damage level in the fillet region would likely reduce valve strength. Based on these NDE results, it was recommended that all SN235P valves be re-processed to remove all rough machining damage before being tested in an engine or a bench rig.

The laser scattering method was also used to characterize defects/damage in cylindrical SN235P silicon nitride specimens that were machined by different vendors at various machining conditions. NDE data identified damage level and distribution at different machining conditions, and a color variation in base material that was probably due to material processing. In addition, NDE data were demonstrated for identification of fracture initiation defects for these cylindrical SN235P specimens.

References

1. M. J. Andrews, "Lightweight Valve Train Materials," quarterly progress report for January 1 through March 31, 2004, Heavy Vehicle Propulsion Materials Program, U.S. Department of Energy.

Publications/Presentations

J. G. Sun, J. Zhang, and M. J. Andrews, "Laser Scattering Characterization of Subsurface Defect/Damage in Silicon Nitride Ceramic Valves," to be published in *Proceedings of the American Ceramic Society's Annual Cocoa Beach Conference*, Cocoa Beach, FL, Janury 25-30, 2004.

Patents

J. G. Sun, "Device and Nondestructive Method to Determine Subsurface Microstructure in Dense Materials," invention report ANL-IN-02-086, DOE case no. S-101,670, U.S. patent filed in December 2003.

E. Durability of Diesel Engine Component Materials

Peter J. Blau with Jun Qu and John J. Truhan, Jr.*
Oak Ridge National Laboratory
P. O. Box 2008, Mail Stop 6063
Oak Ridge, TN 37831-6063
(865) 574-5377; fax: (865) 574-6918; e-mail: blaupj@ornl.gov
**University of Tennessee, Knoxville*

DOE Technology Development Area Specialist: Dr. Sidney Diamond
(202) 586-8032; fax: (202) 586-1600; e-mail: sid.diamond@ee.doe.gov
ORNL Technical Advisor: D. Ray Johnson
(865) 576-6832; fax: (865) 574-6098; e-mail: johnsondr@ornl.gov

---

Contractor: Oak Ridge National Laboratory, Oak Ridge, Tennessee
Prime DOE Contract Number DE-AC05-00OR22725;
Subcontractor: University of Tennessee, Knoxville, Tennessee

Objectives

- Provide test data, analyses, and models that enable the use of durable, lower-friction moving parts in diesel engines in heavy vehicle propulsion systems.
- Develop test methods that simulate the environment of scuffing-prone engine parts.
- Conduct structural and tribological characterizations of promising new materials, surface treatments, composites, and coating technologies.

Approach

- Identify diesel engine components that need advanced materials or surface treatments in order to ensure durability while providing low-friction behavior. These include (a) wastegate bushings for exhaust gas recirculation (EGR) components and (b) fuel injector components.
- Identify materials, coatings, and/or surface treatments that have the potential to increase the durability of the selected engine components.
- Develop test methods to evaluate the performance of candidate materials under simulated use conditions.
- Develop graphical methods and models to portray the effects of operating parameters, like speed, load, and surface finish, on the scuffing response of the materials.

Accomplishments

- Designed, built, and used a high-temperature oscillatory scuffing test system that operates at wastegate bushing temperatures (~ 600–700°C).
- Published results of tests on a range of metallic alloys, ceramics, and coatings to determine which of these had the best durability under high-temperature conditions.
- Developed a novel, “pin-on-twin” scuffing test to evaluate fuel injector materials in diesel fuel and low-sulfur fuel.

- Developed criteria for the onset of scuffing damage and evaluated traditional steel fuel injector materials as well as ceramics, advanced cermets, and hard coatings in diesel fuel and low-sulfur fuel. Represented results in terms of "scuffing maps" and transition diagrams.
- Prepared a model for scuffing tendency that considers lubricant characteristics and solid material characteristics.

Future Direction

- Use scuffing damage maps and test data to support the development of the new scuffing model and to obtain a better understanding of the evolution of localized surface damage. Compare results of the model with laboratory test data on metals, ceramics, and composite materials.

Introduction

The diesel engine industry faces important challenges to improve fuel efficiency in the face of increasingly strict emissions regulations. These challenges can be addressed by modifying the engine design and electronic control systems for engines, and by developing exhaust gas aftertreatments. Such modifications affect the mechanical, thermal, and chemical environments to which the engine materials are subjected; and the current structural materials may not perform as well as they did in previous designs.

The objective of this effort is to enable the selection and development of durable, lower-friction moving parts in diesel engines for heavy vehicle propulsion systems through the systematic evaluation of promising new materials, surface treatments, composites, and coating technologies. The current approach involves test method development, microstructural analysis of candidate materials, mapping the effects of applied parameters on surface damage, and modeling. The focus on EGR components and fuel injector plungers was based on discussions with diesel engine manufacturers. Before developing tests to evaluate materials for improved durability, however, it was necessary to conduct a tribosystem analysis to understand the conditions under which the surfaces of these components materials must perform in an operating diesel engine. The nature of contact damage to engine components was reviewed to ensure that laboratory test methods would adequately reproduce that kind of damage. Then the test development, data analysis, and modeling tasks were begun.

Approach

In FY 2001, based on the definition of several key durability problems, a test method was developed to study the high-temperature friction and wear characteristics of candidate EGR system materials. The testing system we built continues to be used to evaluate metal alloys, ceramics, coatings, and other experimental materials for that application. In FY 2002, this effort was extended to include an investigation of the scuffing of fuel injector component materials. Laboratory tests were developed and refined to produce and measure the type of fine-scale surface damage that is observed in diesel engine fuel system parts. In FY 2003, research continued in two areas: (1) evaluating the effects of diesel fuel sulfur reductions on scuffing and (2) identifying materials and coatings for high-temperature scuffing resistance in EGR components.

During FY 2004, a 3-dimensional (3D) scuffing map was developed to graphically depict conditions for scuffing initiation and propagation in time and space domains. It was applied to explore the effects of surface finish and sliding velocity on materials and coatings for fuel injector systems. Such scuffing maps are intended to aid designers to select more durable materials and to determine optimum surface finishes. Near the end of FY 2004, a new scuffing model was developed that integrates boundary film characteristics with material properties. Chemical analyses of scuffed surfaces were conducted to investigate the wear modes and tribochemical film compositions in a fuel-lubricated environment, underpinning the basis for the model. Plans for FY 2005 involve refining and improving the model using experimental data concerning the friction and surface damage of advanced materials for durable diesel engine components.

Results

As reported previously, a pin-on-twin pins test was developed to evaluate the scuffing tendencies of diesel fuel injector plunger materials in commercial diesel fuel and in a low-sulfur fuel. That test was used to rank a variety of promising new materials such as cermets and ceramics. Data were in the form of exposure time prior to the onset of scuffing. In considering the data, it was quite clear that many different variables could affect scuffing, and there was a need for a better method to display the data for visualizing combinations of variables. Therefore, work in FY 2004 involved studying the current data and developing a format to display it.

After the relevant issues were considered, a 3D friction-scuffing mapping technique was developed to present surface damage progression in the space and time domains. The concept is based on the assumption that an increase of the friction force at a certain location corresponds to lubricant film breakdown and surface morphology changes at that location. Scuffing is associated with asperity-level or grosser surface changes, such as plastic deformation and material displacement. Therefore, we might expect the rise in the plowing contribution of the friction force to reflect an increased incidence of surface deformation and hence become an indicator of scuffing. This correlation was verified by optical surface morphology examinations and electron microscopy.

An example of a 3D friction-based scuffing map is provided in Figure 1. The change of friction coefficient relative to that of the first stroke in the test is portrayed as the vertical axis in Figure 1. One horizontal axis represents the location along the length of the stroke, and the orthogonal axis represents the cumulative time of sliding contact. Shaded horizontal bands, defined in the Figure 1 legend, represent ranges of friction coefficient. The test used to construct Figure 1 used a reciprocating pin-on-twin pins configuration and was conducted on self-mated AISI 52100 steel in ultra-low-sulfur fuel (Jet A aviation fuel). By defining a threshold change in friction coefficient to signal the initiation of scuffing (e.g., an increase of 10% over the initial friction coefficient), it is possible to use the friction-scuffing map to indicate the location and progress of scuffing damage.

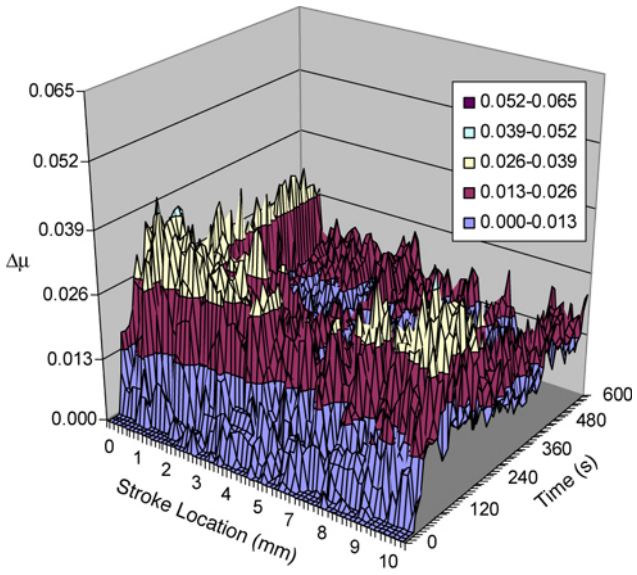

Figure 1. A 3D friction-scuffing map for self-mated bearing steel is plotted in space and time domains.

Three-dimensional friction-scuffing maps like that in Figure 1 were subsequently used to construct scuffing transition diagrams to portray the effects of surface roughness and sliding velocity on scuffing resistance for diesel fuel injector materials, such as AISI 52100 steel and transformation-toughened zirconia (TTZ).

Figure 2 depicts the time until the first instance of scuffing for specimens with different initial surface roughness in ultra-low-sulfur fuel. Scuffing usually initiates locally, generally at the ends of the stroke; and surface damage may or may not spread along the whole sliding stroke during the course of the test. In Figure 2, the 'local scuffing' curve refers to the moment of the onset of local scuffing, and the 'global scuffing' curve implies when the whole stroke was scuffed. The region between these two curves represents the period of scuffing propagation from local spots to the whole stroke. This outside-inward spreading is a consequence of the sliding motion. The velocity of our pin-on-twin reciprocating test follows a sinusoidal wave form. The sliding speed starts at 0 at the turnaround points and reaches a maximum at the stroke's midpoint. Scuffing, if it occurred, generally appeared at the stroke ends first, because there is less effective lubrication there and the lack of lubrication leads to more solid-to-solid contact.

Compared with self-mated steel, zirconia against steel performed better at each surface finish

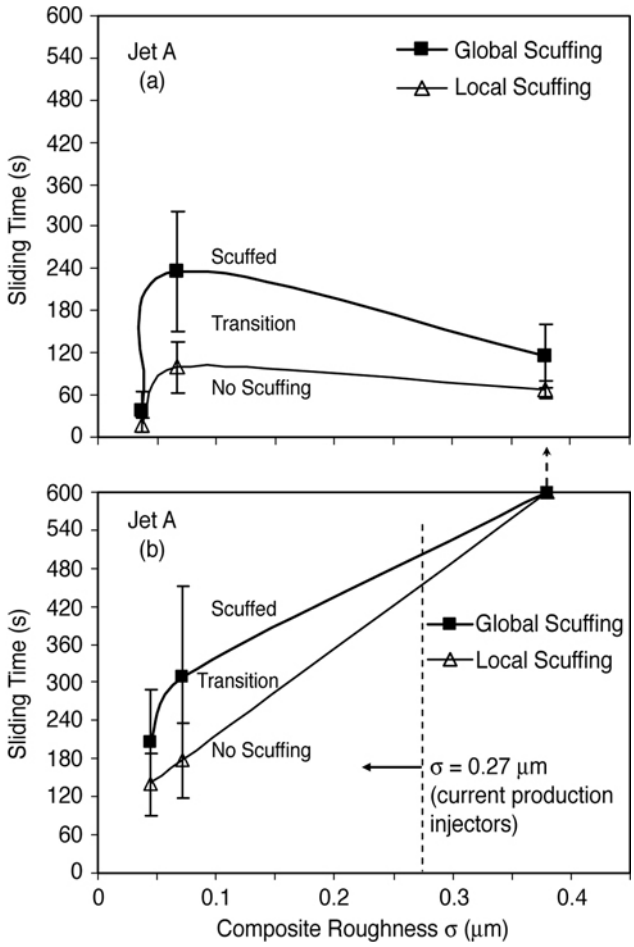

Figure 2. Scuffing transition diagrams for 52100 steel and TTZ in ultra-low-sulfur fuel.

level. Smoother contact surfaces tend to produce thinner lubricant films and more chance for incidental contact, but rougher surfaces have higher local contact pressure under boundary lubrication conditions. Either case may cause the lubricant to fail. Therefore, there is likely to be an optimum surface finish to provide the best scuffing resistance for a given lubricated sliding system. The steel specimens with intermediate roughness outperformed other two surface finish levels (Figure 2a), while rougher surfaces showed higher scuffing resistance for TTZ against steel (Figure 2b). The composite roughness* of the current-production zirconia plunger and 52100 steel bore in heavy-duty diesel engines is about 0.27 μm. To meet stricter diesel engine emissions standards, superior surface finish and tighter tolerances are required to seal the higher injection pressures. Better surface finish would reduce the scuffing resistance of the injector system, according to the scuffing transition diagrams in Figure 2b. This necessitates the investigation of new materials or surface engineering processes to resist scuffing under the more stringent operating conditions.

Under boundary lubrication, tribochemical films formed on contact surfaces play an important role in scuffing behavior. Depending on the specifics of the tribosystem, these in-situ formed films can be either protective or detrimental.[1] In the current investigation, the surface films formed in our fuel-lubricated scuffing tests have been examined and analyzed using optical microscopy, scanning electron microscopy (SEM), energy dispersive spectroscopy (EDS), and scanning auger microprobe (SAM).

For zirconia/steel pairs with relatively smooth surfaces, a tribo-film could easily be observed under a light optical microscope on both sides of the contact surfaces after scuffing. The brown or dark-reddish color suggested the presence of iron oxides such as FeO and/or Fe_2O_3. EDS analysis confirmed that oxygen was present in this layer. The scuffing process of zirconia against steel seemed to be a competition between the formation and removal of this tribochemical film. Although the oxide layer may protect the original surfaces from abrasive wear to some extent, its non-uniformity and the resulting adhesion and spallation problems make it undesirable for fuel-injection systems with very tight geometric clearances.

To better understand the scuffing transition in fuel-lubricated systems, the tribochemical surface films at an early scuffing stage were analyzed using a PHI 680 SAM. Figure 3 shows the sputtering depth profiles of elemental compositions for the surface films on and off the wear scar on a bottom steel pin (against steel) in Jet A fuel. There was a relatively thick (about 80 nm) iron-oxide-rich layer on the worn surface, compared with that (< 4 nm) on the unworn surface. This demonstrated that tribochemical excitation, such as frictional heating and mechanical deformation, significantly accelerated the oxidation process.[2] The surface film formed in #2 diesel fuel showed a thinner oxide-rich layer with lower oxygen concentration than the film formed in Jet A fuel. This implied that the diesel fuel "cooled"

* Composite roughness is defined as the square root of the sum of the squares of the arithmetic average surface roughnesses of both mating surfaces.

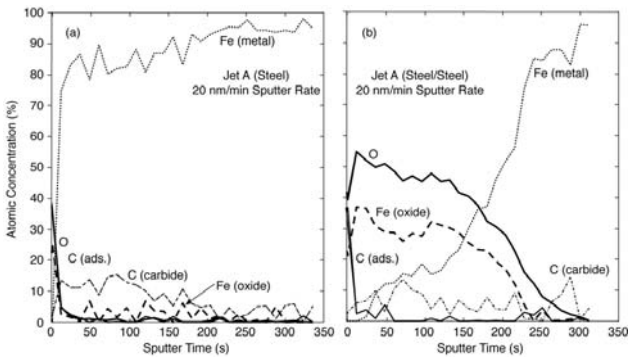

Figure 3. SAM sputtering profiles of surface films that were formed during tests in ultra-low-sulfur fuel.

the contact area more effectively, which probably helped to resist scuffing. The diesel-fuel-lubricated surface also had a higher non-carbide carbon concentration, which suggested that possibly more polymeric materials or organometallic compounds, thought to be generally protective, were deposited on the contact surfaces. These observations helped to explain the higher scuffing resistance in #2 diesel fuel than in Jet A fuel.

In late FY 2004, a new model for scuffing was developed. It was based on the recognition that a sequence of interfacial events needs to occur to set the stage for scuffing. First, the lubricant film must cease to effectively protect and separate the surfaces; next, the solids in contact must begin to accumulate damage to the point that significant deformation, roughening, and elevated friction occur. These phenomena have been embodied in a model for scuffing that was described in a project milestone report (see publications list) and will be further evaluated and refined in the light of additional experiments to be done in FY 2005.

Conclusions

- 3D friction-scuffing maps have been developed to depict scuffing initiation in both time and space domains. These maps were used to construct scuffing transition diagrams that correlate scuffing resistance to surface finish and sliding velocity.
- In the range of surface roughness tested in this study, zirconia against steel showed the scuffing resistance to be proportional to the composite surface roughness, while self-mated steel exhibited optimum performance with an intermediate surface finish.
- A thinner oxide layer and a higher non-carbide associated carbon concentration were detected on the #2 diesel-fuel-lubricated surfaces. This implied lower temperature and more protective organometallic compounds formed on the contact area. These observations could partially explain the higher scuffing resistance in normal diesel fuel than in ultra-low-sulfur fuel
- A combination of experimental data, surface observations, and derived scuffing transition diagrams led to the development of a new scuffing model. This model will be tested and validated in the year to come.

References

1. S.M. Hsu and R. S. Gates, "Boundary Lubrication and Boundary Lubricating Films," in *Modern Tribology Handbook*, ed. B. Bhushan, Vol. I, CRC Press, Boca Raton, pp. 455–492, 2001.

2. G. Heinicke, *Tribochemistry*, Carl Hanser Verlag, Munchen-Wien-Berlin, 1984, p. 97.

Publications/Presentations

P. J Blau, "Challenges for the Application of Engineered Surfaces to Tribosystems with Multiple Contact Modes," invited presentation at the symposium on Integrated Surface Engineering, ASME/STLE Tribology Conference, Ponte Vedra, FL, October 28, 2003.

P. J. Blau, J. J. Truhan, and J. Qu, *Scuffing Transition Diagrams for Fuel Injection System Materials*, Project Milestone Report, Oak Ridge National Laboratory, March, 19, 2004.

J. Qu, J. J. Truhan, and P. J. Blau, "Detecting the Onset of Localized Scuffing with the Pin-on-Twin Fuel-Lubricated Test for Heavy Duty Diesel Fuel Injectors," *International Journal of Engine Research* (in press).

J. Qu, J. J Truhan, and P. J. Blau, "Evaluating Candidate Materials for Heavy Duty Diesel Fuel Injectors Using a 'Pin-On-Twin' Scuffing Test," *Tribology International*, (in press).

P. J. Blau with J. Qu and J. J. Truhan, *On the Definition and Mechanisms of Scuffing in Fuel System Components—An Integrated Process Model*, Project Milestone Report, Oak Ridge National Laboratory, September, 17, 2004.

F. Life Prediction of Diesel Engine Components

H. T. Lin, T. P. Kirkland, A. A. Wereszczak, and M. K. Ferber
Oak Ridge National Laboratory
Oak Ridge, TN 37831-6068
(865) 576-8857; fax: (865) 475-6098; e-mail: linh@ornl.gov

Jeremy Trethewey and M. J. Andrews
Caterpillar, Inc.
Peoria, IL 61656-1875
(309) 578-0056; fax: (309) 578-2953; e-mail: trethewey_jeremy_s@cat.com

DOE Technology Development Area Specialist: Dr. Sidney Diamond
(202) 586-8032; fax: (202) 586-2476; e-mail: sid.diamond@ee.doe.gov
ORNL Technical Advisor: D. Ray Johnson
(865) 576-6832; fax: (865) 574-6098; e-mail: johnsondr@ornl.gov

---

Contractor: Oak Ridge National Laboratory, Oak Ridge, Tennessee
Prime Contract Number: DE-AC05-00OR22725
Subcontractor: Caterpillar, Inc., Peoria, Illinois

Objective

- Generate database and characterize damage mechanisms of candidate advanced ceramics and intermetallic alloys.
- Apply and verify probabilistic life prediction and components design and verification for advanced diesel engine components.

Approach

- Evaluate the dynamic fatigue and rotary bending fatigue performance of candidate silicon nitride ceramics and titanium aluminide (TiAl) alloys at elevated temperatures in air before and after long-term exposure to simulated engine environments, as well as engine field tests.
- Characterize the evolution and role of damage mechanisms, and changes in microstructure linked to the long-term mechanical performance and reliability of ceramics and intermetallic alloys.
- Predict the failure probability and reliability of complex-shaped components subjected to application conditions via the use of life prediction codes.

Accomplishments

- Completed mechanical properties of prototype NT551 silicon nitride exhaust valves after 500-h bench rig test
- Completed dynamic fatigue study for Kyocera SN235P silicon nitride, fabricated from the same powder batch for exhaust valve blanks, after 100-h oil immersion test.
- Completed development of dynamic fatigue database for a commercial-grade silicon nitride, SN147-31E, acquired from Ceradyne, Inc
- Completed mechanical property verification for flexure test bend bars machined from Kyocera SN235 exhaust valve blanks for mechanical performance verification.

Future Direction

- Characterize microstructure and mechanical properties of Kyocera SN235P silicon nitride exhaust valves after engine field demonstration at the National Transportation Research Center (NTRC) and verify the probabilistic component design and life prediction.
- Develop a dynamic fatigue database for Ceradyne SN147-31N silicon nitride fabricated from the same power batch for exhaust valve blanks.
- Verify mechanical properties for Ceradyne SN147-31N silicon nitride machined from the exhaust valve blanks.
- Develop the mechanical database for the specimens extracted from diesel particulate filter (DPF) substrates for long-term mechanical reliability and life prediction.

Introduction

There has been considerable interest in the potential for extensive use of advanced ceramics and intermetallic alloys in advanced diesel engine systems because of their superior thermomechanical properties at elevated temperatures. The implementation of components fabricated from these advanced materials would lead to significant improvement in engine efficiency, long-term durability, and reduction in nitrogen oxides and CO exhaust emission as required in the 21st Century Truck Program. This interest has focused primarily on research aimed at characterization and design methodology development (life prediction) for advanced silicon nitride ceramics and TiAl alloys in order to manufacture consistent and reliable complex-shaped components for diesel engine applications. The valid prediction of mechanical reliability and service life is a prerequisite for the successful implementation of these advanced materials as internal combustion engine components.

This research project has three primary goals, which contribute toward successful implementation:

- the generation of a mechanical engineering database from ambient to high temperatures of candidate advanced materials before and after exposure to simulated engine environments
- the microstructural characterization of failure phenomena in these advanced materials and components fabricated from them
- the application and verification of probabilistic life prediction methods using diesel engine components as test cases

For all three stages, results will be provided to both the material suppliers and component end-users to refine and optimize the processing parameters to achieve consistent mechanical reliability, and to validate the probabilistic design and life prediction of engine components made from these advanced materials.

Approach

All silicon nitride test bend bars were longitudinally or transversely machined according to ASTM standard C1161 from production billets purchased from material suppliers.[1] Flexure testing was conducted in ambient air in four-point bending using 20/40- mm, α-SiC, semi-articulating fixtures at temperatures ranging from 20 to 1000°C and at a stressing rate of 30 MPa/s and 0.003 MPa/s. The 30 MPa/s test condition was chosen to evaluate the inert characteristic strength as a function of temperature; the 0.003 MPa/s test condition was chosen to measure the change in slow crack growth (SCG) susceptibility at elevated temperatures. Pneumatic actuators were programmed to produce the desired loading rate (and corresponding stressing rate) via a personal computer. Load was continuously measured as a function of time, and flexure strength was calculated using ASTM standard C1161. The accumulated strength data were then further analyzed. The strengths for each test set were fit to a two-parameter Weibull distribution using the program CERAMIC,[2] which uses the maximum likelihood estimation advocated in ASTM C1239.[3] Reported results are uncensored because fractography analysis was not conducted in detail to identify strength-limiting flaws for all of the bend bars tested. Following the dynamic fatigue test, both optical and scanning electron microscopy analysis were carried out on fracture surfaces and polished cross-sections of selected bend bars to characterize the fracture as well as degradation mechanisms. X-ray analysis was also carried out to evaluate the possible phase

changes resulting from oxidation during dynamic fatigue testing or after long-term exposure to simulated engine environments, which could possibly cause degradation in mechanical performance and reliability.

Results

Dynamic Fatigue Response of Kyocera SN235P Silicon Nitride

Kyocera SN235P silicon nitride was down-selected by Caterpillar for engine demonstration because of its excellent resistance to slow crack growth and to a simulated diesel engine environment at elevated temperatures. To ensure a consistent microstructure and chemistry in the secondary phase, and thus mechanical reliability, of the valve blank materials, bend bars were machined from co-processed billets for long-term oil immersion as well as exhaust gas study. Bend bars were also machined from the valve blank itself for mechanical comparison. The results obtained would also allow Caterpillar to verify its probabilistic component design and life prediction tasks. The test silicon nitride samples were placed in platinum crucibles and covered with commercial-grade 10W30 engine oil. The crucibles with oil-covered silicon nitride bend bars were heated in a furnace at 600°C for approximately 30 minutes to ash the oil. After completion of oil-ash conversion, the samples covered with 1–2 mm oil ash powder were then heat-treated at 850°C for 1000 h in ambient air. In addition, SN235P bend bars were exposed to exhaust gas for 1000 h. The results previously generated for the as-machined SN235P samples, co-processed with the exhaust valve blanks, showed a very high fatigue exponent (N ~ 93) at 850°C, indicative of no susceptibility to the SCG process.[4,5] Therefore, the dynamic fatigue tests for exposed SN235P samples were carried out only at 850°C and 0.003 MPa/s in air according to ASTM C1465 because of the limited number of specimens.

Results of tests carried out at 20 and 850°C and at 30 MPa/s showed that the SN235P valve blank material exhibited very consistent mechanical characteristic strength and Weibull modulus with respect to those SN235P materials evaluated previously in the program. Dynamic fatigue tests at 850°C and 0.003 MPa/s show that both of the oil-immersed as well as exhaust-gas exposed SN235P silicon nitride specimens exhibit an inert characteristic strength comparable to those obtained from the as-machined samples tested under the same condition (Table 1). Also, results show that there is no difference in characteristic strength values between oil-ash–exposed and exhaust-gas–exposed samples. In addition, both of the exposed SN235P samples showed a higher Weibull modulus than the as-machined samples. The higher Weibull modulus of exposed samples could arise from the surface sealing effect due to the formation of oxide scale after exposure. The dynamic fatigue results suggest that the SN235P-CP exhibits excellent corrosion resistance to diesel engine environments and no susceptibility to the SCG process at test temperatures. Thus the SN235P material would meet the application criteria for exhaust valve components of advanced diesel engines.

Dynamic Fatigue Response of Ceradyne SN147-E Silicon Nitride

Studies of dynamic fatigue properties of a commercial-grade silicon nitride, i.e., SN147-31E, manufactured by Ceradyne Advanced Ceramic, Inc., were completed this year. The objective of this study is to extend the database generation efforts to other potential candidate silicon nitride ceramics, especially those manufactured by domestic material suppliers. The SN147-31E was processed with sintering additives (i.e., Al_2O_3 and Y_2O_3) similar to those employed for SN147-31N that were evaluated and reported previously. However, the SN147-31E contains a crystalline secondary phase achieved by post–heat treatment. Thus it is anticipated that SN147-31E would exhibit a higher temperature mechanical reliability than SN147-31N because of the presence of the crystalline secondary phase.

Dynamic fatigue results showed that the longitudinally machined SN147-13E exhibited a characteristic strength that is 20% lower than that obtained from the SN147-31N machined and tested under the same conditions (Table 2). The lower strength of SN147-31E could be due to the change in internal residual stress resulting from the crystallization process of the secondary phase(s) by post–heat treatment. In addition, the transversely machined SN147-31E showed a minor decrease (~8%) in characteristic strength as compared with the SN147-31N. The minor difference in strength between SN147-31E and –31N, which were transversely

Table 1. Summary of uncensored Weibull and strength distributions for Kyocera SN235P silicon nitride specimens longitudinally machined per ASTM C1161from co-processed billets and exhaust valve blanks before and after exposure to simulated diesel engine environments. Data generated for SN235P evaluated previously in the program are used for reference.

Material	# of spmns. tested	Stressing rate (MPa/s)	Temp. (°C)	Uncens. weibull modulus	± 95% Uncens. weibull modulus	Uncens. chrctstic strength (MPa)	± 95% Uncens chrctstic strength (MPa)
SN235P	10	30	20	32.6	18.8 49.6	792	773, 810
SN235P	10	30	850	30.3	16.5, 48.1	673	643, 691
SN235P	10	0.003	850	23.6	12.7, 38.8	641	662, 641
SN235P-CPB	30	30	20	11.94	8.58. 15.94	820	794, 847
SN235P-CPB	30	0.003	20	14.56	10.93, 18.64	741	721, 761
SN235P-CPB	30	30	850	20.56	15.16, 26.87	684	671, 697
SN235P-CPB	30	0.003	850	19.44	14.49, 25.01	621	608, 633
SN235P-EVB	15	30	20	17.58	11.39, 25.07	895	866, 924
SN235P-EVB	15	30	850	10.42	6.64, 15.23	732	691, 772
SN235P-CPB-Oil	15	0.003	850	30.40	19.47, 44.19	660	647, 672
SN235P-CPB-ExhGas	12	0.003	850	25.07	15.55, 36.81	677	659, 694

CPB: specimens were machined from co-processed billets of exhaust valve blanks.
EVB: specimens were machined from exhaust valve blanks.

machined, could be due to the similarly dominant strength-limiting flaws, i.e., surface machining flaws. However, SN147-31E exhibited a lower Weibull modulus than that obtained for SN147-31N. On the other hand, results at 20°C and 0.003 MPa/s showed that both longitudinally and transversely machined SN147-31E exhibited little or no decrease in characteristic strength as compared with results obtained at 30 MPa/s, as shown in Table 2. Results also show that the Weibull moduli were not sensitive to the stressing rate. In addition, both materials exhibited high fatigue exponents at room temperature (Figures 1 and 2), indicative of no susceptibility to the SCG process. However, results at 850°C showed that the SN147-31E exhibited a relative low fatigue exponent of 56 with respect to SN147-31N ($N \sim 131$), indicative of a susceptibility to the SCG process at test temperatures (Figure 3). The low fatigue exponent obtained for SN147-31E suggests an incomplete crystallization of the glassy phase during post–heat treatment. The presence of these residual glassy phase(s) could play an important role in the high-temperature mechanical performance and susceptibility to SCG.

The study of dynamic fatigue behavior in four-point bending for transversely machined SN147-31N silicon nitride after 1000 h of exposure to an oil ash environment was also completed during this reporting period. The current study was carried out to understand the effect of long-term exposure to a simulated diesel engine environment on the mechanical performance of SN147-31N. As a result of the limited number of bend bars, the dynamic fatigue tests for exposed SN147-31N samples were carried out only at 850°C and 0.003 MPa/s in air according to ASTM C1465. Results of dynamic

Table 2. Summary of uncensored Weibull and strength distributions for Ceradyne SN147-31E silicon nitride specimens transversely machined per ASTM C1161. Data of SN147-31N machined longitudinally as well as transversely are used for reference.

Material	# of spmns. tested	Stressing rate (MPa/s)	Temp. (°C)	Uncens. Weibull modulus	± 95% Uncens. Weibull modulus	Uncens. chrctstic strength (MPa)	± 95% Uncens chrctstic strength (MPa)
SN147-31N-Long	15	30	20	21.73	14.07. 31.09	836	814, 858
SN147-31N-Long	15	30	850	20.35	13.58, 28.20	777	755, 799
SN147-31N-Long	15	0.003	850	16.19	10.57, 23.02	732	706, 757
SN147-31N-Trans	15	30	20	13.76	8.96, 19.59	677	649, 705
SN147-31N-Trans	15	30	850	18.26	11.67, 26.47	639	619, 659
SN147-31N-Trans	15	0.003	850	19.95	12.83, 28.63	620	602, 638
SN147-31E-Long	15	30	20	17.30	10.86, 25.58	668	645, 690
SN147-31E-Long	15	0.003	20	16.19	10.60, 22.98	620	598, 642
SN147-31E-Long	15	30	850	9.36	6.01, 13.62	604	567, 641
SN147-31E-Long	15	0.003	850	12.06	7.70, 17.52	509	485, 533
SN147-31E-Trans	15	30	20	7.44	4.89, 10.58	623	575, 671
SN147-31E-Trans	15	0.003	20	8.99	5.61, 13.45	607	568, 646
SN147-31N-1000hOil*	15	850	0.003	15.54	10.31, 21.65	600	578, 622

*1000h Oil: specimens were transversely machined and exposed to an oil ash environment for 1000h.

fatigue tests at 850°C and 0.003 MPa/s showed that the exposed SN147-31N silicon nitride exhibited an inert characteristic strength comparable to results obtained from the as-machined samples tested under the same condition (Table 2). Also, there is no difference in Weibull modulus between oil-ash exposed and as-machined samples. The dynamic fatigue results suggest that the SN147-31N exhibits excellent corrosion resistance in diesel engine environments, similar to those observed for SN235 and GS44 silicon nitride ceramics evaluated previously. Therefore, one could conclude that silicon nitride ceramics, in general, exhibit superior corrosion resistance in diesel engine environments compared with those metallic alloys.

Mechanical Properties of Diesel Particulate Filters

This study, part of a cooperative research and development agreement between Cummins and Oak Ridge National Laboratory, is carried out to characterize the mechanical properties of a DPF substrate and develop analytical tools for predicting long-term reliability and durability. Miniature test samples have been successfully machined from the substrates of DPFs acquired from Corning (Figure 4a) during this reporting period. The samples have nominal dimensions of 0.20 × 0.90 × 15 mm. A miniature test fixture has also been designed and machined (Figure 4b). The alumina test fixture has inner and outer

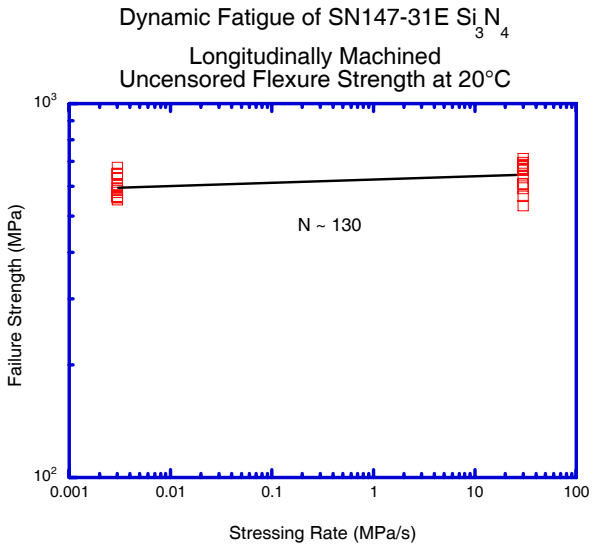

Figure 1. Failure strength vs stressing rate curve of SN147-31E longitudinally machined and tested at 20°C in air.

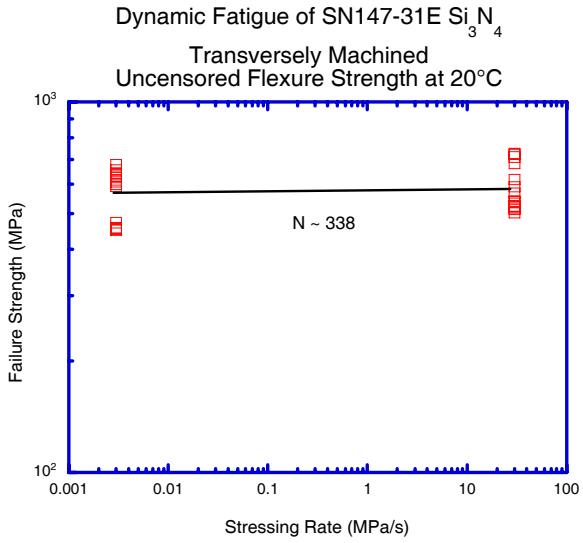

Figure 2. Failure strength vs stressing rate curve of SN147-31E transversely machined and tested at 20°C in air.

spans of 1 and 2 mm, respectively. Figure 5 shows the uncensored Weibull strength distribution of DPF samples. Results indicate that the DPF material exhibits low characteristic strength as well as Weibull modulus because of its porous microstructure. The strength data will be also generated from the full-size DPF samples for comparison. The data gener-

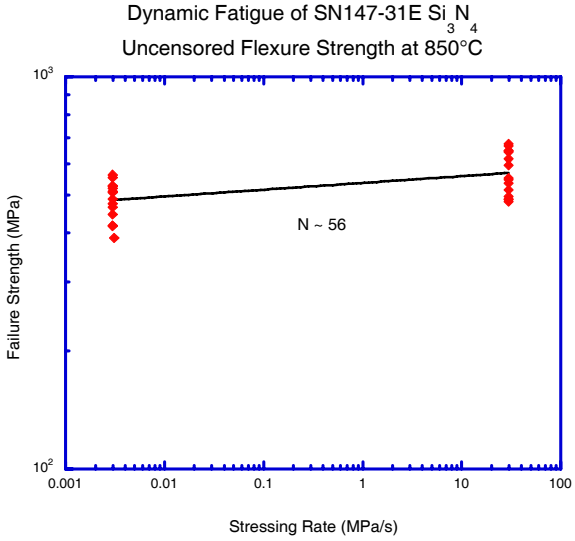

Figure 3. Failure strength vs stressing rate curve of SN147-31E longitudinally machined and tested at 850°C in air.

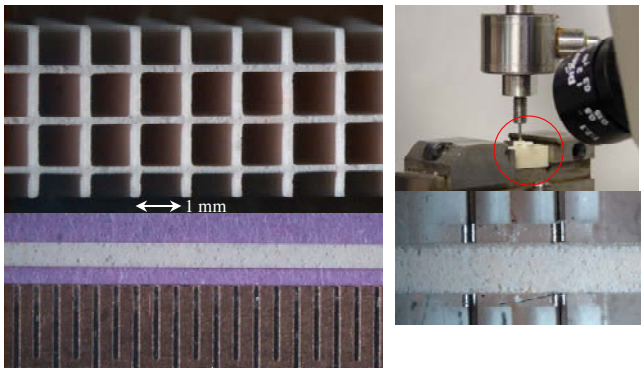

Figure 4. (a) Photos show a section of diesel particulate filter, and sample machined from it. (b) Photos show the micro test system and miniature test fixture.

ated for the miniature test samples from DPF substrates would be used for life prediction.

References

1. American Society for Testing and Materials, "Standard Test Method for Flexural Strength of Advanced Ceramics at Ambient Temperatures," ASTM C1161, *Annual Book of ASTM Standards*, Vol. 15.01, American Society for Testing and Materials, West Conshohocken, PA, 1999.

2. *Life Prediction Methodology for Ceramic Components of Advanced Heat Engines, Phase 1*, ORNL/Sub/89-SC674/1-2, prepared by AlliedSignal

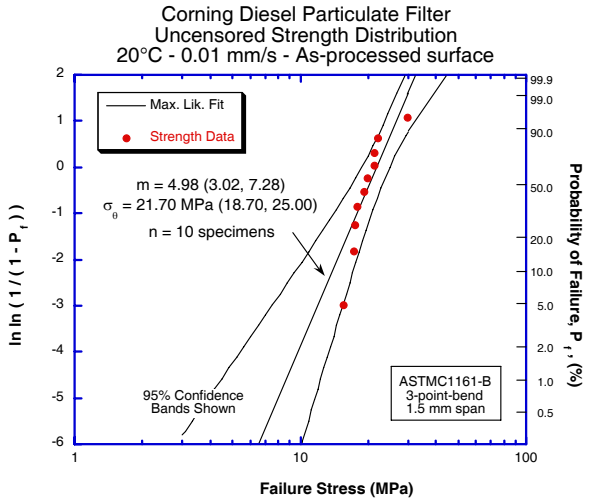

Figure 5. Failure strength vs stressing rate curve of SN147-31E longitudinally machined and tested at 20°C in air.

Engines, Department of Energy Office of Transportation Technologies, Washington, D.C., 1995.

3. American Society for Testing and Materials, "Practice for Reporting Uniaxial Strength Data and Estimating Weibull Distribution Parameters for Advanced Ceramics," ASTM C1239, *Annual Book of ASTM Standards, Vol. 15.01*, American Society for Testing and Materials, West Conshohocken, PA, 1999.

4. A. A. Wereszczak, H. -T. Lin, T. P. Kirkland, M. J. Andrews, and S. K. Lee, "Strength and Dynamic Fatigue of Silicon Nitride at Intermediate Temperatures," *J. Mater. Sci.* **37**, 2669–2684 (2002).

5. H. -T. Lin, T. P. Kirkland, A. A. Wereszczak, and M. J. Andrews "Effect of Long-Term Oil Immersion Test on Mechanical Reliability of Candidate Silicon Nitride Ceramics for Diesel Engine Applications," pp. 261–273 in *Ceramic Transactions*, Vol. 142, "Silicon-Based Structural Ceramics for the New Millennium" (2003).

Publications

1. H. -T. Lin, T. P. Kirkland, A. A. Wereszczak, and M. J. Andrews, "Effect of Long-Term Oil Immersion Test on Mechanical Reliability of Candidate Silicon Nitride Ceramics for Diesel Engine Applications," pp. 261–273 in *Ceramic Transactions*, Vol. 142, "Silicon-Based Structural Ceramics for the New Millennium" (2003).

2. H. T. Lin, T. P. Kirkland, A. A. Wereszczak, and M. J. Andrews, "Strength Retention of Silicon Nitride After Long-term Oil Immersion Exposure," submitted to *J. Mater. Sci.*

G. Low-Cost Manufacturing of Precision Diesel Engine Components

Principal Investigator: P. J. Blau
Oak Ridge National Laboratory
P.O. Box 2008, Oak Ridge, TN 37831-6063
(865) 574-5377; fax: (865) 574-6918; e-mail:blaupj@ornl.gov

DOE Technology Development Area Specialist: Dr. Sidney Diamond
(202) 586-8032; fax: (202) 586-1600; e-mail: sid.diamond@ee.doe.gov
ORNL Technical Advisor: D. Ray Johnson
(865) 576-6832; fax: (865) 574-6098; e-mail: johnsondr@ornl.gov

---

Contractor: Oak Ridge National Laboratory, Oak Ridge, Tennessee
Prime Contract No.: DE-AC05-00OR22725

Objectives

- Develop and demonstrate optimized, cost-effective fabrication processes for producing precision components for use in diesel engines.
- Develop and demonstrate optimized, cost-effective methods to detect, characterize, and minimize machining-induced damage in advanced materials for engine components.

Approach

- Collaborate with manufacturers and suppliers of heavy vehicle engine components to identify enabling technologies for the cost-effective machining of precision components, such as valves, valve guides, and fuel injection system components, from advanced materials.
- Utilize Oak Ridge National Laboratory's (ORNL's) instrumented machine tools and dimensional metrology and surface characterization instruments to correlate the microstructures of advanced materials with their machining characteristics.
- Work with a consortium of software developers and component manufacturers to develop improved models for high-speed machining of titanium alloys.

Accomplishments

- Developed a method to measure the wear of super-abrasive grinding wheels that use "witness blocks" of easy-to-machine material to profile worn and unworn areas of the wheel.
- Machined silicon nitride engine valves from dimensionally-characterized starting blanks provided by Caterpillar Corporation.
- Initiated a new project to correlate the microstructure and hard particle concentration of cermets with their machining behavior.
- Joined and participated in a consortium led by Third-Wave Systems (TWS) to model high-speed machining of titanium alloys.

Future Direction

- Continue to work with the TWS machining consortium to develop computer models and to provide supporting data for those models to enable low-cost machining of advanced, lightweight engine materials.
- Survey the state of the art and conduct systematic studies of the effects of hard particle concentration on the machining characteristics and surface quality of advanced composites based on metal-bond ceramic particles.

Introduction

Manufacturing involves the conversion of raw materials into finished, useful components and products. Historically, it represents a vital industrial component of the economic security of the United States. Manufacturing begins with processed materials, such as metals, ceramics, polymers and composites, and then shapes, joins, and finishes them to meet the functional requirements of machines, machine parts, and structures. Manufacturing comprises a broad range of engineering disciplines that are applied to an even wider range of unit processes. It is necessary, therefore, to focus on an area of manufacturing that, in the present case, enables both the near-term and the longer-term introduction of advanced materials and machining methods for diesel engine components into the commercial marketplace.

For more than 150 years, since the Industrial Revolution, U.S. industry has invested hundreds of billions of dollars in the development of machining technology and the purchase of equipment. However, with the egress of manufacturing to foreign sources in recent years, a significant amount of capital equipment and the knowledge base to develop new machining technology to enable the introduction of advanced materials has eroded. Experienced machinists have retired and, with fewer manufacturing jobs in the United States, they are not being replaced by motivated, young trainees from the next generation. The machine tool industry in the United States also has suffered significant losses and many, if not most, new machine tools are made by foreign sources. It is vital, therefore, to avoid full dependence on foreign sources and to maintain a base of machining science in the United States.

Approach

The approach taken in this project involves three areas of machining technology:

1. Machining engine parts from advanced materials, such as ceramic engine valves.
2. Modeling machining processes with state-of-the-art software.
3. Characterizing the machining response of newly-developed materials, such as composites.

Projects in each of these areas are separately discussed in the Results section.

Results

Machining of silicon nitride diesel engine valves. Silicon nitride valve blanks were received by ORNL from Caterpillar, and their straightness and diameters were measured using a coordinate measuring machine. The appropriate dimensions to use, considering several valve designs and the coordinate measuring machine data for the blanks, were then selected. A set of programming instructions was developed for use with the Weldon grinder. This program was then tested and verified using a bar of machinable alumina silicate ceramic. Profiles on the "dummy part" were checked with the coordinate measuring machine. Particular attention was paid to the dimensions of both the bevel and the blend section between the valve stem and head. The finished valve is shown in Figure 1.

Participation in the machining consortium. In FY 2004, a new collaboration began with TWS of Minneapolis. TWS has been leading a U.S. Air Force Phase II Small Business Innovative Research project, "Improved Titanium Machining Processes," to develop an advanced machining modeling package based on finite element modeling (FEM). TWS has established a consortium of aerospace and ground transportation component manufacturers that are interested in improving machining processes for titanium alloys. Benefits from membership in the consortium are

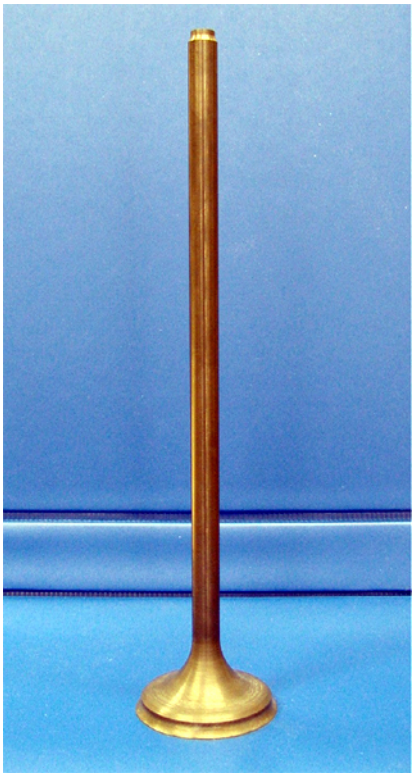

Figure 1. Silicon nitride diesel engine valve machined at ORNL.

1 Members share the latest technologies for titanium machining from other consortium members, such as TWS, Kennametal, Caterpillar, Stork Fokker (Netherlands), and EADS (Germany).
2. Members have the use of the advanced FEM-based machining modeling package called AdvantEdge™.
3. Participants help define the direction of the machining technology being developed, specifically, working with the University of Michigan to develop and verify models for drilling, boring, and face milling of titanium, in addition to having access to other models in the current modeling package.
4. ORNL helps the consortium by conducting material characterization to help select new cutting tool materials and tool coatings for improved machining of titanium.
5. New modeling capabilities will not be limited to titanium but will represent a new in-house resource for materials development programs and the High Temperature Materials Laboratory Machining, Inspection, and Tribology User Center.

The basis for our interest in the TWS consortium stems from recent technology that promises to reduce the cost of titanium raw material[1–3] and therefore expand titanium's potential use as a lightweight material in engines and brakes.[4] However, the difficulty of high-speed machining of titanium alloys is a major technical barrier. Because of the metal's poor thermal conductivity (6.8 W/
m-K), the cutting heat cannot be dispersed efficiently, and the tool tip temperature is much higher than that generated in cutting most other metals. The high tool temperature promotes the diffusion tool wear and limits the cutting speed. Serrated chips with adiabatic shear band are usually produced in titanium machining because of the thermal-mechanical instability. The chip shear band formation creates fluctuation in cutting forces, leading to tool chipping. Therefore, research is needed in titanium machining, including advanced process modeling and development of new tool materials/coatings.

Jun Qu of ORNL and Paul Becker of the University of Tennessee attended the 2004 TWS AdvantEdge international users' conference in March in Gaithersburg, MD, and Jun also took the short course in modeling metal cutting offered by TWS in April.

Output from the model. The TWS modeling package AdvantEdge can be used to improve cutting speeds and evaluate tooling performance by simulating and predicting cutting forces and tool/workpiece /chip temperatures. AdvantEdge may also be used to address other important issues, such as chip breakage, tool wear, and residual stresses.

Simulations were first run on several steel and aluminum alloys using different tool materials, tool geometries, and cutting parameters to become familiar with the modeling technique and test the feasibility of AdvantEdge. Then the focus was shifted to titanium alloys. For example, AdvantEdge was used to simulate performance in cutting (turning) Ti-6Al-4V alloy with different tool inserts (bare WC-Co and TiAlN coatings with thicknesses of 3 and 6 μm). The cutting speed was set to 195 m/min with a 0.381-mm feed and a 1.02-mm depth of cut. The steady-state temperature maps of the cutting areas are shown in Figure 2. Figure 3 displays the ex-

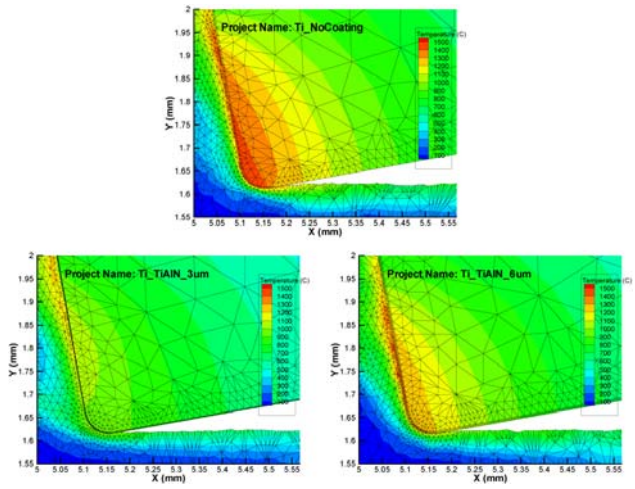

Figure 2. Temperature maps of coated and uncoated tools cutting Ti-6Al-4V.

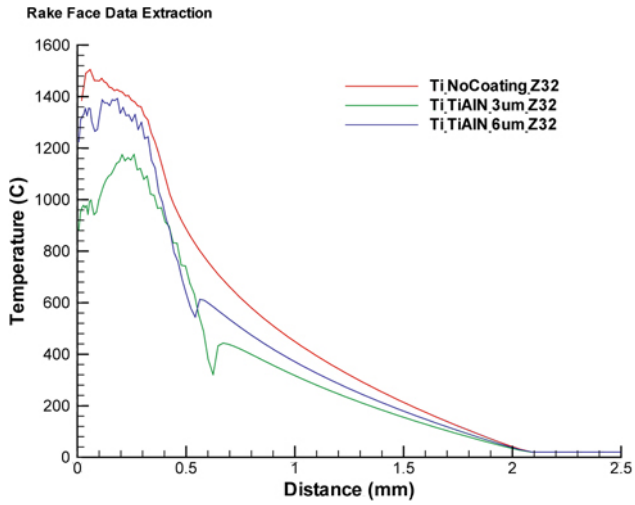

Figure 3. Rake face temperature profiles.

tracted rake face temperature profiles. Apparently, the temperature at the uncoated tool tip is higher than that of the coated tips. It is interesting to note that the tip with the 6-μm coating is hotter than the tip with the 3-μm coating. This implies that a thicker coating may not improve tool performance. Thicker coatings also increase the production cost and are more vulnerable to spalling. In fact, 3 μm is the current industry standard thickness for TiN and TiAlN tool coatings. Besides having lower cutting temperatures, coated tools generate smoother cutting surfaces, as illustrated in Figure 3.

Tooling studies. In addition to process modeling, new tool materials for titanium are being explored. One potential tool material is a TiC (particles)–Ni_3Al (matrix) composite that was initially developed for heavy-duty diesel fuel injector plungers. It contained 40–50 vol % TiC and 50–60 vol % Ni_3Al. Experimental work at the University of Michigan has proved that this composition is inadequate for cutting tools. Rather, TiC–Ni_3Al materials with high concentrations of TiC (90–95 vol %) are being prepared and will be tested in FY 2005.

The physical properties of five production tool materials and coatings are also being characterized. The coating thicknesses and microstructures of each material were examined by both scanning electron microscopy and scanning acoustic microscopy, a novel nondestructive method for observing micrometer-sized surface flaws. The coating hardness and modulus of elasticity have been measured by nanoindentation. The thermal conductivity and thermal diffusivity of the tool coatings significantly affect the cutting performance and tool life. The thermophysical properties of these thin coatings will be measured using a newly developed photoacoustic technique at the Microscale Thermophysical Property Laboratory at Purdue University.

In titanium machining, the high tool wear, particularly diffusion wear, significantly limits the cutting speed and tool life. Measurement and characterization of the tool wear are upcoming to investigate the wear mechanisms and explore an effective method to quantify the wear at the tool tips.

Machining of hard composite materials. Composite materials are used because they can draw from the advantageous properties or two or more materials to create a new material with properties better than those of either constituent alone. They find a wide variety of uses in structural and nonstructural applications. Composite materials in which the various phases in the microstructure differ greatly in hardness represent one of the most challenging problems for machining in cases when it is necessary to achieve high-precision surface finishes and minimal surface damage. Fine particles of grit embedded in the grinding wheel can produce differential grinding of the hard and soft phases. Pull-out of the hard particles may leave holes and other artifacts that can affect surface quality. In the coming year, a series of cermets with different concentrations of hard phases will be prepared by ORNL and used to study the behavior of cermets and metal matrix composites.

In preparation, ORNL is conducting a survey of machining practices for drilling, turning, and grind-

ing cermets and metal matrix composites. Then the cermets will be machined under a range of conditions to study how multi-phase composites respond to varying levels of aggressiveness in material removal parameters. The focus will be on understanding the relationship between microstructure, hard particle concentration, and surface quality in machined composite materials.

Conclusions

- Two diesel engine valves were machined from silicon nitride materials supplied by Caterpillar. In preparing these valves, it was necessary to compensate for a lack of straightness in the stem portion of the blank. A precision coordinate measuring machine first was used to characterize the starting blank, and special mounting methods then were used to ensure that the final part could be prepared from imperfectly shaped stock.
- A new effort in computer-assisted modeling of high-speed machining processes for titanium was initiated through participation in a consortium with TWS. Initial results are encouraging, and the software provides a new capability to ORNL's machining program.
- In FY 2005, there will be a new activity directed toward understanding the machining characteristics and resulting surface quality of composite materials. This work will support the development of precision machining processes for difficult-to-machine materials with relatively hard and soft phases in the microstructure.

References

1. E. H. Kraft, *Summary of Emerging Titanium Cost Reduction Technologies*, U.S. Department of Energy/Oak Ridge National Laboratory, 2004.

2. B. E. Hurles and F. H. Froes, "Lowering the Cost of Titanium," *AMPTIAC Quarterly*, **6**(2) 3–9 (2002).

3. P. C. Turner and J. S. Hansen, "Progress Toward Low-Cost Titanium," *Advanced Materials and Processes*, **143**(1) 42–43 (1993).

4. E. H. Kraft, *Opportunities for Low Cost Titanium in Reduced Fuel Consumption, Improved Emission, and Enhanced Durability Heavy-Duty Vehicles*, U.S. Department of Energy/Oak Ridge National Laboratory, 2002.

H. Cost-Effective Machining of Titanium Materials

Albert J. Shih
Mechanical Engineering
University of Michigan
Ann Arbor, Michigan 48109-9379.
(734) 647-1766; fax: (734) 936-0363; e-mail: shiha@umich.edu

DOE Technology Development Area Specialist: Dr. Sidney Diamond
(202) 586-8032; fax: (202) 586-1600; e-mail: sid.diamond@ee.doe.gov
ORNL Technical Advisor: D. Ray Johnson
(865) 576-6832; fax: (865) 574-6098; e-mail: johnsondr@ornl.gov

---

Contractor: Oak Ridge National Laboratory, Oak Ridge, Tennessee
Prime Contract No: DE-AC05-00OR22725
Subcontractor: University of Michigan, Ann Arbor, Michigan

Objective

- Investigate new technologies for cost-effective machining of titanium (Ti) alloys.
- Gain in-depth knowledge of the effects of process parameters using three-dimensional (3D) finite element modeling (FEM).
- Study machining using a production tool with complicated geometry.
- Investigate tool wear mechanisms and investigate new tool materials and coatings.

Approach

- Experimentally validate force and temperature in 3D FEM.
- Conduct parametric study of the machining parameters using the validated model.
- Investigate the tool wear mechanisms and develop new tools and coatings.

Accomplishments

- Conducted turning and drilling experiments on Ti.
- Conducted 3D FEM of Ti turning and validated the cutting force and chip thickness with experimental measurements.
- Investigated the effects of cutting speed, a limiting factor for productivity in Ti machining.
- Conducted tool wear tests. Used the laser profilometry to study tool wear mechanism in Ti machining.

Future Direction

- Expand the drilling research to Ti drilling, an important and bottleneck process for engine manufacturing.
- Explore advanced tool materials and coatings for Ti machining.

Introduction

Titanium and its alloys are lightweight, corrosion-resistant, high-temperature materials. New emerging technologies have been developed to reduce the cost of producing raw Ti material and have brought the potential for low-cost Ti and for automotive applications.[1,2] While reducing the material cost can go a long way toward increasing the usage of Ti, high machining cost is another major technical barrier that needs to be overcome. To further reduce the cost of effective machining of Ti, a better understanding of the underlying mechanisms of the Ti machining process is necessary through better process and performance models, thermal modeling, and finite element simulation.[3] There is a lack of research in 3D FEM, which can provide detailed information about the stress, strain, and temperature distributions in the tool and workpiece; surface integrity of the part; and mechanics of chip curl. Advancements in machining process modeling have demonstrated the capability to provide reliable predictions of the performance of the cutting process and the influence of the process parameters on the product quality.[4]

Approach

Experimental Setup

The machining experiments were conducted on a Lodge and Shipley 30-hp computer numerically controlled lathe. A grade-two commercially pure (CP) Ti rod, 31.8 mm in diameter, was used. A left-handed tool holder, Kennametal CTAPL-163D, was used to hold the triangular-shaped insert. The tool holder controls the orientation of the tool and workpiece, which is defined by the lead, back rake, and side rake angles in turning.[5] The lead angle and back rake angle were 0°, the side rake angle was 5°, and the relief angle was 6°. A Kistler 9257A 3-axis piezoelectric dynamometer was used to measure cutting forces on the tool insert in three directions, which are designated as tangential force (F_t), radial force (F_r), and axial force (F_a), respectively. The force signal was processed using the charge amplifiers and recorded by a PC-based data-acquisition system.

FEM of 3D Turning of Titanium

The Third Wave Systems AdvantEdge™ 3D machining simulation software was used to model the Ti machining process. The updated-Lagrangian finite element method with continuous remeshing and adaptive meshing techniques was applied.[6] The coupling of the thermal and mechanical modeling of the tool and workpiece deformation was applied.[7] Figure 1 shows the initial 3D finite element mesh using a tool with a corner radius. An XYZ coordinate system is defined to show the relative orientation of the tool and cutting forces. The X-axis is the cutting direction. The Y-axis is the radial direction, which is parallel to the major cutting edge. The Z-axis is parallel to the axial direction of the rod workpiece. The 4-node, 12-degree-of-freedom tetrahedral finite element was used to model the workpiece and tool. The whole model includes approximately 100,000 nodes. The top and back surfaces of the tool are fixed in all directions. The workpiece is constrained in vertical (Z) and lateral (Y) directions on the bottom surface and moves at the cutting speed in the horizontal direction (–X) toward the stationary tool.

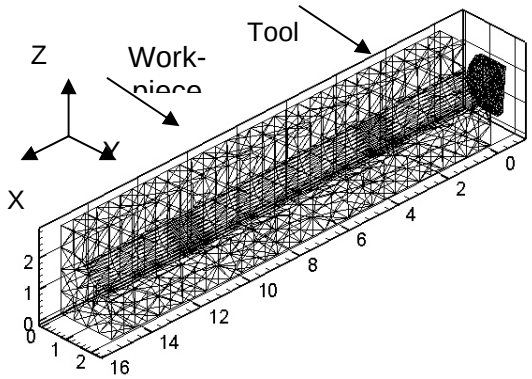

Figure 1. Initial finite element mesh for 3D turning model (unit: mm).

To validate the FEM, a baseline cutting test with four cutting speeds (24.4, 48.8, 97.5, and 195 m/min) and two feeds (0.254 and 0.381 mm/rev) was conducted at 1.02 mm depth of cut. Cutting forces were measured and compared with 3D finite element simulation results. One additional experiment was performed at a small depth of cut (0.254 mm) with a 48.8 m/min cutting speed and 0.254 mm/rev feed. All cutting tests were conducted dry without using cool-

ant. Nine simulations were conducted with the process parameters matched to those of the cutting experiments. The initial temperature was 20ºC.

Tool Wear Test

In the tool wear test, a tool insert was used to cut the Ti for an extended period of time to investigate the wear mechanism. Table 1 lists the corner radius and coating used in tool inserts for the wear test.

Table 1. Inserts and feed used for tool wear test (195 m/min cutting speed and 1.02 mm depth of cut)

Type[a]	TPG322	TPG320
Corner radius (mm)	0.8	0.1
Coating	No coating TiB_2	TiAlN TiB_2
Feed (mm/rev)	0.254	0.0508

[a]Kennametal tool number

The tool with a small, 0.1-mm corner radius was tested with a 0.254 mm/rev feed. The tip fractured prematurely. A smaller feed (0.0508 mm/rev) was therefore used for the tools with a 0.1-mm corner radius.

The flank wear was measured using an optical microscope. The width of flank wear land was recorded. The crater wear was measured using a laser profilometry (Rodenstock RM 600). The 3D surface topography of the tool rake face was recorded, and the volume loss on the tool rake surface was calculated.

Results

Experimental Validation of Cutting Forces

Figure 2 shows the comparison between the FEM (open symbol) and experimental measured (solid symbol) tangential, radial, and axial forces. For the tangential forces F_t, the finite element method generally underestimated by less than 15% with less discrepancy at high cutting speeds. For the radial and axial forces (F_r and F_a), the discrepancy was

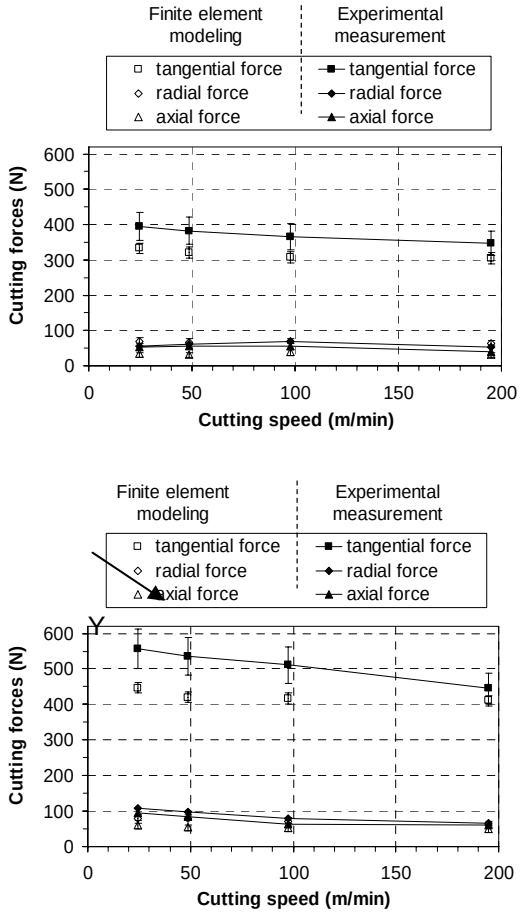

Figure 2. Comparison of cutting forces: (a) 0.254 and (b) 0.381 mm/rev feed.

less than 10% between the finite element simulation and experimental measurement results.

Although some discrepancies exist, the cutting force measurements validate the FEM results and set the direction for further refinement to improve the accuracy in modeling. The feed has a significant effect on the cutting force. At a high cutting speed, cutting forces were reduced slightly.

Cutting Speed Effects

Tool temperature is a key factor that accelerates tool wear and limits the cutting speed and productivity in Ti machining. Experimental measurement of tool temperature is difficult. However, a finite element simulation can provide a quick and accurate prediction of the tool temperature under various cutting conditions. The effect of cutting speed on tool temperature was investigated.

An example of the tool and workpiece temperature distributions of the nine 3D finite element cutting simulations is shown in Figure 3. The process parameters for the selected example are 195 m/min cutting speed, 0.254 mm/rev feed, 1.02 mm depth of cut, and 6.35 μm tool edge radius. The chip curl and the engagement of the tool and workpiece are shown in Figure 3(a). Figure 3(b) shows the tool temperature distribution. The high temperature is concentrated around the straight major cutting edge and the round corner of the tool. The peak temperature is about 480°C.

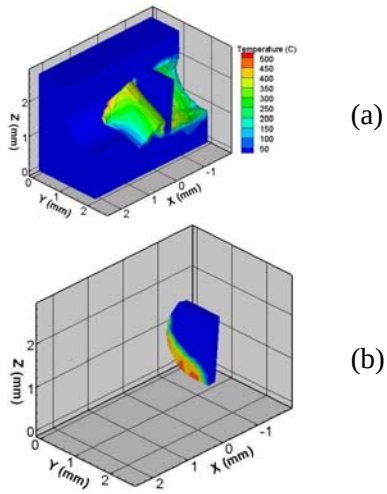

Figure 3. Temperature distributions: (a) workpiece and chip and (b) tool.

Figure 4 shows the peak temperature on the tool rake face of the eight baseline cutting experiments at two feeds and four cutting speeds.

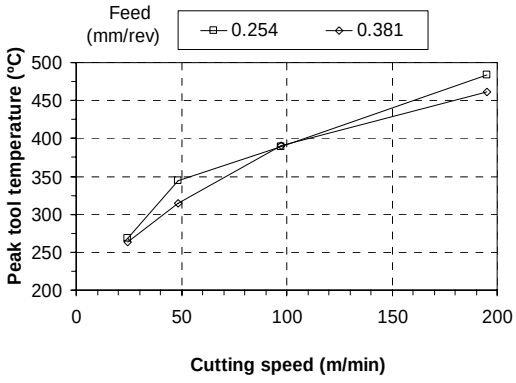

Figure 4. Peak tool temperature as a function of cutting speed.

The peak tool temperature is independent of the feed. This is comprehensible, since the very sharp tool cutting edge radius (6.35 μm) was used. The peak tool temperature increased significantly from about 260°C at a 24.4 m/min cutting speed to 480°C at 195 m/min. This demonstrates the effect of high-speed machining on tool temperature.

Chip Curl

This study explores the use of 3D FEM to predict the chip curl in turning. Figure 5(a) shows an experimental picture of the chip curl in machining of CP Ti with a 0.254-mm depth of cut, 48.8 m/min cutting speed, 0.254 mm/rev feed, and 0.8-mm tool corner radius. The change in cutting speed along the chip thickness is only 1.6%. The small change in cutting velocity across the chip thickness results in the up-curl dominated pattern. The effect of side-curl can also be seen to create the pitch of the curled chip. The tubular type helix chip is formed by rotational and translational motion along an axis parallel to the tool rake face.

The finite element method is applied to simulate cutting using the right-handed tool. Figure 5(b) shows a close-up view of a curled chip 15.2 mm in length in a 3D finite element simulation. Qualitatively, the morphology of the chip curl obtained from experimentation (Figure 5(a)) and FEM (Figure 5(b)) shows a similar pattern. The chip flow directions also match each other in FEM and experimental observation.

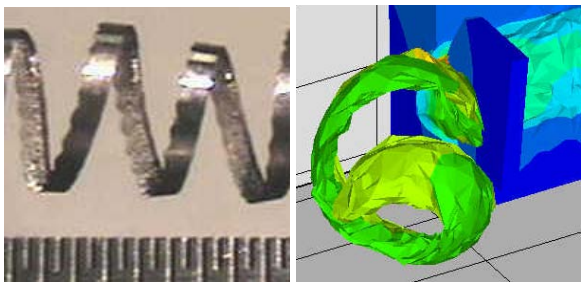

Figure 5. Chip curl with 0.254-mm depth of cut: (a) tubular chip in the experiment and (b) close-up view of the curled chip in simulation.

However, the finite element method underpredicts the radius and pitch of the chip curl by about 50%. One possible cause for this discrepancy is the contact of the chip with the tool, tool holder, and/or workpiece during cutting. Another possible cause is the external force acting on the chip from the weight of the chip after cutting. Since chip formation is con-

tinuous, the chip is pulled by its own weight to make a larger radius and pitch on the curled chip.

Tool Wear Test

Figure 6 shows the tangential forces (F_t) and the maximum width of flank wear land of the tool inserts.

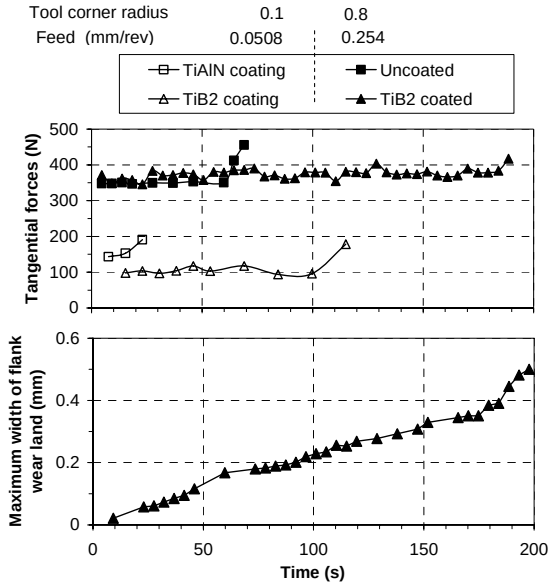

Figure 6. Tangential forces and the maximum width of flank wear land in Ti turning.

The tool life was determined at the time when the sharp increase in cutting forces occurred. For tools with a 0.8-mm corner radius, the life of uncoated and TiB_2-oated tools was 69 and 199 s, respectively. For tools with a 0.1-mm corner radius, the life of the TiAlN and TiB_2-coated tools was 15 and 115 s, respectively. TiAlN is a new type of coating, developed by Kennametal for interrupted cutting of Ti. It was not successful in the continuous turning of CP Ti. The flank wear of a TiB_2-coated tool with a 0.8-mm corner radius was measured by an optical microscope. A gradual increase in the maximum width of flank wear land can be seen in Figure 6. For the uncoated tool and tools with a 0.1-mm corner radius, because the tools were severely blurred with build-up material, no obvious flank wear could be observed.

Laser profilometry was applied to measure the crater wear. Figure 7 shows the SEM micrograph and the corresponding 3D laser profilometry measurement of the crater wear on the rake face of the TiB_2-coated tool with a 0.8-mm corner radius. The shape of crater wear can be observed. From the 3D contour shape of wear land, the volume of crater wear is calculated.

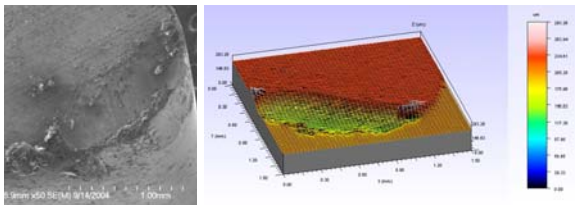

Figure 7. Crater wear of worn TiB_2-coated tool insert with 0.8-mm corner radius: (a) SEM micrograph and (b) 3D laser profilometry image.

Laser profilometry can also be used to quantitatively measure the shape of the build-up edge at the tool tip. Examples of the TiAlN and TiB_2-coated tool with a 0.1-mm corner radius are shown in Figure 8. The TiAlN obviously had a larger build-up edge, which resulted in the premature failure of the tool and the increase in the cutting force in Figure 6.

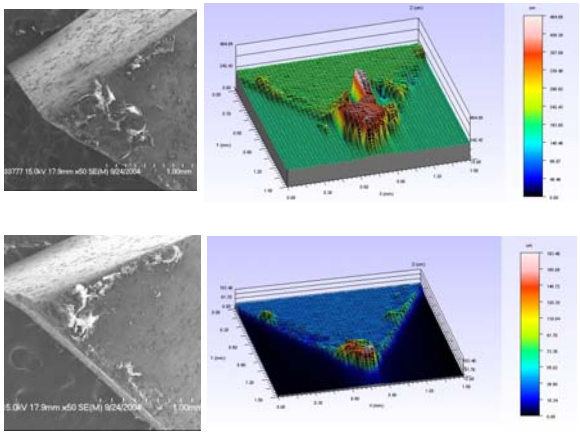

Figure 8. SEM micrograph and 3D laser profilometry image of the build-up edge at the tip of tool inserts with 0.1-mm corner radius: (a) TiAlN coated and (b) TiB_2 coated.

The friction coefficient of two types of tool coating was investigated. By dividing the cutting forces into the force components normal and parallel to the rake face, the coefficient of friction, μ, can be calculated by the following equations with 0° lead angle.

$$P = \sqrt{(F_t \sin\alpha + F_a \cos\alpha)^2 + F_r^2} \quad (1)$$

$$N = F_t \cos\alpha - F_a \sin\alpha \quad (2)$$

$$\mu = \frac{P}{N} \quad (3)$$

where

P is the force parallel to the rake face,
N is the force normal to the rake face,
α is the tool rake angle.

The coefficient of friction of a TiAlN-coated tool with a 0.1-mm corner radius was about 0.84, which was larger than the coefficient fractions of 0.52 and 0.34 of the TiB_2-coated tool with 0.1- and 0.8-mm corner radii, respectively.

Drilling

Drilling modeling is more complex than turning modeling. 3D drilling modeling is ongoing in close cooperation with Third Wave Systems. Figure 9 shows the preliminary result provided by Third Wave Systems. The chip was generated by drilling Al-6061 using a 9.35-mm-diameter WC-Co drill at 1.5 mm/rev feed and 40,000 rpm. The drill has a 30° helix angle, a 118° point angle, a 130° chisel edge angle, and a 2-mm web thickness. The modeling of Ti drilling is currently under development.

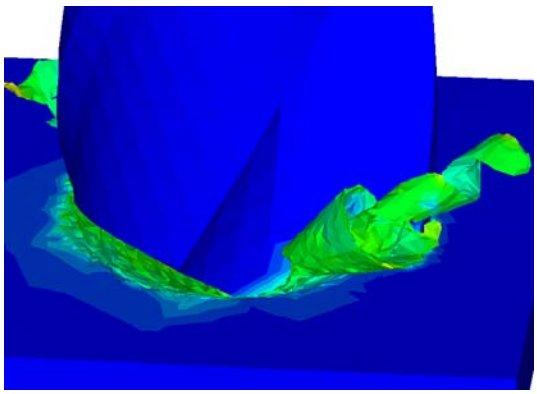

Figure 9. FEM of 3D drilling with chip generation.

Conclusions

The 3D finite element simulation of turning CP Ti was validated by comparing cutting forces with reasonable agreement. The effect of cutting speed on peak tool temperature was investigated. The application of finite element simulation to study the chip curl was explored. Qualitative agreement on the type of chip curl and chip flow direction were achieved for turning with a small depth of cut. The feasibility of using the finite element method to model the complicated 3D machining processes was demonstrated. The tool wear test demonstrated that a large tool corner radius and TiB_2 tool coating are more favorable to tool life than a small corner radius and TiAlN coating.

References

1. B. E. Hurless and F.H. Froes, "Lowering the Cost of Titanium," *The AMPTIAC Quarterly* **6**(2), 3–9 (2002).

2. E. H. Kraft, *Summary of Emerging Titanium Cost Reduction Technologies*, ORNL/Sub/4000023694/1, Oak Ridge National Laboratory, December 2003.

3. X. Yang, C. R. Liu, "Machining Titanium and Its Alloys," *Machining Science and Technology* **3**(1), 107–139 (1999).

4. K. F. Ehmann, S. G. Kapoor, R. E. Devor, I. Lazoglu, "Machining Process Modeling: A Review," *Journal of Manufacturing Science and Engineering* **119**, 655–663 (1997).

5. D. A. Stephenson and J. S. Agapiou, *Metal Cutting Theory and Practice*, Marcel Dekker, 1996.

6. T. D. Marusich, M. Ortiz, "Modeling and Simulation of High-Speed Machining," *International Journal for Numerical Methods in Engineering* **38**(21), 3675–3694 (1995).

7. A. J. Shih, "Finite Element Simulation of Orthogonal Metal Cutting," *ASME Journal of Engineering for Industry* **117**, 84–93 (1995).

Publications/Presentations

R. Li and A.J. Shih, "Finite Element Modeling of 3D Turning of Titanium," presented at the 2004 ASME IMECE, Anaheim, California, November 2004.

R. Li and A. J. Shih, "Finite Element Modeling of 3D Turning of Titanium," accepted for publication in *International Journal of Advanced Manufacturing Technology*.

I. Advanced Cast Austenitic Stainless Steels for High-Temperature Components

P. J. Maziasz, J. P. Shingledecker, N. D. Evans
Metals and Ceramics Division
Oak Ridge National Laboratory
P.O. Box 2008, MS-6115
Oak Ridge, TN 37831-6115
(865) 574-5082; fax: (865) 754-7659; e-mail: maziaszpj@ornl.gov

M. J. Pollard
Advanced Materials Technology
Caterpillar Technical Center
14009 Old Galena Rd.
Mossville, IL 61552
(309) 578-6133; fax: (309) 578-2953; e-mail: pollard_michael_j@cat.com

DOE Technology Development Manager: Dr. Sidney Diamond
(202) 586-8032; fax: (202) 586-1600; e-mail: sid.diamond@ee.doe.gov
ORNL Technical Advisor: D. Ray Johnson
(865) 576-6832; fax: (865) 574-6098; e-mail: johnsondr@ornl.gov

---

Contractor: Oak Ridge National Laboratory, Oak Ridge, Tennessee
Prime Contract No: DE-AC05-00OR22725
Subcontractor: Caterpillar Inc., Mossville, Illinois

Objectives

- Continue and expand commercial scale-up of new CF8C-Plus cast austenitic stainless steel.
- Establish a more complete database for tensile creep and fatigue properties.
- Determine resistance to aging, fatigue, and thermal fatigue to enable redesign or prototype casting trials of stainless diesel exhaust components.

Approach

- Produce 500-lb air-melt heats of static and centrifugally cast CF8C-Plus at MetalTek International or other stainless steel foundries.
- Obtain a more complete tensile and fatigue properties database on CF8C-Plus at Caterpillar.
- Determine improvements in resistance to thermal fatigue at Caterpillar and to creep at ORNL of CF8C-Plus relative to standard CF8C steel and other typical exhaust component alloys.
- Determine the most effective new alloying additions to CF8C-Plus to maximize strength above 800°C and then down-select an alloy for commercial scale-up.

Accomplishments

- Received a 2003 R&D 100 Award for CF8C-Plus cast stainless steel.
- Selected CF8C-Plus for further commercial scale-up based on superior aging, fatigue and thermal resistance at up to 850°C compared with CN-12 or CN-12-Plus.

- Produced new commercial static and centrifugally cast smaller heats of CF8C-Plus and a larger heat for a prototype component trial for a different application.

Future Direction

- Characterize microstructural changes after selected high temperature testing or aging; complete initial aging and expand aging to new alloys and impact properties evaluation.
- Evaluate the effects of different commercial-scale casting processes on properties of CF8C-Plus steel.
- Complete alloy modification studies of CF8C-Plus to boost strength above 800°C, and commercially scale-up and test the most promising new heat.

Introduction

Advanced heavy truck diesel engines must continue to have higher fuel efficiency, as well as reduced exhaust emissions, without sacrificing durability and reliability. More demanding normal duty cycles require exhaust manifolds and turbocharger housing materials to withstand temperatures ranging from 70°C to above 750°C. Such materials must withstand both prolonged, steady high-temperature exposure and rapid and severe thermal cycling. New emissions reduction technology and transient power excursions can push temperatures in these critical components even higher.

Current diesel exhaust components are generally made from SiMo ductile cast iron, and higher engine temperatures push such materials well beyond their current strength and corrosion limits. The first Oak Ridge National Laboratory (ORNL)/Caterpillar (CAT) cooperative research and development agreement (CRADA) produced systematic data comparing a heat-resistant cast CN12 stainless steel with SiMo cast iron for more demanding diesel exhaust component applications. It clearly identified the tensile, creep, and fatigue strength advantages of standard CN12 stainless steel at 550–700°C and above. That first CRADA project also developed new lab-scale heats of modified CN12 and modified CF8C steels with better creep strength and significantly better aging resistance and thermal fatigue resistance than standard CN12. A second ORNL/CAT CRADA project began several years ago for commercial scale-up of these new modified cast stainless steel heats, and for development of a more systematic and thorough database required by designers to redesign stainless components and qualify them for trial component production. In 2003, the initial commercial scale-up data demonstrated clear advantages of the new CF8C-Plus cast steel relative to the other alloys for exhaust components and other applications, and this work won a 2003 R&D 100 Award. In 2004, commercial scale-up focused on the new CF8C-Plus cast stainless steel and expanded to include more commercial heats, several different casting processes (static sand-casting, centrifugal casting), and alloying modifications to increase maximum strength at the highest temperatures.

Approach

Two commercial stainless steel foundries initially produced 500-lb heats of CN12-Plus and CF8C-Plus steels for testing and evaluation compared with similar standard steels. One of those commercial foundries produced additional new static-cast and centrifugally-cast heats of CF8C-Plus. Caterpillar Technical Center obtained tensile, fatigue, and thermal-fatigue data on these new heats of CF8C-Plus steel, while ORNL obtained initial creep-rupture data and aged specimens for various times at 700–850°C. ORNL also cast a new set of lab-scale heats to explore the effects of adding Al, B, Cu, and W to CF8C-Plus to maximize strength and creep resistance at 800–850°C. Results of the testing will be used to expand commercial scale-up of CF8C-Plus and then to down-select a heat of the new modified CF8C-Plus for commercial scale-up.

Technical Progress

Tensile, fatigue, and thermal fatigue testing on the initial commercial heats of CF8C-Plus and CN-12 Plus were completed earlier at Caterpillar. Tensile data clearly showed CF8C-Plus to be as strong as standard CN12 and CN-12-Plus cast steels and much more ductile, with no additional heat treatment required after casting. CF8C Plus has an "engineered microstructure," which includes a very

stable austenite parent matrix phase that is free of the δ-ferrite typically found in standard cast CF8C. The creep strength of CF8C-Plus at high temperatures comes from nano-scale dispersions of NbC precipitates that form and remain stable and are much finer than those found in standard CF8C steel. Because CF8C-Plus has no δ-ferrite, it is also free of σ-phase relative to standard CF8C during aging or creep at 650–850°C.

Creep rupture stress versus rupture life, expressed as the Larson Miller Parameter (LMP), for standard CF8C and CF8C-Plus tested at 750–850°C is plotted in Figure 1, together with data from high-SiMo and Ni-resist cast irons tested at lower temperatures. Clearly the CF8C-Plus cast stainless steel has about twice the creep strength of standard CF8C steel, and both are much stronger than either high-SiMo or Ni-resist cast irons. Figure 2 shows the significant advantage the CF8C-Plus alloy has in low-cycle fatigue resistance compared with standard CN-12 steel at 800°C, which was a factor in choosing CF8C-Plus for further commercial scale-up for diesel exhaust component applications. The fatigue behavior of cast CF8C-Plus with a very coarse as-cast grain structure also compares well with wrought-type 348 stainless steel (similar alloy composition) with a much finer grain size. CF8C-Plus was deliberately designed to have a combination of good strength and ductility at both higher and lower temperatures, in order to achieve its best fatigue and thermal fatigue resistance. Thermal-mechanical fatigue (TMF) testing of these initial commercial heats was completed this year, together with aging of various specimens. There was a significant advantage for CF8C-Plus relative to CN-12 or high-SiMo cast iron in TMF testing to 760°C or higher, and data will be shown next quarter.

Additional lab heats of CF8C-Plus were cast at ORNL to define the effects of other minor alloying additions, including B, Al, Cu and W additions, and establish their limits for commercial heats. Creep-rupture test screening at 750–850°C showed that copper and tungsten were most effective at improving creep resistance, as shown for creep testing at 750°C in Figure 3. Based on these data, a modified CF8C-Plus with copper and tungsten additions was selected for the next step of commercial scale-up and testing.

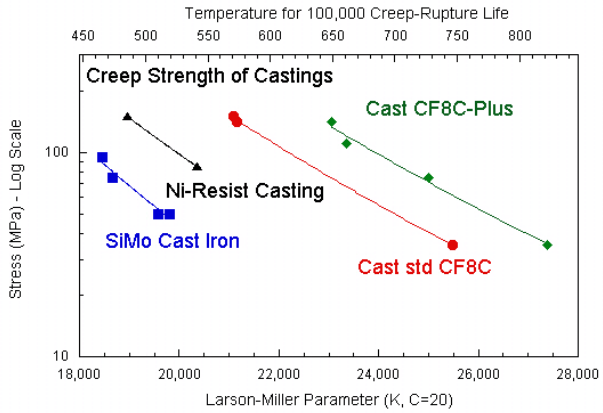

Figure 1. Larson Miller parameter plot of creep rupture stress for high-SiMo and Ni-resist cast irons, standard CF8C, and the new CF8C-Plus cast stainless steels tested in air at various temperatures.

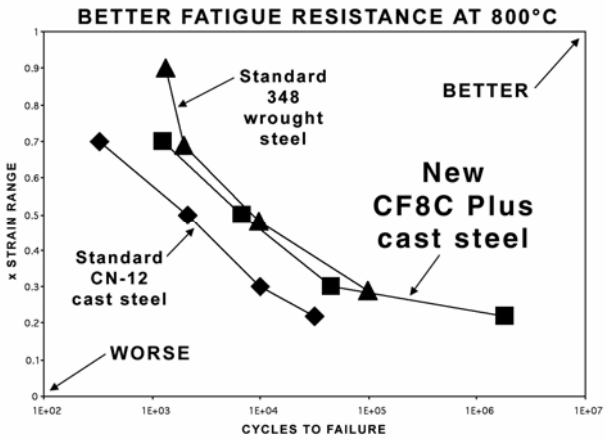

Figure 2. Isothermal strain-controlled fatigue data versus cycles to failure in air at 800°C, for commercial scale-up heats of standard CN-12, CN-12-Plus, and CF8C-Plus cast stainless steels.

Finally, this year, MetalTek International produced additional static sand-cast and centrifugally-cast heats of CF8C-Plus for testing at Caterpillar and ORNL. That testing began this year and will be completed next year. MetalTek International has also produced several heats of a new CF8C-Plus with copper and tungsten additions, selected from the ORNL lab-scale heat data on alloy modifications, and testing will begin next year.

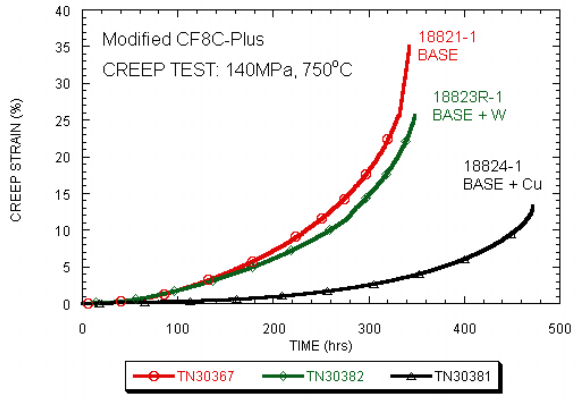

Figure 3. Creep-rupture testing in air at 750°C and 140 MPa of new ORNL lab heats of baseline CF8C-Plus steel and the same steel with additions of copper or tungsten.

Conclusions

ORNL and Caterpillar have chosen CF8C-Plus cast stainless steel as the focus for further scale-up and development, based on the initial commercial scale-up results of CN-12-Plus and CF8C-Plus. The development of CF8C-Plus was recognized with a 2003 R&D100 Award. Several static-cast and centrifugally-cast heats of CF8C-Plus were produced by MetalTek International for further testing for diesel engine exhaust component applications and other high-temperature structural component applications. Another set of ORNL lab-scale heats of CF8C-Plus were made to test the effects of minor alloying additions on improved creep resistance above 800°C, and copper and tungsten additions were found to be most effective. New commercial heats of CF8C-Plus and CF8C-Plus with copper and tungsten were produced by MetalTek this year and will be tested next year.

Publications/Presentations

P. J. Maziasz and M. J. Pollard, "High-Temperature Cast Stainless Steel," *Advanced Materials & Processes* (ASM-International), **161**, 57-59 (October 2003).

P. J. Maziasz, "Development of CF8C-Plus: A New Cast Austenitic Stainless Steel with Improved Heat-Resistance and Performance above 650°C," invited presentation at ASM Peoria Chapter Meeting, April 5, 2004.

M. J. Pollard, P. J. Maziasz, and J. P. Shingledecker, "Development of Low-Cost Cast Austenitic Stainless Steel for Diesel Engine and Gas Turbine Components," Project Review of DOE Programs at Caterpillar, April 2004.

P. J. Maziasz, J. P. Shingledecker, N. D. Evans and M. J. Pollard, "Advanced Cast Austenitic Stainless Steels for Diesel Engine and Gas Turbine Components," presentation at DOE FreedomCAR and Vehicle Technologies Program Review at ORNL, June 15, 2004.

Special Recognitions/Awards/Patents

ORNL and Caterpillar received a 2003 R&D 100 Award for "CF8C-Plus Cast Stainless Steel for High-Temperature Performance," presented at the R&D Awards Banquet in Chicago on October 16, 2003.

P. J. Maziasz, T. McGreevy, M. J. Pollard, C. W. Siebenaler, and R.W. Swindeman, "Heat and Corrosion Resistant Cast CN-12 Type Stainless Steels with Improved High Temperature Strength and Ductility," U.S. patent application 2003/0084967, filed July 15, 2002..

P. J. Maziasz, T. McGreevy, M. J. Pollard, C. W. Siebenaler, and R.W. Swindeman, "Heat and Corrosion Resistant Cast CF8C Stainless Steels with Improved High Temperature Strength and Ductility," U.S. patent application 2003/0056860, filed July 15, 2002.

J. Interfacial Control of Deformation Twinning in Creep-Deformed $TiAl/Ti_3Al$ Nanolaminate

Luke Hsiung
Chemistry and Materials Science Directorate
Lawrence Livermore National Laboratory
L-352, P.O. Box 808
Livermore, CA 9455-9900
(925) 424-3125; fax: (925) 424-3815; e-mail: hsiung1@llnl.gov

DOE Technology Development Area Specialist: Dr. Sidney Diamond
(202) 586-8032; fax: (202) 586-1600; e-mail: sid.diamond@ee.doe.gov
ORNL Technical Advisor: D. Ray Johnson
(805) 576-6832; fax: (865)574-6098; e-mail: johnsondr@ornl.gov

---

Contractor: Oak Ridge National Laboratory, Oak Ridge, Tennessee
Prime Contract No: DE-AC05-00OR22725
Subcontractor: Lawrence Livermore National Laboratory, Livermore, California

---

Objectives

- Exploit thermomechanical-processing techniques to fabricate $TiAl/Ti_3Al$ nanolaminate composites at sizes from lamella width down to nanometer-length-scales.
- Characterize the microstructure and elevated-temperature creep resistance of the nanolaminate composites.
- Investigate the fundamental relationships among microstructures, alloying additions, and mechanical properties of the nanolaminate composites to achieve the desired properties of the composites for high-temperature structural applications.

Approach

- Employ in-situ laminate composites with nominal compositions of Ti-47Al-2Cr-2Nb, Ti-46Al-3Nb-1W-0.1B, and Ti-46Al-3Nb-2W-0.1B (at. %).
- Conduct creep tests in a dead-load creep machine with a lever arm ratio of 16:1. Tests were performed in air in a split furnace with three zones at 760 and 815°C.
- Examine the microstructures of creep-deformed samples using a JEOL-200CX transmission electron microscope (TEM).

Accomplishments

- Collaborated with Oak Ridge National Laboratory (ORNL) (C.T. Liu) to fabricate $TiAl/Ti_3Al$ laminate composites with high tungsten content using hot-extrusion processing techniques.
- Characterized and measured the effect of tungsten addition on creep resistance of the $TiAl/Ti_3Al$ laminate composites.

Future Direction

- Continue to collaborate with ORNL to fabricate an oxidation- and heat-resistant class of $TiAl/Ti_3Al$ laminate composites with high niobium content (>10 at %) using the hot-extrusion processes.

- Continue to investigate the effects of alloying additions and deformation (mechanical) twinning on the microstructural stability and creep resistance of the nanolaminate composites at elevated temperatures of up to 850°C.

Introduction

One of the unique deformation substructures of TiAl/Ti_3Al laminate composite is the formation of deformation twins (DTs) within γ lamellae. The twinning phenomena have been found to be significantly promoted within ultrafine lamellar TiAl as a result of refined lamellar spacing presumably because the increment of lamellar interfaces provides even more nucleation sites for twinning. Although it has been well known that deformation twinning can be activated by the homogeneous glide of *1/6*$<11\bar{2}>$ twinning dislocations on the {111} planes, the underlying twinning mechanism still remains unclear. To better design lamellar alloys for high-temperature applications, it is important to understand and gain insights regarding the role of lamellar interfaces in the twinning process, as well as the mechanical behavior of the alloys. Accordingly, this investigation was conducted to elucidate the deformation twinning mechanisms in TiAl/Ti_3Al nanolaminate.

Approach

A TiAl/Ti_3Al nanolaminate composite was fabricated at ORNL by a hot extrusion process, which involves hot-extrusion of a cast TiAl alloy at 1350°C. After extrusion, the alloy was stress-relieved at 900°C in a vacuum (~ 10^{-4} Pa) for 2 h. Creep tests were conducted in a dead-load creep machine with a lever arm ratio of 16:1. For the current study, the deformation substructures of the specimen were investigated [tested at 760°C, 138 MPa (creep strain: 0.25%); 760°C, 518 MPa (creep strain: 3.6%); and 815°C, 420 MPa (creep strain: 1.7%)]. TEM foils were prepared by twinjet electropolishing in a solution of 60 vol % methanol, 35 vol % butyl alcohol, and 5 vol % perchloric acid at ~15 V and –30°C. The microstructures of the tested samples were examined using a JEOL-200CX TEM equipped with a double-tilt goniometer stage. Images of dislocations were mostly recorded using weak–beam dark field (WBDF) imaging techniques under *g (3g)* two–beam diffraction conditions with the deviation factor $\omega\,(=\xi_g\, s) > \sim 1$, where ξ_g is the extinction distance and *s* is the deviation distance from the exact Bragg position. The $g\bullet b$ invisibility criteria used for determining the Burgers vector of Shockley partials are described as follows:[1] (a) invisible if $g\bullet b = 0$ or ±1/3; (b) invisible if $g\bullet b = -2/3$ but visible if $g\bullet b = +2/3$ provided the deviation factor $\omega > \sim 1$; (c) invisible if $g\bullet b = +4/3$ but visible if $g\bullet b = -4/3$ provided the deviation factor $\omega > \sim 1$.

Results

Microstructure

Figure 1 is a bright-field TEM image showing a typical edge-on microstructure within a TiAl (γ)-Ti_3Al (α_2) nanolaminate. In general, the material contains two types of interfaces:[2]

1. The γ/α_2 interphase interface, which has a usual orientation relationship $(0001)_{\alpha 2} \parallel (111)_{\gamma}$ and $<11\bar{2}0>_{\alpha 2} \parallel <1\bar{1}0>_{\gamma}$.

2. The γ/γ twin-related interface, which includes true-twin (180° rotational) and pseudo–twin (60 and/or 120°rotational) interfaces.

Here, the width of the α_2 layers ranges from 10 to 50 nm, and the width of the γ layers ranges from 150 to 300 nm. Figure 2 is a WBDF TEM image showing a typical dislocation substructure within the nanolaminate. Both lattice dislocations (LDs) within the γ layer and a high density of interfacial dislocations (IDs) on inclined interfaces can be clearly seen. The density of the IDs is much greater than that of the LDs, and the LDs are primarily threading dislocations, which terminate their two ends at the interfaces. While the IDs on semi-coherent γ/α_2 and γ/γ pseudo-twin interfaces are 1/6<112> or 1/3<112> type misfit dislocations,[3] those on the γ/γ true-twin interface are mainly *1/6*$[11\bar{2}]$ type twinning dislocations or geometry necessary dislocations for accommodating the departure of the true-twin interface from the exact (111) twin plane.

Deformation Twinning and Proposed Mechanisms

When the nanolaminate was creep-deformed at 760°C and 518 MPa, a deformation substructure

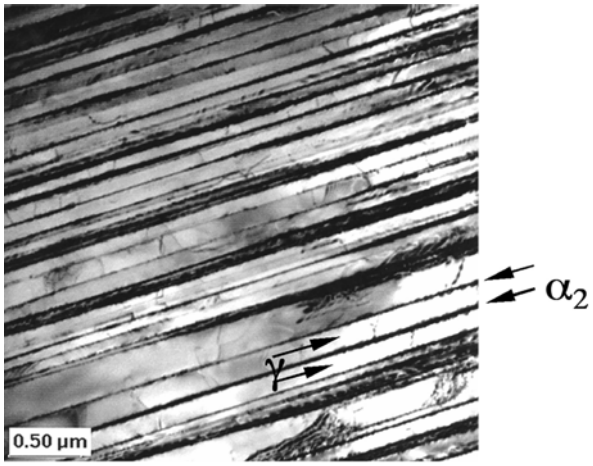

Figure 1. Bright-field TEM image showing a lamellar grain from an edge-on orientation.

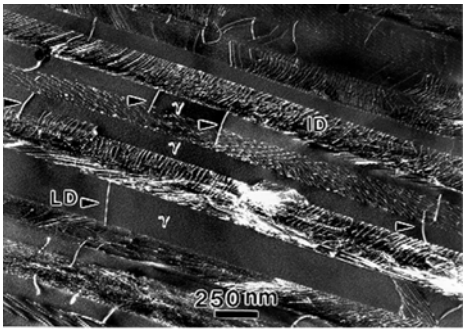

Figure 2. Weak-beam dark-field TEM image showing a typical dislocation structure of TiAl nanolaminate.

associated with DTs within γ layers was developed. Typical examples of the formation of $(\bar{1}11)$ [211]-type DTs within the nanolaminate are shown in Figures 3 (a) and (b). Note that one of the twin lamellae was still growing between two lamellar interfaces, and its growth would be eventually blocked by the lower interface. This observation suggests that the interfaces are preferred nucleation sites for DTs, presumably resulting from the high local stresses caused by the pileup of interface dislocations. Accordingly, it is proposed that deformation twinning in the TiAl-Ti_3Al nanolaminate can be viewed as a stress relaxation process to relief the local stress concentration caused by the pile-up of interfacial dislocations during deformation. The effective stress (τ_e) at the tip of the pile-up of *n* dislocations can be evaluated by $\tau_e = n\tau_i$ [4], where τ_i is the resolved shear stress acting on the interface. To relieve the stress concentration, deformation twinning in γ layers is therefore taking place by a dislocation reaction

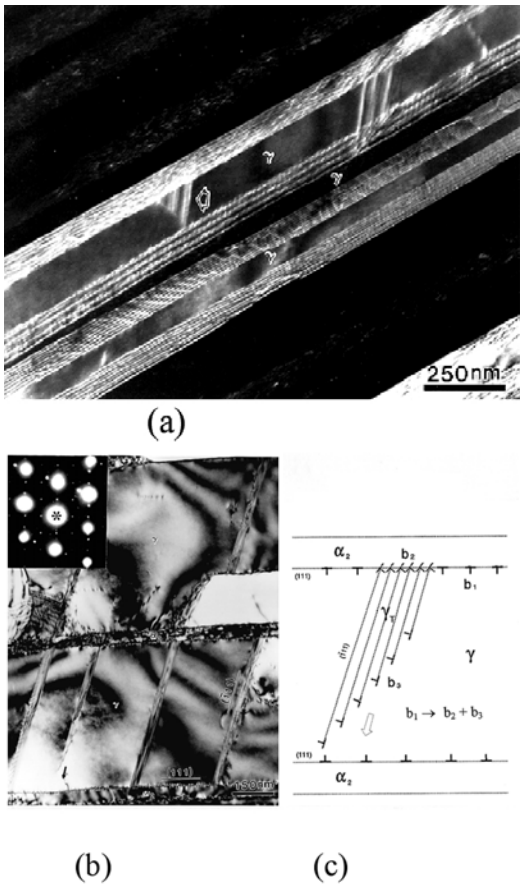

Figure 3. Dark-field (a) and bright-field (b) TEM images showing several $(\bar{1}11)$ type deformation twins formed a growing process toward another interface. Schematic illustration (c) of the nucleation of a $(\bar{1}11)$ type *DT* from a γ/α_2 interface, where b_1, b_2, and b_3 denote the interfacial, stair-rod, and twinning dislocations, respectively.

based upon a stair-rod cross-slip mechanism.[5,6] As for an example of the $(\bar{1}11)$-type DTs formed in the nanolaminate, the corresponding dislocation reaction (dissociation) is proposed to be $1/6[\bar{1}2\bar{1}]_{(111)} \rightarrow 1/6[011]_{(100)} + 1/6[\bar{1}1\bar{2}]_{(\bar{1}\,\bar{1}1)}$. The $(\bar{1}11)$-type DT is accordingly formed by a successive cross-slip of the twinning dislocations $1/6[1\bar{1}2]$ on the $(\bar{1}11)$ plane. leaving the stair-rod dislocations $1/6[011]$ on the (100) plane. Twin (stacking) faults are subsequently formed on the interfaces between the γ layer and the DTs. This is schematically illustrated in Figure 3 (c).

The formation of stair-rod dislocations at the intersections between the DTs and the α_2 layer is evi-

denced in Figure 4, where the array of *1/6*[011] stair-rod dislocations become invisible [Figure 4(a)] or visible [Figure 4(b)] when a reflection vector (***g***) *200* or *021* is used for imaging. It is noted that the individual stair-rod dislocation is not resolvable because of a narrow distance (0.25 nm) between two stair-rod dislocations. The significance of the proposed mechanism is to reveal that there are several barriers to be overcome in order to activate the twinning reaction. These barriers include (1) the repulsive force (*F*) between the interfacial (Shockley) and stair-rod dislocations, (2) the increase of line energy due to the dislocation dissociation, and (3) the increase of interfacial energy due to the formation of twin faults. Among them the repulsive force (*F*) between the interfacial (Shockley) and stair-rod dislocations is considered to be rate-controlling. That is, a critical (minimum) stress (τ_C) is required to activate the dissociation reaction for twinning.

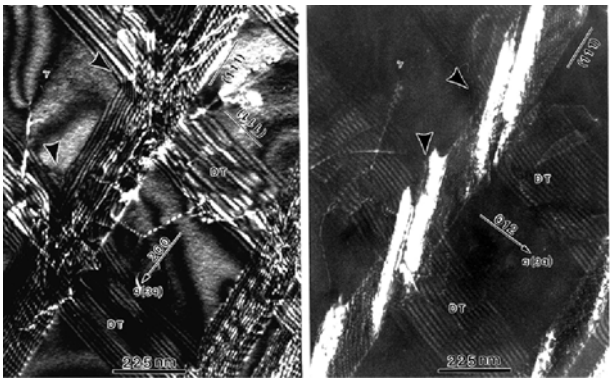

Figure 4. Paired WBDF images demonstrating the existence of the array of *1/6*[011] stair-rod dislocations at the intersections (indicated by arrows) between the $(\bar{1}11)$-type *DT* and α_2 layer: (a) Invisible at *g = 200 (g•b = 0)*, (b) visible at *g = 021*, Z (zone axis) ≈ $[0\bar{1}2]$.

Conclusion

The role of interfaces in deformation twinning of $TiAl/Ti_3Al$ nanolaminate has been investigated. Since the multiplication of lattice dislocations within both γ and α_2 lamellae becomes very limited at a low stress level, the motion of interfacial dislocations (i.e., interface sliding) becomes an important deformation mode. Impinged lattice dislocations were observed to impede the movement of interfacial dislocations, which move in a cooperative fashion along the lamellar interfaces. The impediment of dislocation motion subsequently causes a dislocation pile-up in front of the obstacle as creep strain accumulates. When the laminate deforms at a high stress level, deformation twinning becomes a predominant deformation mode. The deformation twinning is suggested to be a stress relaxation process for the concentration of stress at the head of each dislocation pile-up. An interface-controlled twinning mechanism based upon a stair-rod cross-slip dislocation reaction is proposed and verified.

References

1. J. W. Edington, *Practical Electron Microscopy in Materials Science*, Van Nostrand Reinhold, New York, 1976.

2. M. Yamaguchi and Y. Umakoshi, *Progress in Materials Science* **34**, 1 (1990).

3. L. M. Hsiung and T.G. Nieh, *Mater. Sci. & Eng*. **A239–240**, 438 (1997).

4. J. D. Eshelby, F. C. Frank and F. R. N. Nabarro, *Phil. Mag*. **42**, 351 (1951).

5. Fujita and T. Mori, *Scripta Metall*. **9**, 631 (1975).

6. T. Mori and H. Fujita, *Acta Metall*. **28**, 771 (1980).

Publications/Presentations

1. L. Hsiung, "Interface Sliding and Migration in an Ultrafine Lamellar Structure," invited keynote presentation to the International Conference on Computational and Experimental Engineering & Sciences, Madeira, Portugal, July 28, 2004.

2. Andrea M. Hodge, L. Hsiung, T. G. Nieh, "Creep of Nearly Lamellar TiAl Alloys Containing 1.0 and 2.0 at % W," presented at Materials Science and Technology 2004, September 27, 2004.

3. L. M. Hsiung, T.G. Nieh, "Microstructures and Properties of Powder Metallurgy TiAl Alloys," *Mater. Sci. & Eng*. **A364**, 1 (2004).

4. A. Hodge, L. M. Hsiung, T. G. Nieh, "Creep of Nearly Lamellar TiAl Alloy Containing W," *Scripta Mater*. **51**, 411 (2004) .

5. Luke L. Hsiung and Clyde L. Briant, *Segregation of Tungsten to Interfaces in Lamellar TiAl* , Lawrence Livermore National Laboratory, April 6, 2004.

6. Luke L. Hsiung and Andrea M. Hodge, *Effects of W on Creep Deformation of Nearly Lamellar TiAl*, Lawrence Livermore National Laboratory, July 16, 2004

K. Laser Surface Texturing of Lubricated Ceramic Parts

Peter J. Blau and Jun Qu
Oak Ridge National Laboratory
P. O. Box 2008, Mail Stop 6063
Oak Ridge, TN 37831-6063
(865) 574-5377; fax: (865) 574-6918; e-mail: blaupj@ornl.gov

DOE Technology Development Area Specialist: Dr. Sidney Diamond
(202) 586-8032; fax: (202) 586-1600; e-mail: sid.diamond@ee.doe.gov
ORNL Technical Advisor: D. Ray Johnson
(865) 576-6832; fax: (865) 574-6098; e-mail: johnsondr@ornl.gov

---

Contractor: Oak Ridge National Laboratory, Oak Ridge, TN
Prime DOE Contract Number: DE-AC05-00OR22725

Objectives

- Determine the effectiveness of using regular patterns of micro-scale dimples produced by a laser to reduce the friction coefficient of lubricated surfaces of ceramics.
- Determine the extent to which the laser surface texturing (LST) process affects the structure of the ceramic materials to which the process is applied.

Approach

- Select the proper tests and analyses needed to reveal potential friction reduction benefits of dimpled ceramic surfaces for use in lubricated sliding contacts.
- Obtain transformation-toughened zirconia (TTZ) and silicon carbide ceramic materials, design and fabricate test specimens, and provide them to Surface Technologies, Ltd., for laser dimpling.
- Characterize the ceramic materials after LST, using a variety of techniques, including electron microscopy, nanoindentation, and scanning acoustic microscopy (SAcM).
- Conduct friction tests in lubricants with different viscosities to determine the extent to which the laser surface treatment can reduce friction. Compare results for reciprocating motion, like that in engine components, with results for unidirectional sliding, like that found in rotary bearings or seals.

Accomplishments

- Conducted reciprocating friction tests of LST ceramics in various lubricants, including diesel oil, mineral oil, and water to determine which frictional conditions benefit more from LST.
- Investigated the use of SAcM to identify near-surface micro-fractures due to the laser-induced thermal pulses used to form the dimples.
- Conducted transmission electron microscopy (TEM)of zirconia specimens and determined that a difference in crystal structure occurs in shallow zones affected by LST.
- Obtained nanohardness data on the thermally affected zones in the material below dimples.

- Established the sensitivity of LST effects to precise surface alignment, and the need for sufficiently high sliding velocity to detect frictional effects of the dimpled surfaces. In our experience, achieving friction reduction by LST in reciprocating sliding contacts requires taking extraordinary measures in alignment and apparatus design.
- Explored the effects of solid lubrication with graphite powder on the friction of LST zirconia surfaces under reciprocating motion. There was no apparent improvement due to dimpling.

Future Direction

- Summarize the results of this study in a final report.

Introduction

Improving the fuel efficiency of diesel engines, while still enabling them to meet requirements for emissions, presents both design and material challenges. Reducing parasitic frictional losses in engines can be achieved by a combination of strategies such as

- redesigning the engine components
- reformulating the lubricants
- improving methods of lubricant filtration and delivery
- reducing churning losses in fluids
- changing the operating conditions of the engine
- substituting more durable, low-friction materials
- altering the finish or microscale geometry of the bearing surfaces

This project specifically addresses the last approach by investigating the potential of a technique called LST (developed by I. Etsion of Surface Technologies Ltd., in Israel).

LST was successfully demonstrated by reducing the friction and wear of water pump seals in which the mating surfaces were wide and flat. Work by Japanese investigators on water-lubricated silicon carbide, dimpled by different methods, showed the importance of both dimple spacing and running-in on the extent to which dimpling was able to reduce the friction coefficient.[1]

Initial studies at Oak Ridge National Laboratory (ORNL) in FY 2002–2003 involved conducting reciprocating sliding friction tests with flat-sided (both dimpled and non-dimpled) cylindrical rods oscillating on a flat ceramic specimen. Water, mineral oil, and diesel oil were used as lubricants. By carefully analyzing the data, friction lowering effects of LST were seen. In FY 2003, microstructural characterization of laser-surface-processed ceramics continued, as did the friction experiments. It was eventually concluded that the benefits of LST for reciprocating, narrow contacts could be detected only for very precisely aligned surfaces, and even that was difficult. In fact, the difficulty of detecting LST effects without special experimental procedures was confirmed by a paper by Kato[2] in which more than a day of water-lubricated sliding was required to wear-in the surfaces of the ceramics sufficiently to reveal the frictional benefits of LST. Unspectacular test results on liquid-lubricated LST ceramics during FY 2003 prompted a change in approach for FY 2004.

During the past year, the focus was shifted from using liquid lubricants to filling the dimples with solid lubricants, in this case, graphite. The hypothesis to be tested was that LST-produced dimples in surfaces might help catch abrasive debris and at the same time re-supply solid lubricating material to both lower friction and extend the life of ceramic sliding surfaces. This annual report summarizes the experiments designed to explore the latter approach.

Approach

This project is being conducted in parallel with a complementary effort at Argonne National Laboratory (ANL) on LST metals and LST used in conjunction with coatings. ORNL efforts have focused on ceramic materials. The approach is two-pronged: (1) to conduct controlled reciprocating friction experiments on LST ceramics to evaluate the effects of both velocity and lubricant type on friction

and (2) to characterize the effects of LST on both the microstructure and the near-surface micro-mechanical properties of ceramics. To accomplish the latter, various techniques are being applied—for example, nano-indentation hardness and elastic modulus determination, SAcM, and TEM and scanning TEM (TEM). Results of acoustic microscopy and nanoindentation tests were described in the previous annual report. TEM images and diffraction patterns of the laser-affected zone at the dimple bottoms will be provided in the final report to be prepared during FY 2005. They show indications that the crystal structure of TTZ is affected at a nanometer scale in a thin region near the surface of the dimple.

Results

In FY 2004, experiments were conducted to test the hypotheses that dimples in LST surfaces could serve both as reservoirs to replenish worn-away lubricant and as traps for any harmful, abrasive debris that happened to enter the interface. A flat-on-flat reciprocating sliding configuration was used (see Figure 1). TTZ surfaces in three conditions, as-ground (non-dimpled), laser-dimpled, and dimpled and polished, slid against ground Gall-Tough™ stainless steel (upper specimen) in an ambient air environment. Pressure-indicating plastic film was used to help pre-align the two contact surfaces before each test. The nominal contact area of the sliding contact was 10 × 4 mm. A constant 10-N normal force, 2-Hz reciprocating frequency, and 10-mm stroke length were used. The lubricant was Dixon Ticonderoga 1651 graphite powder. A layer of graphite powder was distributed on the zirconia surface before each test, and no additional lubricant was supplied thereafter. The level of friction force was monitored using a high-speed data acquisition system. Worn surfaces were examined to assess their morphology and to study the distribution of graphite and debris created by prolonged sliding contact.

Results of the first graphite-lubricated test conducted on LST zirconia against Gall-Tough™ were promising. Without re-lubricating, the initially formed graphite lubricating film lasted nearly 90 hours before failure (see Figure 2a). At the beginning of the test, the graphite powder quickly formed a lubricating film under pressure from the

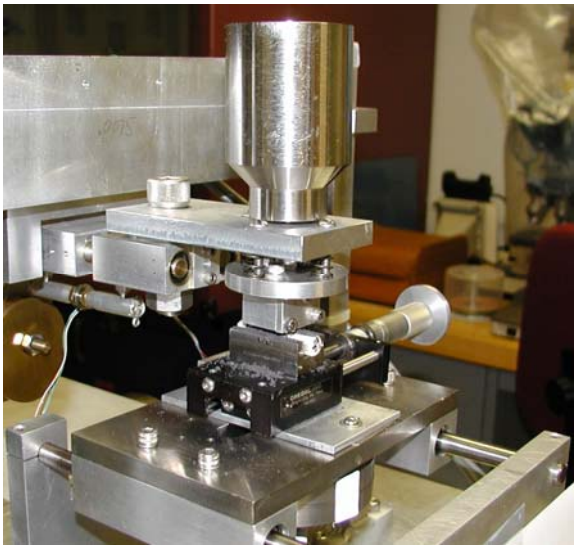

Figure 1. Flat-on-flat reciprocating sliding test setup showing the dead-weight load.

mating surfaces. Since the two sliding surfaces were fully separated by a compressed graphite film, the frictional response reflects the resistance to sliding from adhering graphite particles. Initially, the friction coefficient remained relatively low at ~0.15. However, since this was an open system that allowed particles to escape, the graphite particles were gradually wiped off and the film became progressively thinner. When the lubricating film began to fail, asperity contact occurred between the mating surfaces. In this second stage, the tangential force resulted from a combination of metal/ceramic asperity contacts and the shear of the incomplete graphite film. The friction coefficient in this stage therefore fluctuated more noticeably. Eventually the lubricating film collapsed, leading to large areas of steel-on-zirconia in nominally unlubricated contact. The friction coefficient quickly transitioned to a much higher level, 0.5–0.6 (i.e., stage 3 in Figure 2a). This final frictional transition was used as the criterion for lubrication failure.

The worn LST TTZ surface is shown in Figure 2b. Patches of wear debris, evidently containing both iron oxides and metallic particles, were observed. Many dimples were filled with wear debris, while others still retained some graphite powder. As hypothesized, the dimples acted both as reservoirs for the lubricant and as traps for wear debris.

Although the first test results seemed promising for solid lubricant-filled dimples, subsequent tests

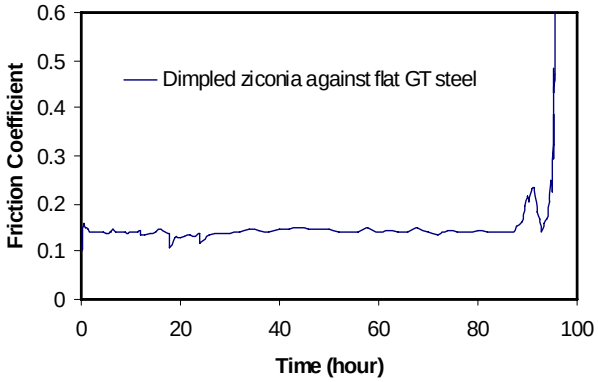

(a) Friction trace

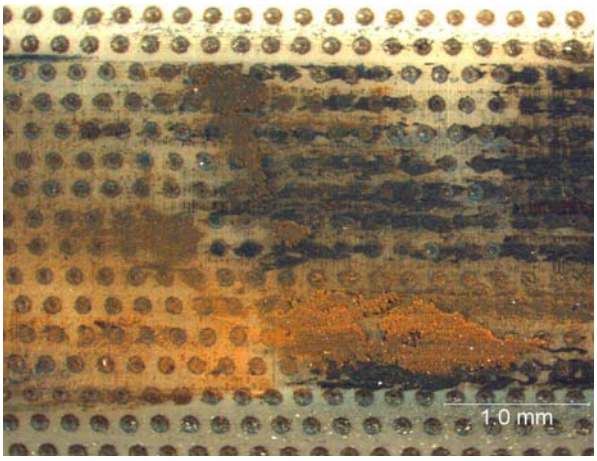

(b) Worn surface

Figure 2. Results for LST TTZ reciprocating against Gall-Tough™, a commercial stainless steel lubricated by graphite powder: (a) friction trace, (b) TTZ surface appearance (optical microscope image).

designed to verify the repeatability of frictional behavior gave inconsistent results. Frictional increases that suggested film failure occurred much earlier in the latter tests. A repetition of the first test failed after only 8 hours, compared with more than 85 hours for the first run. The two causes for this are alleged to be (1) slight variations in the initial alignment of the specimens and (2) an alignment change due to the effects of fixture vibration and loosening during sliding. These minute, but not insignificant, misalignments turned the relatively large, rectangular area of initial contact into a more concentrated line or point contact, which in turn caused the lubricating film to break through much more quickly. Considering the three stages of frictional behavior shown in Figure 2, initial alignment controls the length of the first sliding stage in which the friction is fairly low, the sliding is relatively smooth, and the vibration is minimal. When the lubricating film starts to fail and frictional behavior enters the second stage, the higher and more erratic level of friction induces more vibration. Higher vibration loosens the fixtures, changing the alignment and accelerating lubricant failure. After this behavior was observed, modifications were made to the equipment to eliminate vibration-induced misalignment. Tests were then rerun on both the dimpled and non-dimpled surfaces.

As shown in Figure 3, the lubricating films survived fairly long in both tests. Although the low-friction stage did not last as long as on the first run, the second stage, with its partially lubricated surface, persisted for more than 100 hours. After 115 hours of sliding, the friction behavior of dimpled and non-dimpled tests diverged. In the test of the dimpled surface, the friction coefficient became unstable and quickly transitioned to 0.5, indicating lubrication failure. However, the friction coefficient for the non-dimpled surface fluctuated between 0.2 and 0.3 for another 50 hours or more, implying that it could survive under partial coverage by lubricant better than the dimpled specimen. Thus for solid lubrication by thin films, smoother surfaces seemed to perform better than dimpled surfaces. Perhaps if the surface wore down, it would expose more solid lubricant from the dimples to replenish the film, but in the case of ceramics such as zirconia and silicon carbide, their high wear-resistance would not allow this to happen.

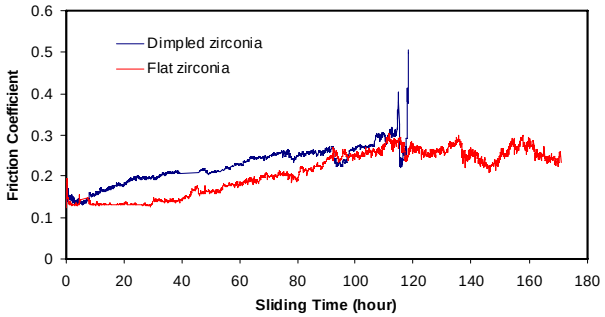

Figure 3. Friction traces for laser dimpled and non-dimpled zirconia surfaces after stabilizing the test fixtures.

A final report that summarizes the current research findings on LST ceramics will be prepared in FY 2005. It will include both tribology results and microstructural characterization.

Conclusions

Although dimples can serve as reservoirs for graphite powder and traps for wear debris, they did not appear to effectively re-supply the lubricating film. In fact, the smoother non-dimpled surfaces sometimes remained at a low-friction condition longer than the LST dimpled ones.

The present results on solid lubricated surfaces have reinforced earlier conclusions from experiments with liquid lubricants: contact alignment is critical for optimizing the effects of dimpled surfaces. With utmost care in establishing good initial alignment and fixture stability, the lubricating film that formed from an initial application of graphite powder can be made to survive more than 100 hours of sliding (10-N load, 2-Hz frequency, 10-mm stroke length). But even with added care in testing, LST offered no apparent advantages over non-dimpled, smooth surfaces tested under graphite lubrication.

References

1. X. Wang, K. Kato, K. Adachi, and K. Aizawa, "The Effect of Laser Texturing of SiC on the Critical Load for the Transition of Water Lubrication Mode from Hydrodynamic to Mixed," *Tribology International*, **34**, 703–711 (2001).

2. K. Kato, "Water Lubrication of Textured Silicon Carbide," presented at the conference on Boundary Lubrication for Transportation, Copper Mountain, CO, August 3–8, 2003.

Publications/Presentations

P. J. Blau, "Challenges for the Application of Engineered Surfaces to Tribosystems with Multiple Contact Modes," invited presentation at the Symposium on Integrated Surface Engineering, ASME/STLE Tribology Conference, Ponte Vedra, FL, October 28, 2003.

P. J. Blau with J. Qu and L. Riester, *Laser Surface Dimpling Effects on the Frictional Behavior and Microstructure of Transformation-Toughened Zirconia and Silicon Carbide Ceramics*, Milestone Progress Report, submitted October 2003.

L. Ti-6Al-4V Billet Feedstock Manufacture and Evaluation

P. Schwartz, S. M. Abkowitz, and S. Abkowitz
Dynamet Technology, Inc.
Eight A Street, Burlington, MA 01803
(781) 272-5967; fax: (781) 229-4879; e-mail: sabkowitz@dynamettechnology.com

DOE Technology Development Manager: Dr. Sidney Diamond
(202) 586-8032; fax: (202) 586-1600; e-mail: sid.diamond@ee.doe.gov
ORNL Technical Advisor: D. Ray Johnson
(865) 576-6832; fax: (865) 574-6098; e-mail: johnsondr@ornl.gov

---

Contractor: Oak Ridge National Laboratory, Oak Ridge, Tennessee
Prime Contract No: DE-AC05-00OR22725
Subcontractor: Dynamet Technology, Inc., Burlington, Massachusetts

---

Objectives

- Develop low-cost Ti-6Al-4V billet feedstock using a blend of titanium (Ti) and alloy powders and inexpensive Ti-6Al-4V machine turnings, or using 100% turnings.
- Evaluate this low-cost Ti alloy feedstock as a starting billet material for casting, forging, and extrusion operations.

Approach

- Develop a procedure for producing low-cost Ti billet using a combination of inexpensive Ti alloy machine turnings and Ti and alloy powders, or 100% machine turnings. Evaluate the billet for density and microstructure.
- Subject the feedstock billets to casting, forging, and extrusion operations. The three operations will yield Ti-6Al-4V test bars.
- Evaluate the quality of the test bars produced through chemistry and mechanical testing.

Accomplishments

- Produced a high-density billet containing 60% turnings/40% Ti alloy powder that was produced using a core of 100% turnings, surrounded by a “can” made from Ti alloy powder.
- Produced a billet using 100% turnings, achieving full density, using cold+hot isostatic pressing (CHIP) technology with conventional canning in mild steel for the HIP operation.
- Extruded a billet, composed of 100% turnings surrounded by a “can” made from Ti alloy powder, to high-density barstock.
- Demonstrated that billets of 100% Ti-6Al-4V machine turnings can be successfully cast from billets in the sintered condition, without the additional step of HIP of the billet. The resulting castings demonstrated tensile strength and ductility that met or exceeded the typical properties of Ti-6Al-4V castings.

Future Direction

- Produce an additional extrusion billet, using specially selected and processed high-quality Ti-6Al-4V turnings (according to the process now developed), that will maintain oxygen content at 0.25% maximum.
- Increase the parameters for consolidation. A higher HIP cycle (temperature, hot pressing temperature, and time) will be employed to produce a higher-density feedstock (full density will be the target).
- Increase the extrusion reduction ratio so that a 5-in.-diameter billet will be extruded to a 1-in.-diameter bar (25:1 extrusion ratio).
- Evaluate the resulting test bars for chemistry and tensile properties.

Introduction

Dynamet Technology is developing a novel method of producing low-cost Ti alloy billet from Ti scrap turnings by powder metallurgical processing. Dynamet's process consists of consolidating the turnings using a combination of cold isostatic pressing and vacuum sintering, followed by HIP, if necessary (Figure 1). The result is feedstock that can be used as extrusion billet, forging stock, or casting electrodes. This process promises to produce billets that are a low-cost alternative to billets produced from ingot.

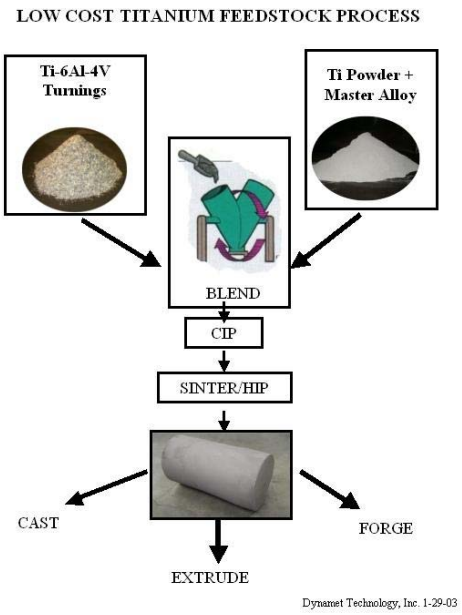

Figure 1: Dynamet's CHIP process for producing low-cost feedstock.

The use of low-cost billet made by Dynamet's process in manufacturing Ti alloy parts for heavy-duty vehicles will save energy, increase payloads, and reduce emissions. Indeed, the availability of low-cost Ti would make Ti attractive to any industry that can benefit from the metal's advantages as a structural material. In addition to the energy, environmental, and economic benefits that result from vehicle weight reduction, the recycling of Ti turnings through Dynamet's process would result in significant energy reduction because it would supply low-cost Ti for new applications that would not require new Kroll process sponge as a raw material.

Future Direction

To complete the promising aspect of this highly desirable concept, it is necessary to successfully extrude Ti-6Al-4V turnings to produce barstock meeting the conventional Ti-6Al-4V mechanical properties. Based upon what we have learned thus far, it is believed that such successful extruded product can be demonstrated. A supplementary program to accomplish this goal has been designed.

At the completion of this supplementary study, a detailed effort would be proposed to lead to commercialization of a low-cost specific grade of Ti-6Al-4V manufactured using processed turnings emanating from Ti-6Al-4V machining operations. This effort will not only generate a low-cost product but also use an energy-efficient and environmentally beneficial manufacturing process.

Publications

Dynamet Technology, Inc., *Ti-6Al-4V Billet Feedstock Manufacture and Evaluation—Final Report*, Burlington, MA, July 15, 2004.

M. High-Density Infrared Surface Treatment of Materials for Heavy-Duty Vehicles

T. N. Tiegs, F. C. Montgomery, D. C. Harper, and C. A. Blue
Oak Ridge National Laboratory
P.O. Box 2008, MS-6087
Oak Ridge, TN 37831-6087
(865) 574-5173; fax: (865) 574-4357; e-mail: tiegstn@ornl.gov

DOE Technology Development Area Specialist: Dr. Sidney Diamond
(202) 586-8032; fax: (202) 586-2476; e-mail: sid.diamond@ee.doe.gov
ORNL Technical Advisor: D. Ray Johnson
(865) 576-6832; fax: (865) 574-6098; e-mail: johnsondr@ornl.gov

Contractor: Oak Ridge National Laboratory, Oak Ridge, Tennessee
Prime Contract No:DE-AC05-00OR22725

Objectives

- Use high-density infrared (HDI) technology to produce corrosion- and/or wear-resistant coatings on metal substrates.
- Use lighter or more cost-effective bulk materials with coatings applied to surfaces where improved properties are required.

Approach

- Examine approaches to surface modification that would be of interest for materials for heavy-duty vehicles.
- First examine the application and formation of adherent, wear-/corrosion-resistant coatings.
- Base the initial tests on hardmetal compositions applied onto iron-based parts that are currently used in diesel engines.

Accomplishments

- Demonstrated the ability to produce adherent hardmetal-based coatings with low trapped porosity on three different metal substrates.
- Showed improved wear resistance for coatings produced using HDI.

Future Direction

- Examine the relationships between processing parameters, microstructural development, and wear resistance.

Introduction

HDI technology is relatively new in the materials processing area and is gradually being exploited. The HDI processing facility at Oak Ridge National Laboratory (ORNL) uses a unique technology to produce extremely high power densities of up to 3.5 kW/cm^2 with a single lamp. Instead of using an electrically heated resistive element to produce radiant energy, a controlled and contained plasma is used.

Since the technology is relatively new, its utility in the surface treatment of materials for applications in heavy-duty vehicles is being explored. In most

cases, wear resistance, corrosion resistance, or high strength is necessary only in selected areas of the part that are exposed to the working environment or under high stress. Therefore, it would be desirable to use materials that are lighter or less expensive for the bulk of the part and have the appropriate surface properties only where required. In addition, the HDI approach would be more cost-effective than other competitive processes such as physical vapor deposition.

Results

Earlier work showed that adherent coatings of hardmetal compositions could be applied to a variety of metal substrates. Cross-sections of the coatings and base alloys revealed some large porosity within the coatings and at the interface with the underlying alloy. These bubbles are believed to be porosity that is trapped during the melting of the coating. To minimize the presence of the bubbles, the infrared (IR) treatment procedure was modified to expose the coating twice to cause the coating to remelt. The idea was that this procedure would allow the bubbles to escape during the second melting. A similar technique has been used before with silica refractories to reduce trapped porosity. The effects of double exposure on the properties of the coating and underlying base metal were mixed.

Samples of WC-(Ni-Cr-Fe) on 4140 steel are shown in Figures 1 and 2 for one-step and two-step HDI processing. No reduction in the presence of the trapped porosity was observed. However, the level of trapped porosity was decreased by allowing additional time during a one-step IR exposure, as shown in Figure 3. Evidently, the additional time during liquid formation allowed the trapped gas to escape. Some cracks in the coating were observed with the additional exposure times. In another sample, the double exposure resulted in a reduction of the trapped porosity, as shown in Figures 4 and 5. The additional exposure also appeared to increase the mixing between the coating and the underlying base metal.

As indicated, previous results had shown that adherent coatings of hardmetal compositions could be applied to a variety of metal substrates (D-2 tool steel, 4140 alloy steel, and cast iron). Selected samples with visually adherent and uniform coatings were wear-tested under dry sliding conditions using a block-on-disc tribometer. The tests were conducted with 4.5 m/s linear speed and a 60-N contact load.

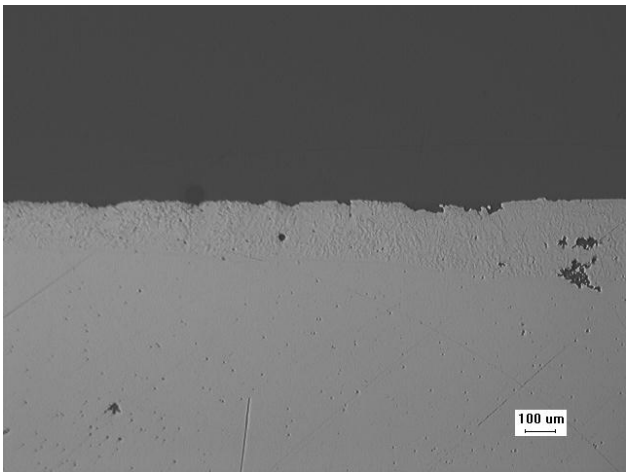

Figure 1. Cross-section of WC-(Ni-Cr-Fe) coating on 4140 steel after one-step HDI processing. IR exposure consisted of a lamp power of 900 amps for 2 sec.

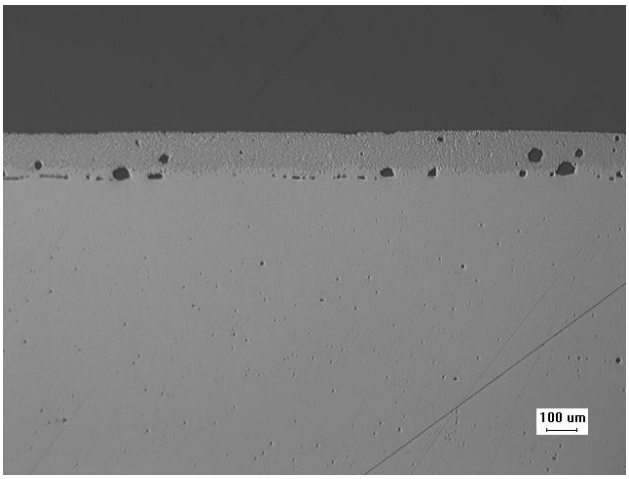

Figure 2. Cross-section of WC-(Ni-Cr-Fe) coating on 4140 steel after two-step HDI processing. IR exposure consisted of a lamp power of 900 amps for 2 sec, 15 sec non-exposure, followed by 900 amps for 1 sec.

The results are summarized in Figures 6 through 9. The wear test results on the D-2 tool steel samples showed that the HDI-coated samples exhibited significantly less wear than the as-received material. The expanded view shown in Figure 7 reveals that the WC and TiC bonded with Ni_3Al exhibited less wear than the other coated samples. A similar trend is also present in the 4140 alloy steel samples shown in Figure 8, where the TiC-Ni_3Al coating showed the best wear behavior. The cast iron samples actually showed that the WC-Ni coating performed worse than the as-received material in the wear test. How

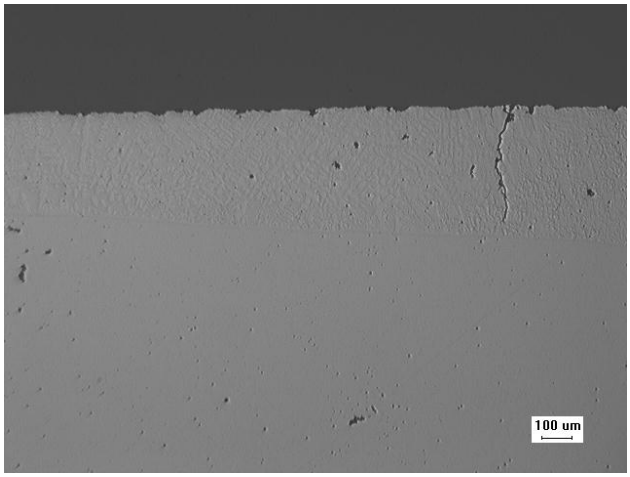

Figure 3. Cross-section of WC-(Ni-Cr-Fe) coating on 4140 steel after one-step HDI processing. IR exposure consisted of a lamp power of 900 amps for 3 sec.

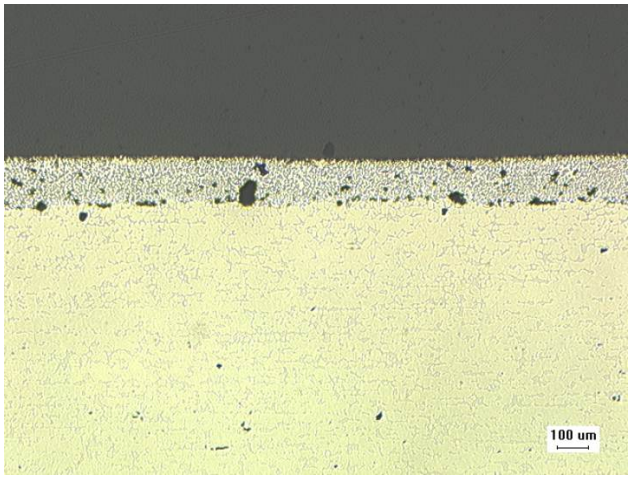

Figure 4. Cross-section of WC-Ni_3Al coating on D2 tool steel after one-step HDI processing. IR exposure consisted of a lamp power of 900 amps for 2 sec.

ever, as observed before, the Ni_3Al bonded sample exhibited the best wear behavior.

Conclusions

It was determined that adherent hardmetal-based coatings could be produced using cost-effective slurry deposition followed by boning with the HDI lamp. Hardmetal-based coatings with reduced porosity were fabricated on three different metal substrates. The wear resistance of the HDI-coated samples was significantly better than that of the as-received materials. In addition, coatings using Ni_3Al as the binder phase had superior behavior in all of the wear tests.

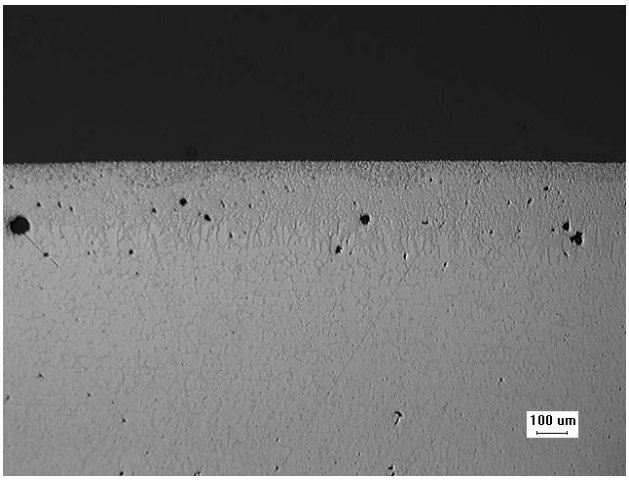

Figure 5. Cross-section of a WC-Ni_3Al coating on D2 tool steel after a two-step HDI processing exposure. IR exposure consisted of a lamp power of 900 amps for 2 sec, 15 sec non-exposure, followed by 900 amps for 1 sec.

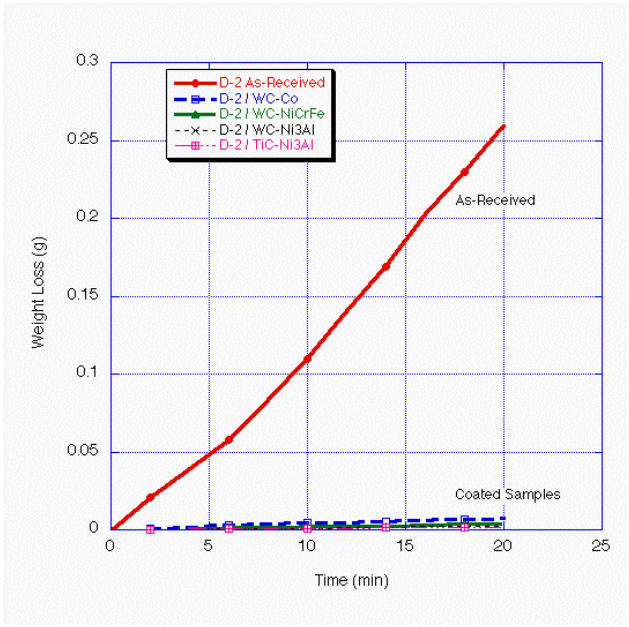

Figure 6. Wear test results on as-received and HDI-coated D-2 tool steel samples. As shown, the coated samples exhibited significantly less wear than the as-received material.

Publications/Presentations

T. N. Tiegs, "Ceramic-Metal Coatings Applied Using High Intensity Infrared Heating," presented at the American Ceramic Society Pacific Coast Conference, Seattle, WA, September 13–16, 2004.

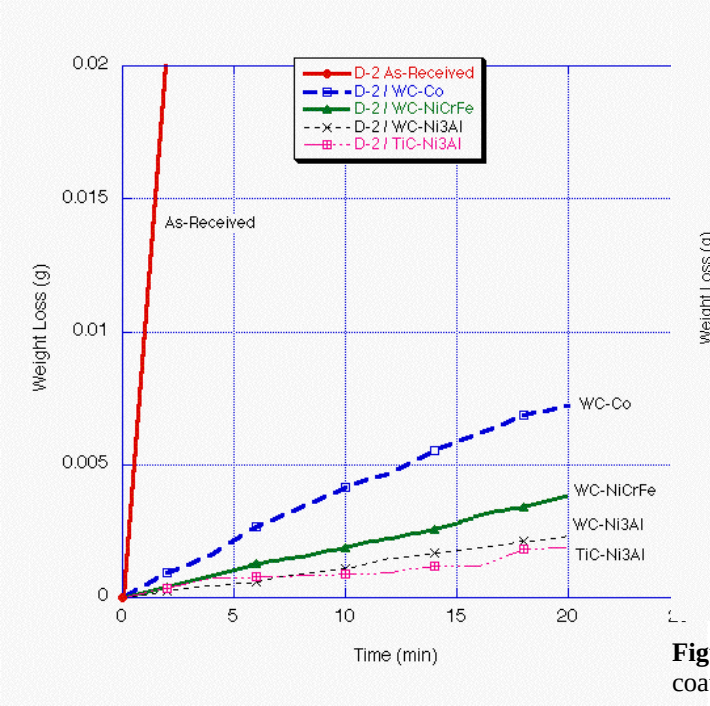

Figure 7. Wear test results on as-received and HDI-coated D-2 tool steel samples.

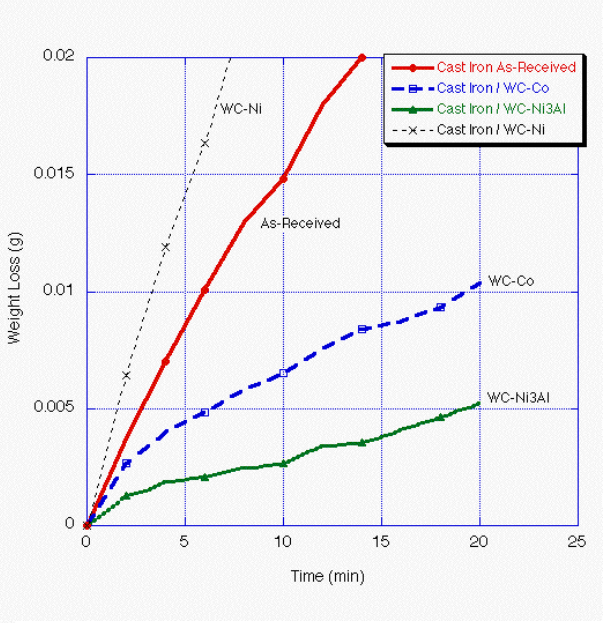

Figure 9. Wear test results on as-received and HDI-coated cast iron samples.

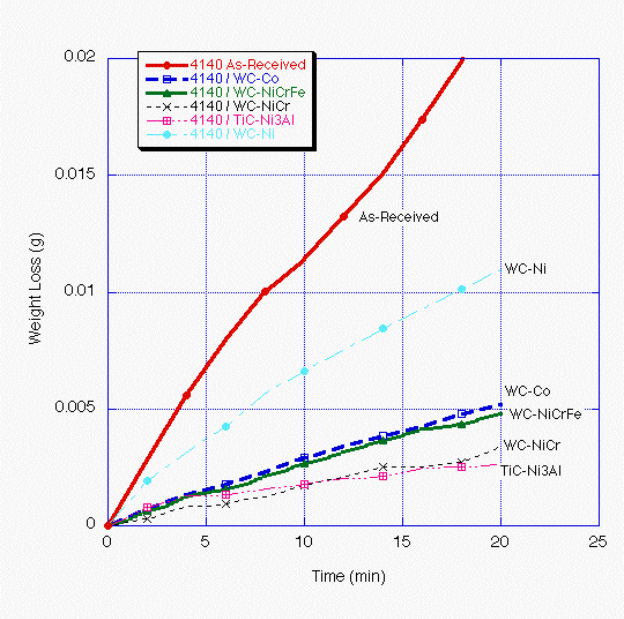

Figure 8. Wear test results on as-received and HDI-coated 4140 alloy steel samples.

N. High-Temperature Aluminum Alloys

Yong-Ching Chen and Randy Stafford
Materials Engineering
Cummins Inc.
1900 McKinley Ave.
Columbus, IN 47201-3005
(812) 377-8349; fax: (812) 377-7226; e-mail: yong-ching.c.chen@cummins.com

DOE Technology Development Area Specialist: Sidney Diamond
(202) 586-8032; fax: (202) 586-1600; e-mail: sid.diamond@ee.doe.gov
ORNL Technical Advisor: D. Ray Johnson
(865) 576-6832; fax: (865) 574-6098; e-mail: johnsondr@ornl.gov

Contractor: Oak Ridge National Laboratory, Oak Ridge, Tennessee
Prime Contract Number: DE-AC05-00OR22725
Subcontractor: Cummins Inc., Columbus, Indiana

Objective

- Develop high-temperature aluminum alloys with adequate properties and shape capability for turbocharger compressor wheels and housing applications.

Approach

- Develop ternary-phase compositions by modeling the equilibrium phase diagram, making castings, and evaluating the properties of alloys identified.
- Perform physical and mechanical property measurements on specimens provided by the National Aeronautics and Space Administration (NASA) and by Eck Industries to characterize the material and determine the optimal properties attainable by this method.
- Evaluate a nanophase particulate-reinforced aluminum alloy patented by Chesapeake Composites, Inc.

Accomplishments

- Accurately predicted and verified the binary-phase diagrams of Al-Y and Al-Yb using ThermoCalc.
- Studied the age-hardening behavior in NASA 388-T5 alloy. The improvement in high-temperature strength of the NASA 388 alloy was found to be not significant enough to pursue further.
- Demonstrated impressive high-temperature tensile strength, fatigue strength, and thermal stability with the dispersion-strengthened composite (DSC) material.

Future Direction

- Use ThermoCalc to generate the Al-Y-Yb ternary system and identify optimal compositions for casting trials and material property characterization.
- Conduct fatigue tests, creep tests, notch sensitivity tests, and machinability studies of DSC material.
- Fully characterize the DSC material

Introduction

The new emission requirements for diesel engines mandate that the turbocharger compressor be operated at a significantly higher temperature and pressure. This condition makes standard castable aluminum alloys unusable as new-generation turbocharger materials because their strength deteriorates at elevated temperatures. Therefore, there is a need to develop high-strength, high-temperature aluminum alloys, which will replace these standard alloys. Work at Cummins has identified three potential paths to improve the high-temperature strength and fatigue resistance of aluminum casting alloys. These paths have been partially investigated under cooperative agreement DE-FC05-97OR22582. Each path showed some promise, and further work is needed to determine the useful applications.

Approach

The scope of work in the program covers the investigation of three different paths for providing strength retention in aluminum alloys at high temperatures. Path 1 uses a ternary-phase aluminum alloy using rare earth metals to provide precipitate size control and stability. Limited information on these alloys indicates high-temperature strength and stability; however, the predicted cost of the alloy is high. Additional work was performed to determine if there are other rare earth (or other metal) elements that produce beneficial properties at a reasonable cost. The main goal of this path is to generate the phase diagram of Al-Y-Yb (aluminum-yttrium-yterrbium), using ThermoCalc software. Since there are very few published data and assessments on these rare-earth elements, a prudent approach demands that a systematic investigation be carried out. Path 2 uses a conventional aluminum alloy, which has been chemically modified by a process developed at NASA–Huntsville. The elevated-temperature properties reported by NASA are attractive, but Cummins prefers to use an alloy with a lower silicon content. Eck Industries purchased the license for the NASA-developed technology for high-silicon casting alloys and has expanded the range to include conventional low-silicon casting alloys. Limited testing of these modified conventional low-silicon alloys at Cummins has not shown the property improvement anticipated. Currently, NASA 388-T5 alloy is being evaluated to characterize the material and to determine possible process improvement. Path 3 uses a particulate-loaded aluminum alloy patented by Chesapeake Composites. The nanophase particulates at 50 vol % provided adequate high-temperature strength in early experiments; however, the particulate-loaded alloy could only be forged or squeeze cast, so its complex-shape capability was limited. The mechanical behavior of this DSC material is being fully characterized. Casting modifications will be investigated to determine the shape capability for the alloy.

Results

Path 1: Ternary-Phase Aluminum Alloy Development

In the previous report, the binary-phase diagrams of Al-Fe and Al-Mn and a ternary-phase diagram of Al-Fe-Mn were generated using ThermoCalc. The versatility of the software has been clearly demonstrated in the plotting of the phase diagrams. A major aspect of this project is to be able to examine the minute details of any region of interest, which happens to be the aluminum-rich region of the phase diagram. This type of plot simplifies the task of accurately determining the limits of the phase fields in the aluminum-rich corner (or any region of interest) of the phase diagram

Although the software features a wide spectrum of thermodynamic models, databases, and modules, it requires accurate assessment of the elements in order to perform phase equilibrium/diagram calculations. The Al-Y-Yb alloy poses a peculiar challenge, because there has been limited assessment of rare earth elements, especially alloys containing Yb. Although it is not presented, an extensive literature search has been conducted on the thermodynamic assessment of Y and Yb elements. In spite of this fundamental problem, the binary-phase diagrams of Al-Y and Al-Yb have been generated (using ThermoCalc) and validated. Figures 1 and 2 present the phase diagrams of Al-Y and Al-Yb, respectively.

With the prediction of Al-Y and Al-Yb systems, work will begin on predicting the Al-Y-Yb ternary system. Upon deciding on the actual composition of interest, a material supplier will be asked to cast a prototype of the material. A detailed characterization of the material will be carried out at the Florida A&M University–Florida State University College of Engineering. Microcharacterization of the material will rely on scanning electron microscopy

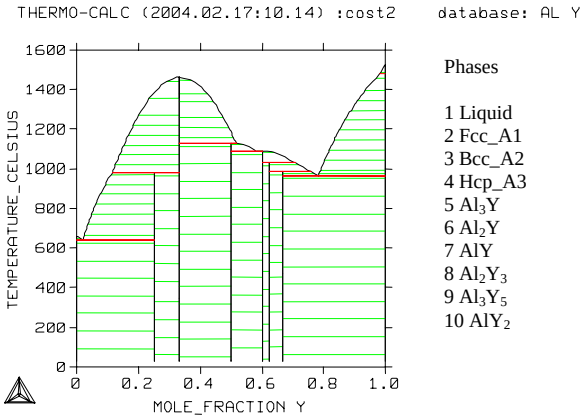

Figure 1. The Al-Y binary phase diagram generated using ThermoCalc.

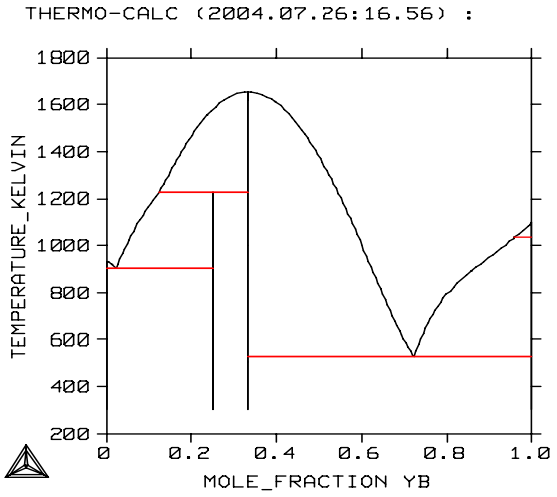

Figure 2. The Al-Yb binary phase diagram generated using ThermoCalc.

(SEM) and transmission electron microscopy (TEM), while the mechanical properties will be evaluated by tensile tests.

Path 2: NASA 388-T5 Aluminum Alloy

The microstructure of 388-T5 Al alloy with NASA modification was characterized. The results indicate that compositional modification leads to some refinement in the size of the silicon particles. A variety of coarse precipitates—$Cu_2Mg_8Si_6Al_5$, $(Cu,Fe,Mn,Ni,V)_3Si_2Al_{15}$, $(Cu,Ni)_2Al$ and $CuAl_2$—were observed. The aluminum matrix was dominated by the presence of plate-shaped precipitates of the metastable θ' phase. These precipitates appear to be mainly responsible for the strengthening. In addition, very fine spherical precipitates having the $L1_2$ structure and presumably the $Al_3(Ti,Zr)$ chemistry were noted. Figure 3 shows the SEM microstructure of NASA 388-T5 alloy.

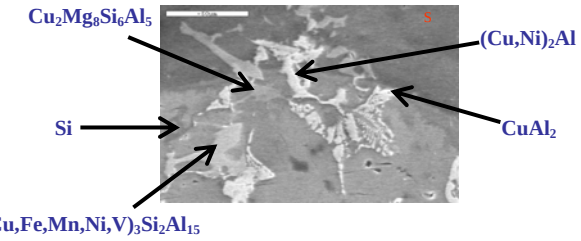

Figure 3. SEM micrograph showing microstructure of the NASA-modified 388 T5 alloy. Several indicated coarse intermetallic precipitates can be noted.

The tensile strength of the thermally soaked and unsoaked NASA 388-T5 material increased slightly from room temperature and reached a peak at 300°F, after which it dropped almost linearly with the increase in temperature. The fracture morphology correspondingly changed from brittle to ductile/dimpled rupture, and microvoids containing second-phase particles in their interior were present. Thermal soaking at high temperatures for times up to 500 hours led to some degradation of the tensile properties.

Extensive mechanical tests were conducted on the NASA 388-T5 and T6 alloys. Tests included elevated-temperature tensile tests and rotating beam fatigue tests of samples, with or without long-term thermal soaking. Test results were compared with those of the current production materials, C355-T61 and 354.0-T61 alloys. A slight improvement in the tensile strength was realized only at test temperatures above 300ºC for the NASA 388-T5 alloy, compared with the strength of the current materials. The degree of improvement was deemed to be insignificant compared with the further development needed for the new casting process and prototype trials. The decision was made to discontinue the evaluation work for the NASA 388-T5 alloy for turbocharger application.

Path 3: Particulate-Reinforced Alloy

This task involves a nanophase particulate-loaded aluminum alloy patented by Chesapeake Composites. A patented, low-cost, liquid metal infiltration process is used to produce a billet form ready for secondary operations. This composite material combines the enhanced elevated-temperature

strength, toughness, and ductility of dispersion-strengthened alloys with the stiffness and low coefficient of thermal expansion of metal matrix composites. It is claimed that this composite can be readily turned using tungsten carbide tooling and drilled and tapped using high-speed steel tools. Potential applications include pistons, compressor wheels, and engine components.

As-infiltrated billets of the DSC with a 40 volume fraction of nanoscale Al_2O_3 particles in either 1090Al matrix or 2024Al matrix were supplied by Chesapeake Composites for testing. Tensile specimens were prepared from the billets and thermally soaked at 204, 260, 316, and 371°C for 500 hours prior to testing. Figure 4 shows the tensile test results for the DSC material at elevated temperatures. The tensile strength of the DSC material decreased nearly linearly from ~58 ksi at room temperature to ~20 ksi at 371°C, the latter value being impressively high for an aluminum alloy. It was noted that essentially no reduction in the tensile strength of the DSC material was observed. This indicated that the DSC material exhibited a very good thermal stability even after long-tem usage at high temperatures. The properties of the 2024Al-DSC material are comparable to those of the 1090Al-DSC material over the entire temperature range, suggesting that the second-phase precipitates expected in the former have little or no influence and that the properties are dominated by the presence of a high volume fraction of submicron-scale Al_2O_3 particles.

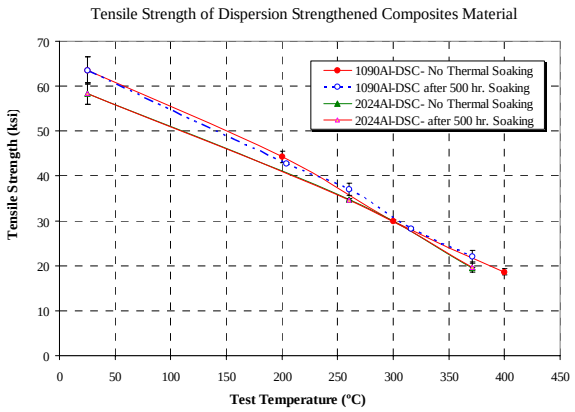

Figure 4. Tensile strength of DSC material at elevated temperatures.

Rotating beam fatigue tests of 2024Al-DSC and A354-T6 alloy were conducted at 260°C (500°F). Figure 5 shows the fatigue test results. The fatigue

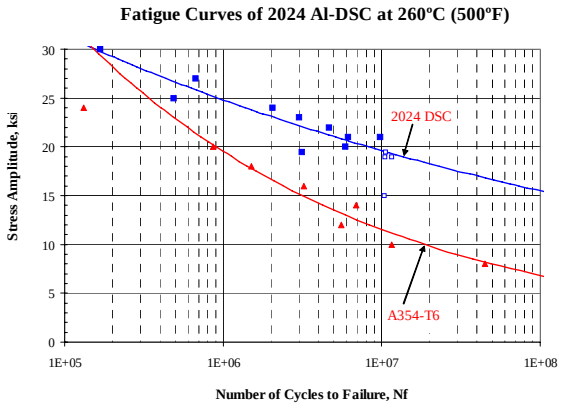

Figure 5. Rotating beam fatigue strength of DSC material and 354-T6 alloy at 260°C.

strength of the 2024Al-DSC material was determined to be far superior to that of A354-T6 alloy, which is a premium aluminum alloy. A very impressive 19 ksi fatigue strength at 10^7 cycles was obtained in the 2024Al-DSC material. The fatigue strength of A354-T6 alloy was determined to be about 10 ksi at 10^7 cycles.

The microstructure of the DSC material (as-received and following thermal treatment) was characterized by TEM. The aluminum matrix grains were found to contain a moderate density of dislocations. The nanoparticles were found to have the structure and composition of α-Al_2O_3. The particles are nano-sized (30–100 nm) in the as-synthesized material, but they coarsen to 100–1000 nm following high-temperature thermal treatment, independent of time or temperature. After the initial holding times, little or no change in the sizes of the particles occurred at longer times and independent of temperature. This points to great thermal stability of these materials and a high, nearly constant hardness as a function of time and temperature. The TEM results are consistent with the SEM observations reported previously.

Conclusions

Three different paths were adopted to develop and evaluate high-temperature aluminum alloys for turbocharger compressor wheels and housing applications. The versatility of the ThermoCalc software was demonstrated in the plotting of the phase diagrams. The Al-Y and Al-Yb binary-phase diagrams were generated and validated. The Al-Y-Yb ternary system will be modeled. Slight improvement in the

tensile strength was realized only at test temperatures above 300ºC for the NASA 388-T5 alloy compared with the current materials. The degree of improvement was deemed to be insignificant compared with the further development needed for the new casting process and prototype trials. The decision was made to discontinue the evaluation work for the NASA 388-T5 alloy for turbocharger applications. The DSC material exhibited very impressive high-temperature tensile and fatigue strength. Excellent thermal stability was confirmed with SEM and TEM studies. The DSC material has high potential to be used to replace the current C355 alloy to achieve improved material strength and thermal stability. Other important material properties such as creep resistance, notch sensitivity, and machinability will be further evaluated.

Publication/Presentations

P. Prasad, Y-C. Chen, and V. K. Vasudevan, "Microstructure and Mechanical Properties of New, Cast Aluminum Alloys for High Temperature Diesel Engine Applications," in *Symposium of Challenges for High temperature Alloys in Aerospace, Land-based Gas Turbines, Power and Transportation Systems,* ASMI Fall Meeting, Columbus, OH, October 18–20, 2004.

P. Prasad, Y-C. Chen, and V. K. Vasudevan, "Characterization and Aging Studies of New, Cast Aluminum Alloys for High Temperature Diesel Engine Applications," in *General Abstracts Session on Mechanical Behavior and Characterization,* TMS/MST 2004 Fall Meeting, New Orleans, September 26–29, 2004.

P. Prasad, P. C. Becker, Y-C. Chen, and V. K. Vasudevan, "Microstructure of New, Cast Aluminum Alloys for High Temperature Diesel Engine Applications," in *General Abstracts Session on High Temperature Alloys*, TMS/MST 2003 Fall Meeting, Chicago, November 7–11, 2003.

O. Applications of Titanium Alloys for Heavy-Duty Vehicles

P. C. Becker
Oak Ridge National Laboratory
P.O. Box 2008, MS-6068
Oak Ridge, Tennessee 37831-6068
(865) 576-4844; fax:(865) 574-6098; e-mail:beckerpc@ornl.gov

DOE Technology Development Area Specialist: Dr. Sidney Diamond
(202) 586-8032; fax:(202) 586-1600; e-mail:sid.diamond@ee.doe.gov
ORNL Technical Advisor: D. Ray Johnson
(865) 576-6832; fax:(865) 574-6098; e-mail:johnsondr@ornl.gov

---

Contractor: Oak Ridge National Laboratory, Oak Ridge, Tennessee
Prime Contract No.: DE-AC05-00OR22725

Objectives

- Determine if it is feasible to substitute a high-strength titanium (Ti) casting alloy for the heavier gray cast iron in a heavy-duty diesel engine head and block.
- Determine if it is feasible to substitute a high-strength aluminum (Al) casting alloy for the heavier gray cast iron in the same engine.
- Determine if it is feasible to substitute a high-strength magnesium (Mg) casting alloy for the heavier gray cast iron in the same engine.

Approach

- Use mechanical and physical property data for finite element analysis (FEA) to compute the temperatures, stresses and fatigue cover factors (safety factors) at various locations on the head and block of a 5.9L Cummins ISB engine, run at maximum designed power (305 hp), for three lightweight casting alloy systems.
- Compare these data to those computed for a production engine (all cast iron engine) to determine the feasibility of substituting any or all of these alloy systems for cast iron. (Ricardo, Inc. was contracted to conduct the FEA.) Note that fatigue analyses assumed that the engine was always stressed at the maximum for the life of the engine. In reality, this stress level is much higher than for typical duty cycles for this engine.

Accomplishments

- Determined the following through the FEA.
  - — Cast Ti-6Al-4V can be used as a direct substitution for gray cast iron in the engine block without any design changes as long as a cast iron liner is used. Ti was far superior to cast iron from a fatigue perspective.
  - — Cast Ti-6Al-4V can be used to replace cast iron in the engine head, but the valve bridge temperatures are too high (700°C); thus, without some design or materials changes, the head will not function well when made of Ti.
  - — To preserve the weight reduction and superior strength benefits of Ti for the block, without any design changes, the analyses demonstrated that an engine having either a cast iron or an Al head (15% overall engine weight saving) in combination with a Ti block with cast iron liners is feasible.

— The use of a Be-Cu alloy insert in the valve bridge regions of the Ti head, in combination with up-rating the engine to 450 hp, was shown to be a feasible way of reducing the temperatures in this region. The superior mechanical properties of Ti would enable the engine to operate at a higher power rating while achieving lighter weight (11% overall engine weight saving). The Ti block had no problem withstanding the higher stresses created by the up-rating.

— A high-strength Al casting alloy, A354-T6, could be used as a substitute for gray cast iron in both the head and block of the engine running at 305 hp if a gray cast iron cylinder liner were used. This would result in a 20% overall engine weight saving. Since Al does not have a fatigue endurance limit, the use of Al would be duty-cycle limited.

— A high-strength Mg casting alloy, WE 43, could be used as a substitute for gray cast iron in both the head and block of the engine running at 305 hp if a gray cast iron cylinder liner were used. This would result in an overall engine weight saving of 33%.

— Although the head temperature at the valve bridges is about 50°C higher than the recommended maximum for WE 43, it is considered a feasible substitute for gray cast iron if design changes are made to lower the temperature.

Future Direction

- Seek funding from either a major diesel engine manufacturer or a major customer to construct and test engines. A potential customer is the Department of Defense, since there is a strong desire to reduce the weight and/or increase the power of engines in military vehicles.

Introduction

Many programs are focused on reducing the cost of Ti powder and ingot by 50%. If any of these programs reaches this target, the cost of Ti might be become attractive enough for use in heavy duty diesel engines for certain applications where weight reduction is critical. In addition, there is a desire on the part of the military both to reduce the weight of transportation and to reduce the magnetic signature. This project explores the feasibility of replacing the cast iron in diesel engine heads and blocks with Ti, which is about 40% lighter than cast iron and is nonmagnetic. Using a Ti-6Al-4V casting alloy in place of gray cast iron in just these two components could save hundreds of pounds of weight, depending on the size of the engine. In addition, because of its superior strength and fatigue properties compared with cast iron, Ti affords the opportunity to upgrade the power of the engine without extensive design changes. It is recognized that Ti has some few disadvantages compared with cast iron, including lower thermal conductivity, poorer machineability, and higher cost.

The approach used with Ti was also used to model the same engine with either an aluminum or a magnesium casting alloy. Thus this project studied the application of the three major lightweight metals systems to determine if it were feasible to replace gray cast iron in the engine head and block with alloys of one or all of these metals.

Table 1 shows the weight savings that can be achieved when Ti, Al, or Mg is used to replace gray cast iron in a Cummins ISB 5.9-L diesel engine.

Table 1. Weight savings produced by replacing cast iron with cast lightweight alloys in a Cummins ISB diesel engine (total engine wt. of about 1000 lbs)

Material	Wt. saving (lb)
Ti-6-4 head and block	147
Ti-6-4 head and block with Cu inserts and cast iron (CI) liners	107
Al(A354) head and Ti block with CI liners	149
Al head and Al block with CI liners	200
Mg (WE43) head and block with CI liners	335

Note: The liners weigh 7 lb each; the Cu inserts weigh 1.5 lb each.

Results

Ti Alloy Feasibility Study

This project employed FEA to model a Cummins 5.9-L, B-series diesel engine running at 305 hp. The temperatures and stresses were computed at various locations on the head and block castings for both the cast iron currently used and the Ti-6-4 alloy. Since the production engine is a parent bore engine (no cylinder liners), cast iron liners were incorporated into the model when evaluating the engine made with lightweight alloys. Based on the modeling and a comparison of the two materials, the feasibility of using Ti-6-4 in place of gray cast iron was determined. The modeling work was contracted to Ricardo, Inc. which has in-house the model for this engine and the experience to perform the necessary computer operations and interpret the results.

As a result of the initial modeling, additional modeling iterations were needed to obtain the optimum combination of materials for the head and block. For example, a cast iron head or an Al head coupled with a Ti block was modeled. Even a copper alloy insert to the valve bridges of the Ti head was modeled in conjunction with up-rating of the engine. Table 2 compares Ti with gray cast iron in terms of major advantages and disadvantages.

Figures 1 and 2 show the FEA model summary and block mesh; Table 3 shows the engine operating conditions.

Tables 4 and 5 show the materials properties of gray cast iron and Ti-6Al-4V, respectively. Table 6 shows the thermal conductivity data for gray cast iron, Ti, and Al. It is obvious that Ti has a much lower conductivity than the other two materials, and Al has very high thermal conductivity.

The temperatures in the flame face of the head were computed for the all cast iron engine (production engine), labeled Fe/Fe/Fe, and for three alternatives. The first was an iron head on a Ti block with a cast iron liner (Ti/Fe/Fe); the second was a Ti head on a Ti block having a cast iron liner (Ti/Fe/Ti); the third was an Al head on a Ti block having a cast iron liner (Ti/Fe/Al). As can be seen from Figure 3, the temperatures in the valve bridge areas of the Ti head are high (709°C). The temperatures in the same location on the three other combinations are low enough not to cause problems. The temperatures in the other parts of the head were considered low enough in all the combinations that they posed no problem. Figure 4 shows the temperature determina-

Table 2. Advantages and disadvantages of using Ti in place of gray cast iron

Advantages of Ti	**Disadvantages of Ti**
1. Weight savings —Cummins B-Series • 100 lb saving from the machined block • 47 lb saving from the whole engine. (total dry wt. of 1036 lb) • 14% weight saving from the whole engine (total dry wt. of 1036 lb) 2. Performance (room temp) • UTS of TI-6-4:125 ksi • UTS of grey cast iron (CI): 28 ksi • Fat. Str. of CI: 10 ksi • E for Ti-6-4: 17 msi • E for CI: 15 msi 3. Non-magnetic	1. Cost —Ti is about $10/lb and must be vacuum investment cast - Gray CI <$ 0.20/lb. and is green sand cast in air 2. Machinability —Ti has much lower throughput and much higher tool wear 3. NVH attenuation 4. Thermal conductivity (300°C) —K_{CI}: 49 W/m-k —K_{Ti}: 12 W/m-k

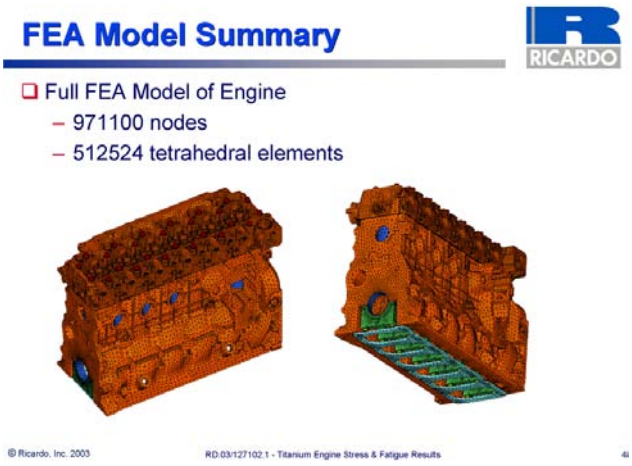

Figure 1. FEA model summary.

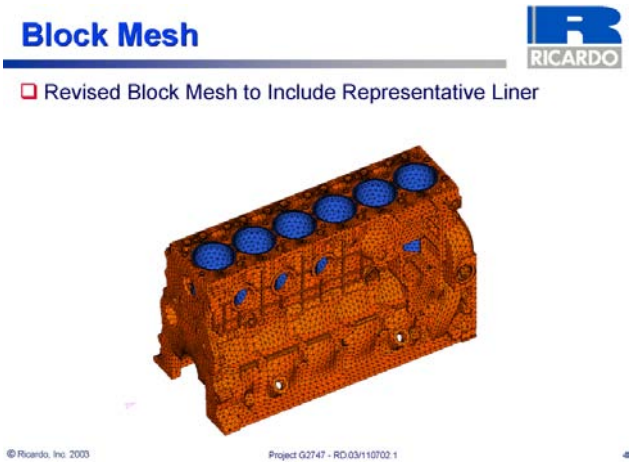

Figure 2. Block mesh.

Table 3. Engine operating conditions for the purpose of modeling

Number of cylinders	6
Engine displacement	5.59L
Rated speed	2900 rpm
Rated power	305 hp
Cylinder pressure	160 bar

Table 4. Materials properties of gray cast iron used in the Cummins engine

Block – gray cast iron —data supplied by Cummins
—Young's modulus = 103.4 GPa
—Poisson's ratio = 0.25
—Ultimate tensile strength = 189.6 MPa
—Tensile yield strength = 136.5 MPa
—Compressive yield strength = 284.4 MPa
—Fatigue strength = 72.39 MPa
Head – gray cast iron– data supplied by Cummins
—Young's modulus = 103.4 GPa
—Poisson's ratio = 0.25
—Ultimate tensile strength = 206.8 MPa
—Tensile yield strength = 148.9 MPa
—Compressive yield strength = 317.2 MPa
—Fatigue strength = 110.3 MPa

tions for the tops of the liners in the engine block, determined for the same material combinations.

Table 7 summarizes the temperatures in the key locations on the head and block for the four head and block material combinations.

Figure 5 shows how the fatigue calculations were predicted based on modified Goodman diagrams and where on the diagram the cover factors (safety margins) are determined. Fatigue cover factor is defined as the ratio of the length of the line

Table 5. Mechanical properties of Ti-6Al-4V used in this study

Comparison of mechanical properties of Ti-6AI-4V from the literature vs. values used in this study		
Literature		
(Crucible steel)		
Temp (°C)	UTS (Mpa)	Y.S. (Mpa)
21	1063	973
315	814	725
538	635	531
This study		
(Mil Handbook 5, annealed, HIPed castings)		
Temp.(°C)	UTS ,(Mpa)	Y.S. (Mpa)
21	862	820
315	608	502
538	431	362

Table 6. Thermal conductivity of gray cast iron, Al and Ti at various temperatures

Temperature-dependent conductivity Aluminum data supplied by Cummins			
	K (W/m-K)		
Temperature (°C)	Cast iron	Titanium (Ti6AI4V)	Aluminum (A354T6)
–18		6.7	
21			168.8
27		7.3	
38		7.4	
50			170.9
93		7.6	
100	48.8		175.5
149		8.1	
150			177.6
200	47.8		179.3
204		8.7	
260		9.6	180.8
300	46.8		
316		10.4	
371		11.2	
400	45.8		
427		11.9	
482		12.7	
50	44.8		
538	13.5		

from (0,0) through (δ_m, δ_a) to the point where it intersects the boundary of the safe working area, to the length of the line from (0,) to (δ_m, δ_a). The factor will be greater than 1 for points within the safe working area, and less than 1 everywhere else. Ricardo's acceptable cover factor for this type of application is 1.5 or greater.

Table 7. Temperatures at key locations in the head and block for four material combinations

Summary of temperatures @ areas of interest All temperature in degrees centigrade					
	From previous iterations		1	2	3
Location	All iron	All titanium	Ti block Fe liner Fe head	Ti block Fe liner Fe head	Ti block Fe liner Fe head
Top of block	227	410	228	287	194
Top of liner	-	-	248	289	214
Cylinder head exhaust valve bridge	370	710	381	709	220
Intake valve seat	357	550	360	551	249
Exhaust valve seat	444	741	455	741	326

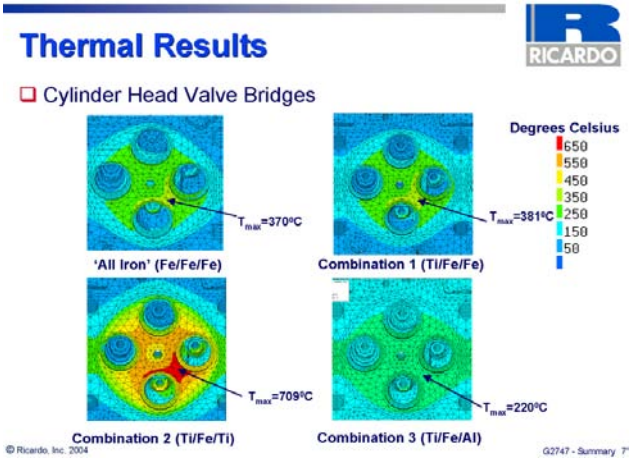

Figure 3. The computed flame face temperatures of the engine head for four head and block material combinations.

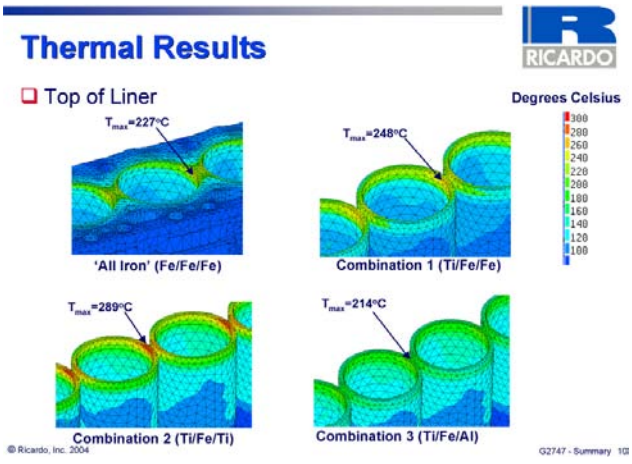

Figure 4. The computed temperatures for the tops of the cast iron liners for four head and block material combinations.

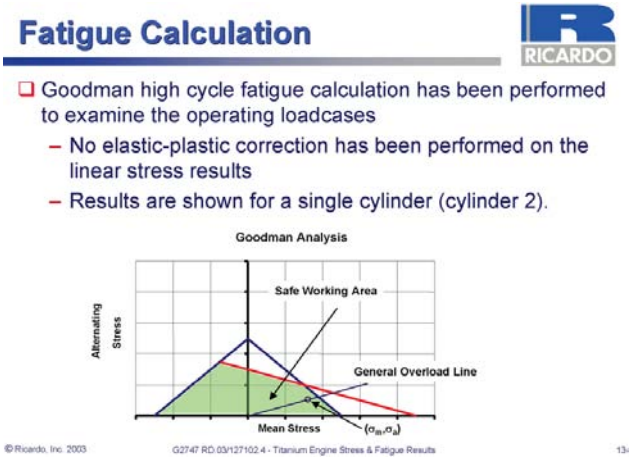

Figure 5. Goodman high cycle fatigue calculations.

Table 8 shows a summary of the computed stresses and fatigue cover factors for the cast iron head from the production engine and for the Ti head on a Ti block with a cast iron liner. The table shows many key locations on the heads.

It can be seen from Table 8 that the Ti head has more fatigue resistance than the cast iron head of the production engine in all of the key locations of the head, and that there are many locations on the production engine head that have a cover factor of less than 1. Even with the low cover factors, the production engine survives in service with a high degree of reliability. This is because, in this study, the analyses assumed that the components see only the maximum operating conditions. In real life, the engine does not operate at this maximum all the time. Thus the stresses are lower for a large portion of the duty cycle of the engine. This study can be considered a worst-case scenario.

Table 8. Computed stresses and fatigue cover factors in the head for the combinations Fe/Fe/Fe and Ti/Fe/Ti

			Cast iron							Titanium
Location	(lwj = lower water jacket) (uwj – upper water jacket) Description	Node #	Minimum stress (N/m^2)		Maximum stress (N/m^2)		Mean stress (N/m2	Alternating stress (N/m2)	Fatigue cover factor	Fatigue cover factor
A	uwj fillet between bolt box and valve guide	3759825	Cyl 5	156.3E+6	Cyl 2	279.3E+6	217.8E+6	61.5E+6	0.53	1.62
B	lwj floor fillet between exh. Port and inj. bore	3785105	Cyl 5	221.6E+6	Cyl 2	242.4E+6	232.0E+6	10.4E+6	0.61	1.22
C	lwj floor fillet to exhaust port	3783535	Cyl 5	202.5E+6	Cyl 1	228.7E+6	215.6E+6	13.1E+6	0.65	1.23
D	lwj roof fillet to head bolt boss	3784266	Cyl 1	107.2E+6	Cyl 2	219.1E+6	163.2E+6	56.0E+6	0.68	2.37
E	uwj rof fillet to head bolt boss	3759206	Cyl 6	121.4E+6	Cyl 2	217.0E+6	169.2E+6	47.8E+6	0.69	2.26
F	lwj floor fillet to exhaust port	3780615	Cyl 3	136.0E+6	Cyl 2	207.4E+6	171.7E+6	35.7E+6	0.72	1.72
G	intake port to valve seat area	3879902	Cyl 2	190.5E+6	Cyl 1	206.8E+6	198.7E+6	8.2E+6	0.72	2.07
H	lwj roof fillet to head bolt boss	3776708	Cyl 3	186.1E+6	Cyl 2	198.8E+6	192.5E+6	6.4E+6	0.75	1.68
I	exterior on exhaust side near flame deck	3793591	Cyl 2	160.2E+6	Cyl 1	184.2E+6	172.2E+6	12.0E+6	0.81	2.44
J	uwj roof fillet to head bolt boss	3777863	Cyl 1	109.2E+6	Cyl 2	181.1E+6	145.2E+6	36.0E+6	0.82	2.90
K	uwj roof fillet to head bolt boss	3779640	Cyl 6	123.3E+6	Cyl 2	174.0E+6	148.7E+6	25.4E+6	0.86	2.66
L	lwj roof fillet to head bolt boss	3775260	Cyl 1	108.7E+6	Cyl 2	170.1E+6	139.4E+6	30.7E+6	0.88	2.27
M	uwj fillet between head bolt boss exhaust port	3780476	Cyl 1	132.2E+6	Cyl 3	169.8E+6	151.0E+6	18.8E+6	0.88	2.83
N	exterior pocket @ top deck near bolt boss	3791833	Cyl3	89.8E+6	Cyl 2	161.7E+6	125.7E+6	36.0E+6	0.92	3.10
O	uwj roof fillet to top deck	3779648	Cyl 6	141.8E+6	Cyl 2	160.3E+6	151.1E+6	9.3E+6	0.93	3.10
P	lwj fillet – valve guide to fuel drilling	3787973	Cyl 6	113.8E+6	Cyl 3	158.4E+6	136.1E+6	22.3E+6	0.94	2.80
Q	top deck rib between guides	3783137	Cyl 6	85.9E+6	Cyl 2	158.4E+6	122.2E+6	36.2E+6	0.94	3.60
R	lwj floor between exh. Ports and inj, bore	3785319	Cyl 2	107.9E+6	Cyl 3	156.9E+6	132.4E+6	24.5E+6	0.95	1.47
S	top deck exterior	3783291	Cyl 6	115.6E+6	Cyl 2	156.7E+6	136.2E+6	20.6E+6	0.95	3.25
T	exterior pocket @ top deck near head bolt boss	3792836	Cyl 1	112.2E+6	Cyl 2	155.3E+6	133.8E+6	21.6E+6	0.96	2.75
U	uwj roof to coolant hole	3778568	Cyl 5	110.5E+6	Cyl 2	155.2E+6	132.9E+6	22.4E+6	0.96	3.60
V	lwj fillet – exh. guide to exh. port	3780566	Cyl 5	85.0E+6	Cyl 2	151.4E+6	118.2E+6	33.2E+6	0.98	2.50
W	lwj floor fillet to exhaust port	3776526	Cyl 3	129.3E+6	Cyl 2	150.2E+6	139.8E+6	10.5E+6	0.99	1.66

Figure 6 shows the results of the fatigue analyses of the block in cast iron and Ti, and Table 9 summarizes the results of the fatigue prediction study for various locations on the block for both cast iron and Ti. As can be seen, there is only one small location on the block with a low cover factor for both materials, although the Ti value is more than four times that of the cast iron. This location is so small that it should be easy to increase the cover factor by adding some material in that location in the casting.

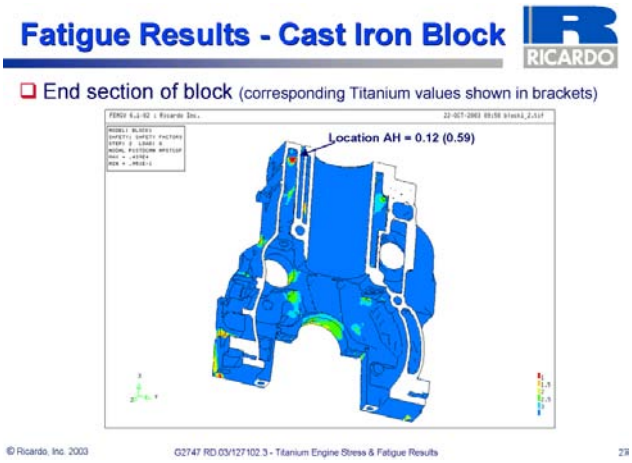

Figure 6. Description of fatigue cover factors (safety factors).

One approach for dealing with the unacceptably high temperatures in the valve bridge regions is to replace the whole head with either cast iron or Al. In the former case, the only weight saving would be from using Ti for the block. In the latter case, a further weight saving would be achieved because Al is 57% lighter than Ti but less durable at high temperatures and fatigue stresses. Another approach, which would preserve the advantages of Ti, would be to make the head of Ti but replace the valve bridge regions with an insert of a material that has a high thermal conductivity and high elevated temperature strength.

To this end, a literature study was conducted of materials of known high thermal conductivity and high strength. A copper alloy was considered to be the best candidate insert material. The insert design in the valve bridge region of the head was therefore modeled by FEA; but at the same time, the engine was up-rated to 450 hp to see if the superior mechanical properties of Ti-6-4 would enable the engine to be rated at a much higher horsepower than current production engines. Figure 7 illustrates the concept. It shows an Al head with cast iron inserts showing where the copper alloy insert would be located.

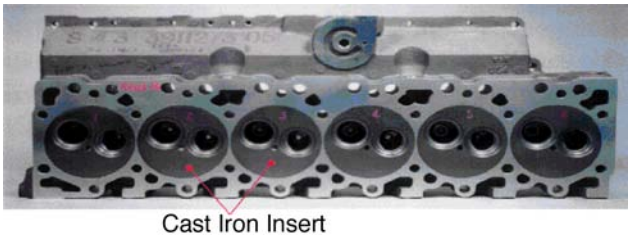

Figure 7. The FEA model of one cylinder of the block showing the only location that has a low cover factor for both materials studied

To determine if the insert strategy described was feasible, the physical and mechanical properties of a 2% Be-Cu alloy were used. Figure 8 shows a graph of ultimate tensile strength vs. temperature for Ti-6Al-4V, A354-T6, 2% Be-Cu, and gray cast iron. The 2% Be-Cu alloy has excellent elevated temperature strength and exceeds or equals Ti up to about 350°C. The thermal conductivities of the four key alloys shown in Figure 8 are shown in Figure 9. The design of the BE-Cu insert is shown in Figure 10.

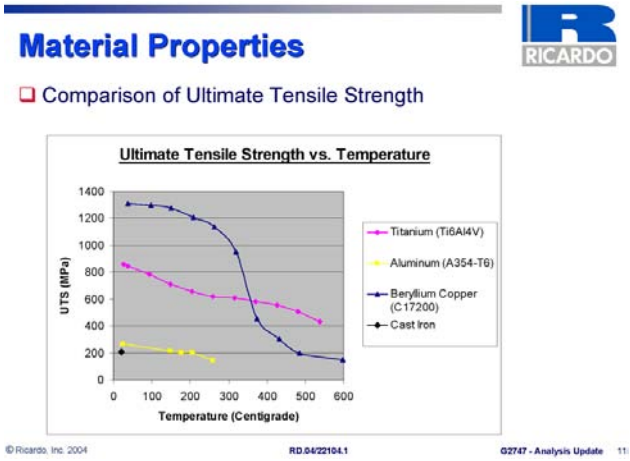

Figure 8. Photo of an Al engine showing cast iron inserts in the fire deck as a way of showing how a Cu alloy insert would be placed in a Ti head. The actual engine has four valves instead of the two shown here.

Table 9. Summary of the computed stresses and fatigue cover factors for the cast iron and the Ti blocks

			Cast iron							Titanium
Location	Description	Node #	Minimum stress (N/m^2)		Maximum stress (N/m^2)		Mean stress (N/m2	Alternating stress (N/m2)	Fatigue cover factor	Fatigue cover factor
AH	interior fillet to top deck @ end face	6187310	Cyl 1	758.0E+6	Cyl 4	1.1E+9	944.0E+6	186.0E+6	0.12	0.59
AI	oil hole edge to brg. shell	6468000	Cyl 1	130.0E+6	Cyl 6	206.0E+6	168.0E+6	38.0E+6	0.66	2.75
AJ	corner of side inlet to water jacket	6215232	Cyl 6	17.1E+6	Cyl 2	129.0E+6	73.1E+6	56.0#+6	0.87	3.76
AK	internal fillet to head bolt boss	6173813	Cyl 3	70.7E+6	Cyl 1	149.0E+6	109.9E+6	39.2E+6	0.89	3.53
AL	corner of side inlet to water jacket	6214185	Cyl 5	70.8E+6	Cyl 1	139.0E+6	104.9E+6	34.1E+6	0.98	3.54
AM	‘liner’ to top deck	6166821	Cyl 3	107.0E+6	Cyl 1	139.0E+6	123.0E+6	16.0E+6	0.98	2.86

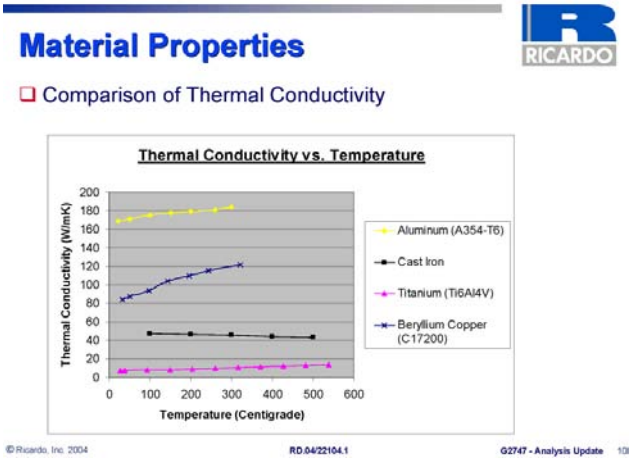

Figure 9. Ultimate tensile strength vs. temperature for four key diesel engine head and block alloys.

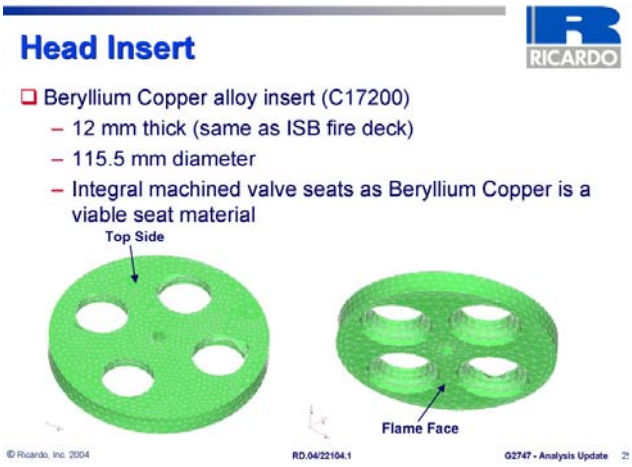

Figure 10. Thermal conductivity vs. temperature for four alloys.

Figure 11 shows the location of the insert in the flame face.

The FEA model was modified so that part of the back face of the insert makes direct contact with the coolant (Figure 12).

The engine with the Be-Cu insert was modeled with the engine up-rated to 450 hp from the standard 305 hp. This means that the peak cylinder pressure was increased from 2320 to 3191 psi. The block model showed that the Ti-6Al-4V alloy allowed the block to function acceptably at the new rating. The head temperatures were reduced in valve bridge regions from 709°C at 305 hp to 545°C at 450 hp (Figure 13). The temperature in the region of the valve seats is still about 50°C too high, but considering that this model assumes that the engine is run-

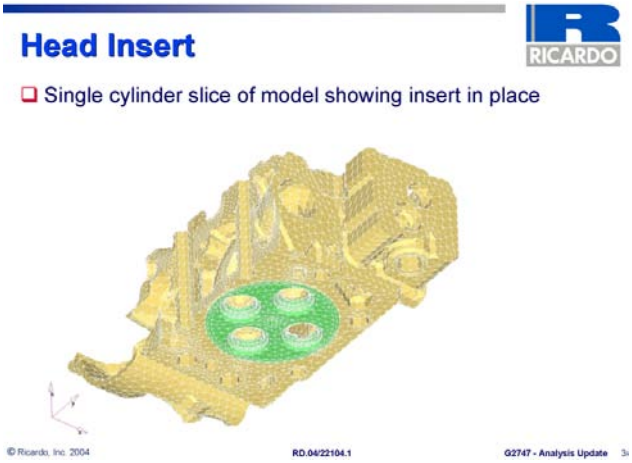

Figure 11. Solid model of the Be-Cu flame face insert.

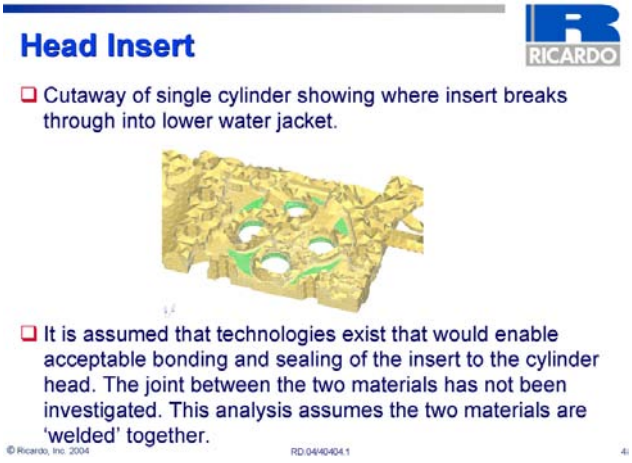

Figure 12. Location of the insert in the flame face.

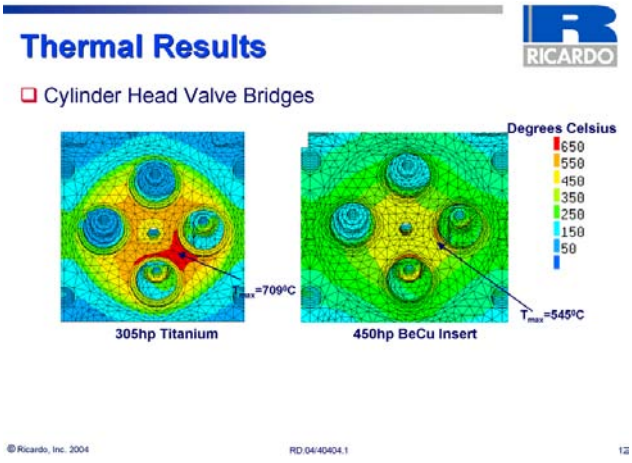

Figure 13. Model of the back face of the insert showing where the insert makes direct contact with the coolant (darker gray).

ning at 450 hp all the time, this temperature is considered acceptable from a feasibility standpoint.

Up-rated engine parameters:

- Maximum cylinder pressure increased from 160 to 220 bar (3191 psi). This was the only parameter changed.
  - — Power increased by 48% to 450 hp (current ISB—305 hp)
  - — All other engine operating conditions unchanged
- Speed: 2900 rpm
- AFR: 24.4:1
- Compression ratio: 17:1
  - — Flame face thermal boundary conditions have been modified to account for material changes. However, the baseline coolant side boundary conditions (obtained from computational fluid dynamics analysis at 305 hp) are unchanged because the coolant flow remains the same as a result of the engine speed.

Figure 14 shows a graph of the thermal expansion coefficients vs. temperature of the Ti alloy and the Be-Cu alloy. Note that the level Be-Cu is more than an order of magnitude greater than the Ti alloy. This leads to a high stresses at the interface between the Ti and the insert, as shown in Figures 15 and 16.

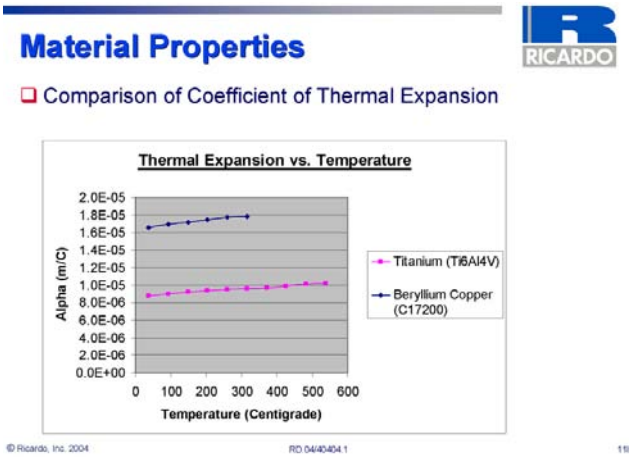

Figure 14. Description of up-rated engine parameters.

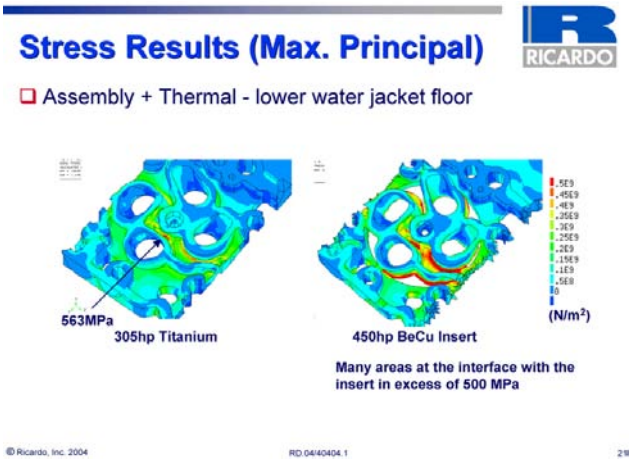

Figure 15. FEA model of the temperature distribution in the valve bridge area of the flame face for the Ti head rated at 305 hp and the Ti head with a Be-Cu insert.

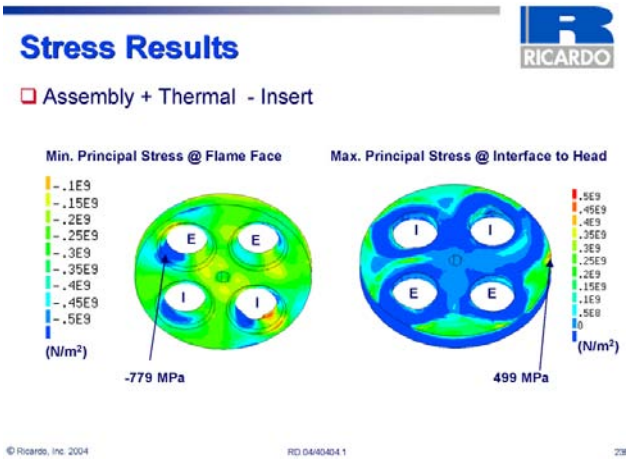

Figure 16. Coefficient of thermal expansion vs. temperature for Ti and Be-Cu.

The thermal results for the top of the block cylinder are shown in Figure 17. This region is the only location where the temperatures get high enough to be of concern.

Thermal Results Summary

- Using Ti-6Al-4V to replace cast iron in the engine block is feasible.
- Using Ti-6Al-4V to replace cast iron in the head poses some problems associated with the poor thermal conductivity of Ti compared with gray cast iron.

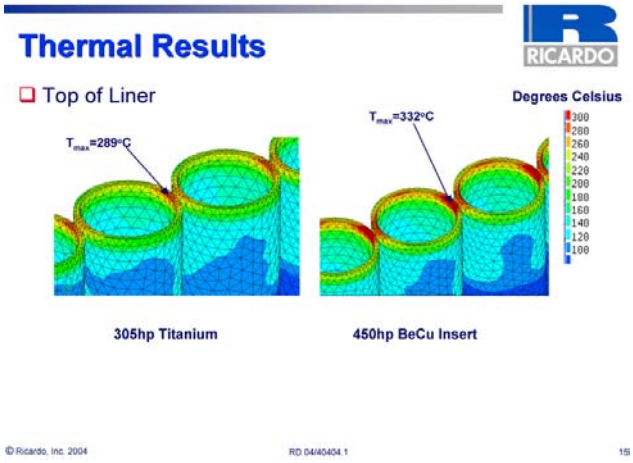

Figure 17. FEA model of the Ti alloy lower water jacket showing the principal stresses generated at the interface between the back face of the insert and the Ti as a result of the differences in thermal expansion coefficients of the two materials.

  - The valve bridge regions of the fire deck get to about 700°C, which is too high for acceptable durability.
  - The valve seats see too high a temperature for durable use.
- To take advantage of the Ti alloy's favorable properties for the block (lower weight and higher strength), the engine could be constructed with a Ti block and either a gray cast iron head or an aluminum head. This leads to the following limitations:
  - The weight advantages of using Ti for the engine are limited if a cast iron head is used.
  - A larger weight saving can be achieved by using Al for the head, but durability may be limited.

A novel approach to solving the high temperatures in the head of the "all Ti engine" was proposed: using a high-thermal-conductivity alloy as an insert in the valve bridge regions.

  - A 2% Be-Cu alloy was selected as the insert material for the purpose of FEA modeling.
  - Rather than model the insert at the normal 305 hp rating, the insert was modeled in an engine that was up-rated to 450 hp. This was done to determine if the use of Ti would allow engines normally designed for cast iron to be used at higher power ratings.
- The Be-Cu alloy insert resulted in a valve bridge temperature of 545°C when the engine was run at 450 hp (3190 psi peak cylinder pressure). Since this modeling run assumed that the engine was run at these values for its whole life, which is not the normal way an engine is used, it is concluded that the insert strategy is feasible for an up-rated Ti engine. Note that it is possible that increased coolant flow and some design changes may be needed to guarantee the durability of the engine.
- Owing to the large difference in the coefficients of thermal expansion of the Be-Cu and Ti alloys, large stresses are generated at the interface between the insert and the Ti lower water jacket.

Conclusions

- FEA modeling of stress, fatigue, and temperature shows that cast Ti–6Al-4V is a feasible replacement for gray cast iron in heavy-duty diesel engine blocks with cast iron liners, whether the engine is rated at the normal (305 hp) or a 50% higher level (450 hp).
- FEA modeling of stress, fatigue, and temperature shows that cast Ti–6Al-4V is a feasible replacement for gray cast iron in heavy-duty diesel engine heads rated at 305 hp if the high valve bridge temperatures can be overcome.
- FEA modeling shows that using a cast iron head or an Al head in conjunction with a Ti block is a feasible way of taking advantage of the high strength of Ti for the blocks without concern for high temperatures in the head for an engine rated at 305 hp. However, if a gray cast iron head is used, there will not be much of weight saving for the engine. If the head is made from Al, a great weight saving can be achieved, since Al is 54% lighter than Ti.
- FEA modeling shows that if a 2% Be-Cu insert is used to replace Ti in the valve bridge regions in the flame face for an engine that was up-rated by 50% (450 hp), the high temperatures in the flame face are reduced substantially, and it is feasible to use it at high power ratings.
- The high stresses generated at the interface between the insert and the Ti lower water jacket, caused by the differences in coefficients of

thermal expansion, can be overcome by some design changes.

Aluminum and Magnesium Feasibility Study

Aluminum

The FEA modeling for these studies was for the engine rated at 305 hp, which is the maximum for the production engine.

Thermal analysis

Table 10 provides the mechanical and physical properties of gray cast iron and the aluminum alloy, A354-T6 used in this modeling study.

Figure 18 shows the calculated temperatures in the valve bridge region of the fire deck for the production cast iron engine and for the engine having an Al head and block. Owing to the very high thermal conductivity of Al, the maximum temperature in the valve bridge region is only slightly above 200°C, well below Ricardo's recommendation for maximum temperature in this region. Figure 19 shows the calculated temperatures for the top of the engine block for both the cast iron production engine (parent bore) and the Al engine. Again, the temperatures at the top of the Al block are well below any level of concern.

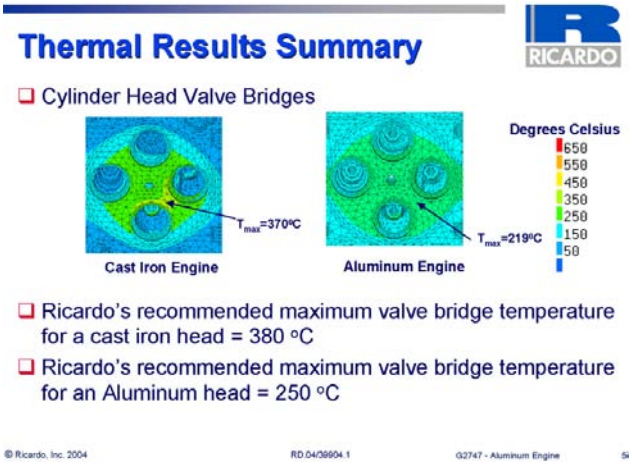

Figure 18. FEA model of the Be-Cu insert showing the stresses generated in the Be-Cu insert caused by the differences in thermal expansion coefficients between the Ti alloy head and the insert when the engine is run at 450 hp.

Table 11 shows a summary of temperatures at key locations in the head and block for cast iron and

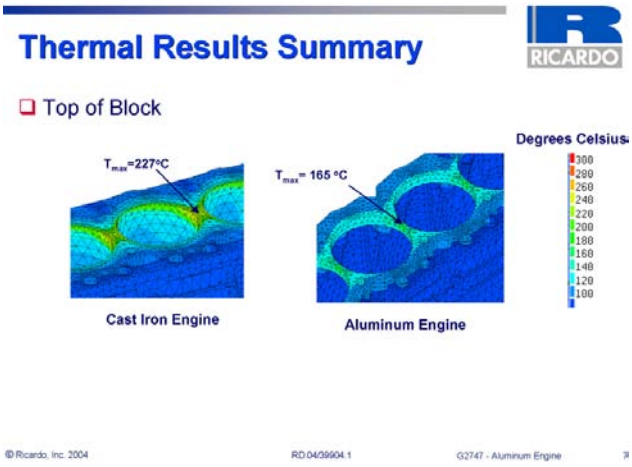

Figure 19. Computed temperatures at the top of the cylinder liner for the Ti engine rated at 305 hp and at 450 hp.

Table 11. Computed temperatures at key locations in the head and block for cast iron and aluminum

Location	All-cast-iron engine	All-aluminum engine
Top of block	227	165
Top of liner	230	192
Cylinder head exhaust valve bridge	370	210
Intake valve seat	357	249
Exhaust valve seat	444	325

Al. FEA modeling of high cycle fatigue was performed on the Al head and block and compared with modeling for cast iron. Figure 20 shows an example of the model for cover factors (safety margin) greater than 1 (no failure). It can be seen that the aluminum compares very favorably with the cast iron.

FEA modeling of fatigue was performed for the block. The cover factors at key locations on the aluminum block were compared with those locations on the cast iron production block (see Table 12). With the exception of one location, the cover factors for the aluminum block were equal to or greater than those for the cast iron block. The one exception is the region from the bearing saddle to the block fillet (location AJ), shown in Figure 21. The cover factor in this region can easily be increased by making the fillet region thicker. The higher fatigue cover factors of Al compared with cast iron are caused by lower temperatures, lower thermal stresses, and the higher strength of aluminum. The low cover factors near the head bolt bosses are caused by high compressive

Table 10. Mechanical and physical properties of gray cast iron and A354-T6

Gray cast iron (liner insert)

Temperature (Centigrade)	Young's modulus (GPa)	Poisson's ratio	Thermal conductivity (Wm-K0	Thermal expansion (μm/m-C)	Ultimate tensile strength (MPa)	Compressive yield strength (MPa)	Tensile yield strength (MPa)	Fatigue strength (MPa)
20.0	117.2	0.25	48.80	1.10E-05	189.6	284.4	136.5	72.4
200.0			47.80	1.10E-05				
300.0			46.80					
400.0			45.80	1.25E-05				
500.0			44.80					

Aluminum (A3540-T6) – Data supplied by Cummins, Inc.

Temperature (Centigrade)	Young's modulus (GPa)	Poisson's ratio	Thermal conductivity (Wm-K0	Thermal expansion (μm/m-C)	Ultimate tensile strength (MPa)	Compressive yield strength (MPa)	Tensile yield strength (MPa)	Fatigue strength (MPa)
20.0	76.1	0.33	168.80	2.03E-05	265.2	233.8	241.3	95.5
50.0			170.90					
100.0			175.50	2.09E-05				
150.0	62.1	0.33	177.60		213.3	216.7	205.0	76.8
175.0	65.6	0.33			204.1	212.6	201.7	73.5
200.0	66.7	0.33	179.80	2.16E-05	202.5	215.6	199.1	72.9
260.0	54.5	0.33	180.80		142.7	142.2	142.7	51.4
300.0				2.24E-05				

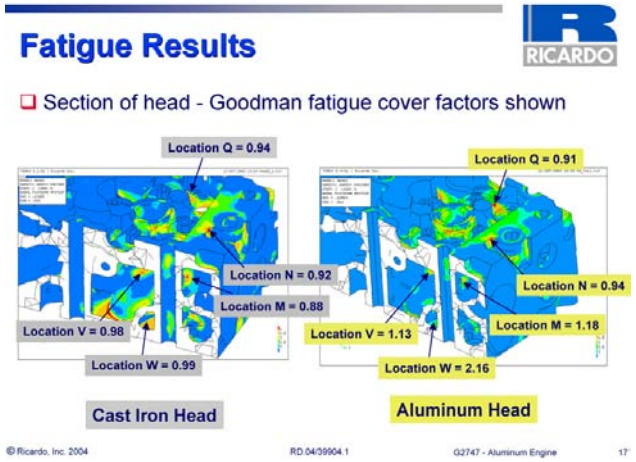

Figure 20. FEA model of temperatures in the valve bridge region of the fire deck for the production cast iron engine and the Al engine.

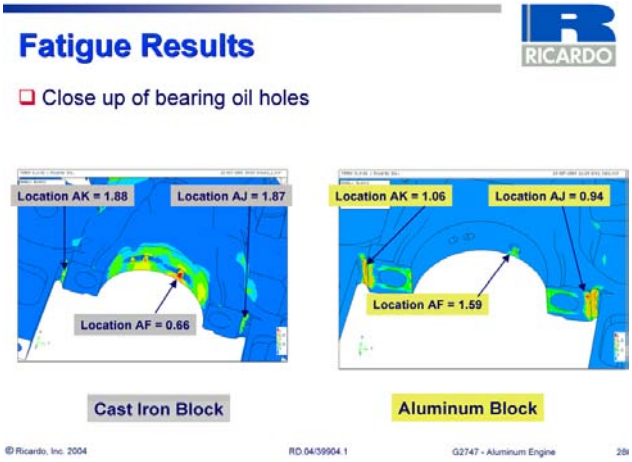

Figure 21. FEA calculations of temperature at the top of the engine block for the cast iron production engine and for the Al block.

Table 12. Fatigue cover factors at key locations of the cast iron and aluminum blocks

		Cast iron	Aluminum
Location	Description	Fatigue cover factor	Fatigue cover factor
AE*	interior fillet to top deck @ end face	0.12	0.13
AF	oil hole edge to brg. shell	0.66	1.59
AG	corner of side inlet to water jacket	0.87	1.04
AH	internal fillet to head bolt boss	0.89	0.89
AI	corner of side inlet to water jacket	0.98	1.26
AJ	Bearing saddle to block fillet	1.87	0.94
AK	Bearing saddle to block fillet	1.88	1.06

*Model geometry found not to be representative of actual casting

stresses induced by bolt loads. Washers under the bolt heads to reduce embedment are a possible solution to this issue.

Conclusions

- Aluminum can be a viable substitute for cast iron in this and many other diesel engines, resulting in at least an overall engine mass reduction of about 20%.
- Some design changes would be needed for the Al engine to
  - — support the cast iron liner
  - — increase the stiffness of the cylinder head top deck
  - — modify the interference fits between valve seat inserts and the head
- Since Al has no fatigue endurance limit, it would be prudent to determine acceptable life targets so as not to have cracking after many miles or hours of use.

Magnesium

An FEA study of Mg, identical to the one for Al, was conducted to determine if Mg is a feasible replacement for cast iron in heavy duty diesel engine heads and blocks. The FEA analysis was performed on the same Cummins ISB engine at 305 hp, but with cast iron cylinder liners.

From previous analyses, it was considered important that a Mg alloy be selected that had maximum elevated temperature properties. A high-performance Mg casting alloy, WE-43, was selected for the study. Table 13 contains the composition of the alloy along with T-6 heat treatment details.

Table 13. Composition and heat treatment of WE-43 Mg alloy

• Composition • Yttrium 3.7 – 4.3 - Rare Earths (Ce,La,Nd) - 2.4 – 4.4 - Zirconium 0.4 min.	• Optimum heat treatment - Solution treat for 8 h at 525°C. - Air cool, hot water or polymer quench. - Age for 16 h at 250°C, air cool

Table 14 shows a comparison between the mechanical and physical properties of cast iron and WE-43, while Figure 22 is a graph of the thermal conductivities of cast iron and WE-43 vs. temperature.

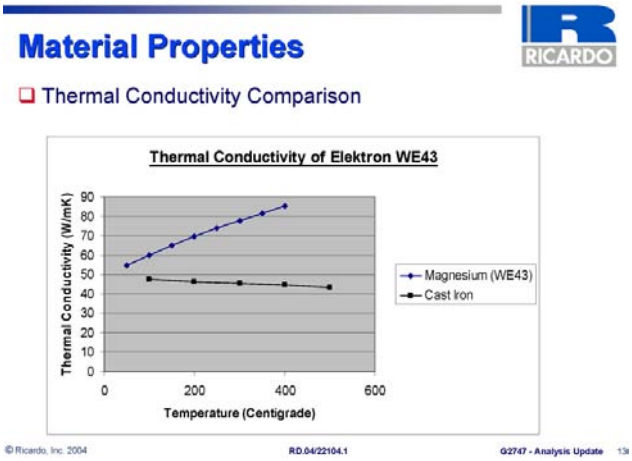

Figure 22. FEA model of the cast iron and aluminum heads showing fatigue cover factors in key locations.

The FEA of the valve bridge region of the head is shown in Figure 23 for production cast iron and for WE-43. It can be seen that although the temperature of the valve bridge region in the Mg head is lower than for the gray cast iron, it is 60°C above the maximum recommended use temperature for this alloy. Figure 24 shows the FEA temperature predictions for the top of the block. It shows that there are no temperature issues with using Mg for the block.

Fatigue cover factors were calculated for the Mg head and compared with those for the production cast iron head. The data are shown in Table 15. With one exception, location N, the cover factors for Mg (WE-43) are the same or higher than for the cast iron and are nearly the same at location N. FEA analysis of fatigue cover factors for the Mg block at key locations is summarized in Table 15. The cover factor for the Mg block is higher or the same in all key locations, compared with the cast iron block. Location AE is low no matter which material is used: cast iron, Ti, Al, or Mg. It can be raised by adding more material to that location.

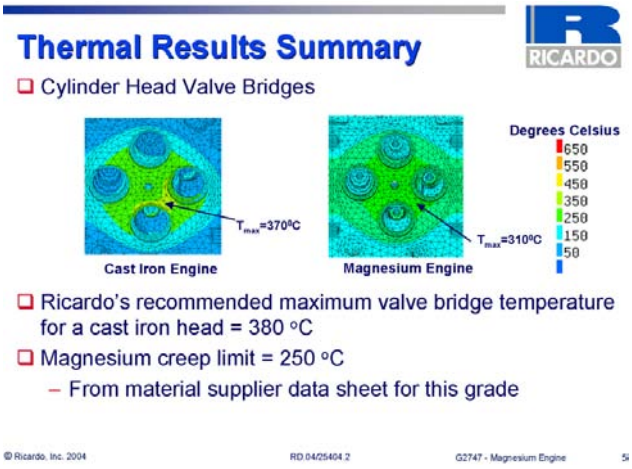

Figure 23. FEA model of the cast iron and aluminum blocks showing cover factors at key locations.

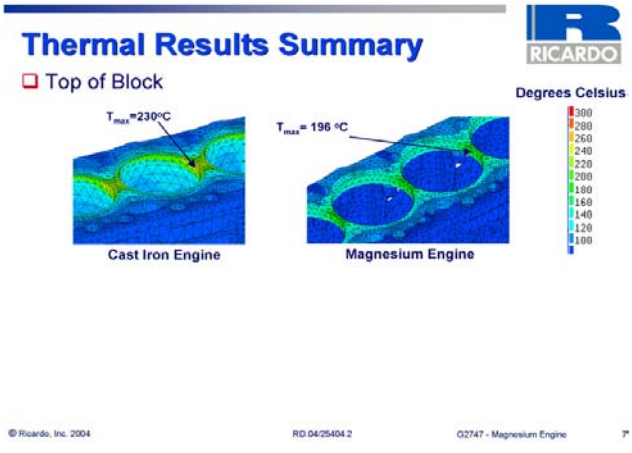

Figure 24. Thermal conductivity vs. temperature for WE-43 and grey cast iron.

Conclusions

FEA has shown that it is feasible to substitute a high-performance Mg casting alloy, WE-43, for gray cast iron in heavy-duty diesel engine heads and blocks, for a potential overall engine weight savings of over 30%. However, to do this, certain issues must be addressed:

- Compressive yielding is likely to occur in the valve bridge areas of the flame face of the head

Table 14. Mechanical and physical properties of gray cast iron and Mg (WE-43)

Gray cast iron (liner insert)

Temperature (Centi-grade)	Young's modulus (GPa)	Poisson's ratio	Thermal conduc-tivity (Wm-K0	Thermal expan-sion (μm/m-C)	Ultimate tensile strength (MPa)	Compressive yield strength (MPa)	Tensile yield strength (MPa)	Fatigue Strength (MPa)
20.0	117.2	0.25	48.80	1.10E-05	189.6	284.4	136.5	72.4
200.0			47.80	1.10E-05				
300.0			46.80					
400.0			45.80	1.25E-05				
500.0			44.80					

Magnesium (WE43-T6).

Temperature (Centi-grade)	Young's modulus (GPa)	Poisson's ratio	Thermal conduc-tivity (Wm-K0	Thermal expan-sion (μm/m-C)	Ultimate tensile strength (MPa)	Compressive yield strength (MPa)	Tensile yield strength (MPa)	Fatigue Strength (MPa)
20.0	44.1	0.27	51.30	2.67E-05	265.0	185.0	185.0	91.0
150.0	42.0	0.27	64.80	2.92E-05	250.0	175.0	175.0	83.0
200.0	39.0	0.27	69.50		245.0	170.0	170.0	
250.0	36.0	0.27	73.80	3.00E-05	220.0	160.0	160.0	62.0
300.0	36.0	0.27	77.90		160.0	120.0	120.0	
350.0			81.70					
400.0			85.20					

Table 15. Fatigue cover factors at key locations in the head for cast iron and Mg (WE-43)

Location	Description (lwj = lower water jacket) (uwj = upper water jacket)	Cast iron Fatigue cover factor	Aluminum Fatigue cover factor
A	uwj fillet between bolt boss and valve guide	0.53	0.58
B	lwj floor fillet between exh. port and inj. bore	0.61	1.01
C	lwj floor fillet to exhaust port	0.65	1.07
D	lwj roof fillet to head bolt boss	0.68	0.75
E	uwj roof fillet to head bot boss	0.69	0.73
F	lwj floor fillet to exhaust port	0.72	1.05
G	intake port to valve seat area	0.72	1.50
H	lwj roof fillet to head bolt boss	0.75	0.98
I	exterior o exhaust side near flame deck	0.81	1.14
J	uwj roof fillet to head bolt boss	0.82	0.94
K	uwj roof fillet to head bolt boss	0.86	0.93
L	lwj roof fillet to head bolt boss	0.88	1.18
M	uwj fillet between head bolt boss exhaust port	0.88	1.04
N	exterior pocket @ top deck near head bolt boss	0.92	0.88
O	uwj roof fillet to top deck	0.93	0.98
P	lwj fillet – valve guide to fuel drilling	0.94	1.57
Q	top deck rib between guides	0.94	0.98
R	lwj floor between exh. Ports and inj. bore	0.95	1.34
T	Exterior pocket @ top deck near head bolt boss	0.96	1.08
U	uwj roof to coolant hole	0.96	1.01
V	lwj fillet – exh. guide to exh. port	0.98	1.09
W	lwj floor fillet to exhaust port	0.99	1.47

as a result of high temperatures coupled with high stresses. Low cycle fatigue or creep could be the result.

- Ways to reduce the temperature in the valve bridges to below 250°C must be explored. Some ideas are
  - — design changes to reduce the stresses in the area
  - — thinning of the fire deck to improve cooling
  - — higher coolant flow to accommodate the heat flow
  - — slight de-rating of the engine so less heat and lower stresses would be generated in the area
- Other design changes should be explored in order to modify the interference fit between the valve seat inserts and the head and to bolster the support for the cast iron liner.
- An alternative to making the design changes is to use an Al head on the Mg block.
- Mg is well known as a metal that promotes galvanic corrosion. Should the engine contain substantial amounts of Mg, then the issues of galvanic corrosion must be explored.

Conclusions of Overall Study

- FEA modeling of a Cummins ISB 5.9-L diesel engine has shown that all three lightweight alloys, Ti-6Al-4V, A354-T6 (Al), and We-43 (Mg), are feasible substitutes for gray cast iron in a heavy duty diesel engine. The modeling incorporated a gray cast iron liner in the block for the lightweight alloys because the production cast iron engine has no liner (parent bore). The liner acts in two ways: it provides a viable tribological surface for the piston rings, and it makes the study more generic and less engine-specific.
- Each lightweight material posed unique challenges to making the material work in this engine:
  - — The Ti alloy could be used as a direct substitute for cast iron in the block when the engine was rated at either 305 hp, as designed, or up-rated to 450 hp.

- The Ti alloy posed a problem in the valve bridge region of the fire deck of the head because of its low thermal conductivity. It was shown that if a Be-Cu insert were employed in that region, it would be feasible to use Ti when the engine was up-rated to 450 hp. This strategy would allow for a 10% weight saving and an up-rating of 50%.
- Using the Al alloy for the head and block would allow for a 20% weight saving. FEA of the engine rated at 305 hp showed that Al is a feasible substitute for gray cast iron. Note that since Al has no fatigue endurance limit, life cycle analysis needs to be performed to determine when to use this material.
- It is feasible to substitute a high-performance Mg alloy for gray cast iron in this engine rated at 305 hp. However, the temperatures and stresses in the valve bridge areas of the fire deck in the head are slightly too high and need to be reduced. This can be done by increased coolant flow, some design changes, or a slight de-rating of the engine.

Presentations

Presentation to TACOM, March 2004.

Presentation to Cummins Engine Co., April 2004

Presentation to Caterpillar, April 2004.

Presentation at a low-cost Ti users conference sponsored by the Defense Advanced Research Projects Agency, April 2004.

P. Mechanical Behavior of Ceramic Materials for Heavy-Duty Diesel Engines

Andrew A. Wereszczak
Ceramic Science and Technology Group (CerSaT)
Oak Ridge National Laboratory
PO Box 2008, MS 6068,
Oak Ridge, TN 37831-6068
(865) 576-1169; fax: (865) 574-6098; e-mail: wereszczakaa@ornl.gov

DOE Technology Development Area Specialist: Dr. Sidney Diamond
(202) 586-8032; fax: (202) 586-1600; e-mail: sid.diamond@ee.doe.gov
ORNL Technical Advisor: D. Ray Johnson
(865) 576-6832; fax: (865) 574-6098; e-mail: johnsondr@ornl.gov

Contractor: Oak Ridge National Laboratory, Oak Ridge, Tennessee
Prime Contract No.: DE-ACo5-00OR22725

Objective

- Characterize and model contact-induced damage mechanisms in ceramics and link them to microstructure and ultimately to wear performance, the optimization of machining, rolling contact fatigue, etc.
- Characterize the influence that independent parameters such as grain size, loading rate, confinement or residual stresses, temperature, and field effects have on the evolution of contact-induced damage.

Approach

- Develop and use instrumented static and dynamic indentation and instrumented scratch test methods to interrogate quasi-plasticity and fracture processes in ceramics.
- Model contact-induced quasi-plasticity and fracture processes.
- Link damage mechanism activity to wear performance, machining, contact fatigue, etc.
- Develop strategies for engineering control (e.g., confinement, temperature) that promote the dominance of one mechanism (e.g., one that causes strengthening or hardening) over others.

Accomplishments

- Established dynamic indentation and instrumented scratch testing facilities.
- Nearly completed indentation rate effect studies on several silicon nitride ceramics.
- Developed an ANSYS model that enables the study of indenter depth-of-penetration in a target material while considering elastic and yield properties of the indenter and target material, indenter diameter, etc.).

Future Direction

- Characterize the influences that grain size and residual/confinement stress have on damage evolution.
- Link indentation-induced damage evolution to that produced by scratch testing.
- Add tension-compression strength/yield anisotropy effects to indentation model.

Introduction

More ceramic components could be used in engines and transportation systems if they could be confidently used in more wear-related applications and if they could be manufactured and machined faster (i.e., more cost-effectively). This would occur if contact-induced damage mechanisms (which limit their mechanical performance or dictate their machinability) were understood, predictable, and controlled.

This project quantifies the loads and stresses associated with the initiation of quasi-plasticity and fracture processes in ceramics, using instrumented indentation and scratch testing. Understanding the competition and interaction among those processes is a critical part of this project as well. Though more traditional structural ceramics (e.g., Si_3N_4 and ZrO_2) under consideration for diesel engine components are the primary focus, other classes of ceramics and brittle materials that could provide greater understanding of damage evolution fundamentals are also studied. These include cubic oxides and non-oxides, nanoceramics and nanocermets, piezoelectric ceramics, and micaceous ceramics.

Through quantifying the loads or stresses that initiate quasi-plasticity and fracture, contact-induced damage mechanisms in ceramics are characterized; modeled; and linked to microstructure and ultimately to wear performance, optimization of machining, rolling contact fatigue, etc. Additionally, the influence of independent parameters such as grain size, loading rate, confinement or residual stresses, temperature, and field effects on the evolution of contact-induced damage are examined. A thorough understanding of the competition of fracture and quasi-plasticity in ceramics will enable improved and faster means of manufacturing ceramic components and surface engineering (e.g., ductile regime machining) and will maximize mechanical performance in cases when surface conditions (e.g., bending) or surface-located events (e.g., wear, impact) are service-life limiters in engine and transportation system components.

Approach

FY 2004 was the first full year of this project, and numerous parallel efforts were initiated. The project has five primary elements; three represent ongoing and near-term efforts, and the other two represent longer-term efforts. The first element is to develop and use instrumented static and dynamic indentation and instrumented scratch test methods (see Figure 1) to interrogate quasi-plasticity and fracture processes in ceramics. Second, contact-induced quasi-plasticity and fracture processes are modeled. Third, ceramic materials are characterized that either are of strategic relevance to heavy-duty diesel engine components or serve as model materials for the examination of damage evolution. Fourth, damage mechanism activity is linked to wear performance, machining, contact fatigue, etc. Finally, strategies are developed for engineering control (e.g., confinement, temperature) that promote the dominance of one mechanism (e.g., one that causes strengthening or hardening) over others.

Results

In order to quantify quasi-plasticity and fracture processes, instrumented static and dynamic indentation test systems were established in FY 2004, as well as instrumented scratch testing capabilities. Each of the instruments is shown in Figure 1a–c, and are all in use to experimentally characterize quasi-plasticity and fracture processes. A dedicated acoustic emission (AE) system is interfaced with all these instruments and is used to detect damage processes that result during indentation or scratch testing.

An example of a Hertzian indent is shown in Figure 2. The depth of the crater-like indent is an indication that quasi-plasticity was initiated. A circular ring crack and a median crack (2 and 8 o'clock positions) are indications that at least two different crack systems were initiated. The loads and indenter depth-of-penetration associated with the initiation of the damage mechanisms are measurable using the static instrumented indentation test system (IITS) and the dynamic indentation test systems (DITS). Their values are compared with those for other ceramics and interpreted with respect to traditionally measured mechanical properties, such as hardness, fracture toughness, and tensile strength.

AE testing and analysis was an integral part of the indentation testing because it can be efficiently used to identify the loads associated with the initiations of cracks (i.e., fracture processes). Measured load-unload histories and the loading predicted by finite element analysis (FEA) provide a reference to the AE interpretation. For example, for the spherical indent-generated ring cracks formed in the concentric pattern shown in Figure 3a, the AE spectrum

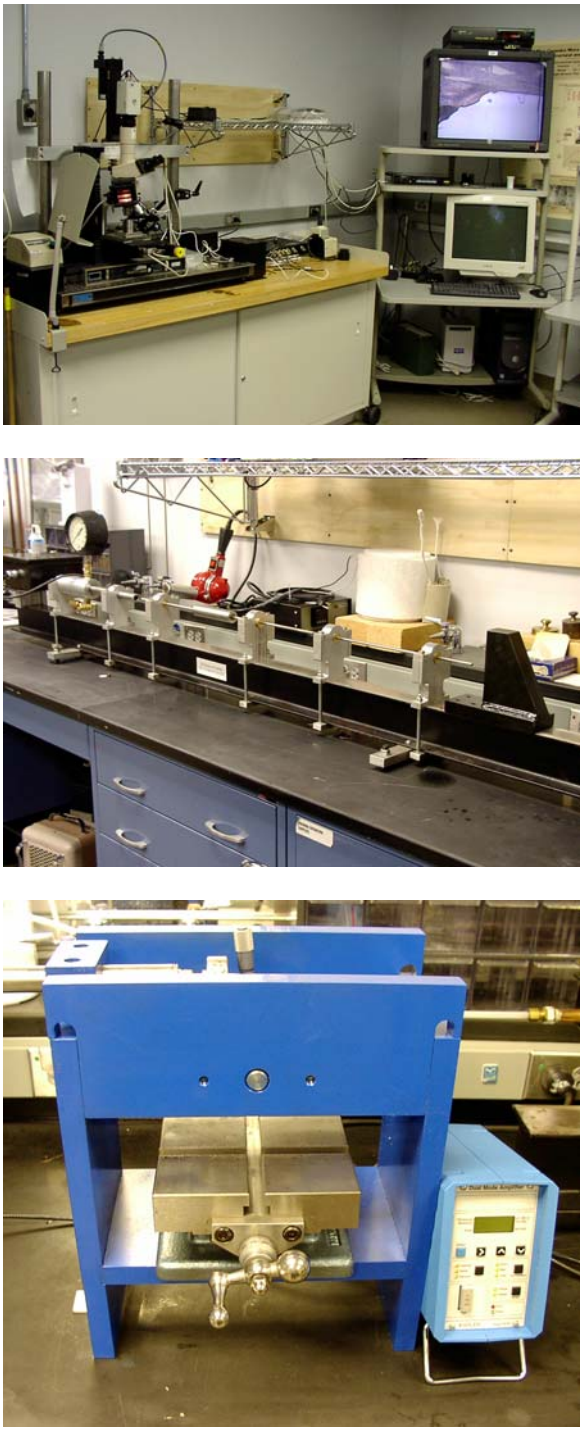

Figure 1. Facilities established included instrumented static (a) and dynamic (b) indentation test systems and a scratch tester (c).

(Figure 3b) shows that numerous acoustic events had occurred, with some events having greater amounts of energy than others (e.g., the event that occurred at ~ 175 N). Additionally, acoustic events

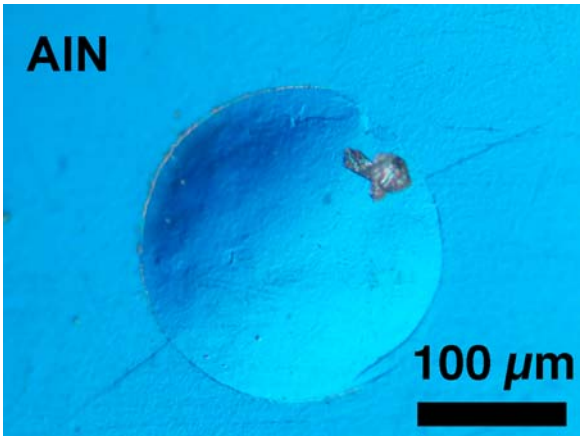

Figure 2. Hertzian indent illustrating quasi-plasticity (dimple) and fracture processes (ring and median crack). Indent was generated with a 2.25-mm-diam diamond indenter and 300 N maximum load.

did not occur until a load of ~ 48 N, indicating that the material behaved elastically below that load. The load at which divergence of the black and red curves (i.e., where permanent damage is introduced) occurred in the indenter depth-of-penetration load curve matches fairly well with the load where acoustic signals begin to be produced, and the load where the highest-energy acoustic peak occurred matches the load on the experimental loading curve (black curve) where the slope arguably begins to increase (i.e., a relatively large increase in specimen compliance).

The DITS and instrumented (pendulum) scratch tester were interfaced with a high-speed data acquisition system, and experimental familiarity was gained with both testers. Gas gun settings, shape pulsing, and overall test approaches were optimized with the dynamic indenter to produce controllable low-load dynamic indentations (i.e., a few to tens of Newtons). Also, an ability to test specimens having a nominal geometry of 3×4×4 mm (a specimen cut from conventional ASTM C1161B bend bars—a geometry that is readily available for many materials in the Ceramic Science and Technology Group) was established with the scratch tester. The specimen holder that came with the instrument (which also houses two load cells for normal and thrust force measurements) was designed to test specimens having the geometry of a ¼-in. (6.35-m) cube—an inconvenient size.

An indentation model was developed using ANSYS FEA software that predicts the stress state

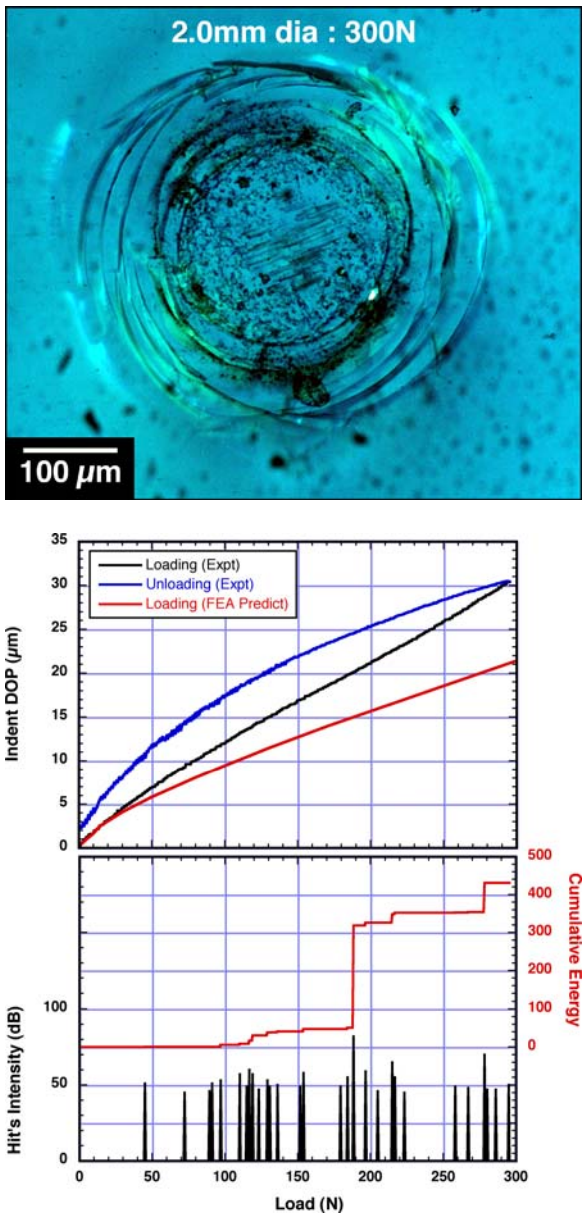

Figure 3. Hertzian indent of a soda lime glass (a), and (b) its measured load-unload waveform compared with the predicted loading waveform and the acoustic emission history associated with the generated crack pattern. The indent was generated with a 2.0-mm-diam diamond indenter and 300 N maximum load.

in a material subjected to Hertzian (spherical) indentation. An illustration of the model is shown in Figure 4 with a predicted response shown in Figure 5. Independent parameters that may be considered in the model are elastic properties and hardness (i.e., yielding) of the target or indenter material, indenter diameter, coefficient of friction, confinement pressure, and, of course, applied indenter load. In-

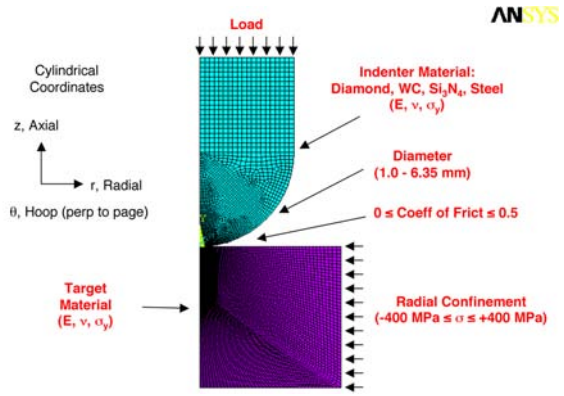

Figure 4. ANSYS Hertzian indentation model.

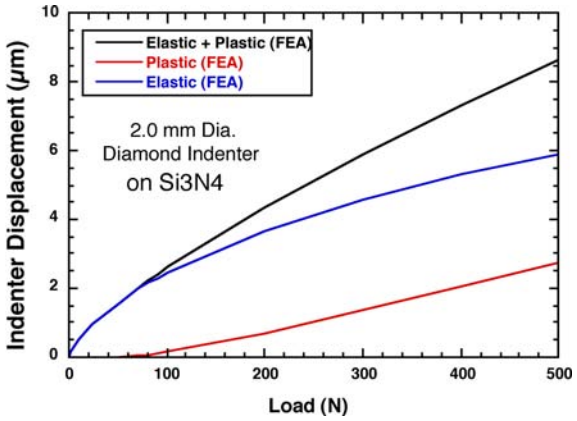

Figure 5. Example of predicted indentation response. The total indent-depth-of-penetration (top curve) is the sum of elastic (middle curve) and permanent deformation (bottom curve).

terpretation of the von Mises and First Principal tensile stresses is enabling the study of the competition between plasticity and fracture processes in the test material (linkable to machining and wear phenomena), and the results are being correlated to experimental observation.

μ-FEA, a microstructure-based FEA computer program, was developed and its copyrighting is under way through ORNL's Technology Transfer and Economic Development organization. *μ-FEA* is a graphics-user-interfaced LabVIEW executable program that serves as a pre- and post-processor to the ANSYS FEA solver, and it enables stress analyses of both real (e.g., imaged with scanning electron microscopy or optical microscopy) and simulated material microstructures. An example of an analyzed microstructure and its subsequent residual stress calculation is shown in Figures 6a and b. For one of its applications, *μ-FEA* is being used to study stress concentrators, deformation, and microcracking

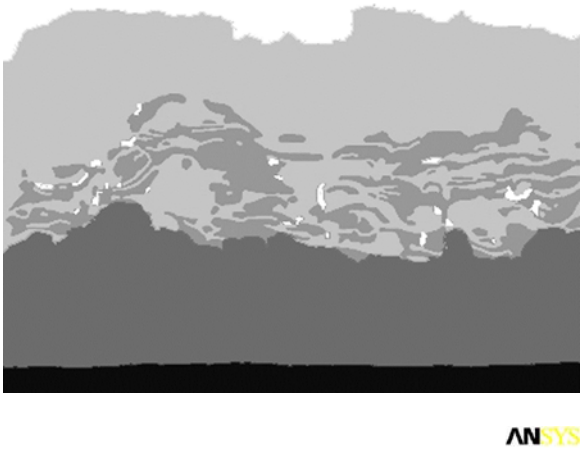

Figure 6. Digital microstructure of (a) coating and (b) μ-FEA residual stress evaluation induced from thermal expansion mismatches between material constituents.

around pores and large grains and in secondary phases in materials subjected to a Hertzian contact stress gradient.

Silicon nitride specimens of Ceralloy 147-31N, NBD200, SN101C, NC132, and TSN-03NH were sectioned and either underwent or are undergoing instrumented static and dynamic indentation and instrumented scratch testing. An apparent rate dependence (i.e., quasi-plasticity rate dependence) on Vickers Hardness for Ceralloy 147-31N is shown in Figure 7. There is a rationale behind the choice of testing each silicon nitride composition. The 147-31N grade is presently used as a cam roller follower material, so interest exists in quantifying its indentation and scratch responses. NBD200, SN101C, and TSN-03NH are ball bearing grades, so their testing is relevant to the examination of rolling contact fatigue behavior. NBD200 is a NIST standard reference material for Knoop hardness, and NC132 is a

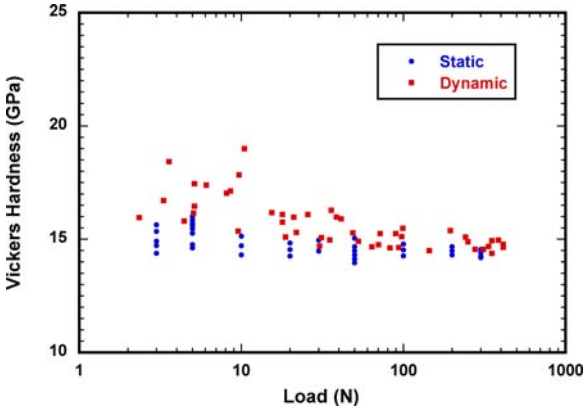

Figure 7. Static and dynamic Vickers hardness of Ceralloy 147-31N as a function of indentation rate.

NIST standard reference material for fracture toughness, so they serve as references for performance comparison among all the silicon nitrides.

To examine the effect of grain size on damage due to cracking and quasi-plastic yielding generated with instrumented indentation and scratch testing, three different mean-grain-sized (2–3, 15, and 25 μm) aluminas were acquired (Ceradyne, Costa Mesa, CA). Microstructures of the three materials are shown in Figure 8. The alumina has 99.9% purity, has magnesium as a sintering aid, and has relatively narrow size distributions. Alumina was chosen as the model material in which to examine grain size effects because of the ease associated with measuring residual stresses on it using optical fluorescence, and because of the immediate availability of such an analytical tool. Residual stresses will be measured in, around, and under generated indents and scratches, and the results will likely prove to be valuable for interpreting grain size effects on cracking and quasi-plasticity.

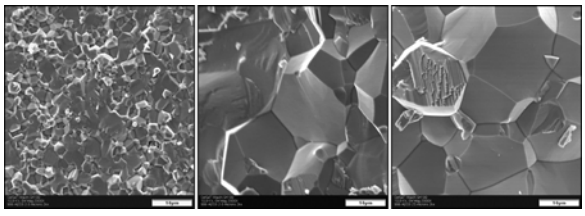

Figure 8. Microstructures of 99.9% alumina with average grain sizes of (left) 2–3 microns, (middle) 15 microns, and (right) 25 microns.

The effects of confinement (i.e., pressure) on instrumented static and dynamic indentation, instrumented scratch testing, and the competition of

fracture and quasi-plastic damage mechanism behaviors are under examination. The 99.9% alumina is being machined, and metal sleeves/tubes will be shrink-fitted about it to produce a radial confinement. The residual stress field on the surface of the radially confined alumina will be quantified using optical fluorescence; and the static, dynamic, and instrumented scratch testing will commence on it. Because the aluminas described will also serve as the model materials for this examination, grain size will also be an independent parameter in this confinement effect study. If confinement introduces beneficial effects related to damage associated with indentation or scratch testing, then the characterization of that effect will lead to its implementation into grinding or wear applications.

Experimental strategies are being pursued to enable the study of the effect of temperature on instrumented static and dynamic indentation and instrumented scratch testing. The characterization of this effect will have a direct link to optimizing heat-assisted machining of ceramic materials or promoting minimized surface damage that will result in improved wear resistance and strength.

Conclusions

Static and dynamic indentation and instrumented scratch testing facilities were established to quantify the loads and stresses associated with the initiation of quasi-plasticity and fracture processes. Numerous silicon nitride ceramics are under investigation, and rate effects on hardness (i.e., quasi-plasticity) are evident. An ANSYS model was developed that enables the study of indenter depth-of-penetration in a target material while considering elastic and yield properties of the indenter and target material, indenter diameter, etc. A microstructure-based FEA software (μ-FEA) was developed to enable stress analysis characterization at the microstructural scale and to help with the interpretation of quasi-plastic and fracture processes.

FY 2004 progress provides a nice springboard for planned FY 2005 work. The influences that grain size and residual/confinement stress have on damage evolution will be characterized. Indentation-induced damage evolution produced by scratch testing will be linked to that generated from static and dynamic indentation. Tension-compression strength/yield anisotropy effects will be added to the indentation model and will enable the study of how (or if) hardness is linked to quasi-plasticity and how (or if) tensile strength and fracture toughness are linked to fracture processes.

Publications/Presentations

"Evaluation of Ceramic Deformation Processes Through Hertzian Indentation," presented at the Tank and Automotive Research Development and Engineering Center-ORNL-Army Research Laboratory Advanced Materials Meeting, Network Computing Services, Minneapolis, February 5, 2004.

"ORNL Characterization of Ceramics for Armor, Transportation, and Energy Applications," presented at Cercom, Inc., Vista, CA, February 25, 2004.

"ORNL Characterization of Ceramics for Armor, Transportation, and Energy Applications," presented at Ceradyne Inc, Costa Mesa, CA, February 26, 2004.

"Evaluation of Ceramic Deformation Processes Through Instrumented Hertzian Indentation," presented at 2004 Interagency Coordinating Committee on Structural Ceramics, National Science Foundation, Arlington, VA, April 14, 2004.

"Evaluation of Ceramic Deformation Processes Through Hertzian Indentation," presented at Saint-Gobain, Worcester, MA, August 3, 2004..

Copyrights

μ-FEA, a microstructure-based finite element analysis computer program, was developed and is undergoing copyrighting through ORNL's Technology Transfer and Economic Development organization. *μ-FEA* is a graphics-user-interfaced LabVIEW™ executable program that serves as a pre- and post-processor to the ANSYS finite element analysis solver and enables stress analyses of both real (e.g., imaged with scanning electron microscopy or optical microscopy) and simulated material microstructures.

Q. Powder Processing of Nanostructured Alloys Produced by Machining

S. Chandrasekar, K. P. Trumble, and W. D. Compton
College of Engineering
Purdue University, IE, GRIS
315 North Grant Street
West Lafayette, IN 47907-2023
(765) 494-3623; fax: (765) 494- 5448; e-mail: chandy@purdue.edu

DOE Technology Development Area Specialist: Dr. Sidney Diamond
(202) 586-8032; fax: (202) 586-1600; e-mail: sid.diamond@ee.doe.gov
ORNL Technical Advisor: D. Ray Johnson
(865) 576-6832; fax: (865) 574-6098; e-mail: johnsondr@ornl.gov

Contractor: Oak Ridge National Laboratory, Oak Ridge, Tennessee
Prime Contract No: DE-AC05-00OR22725
Subcontractor: Purdue University, West Lafayette, Indiana

Objective

- Develop manufacturing technologies for creating advanced nanostructured alloys with enhanced mechanical properties for transportation applications.

Approach

- Create nanostructured chips by machining alloys of aluminum, titanium, and iron under controlled machining conditions.
- Characterize microstructure and mechanical properties of the nanostructured chips.
- Develop methods for converting the nanostructured chips into particulates suitable for processing into bulk forms.
- Develop powder processing methods, including shear-based densification (e.g., extrusion, rolling, forging) and infiltration processing, for creating monolithic and composite materials in bulk form with nanocrystalline microstructure.
- Characterize microstructure, mechanical properties, and performance of the bulk forms.

Accomplishments

- Produced nanostructured chips of a variety of alloys and metals—including Al6061-T6, copper, iron, commercially pure titanium, stainless steel and Inconel—by machining. The nanostructured chips are up to three times as hard as the bulk material.
- Achieved typical grain sizes in the chips of 50–700 nm, depending on the strain and temperature induced by the machining.
- Consolidated cylindrical bulk samples of nanostructured Al-6061T6/pure aluminum composites by powder extrusion. Densification in excess of 95% has been obtained while retaining the hardness of the nanocrystalline structures.
- Fabricated bulk samples of nanostructured Al-6061T6, with small amount of polymer as binder, by infiltration and pressing.

Future Direction

- Continue development of shear-based densification and infiltration methods to produce bulk monolithic and/or composite alloy samples with nanocrystalline microstructure, using the chips as precursor materials.
- Characterize microstructure and properties of the bulk forms to demonstrate retention of the nanostructures and enhanced mechanical properties.
- Determine tensile strength, ductility and density of the bulk forms to demonstrate integrity of the consolidated alloy samples.
- Identify 1–2 applications in the transportation sector for prototype development.

Introduction

It has been widely reported that nanostructured materials, composed of nanometer-scale grains, have properties significantly different from those of conventional materials.[1,2] These properties include higher hardness, strength and ductility, and superplasticity at relatively low temperatures and sintering temperatures that are several hundred degrees below those of microcrystalline powders.[3,4] Widespread use of these materials, including bulk forms (components and solid bodies) with nanocrystalline microstructure, has been sought; however, the cost of creating these materials, frequently quoted as being more than $100 per pound, and the inability to produce them in tonnage quantities with reproducible properties have restricted their broad application.[5]

This project builds on the recent discovery of a low-cost means of producing nanostructured materials in essentially any alloy.[6,7] The discovery that chips produced during normal machining operations are composed entirely of nanocrystalline structures of high hardness (strength) provides a low-cost, direct way of making these materials in large volumes. Comminution of the nanostructured chips will enable large-scale production of nanocrystalline particulate, which can be converted into nanostructured bulk forms using powder processing methods. Alternatively, the chips and particulates may be used as continuous or discontinuous reinforcements in metal or polymer matrices to create advanced composite bulk forms.

Approach

Chips were produced by machining, ranging from soft alloys [e.g., oxygen-free high-conductivity (OFHC) copper, aluminum 6061-T6[to high-strength alloys (e.g., Inconel, 52100 steel); and the microstructure and hardness of the chip and bulk (workpiece) material was characterized.[7,8] The bulk materials were annealed in an inert atmosphere before machining so that he initial grain size in all cases was greater than 20 μm. Typical dimensions of chip samples examined were 100–3000 μm width, 100–1000 μm thickness, and at least 5 mm length, with the smaller chips coming from the higher-strength steels. The machining conditions were selected so that the temperature increase in the deformation zone was minimal for all materials.

Transmission electron microscopy (TEM) was used to characterize the nanoscale defect structures in the metal chips and to measure grain size, grain size distribution, and grain misorientation. Specimens for TEM examination were prepared from chips produced under well-defined deformation conditions (strain, strain rate, temperature) by standard mechanical, ion beam, and electrochemical thinning techniques. Bright-field imaging coupled with electron diffraction analysis was conducted in a scanning TEM at Purdue and at the High Temperature Materials Laboratory (HTML) at Oak Ridge National Laboratory (ORNL). The hardness of the chip and bulk samples was measured by Vickers and nano-indentation. Uni-axial tests were carried out on miniature copper tension samples prepared from the chips.

Preparation of bulk forms from nanostructured particulate derived from the machining chips was initiated using powder extrusion and infiltration processing. For powder extrusion, nanostructured Al6061-chips were converted into particulate using attrition milling. The resulting particulate was mixed with varying weight percentages of commercially available, gas-atomized aluminum powder; this mixture was powder-extruded through steel dies at extrusion ratios of 10–60. The extruded samples were

prepared in the form of cylinders of up to 10 mm in diameter and 5–25 mm in length.

Results

Figure 1 shows a TEM image of a typical Al 6061-T6 chip. Shown in the inset is the corresponding selected area diffraction pattern, typical of a polycrystalline structure. The grain size is seen to be in the range of 50–80 nm. Misorientation measurements carried out using convergent beam electron diffraction in the TEM have established that more than 50% of the grain boundaries in the Al 6061-T6 chips are large-angle; the fraction of the large-angle boundaries is greater in chips produced at higher levels of strain. Evidence for mechanical twinning has been seen in some of the highly strained chips, akin to that reported elsewhere.[9] Similar nanocrystalline structures have been observed in a variety of alloys, including high-strength 52100 and M2 steels (Figure 2). Ultrafine sub-grain structures, nanoscale grains, and dynamic recrystallization have been demonstrated in a variety of materials by varying the conditions of strain and temperature during chip formation. An example of such nanostructural changes can be seen in the sequence of TEM pictures in Figure 3 of OFHC copper chip samples produced with different levels of shear strain (~ 3–20). A *switchover* from sub-grain to nanoscale, equiaxed grain structures at the higher levels of strain (Figure 3) appears to be a consequence of the onset of dynamic recrystallization at a strain of ~ 13. This switchover, which appears controllable in different materials by varying the deformation conditions, has not been realized in a single stage of deformation in any of the frequently studied severe plastic deformation processes. These observations suggest that machining also offers a unique framework in which to systematically explore the formation of nanocrystalline structures by large strain deformation.

Table 1 gives a summary of the hardness values measured on the chips and the bulk samples. The chips are seen to be up to three times as hard as the corresponding bulk samples prior to machining. The hardness of the 52100 steel chip is 1310 kg/mm^2, which is comparable to that of patented steel wire, one of the hardest and strongest steel structures known.[10] As has been reported in many studies,[1–4] nanostructured alloys have significantly greater strength than their microcrystalline counterparts. Uni-axial tensile tests carried out on miniature

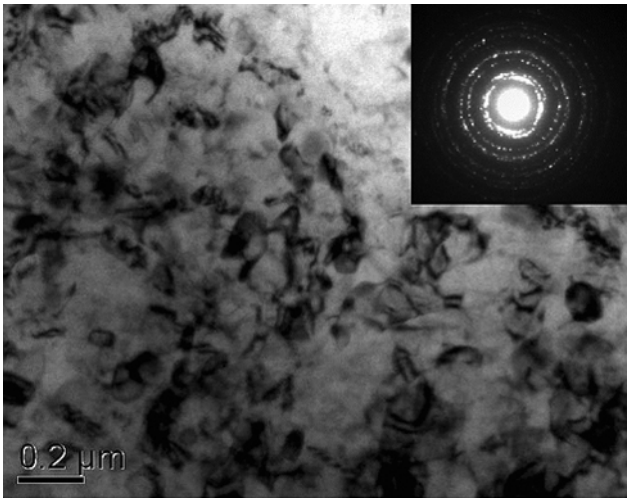

Figure 1. Nanostructured Al 6061-T6

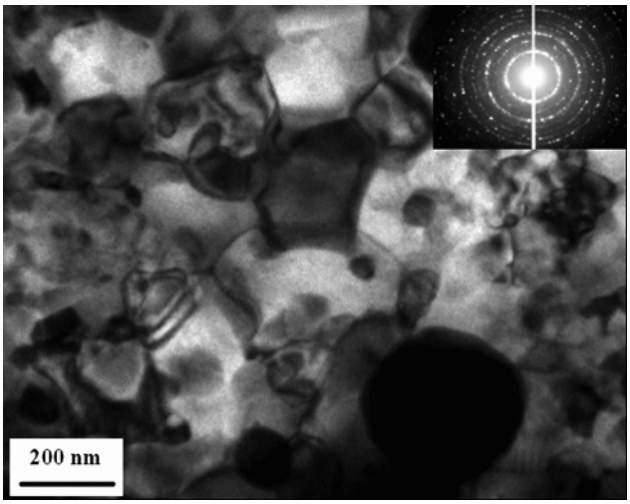

Figure 2. 52100 steel showing nanoscale ferrite grains and carbide particles.

OFHC copper chip samples have shown the increases in strength to parallel those in hardness. These increases in chip strength and hardness are much higher than those that result from extrusion, forging, and rolling.[11]

Figure 4 shows an optical micrograph of a partially formed OFHC copper chip, as yet not separated from the bulk.[6] Superimposed on the micrograph are Vickers hardness (strength) values recorded at different locations. The hardness shows a steep increase over a very narrow deformation zone between the chip and the bulk. This zone, where chip formation occurs, is characterized by very large deformations, as highlighted by the flow lines in the chip in Figure 4. While grains are clearly

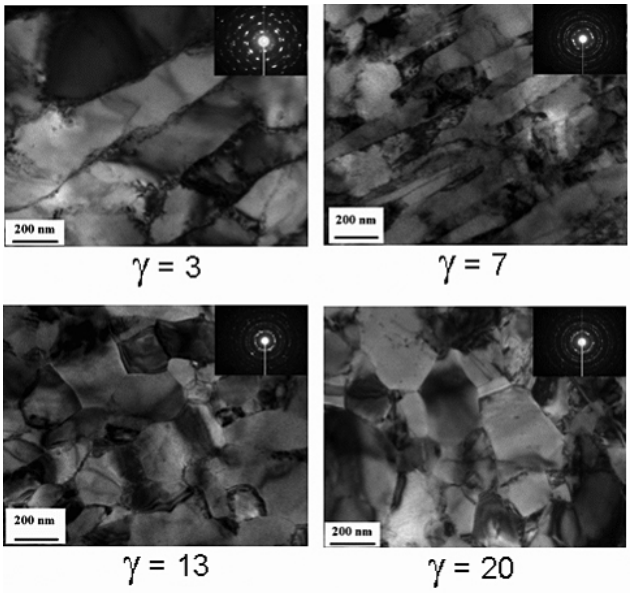

Figure 3. Microstructure of OFHC copper chips at different levels of shear strain (γ). Features typical of onset of dynamic recrystallization are visible in the chip produced with a shear strain of ~13.

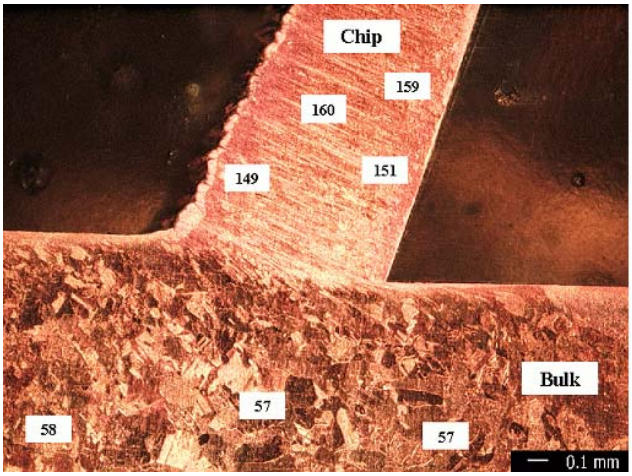

Figure 4. Partially detached OFHC copper chip. Note large hardness increase across shear plane.

visible in the bulk OFHC copper sample, no grains can be resolved in the chip or near the deformation zone, consistent with TEM observations that the microstructure is nanoscale.

Figure 5a shows a cylindrical sample of Al6061-T6/Al composite produced by powder extrusion. This composite is composed of 50% by weight of nanostructured 6061 chip particulate blended with an equal weight of aluminum powder. Density measurements showed the sample to be consolidated to 97% of the theoretical density. Figure 5b shows a transverse cross-section of this sample; the porosity is seen to be negligible, consistent with the measured density. Figure 5c shows the distribution of hardness over the cross-section. The higher hardness values of ~160 VHN are similar to those measured in the nanostructured chip particulate, suggesting that the nanostructure is retained. The remainder most likely correspond to that of the aluminum powder strain-hardened by the extrusion. The early observations pertaining to hardness, density, and microstructure, made on the powder-extruded samples, are promising vis-à-vis densification and nanostructure retention.

We have also been successful recently at producing bulk Al6061-T6 samples from nanostructured chip particulate via an infiltration/pressing approach using a small amount (<10%) of epoxy as binder.

Conclusions

Nanostructured materials with grain sizes as small as 70 nm have been produced by controlled 2-dimensional machining in a wide variety of metals and alloys. The hardness of these alloys is up to three times that of their micro-crystalline counterparts. Preliminary results on consolidation of these materials using shear-based densification and infiltration processes are promising. A variety of low-temperature consolidation protocols have been identified for producing bulk forms using these nanostructured chips as precursor materials. These include powder extrusion, rolling, and forging; infiltration processing; dynamic compaction; rapid prototyping; and spraying. In the next year, intensive efforts are planned on using these processes to address the grand challenge of consolidating these nanostructured materials into high-performance bulk forms. Property and performance studies will be initiated on these consolidated samples to determine indices of relevance to transportation applications. Close collaboration with the HTML is envisioned on various aspects of this work.

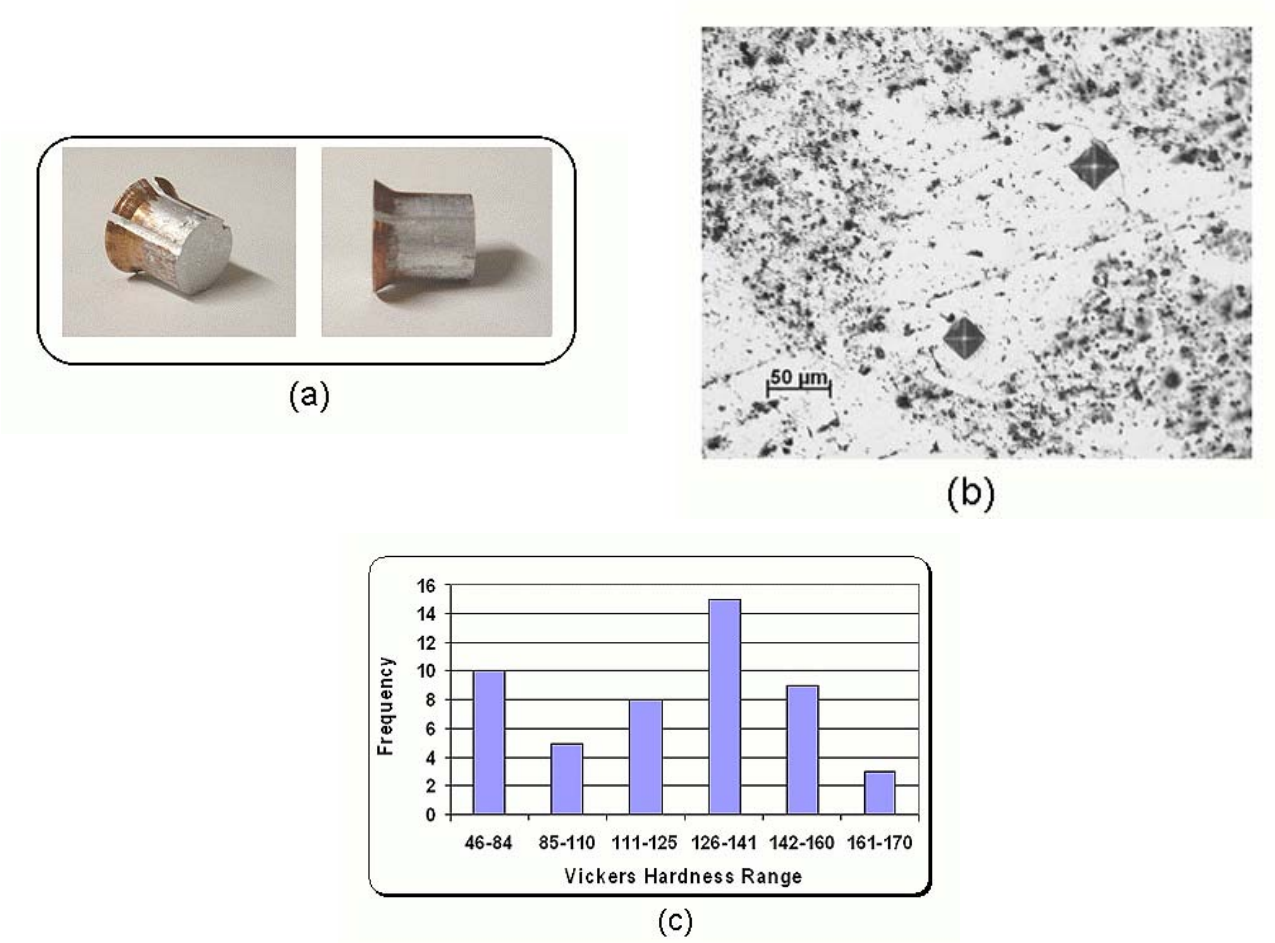

Figure 5. Characteristics of powder-extruded Al-6061T6/Al composite: (a) typical extruded samples, (b) microstructure of a transverse cross section, and (c) hardness distribution determined by Vickers indentation.

References

1. H. Gleiter, *Progress in Materials Science* **33**, 1 (1989).

2. R. W. Siegel, *Scientific American* **275** 74 (1996).

3. L. Lu, M. L. Sui, and K. Lu, *Science* **287**, 1463 (2000).

4. X. McFadden, R. S. Mishra, R. Z. Valiev, A. P. Zhilyaev, and A. K. Mukerjee, *Nature* **398**, 684 (1999).

5. H. Breisen, A. Fuhrmann, and S. E. Pratsinis, "Nano-Powder and Industrial Applications," *MRS Proc.* **520**, 3 (1998).

6. T. L. Brown, S. Swaminathan, S. Chandrasekar, W. D. Compton, A. H. King, and K. P. Trumble, *J. Matls. Res.* **17** (2002).

7. S. Chandrasekar, W. D. Compton, T. N. Farris, and K. P. Trumble, "Method of Forming Nanocrystalline Structures and Product Formed Thereof," U.S. Patent, 6,706,324, March 16, 2004.

8. S. Swaminathan, S., T. L. Brown, M. Ravi Shankar, B. C. Rao, K. P. Trumble, W. D. Compton, and S. Chandrasekar, "Large Scale Manufacturing of Ultra-fine grained Materials," *Ultrafine Grained Materials III*, Ed. Y. T. Zhu, T. G. Langdon, R. Z. Valiev, S. L. Semiatin, D. H Shin, and T. C. Lowe, TMS (The Minerals, Metals and Materials Society), 2004.

10. Y. M. Wang, M. W. Chen, F. H. Zhou, and E. Ma, *Nature* **419**, 912–915 (2002).

11. A. Kelly and N. H. MacMillan, *Strong Solids*, Clarendon, Oxford, UK, 1986.

12. W. A. Backofen, *Deformation Processing*, Addison Wesley, Reading, Massachussets, 1972.

Publications/Presentations

S. Swaminathan, S. Chandrasekar, W. D. Compton, K. P. Trumble, and A. H. King, "Microstructural Refinement in Single-Phase Copper Solid Solutions by Machining," p. 8.27 in *Nanoscale Materials and Modeling-Relations Among Processing, Microstructure and Mechanical Properties, Materials Research Society (MRS) Proceedings*, **821**, 2004.

S. Swaminathan, C. Swanson, T. L. Brown, R. F. Kezar, S. Chandrasekar, W. D. Compton, and K. P. Trumble, "Microstructure Refinement in Steels by Machining," p. 9.5 in *Nanoscale Materials and Modeling-Relations Among Processing, Microstructure and Mechanical Properties, Materials Research Society (MRS) Proceedings*, **821**, 2004.

S. Swaminathan, T. L. Brown, M. Ravi Shankar, B. C. Rao, K. P. Trumble, W. D. Compton and S. Chandrasekar, "Large Scale Manufacturing of Ultrafine Grained Materials," pp. 161–166 in *Ultrafine Grained Materials III*, The Minerals, Metals and Materials Society (TMS) Proceedings, 2004.

T. L. Brown, S. Swaminathan, B. C. Rao, R. F. Kezar, S. Chandrasekar, W. D. Compton, K. P. Trumble, and A. H. King, "Machining as a Method for Studying Effects of Very Large Strain Deformation," pp. 167–172 in *Ultrafine Grained Materials III*, *The Minerals, Metals and Materials Society (TMS) Proceedings*, 2004.

S. Chandrasekar, W. D. Compton, and K. P. Trumble, "Low-cost Nanocrystalline Materials for Structural Components," presented at the U.S. Air Force Propulsion Environmental Working Group Meeting, Las Vegas, April 2004.

S. Chandrasekar, W. D. Compton, "Low-cost Nanocrystalline Materials for Structural Components," presented at the SAE Inner Value Symposium—Nanotechnology for the Automotive Sector, invited talk, Carnegie Mellon University, Pittsburgh, May 2004.

S. Chandrasekar, "Emerging Manufacturing Technologies," presented at the State of Indiana Advanced Manufacturing Summit, Purdue University, West Lafayette, IN, May 2004.

S. Chandrasekar, W. D. Compton, K. P. Trumble, and A. H. King, "Large-scale Manufacturing of Nanocrystalline Materials," Indian Institute of Technology, Madras, India, July 2004.

S. Chandrasekar, W. D. Compton, K. P. Trumble, and A. H. King, "Large-scale Manufacturing of Nanocrystalline Materials," presented at the Timken Global Engineering Center, Bangalore, India, July 2004.

Patents

S. Chandrasekar, W. D. Compton, T. N. Farris, and K. P. Trumble, "Method of Forming Nanocrystalline Structures and Product Formed Thereof," U.S. Patent, 6,706,324, March 16, 2004.

R. Deformation Processes for Next-Generation Ceramics

P. F. Becher
Oak Ridge National Laboratory
P.O. Box 2008, MS-6068
Oak Ridge, Tennessee 37831-6068
(865) 574-5157; fax: (865) 574-6098; e-mail: becherpf@ornl.gov

DOE Technology Development Area Specialist: Dr. Sidney Diamond
(202) 586-8032; fax: (202) 586-1600; e-mail: sid.diamond@ee.doe.gov
ORNL Technical Advisor: D. Ray Johnson
(865) 576-6832; fax: (865) 574-6098; e-mail: johnsondr@ornl.gov

Contractor: Oak Ridge National Laboratory, Oak Ridge, Tennessee
Prime Contract No: DE-AC05-00OR22725

Objectives

- Assess the plastic deformation behavior in nanocrystalline oxide ceramics and its applicability to fabrication of complex shapes.
- Characterize the ability to deform nanocrystalline ceramics at temperatures well below 1000°C through control of microstructure and external parameters (e.g., electric fields, environment).
- Characterize thermal and mechanical properties to assess the influence of nanocrystalline microstructures for gaining improved performance for wear and other components.

Approach

- Collaborate with members of the Pennsylvania State University task on Synthesis of Nanocrystalline Ceramics to develop advanced colloidal technology-based processing to fabricate monolithic bodies and sintering technology to fabricate dense monolithic nanocrystalline bodies (i.e., grain sizes <100 nm).
- Conduct both compressive creep and plastic deformation studies as a function of temperature, environment, and applied electric fields on nanocrystalline oxides with grain sizes of <100 nm.

Accomplishments

- Established a novel pressureless sintering method to fabricate dense monolithic zirconia bodies with selected grain sizes in the range of 20 to 90 nm.
- Developed data on the deformation of dense zirconia ceramics with a grain size of 350 nm to serve as a baseline for comparison of future observations. Initial observations have been obtained on the enhancement of deformation of this dense zirconia ceramic with sub-micron-sized grains from applied electric fields through collaboration with North Carolina State University researchers.

Future Direction

- Exploit the ability to sinter monolithic nanocrystalline oxides to full density to characterize the enhanced plastic deformation below 1000°C in zirconia ceramics having grain sizes below 100 nm. The goal is to explore the minimum temperature at which permanent deformation can still be achieved.
- Evaluate conditions required for optimizing deformation-shape forming.

- Examine room temperature fracture and wear properties to seek approaches for developing ceramics with greater wear resistance.

Introduction

In addition to lower specific weight, ceramics have a number of attractive properties for application as components in various heavy vehicle systems. However, many heavy vehicle components require ceramics with complex shape as well as function. Furthermore, the demanding service conditions necessitate improved mechanical reliability together with fracture and/or wear resistance. Underlying the performance and use of ceramics is their tendency to fail in a brittle fashion except at temperatures generally well above 1000°C. Complex-shape-forming processes for ceramics are relegated to approaches based on powder processing as a result of the excessive temperatures for hot forming. On the other hand, metallic alloys can be hot-worked at temperatures below 1000°C not only to form the desired shape but also to enhance their properties. The ductility (>20% plastic strain) of metallic alloys at temperatures below 500°C is the source of their 10- to 100-fold greater fracture toughness compared with ceramics.

In ceramic systems, processing to tailor microstructures needs to be combined with novel concepts that offer the potential to enhance deformation. One such concept that has been of considerable interest is superplastic deformation of ceramics with submicron-size grains at temperatures above 1000°C.[1] Recent studies suggest that reducing the microstructure to achieve grain sizes of <100 nanometers could lead to permanent/plastic deformation in ceramics at quite modest temperatures.[2,3] Indeed, classical deformation behavior suggests significant decreases in yield stresses at a fixed temperature or decreases in temperature at which deformation can be induced via the reduction in grain size.[4] Typically, temperature, strain rate or stress, and grain size are the parameters to alter the deformation or creep rates in single-phase oxides. Recent studies have shown that the application of electric fields can reduce the yield stress or increase the creep rates of ceramic systems.[5] To date, this has not been exploited to determine the effects on the deformation of nanocrystalline oxides. The present study seeks to examine the influence of true nanocrystalline microstructures on the mechanical properties of ceramics, as well as approaches to economically fabricate nanocrystalline ceramic monoliths.

Approach

This project involves two major thrusts. The first is a collaborative effort in the processing and sintering of nanocrystalline ceramics with researchers in the Synthesis of Nanocrystalline Ceramics task at Pennsylvania State University. The goal is to develop the technology to form "green" (unfired) bodies of nanocrystalline particles with densities well in excess of 50% of the theoretical density, which will allow us to devise pressureless sintering profiles to produce dense monolithic bodies with grain sizes of <100 nm (see ref. 6 for a review of processing of nanocrystalline ceramics). This is aimed at finding approaches to produce sizeable monolithic bodies for subsequent evaluation.

The second thrust focuses on the mechanical and wear behavior of nanocrystalline ceramics and the influence of external parameters [e.g., stressing rate, temperature, environment (e.g., air, vacuum), and electric fields] on the plastic deformation behavior.

Synthesis, Evolution, and Stability of Nanostructures in Bulk Materials

Outstanding challenges in particle processing to form bulk, dense nanograin-size materials include the dispersion of the nanosize particles and control of gas evolution from the very-high-surface-area compacts during sintering. Typically, nanometer-size particulates suffer from a high degree of agglomeration, which results in poor particle packing (green densities < 40% of theoretical); this inhibits sintering and promotes undesirable grain growth. Two routes to obtaining well-dispersed powders include comminution and colloidal processing.[7,8] By optimizing colloidal processing approaches, it should be possible to produce green bodies with densities of more than 60% of the theoretical by control of interparticle forces. This control is achieved through appropriate chemical additives to suspensions of nanoparticulates, combined with filter pressing or pressure casting of the high-solids-

content slurries. By controlling the packing of nanoparticulates, one should be able to control the porosity to achieve the narrow size distribution necessary, which then will enhance densification.

Densification of nanocrystalline ceramics has typically involved the use of applied pressure to achieve dense samples with sub–100-nm grain size.[9] In those few cases where pressureless sintering has been employed successfully, long hold times at the sintering temperatures were required to achieve densities ≥95% of theoretical, which allow undesired grain growth to proceed.[10] Heating to a temperature sufficient to achieve densities of ≥75% of theoretical, and then rapidly lowering the temperature to obtain sufficient boundary diffusion to remove pores trapped on boundaries while minimizing grain growth, has been only partially successful. Long hold times at the lower temperature were still required.[11] Here we seek to optimize the processing of the green bodies and use modified sintering cycles to achieve dense oxides with sub–100-nm grain sizes.

Deformation Behavior in Nanostructured Materials

To evaluate the influence of nanocrystalline microstructures, baseline deformation data will be established through studies of high-purity, dense zirconia ceramics with sub-micron-size grains. These studies will then be extended to ceramics with <100 nm grain size. This will include

- nanostructured ceramics, to explore for the softening effects observed in nanocrystalline metals by evaluating both (1) the creep response over a range of temperatures and applied stresses and (2) the yield stress as a function of strain rate and temperature
- the influence of external factors (e.g., electric fields) that have been shown to enhance deformation processes in ceramics with micrometer grain sizes

Modeling studies will be conducted to describe the deformation behavior and to address such phenomena as space charge/solute segregation coupled with electric field effects. Additionally, the fracture, hardness, and wear response of nanocrystalline oxides will be evaluated to assess their application in wear components.

Results

Sintering

Advanced colloidal processing in the task on Synthesis of Nanocrystalline Ceramics has provided monolithic green bodies of both yttria-doped and undoped zirconias with densities from 55 to 68 % of theoretical and an average particulate size of 15 nm. Advanced sintering cycles now allow the production of dense monolithic zirconias with grain sizes well below 100 nm (Figure 1). As noted, sintering in a vacuum promotes densification at lower temperatures than sintering in air. At this point, we assume this is due to lower capillary pressure within pores and faster removal of any residual organics or moisture used in the colloidal processing.

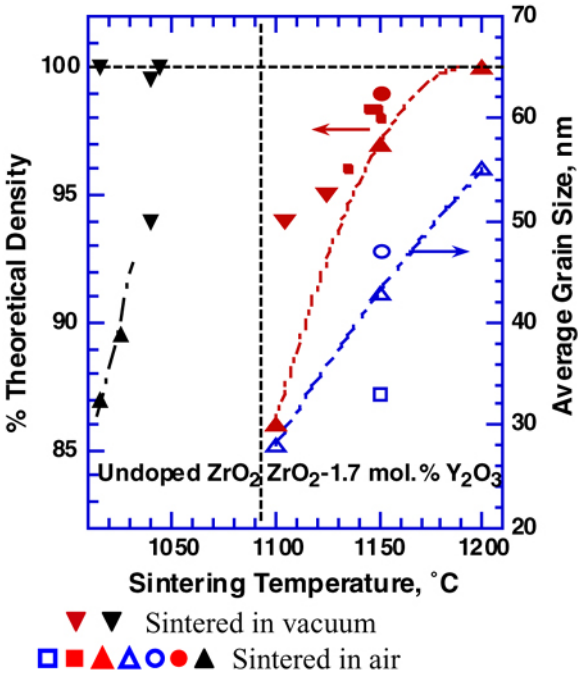

Figure 1. Pressureless sintering of colloidally processed zirconias yields dense ceramics with grain sizes < 100 nm (density—closed symbols; open symbols—grain size).

Based on the data shown in Figure 1, it is obvious that the addition of yttria inhibits the densification of nanocrystalline zirconia. Recent work indicates that space charge effects due to yttrium segregation may inhibit Zr^{+4} lattice diffusion,[12,13] which would explain the lower-than-expected creep deformation observed in yttria-doped zirconia with grains of sub–100-nm size (Figure 2).[14] While grain boundary diffusion is a critical factor in the removal of pores

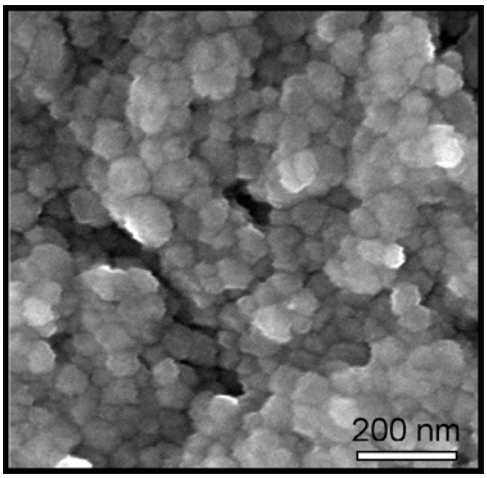

Figure 2. Microstructure of ZrO_2—1.7 mol % Y_2O_3 ceramic sintered in air at 1150°C.

during the densification of nanoparticulate bodies, lattice diffusion might be a limiting parameter in sintering.

Deformation Studies

In the first year of this project, a fully dense, hot-isostatically-pressed zirconia—2 mol % yttria ceramic with a grain size of ~ 350 nanometers (Figure 3)—was selected for studies of compressive deformation. These include compressive creep and constant strain rate deformation studies conducted in air at temperatures above 1000°C to obtain measurable deformation. These results will serve as a baseline for assessing the effectiveness of increasing the plasticity by producing microstructures of sub–100-nm grain size. In addition, data on the tetragonal zirconia ceramic with 350-nm grain size can be used to correlate with data in the literature on zirconias with sub-micron grain size.

The creep behavior illustrates the creep rate dependence on applied stress above 1100°C with stress exponents of 1.7 to 1.9, while at 1100°C the stress exponent is ~ 0.6 (Figure 4a). The activation energy ranges from 625 to 645 kJ/mol with a discontinuity at 1100°C with a stress of 30 MPa (Figure 4b). The stress exponent and the activation energy values are similar to those reported in the literature for high-purity zirconias with grains of sub-micron size;[14] however, the test temperatures were typically greater than 1200°C. The extent of permanent deformation was limited by the displacement range of the contact extensometers, which require repositioning for displacements of 150 to 200 microns, or by the length

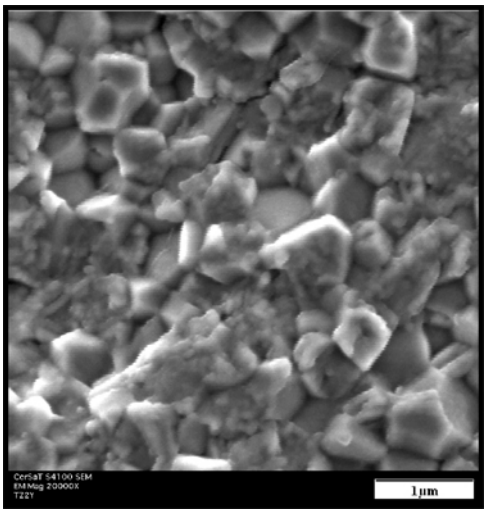

Figure 3. Fracture surface microstructure of 350 nm grain sized tetragonal zirconia—2 mol. % yttria ceramic used to establish baseline data on deformation behavior.

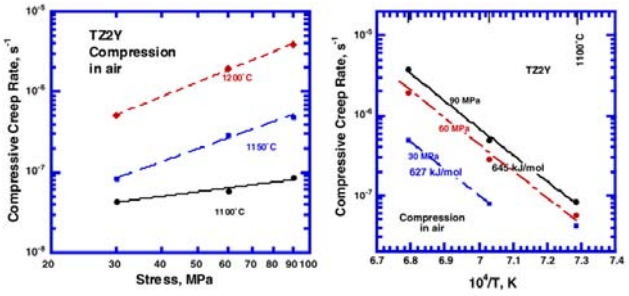

Figure 4. Applied stress (a) and temperature (b) dependence of the compressive creep rates of submicron grain sized ZrO_2–2 mol% Y_2O_3 in air.

of the test in the case of those conducted at 1100°C. However, permanent strains of ≥2 % were obtained based on measurements prior to and after testing.

Initial assessments of the compressive yield stresses of this sub-micron-grain-size zirconia were obtained in air. Data at 1300°C reveal a typical decrease in the yield stress as the stress rate is reduced (Figure 5a). At the same time, the yield stress increased significantly when the temperature was reduced to 1200°C for comparable stress rates (Figure 5b). Thus permanent strains under dynamic loading in air were limited to <2 %. On the other hand, observations reveal that extensive plastic strain (~ 45%) could be achieved at 1200°C with the application of a dc field of 1 kV/cm in this sub-micron-grain-size zirconia. In view of the recent observations of plasticity in nanocrystalline zirconia

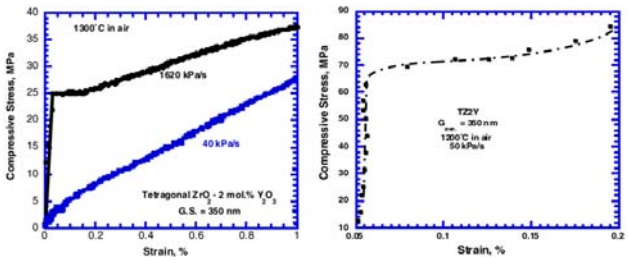

Figure 5. Compressive yielding of 350-nm-grain sized ZrO_2; 2 mol % Y_2O_3 exhibits typical decrease in yield stress due to reduction in stressing rate at 1300°C in air (a) and an increase with decrease in test temperature (b).

ceramics at 1000°C,[3] there would appear to be significant potential for enhanced plasticity in nanocrystalline zirconias. The demonstrated ability in the current task to fabricate dense monolithic nanocrystalline zirconia ceramics will now allow us to evaluate the plastic deformation behavior of doped and undoped zirconia ceramics over a range of grain sizes (i.e., 30 to 100 nm).

Conclusions

Advances in the processing of monolithic nanoparticulate zirconia bodies with green densities in excess of 55% of theoretical, through our collaboration with the task on Synthesis of Nanocrystalline Ceramics, now allow us to fabricate dense monolithic bodies of both yttrium-doped and undoped zirconias with grain sizes well below 100 nm by pressureless sintering. This is a substantial innovation and provides the critical path forward to assessing the plastic deformation behavior of nanocrystalline oxides, as well as other properties (e.g., wear, strength) that would prove advantageous for improvements in heavy vehicle component fabrication and performance.

Baseline data on the deformation response of zirconia ceramics are being established using a fully dense 350-µm grain-size tetragonal zirconia containing 2 mol % yttria. Results show that this ceramic can be plastically deformed in compression to permanent strains in excess of 2% at stresses below 100 MPa and temperatures of 1200 to 1300°C in air. Current work is focusing on the preparation of compression samples with sub–100 nm grain size to begin evaluating the deformation behavior of nanocrystalline (<100 nm) ceramics.

References

1. T. G. Nieh and J. Wadsworth, "Superplastic Behavior of a Fine-Grained Yttria-Stabilized, Tetragonal Zirconia Polycrystal (Y-TZP)," *Acta Metall et Mater.* **38**, 1121–1133 (1990).

2. H. Conrad and J. Narayan, "On the Grain Size Softening in Nanocrystalline Materials," *Script. Mater.* **42,** 1025–30 (2000).

3. M. Yoshida, Y. Shinoda, T. Akatsu, and F. Wakai, "Deformation of Monoclinic ZrO_2 Polycrystals and Y_2O_3-Stabilized Tetragonal ZrO_2 Polycrystals below the Monoclinic-Tetragonal Transition Temperature," *J. Am. Ceram. Soc*. **85**(11), 2834–36 (2002).

4. M. F. Ashby and R. A. Verrall, "Diffusional-Accommodated Flow and Superplasticity," *Acta Metall*. **21**, 149–163 (1973).

5. H. Conrad, "Space Charge and the Dependence of the Flow Stress of Ceramics on an Applied Electric Field," *Scripta Mater*. **44**, 211–16 (2001).

6. M. J. Mayo, "Processing of Nanocrystalline Ceramics from Ultrafine Powders," *Int'l Mater. Rev*. **41**(3), 85–115 (1996).

7. J. H. Adair et al., "Dynamic Control and Enhanced Chemical Milling of Ceramics to Submicron Particle Sizes," U.S. Patent 6,415,966 B1, July 9, 2002.

8. A. Bleier, P. F. Becher, K. B. Alexander, and C. G. Westmoreland, "The Effect of Aqueous Processing Conditions on the Microstructure and Transformation Behavior of Al2O3-ZrO2(CeO2) Composites," *J. Am. Ceram. Soc.* **75**(10) 2649–2658 (1992).

9. R. Chaim and M. Hefetz, "Fabrication of Dense Nanocrystalline ZrO_2-3 wt. % Y_2O_3 by Hot-Isostatic Pressing," *J. Mater. Res*. **13**(7), 1875–80 (1998).

10. A. Bravo-Leon, Y. Morikawa, M. Kawahara, and M. J. Mayo, "Fracture Toughness of Nanocrystalline Tetragonal Zirconia with Low Yttria Content," *Act. Mater.* **50**, 4555–62 (20002).

11. I. W. Chen and X. –H. Wang, "Sintering Dense Nanocrystalline Ceramics Without Final-Stage Grain Growth," *Nature* **404**, 168–71 (2000).

12. D. Gomez-Garcia, C. Lorenzo-Martin, A. Munoz-Bernabe, and A. Dominguez-Rodriguez, "Model of High-Temperature Plastic Deformation of Nanocrystalline Materials: Application to Yttria Tetragonal Zirconia," *Phys. Rev.* **B67**(14), 144101-1 to –8 (2003).

13. A. Dominguez-Rodriguez, F. Gutierrez-Mora, M. Jimenez-Melendo, J. L. Routbort, and R. Chaim, "Current Understanding of Superplastic Deformation of Y-TZP and Its Application to Joining," *Mater. Sci. and Eng.* **302**, 154–61 (2001).

14. M. Jimenez-Melendo and A. Dominguez-Rodriguez, "Like-Metal Plasticity of Fine-Grained Y2O3-Stabilized Zirconia Ceramics," *Phil. Mag.* **A 79**(7) 1591–1608 (1999).

Publications

C. H. Hsueh and P. F. Becher, "Effects of Dopant Segregation on Lattice-Diffusional Creep of Nanocrystalline Ceramics," *Phys. Rev. B*, accepted for publication.

S. Synthesis of Nanocrystalline Ceramics

Dr. James H. Adair, Principal Investigator
Christopher J. Szepesi, Graduate Assistant
The Particulate Materials Center, The Pennsylvania State University
249 Materials Research Laboratory
University Park, PA 16802
(814) 863-6047; fax (814) 863-9704; e-mail: jha3@psu.edu

DOE Technology Development Area Specialist: Dr. Sidney Diamond
(202) 586-8032; fax: (202) 586-1600; e-mail: sid.diamond@ee.doe.gov
ORNL Technical Advisor: D. Ray Johnson
(865) 576-6832; fax: (865) 574-6098; e-mail: johnsondr@ornl.gov

Contractor: Oak Ridge National Laboratory, Oak Ridge, Tennessee
Prime Contract No.: DE-AC05-00OR22725
Subcontractor: The Pennsylvania State University, University Park, Pennsylvania

Objectives

- Synthesize well-dispersed, concentrated aqueous suspensions of nominally 8–10 nm tetragonal ZrO_2.
- Form nano-grained green bodies from concentrated ZrO_2 suspensions.
- Dry nano-grained green bodies while avoiding crack formation.
- Sinter nano-grained green bodies to high theoretical density while maintaining nano-scale grain structure.

Approach

- Complex zirconyl nitrate with bicine in aqueous solution, which is then hydrothermally treated to precipitate 8–10 nm tetragonal ZrO_2.
- Increase ZrO_2 yield by increasing reagent concentrations.
- Form green bodies using constant-rate filter pressing.
- Dry green bodies under controlled humidity conditions or through a solvent exchange procedure.
- Fire green bodies at Oak Ridge National Laboratory using transient sintering cycles.[1]

Accomplishments

- Hydrothermally synthesized 10–20 nm tetragonal ZrO_2 using a procedure developed by R.A. Kimel and J.H. Adair.
- Increased ZrO_2 yield from about 25 g/L to 100 g/L by increasing reagent concentrations and modifying the dispersant concentration to accommodate the higher surface areas in solution.
- Routinely made nano-grained green bodies ¾ in. in diameter and 1–4 mm thick using constant-rate filter pressing.
- Successfully dried nano-grained green bodies using controlled humidity drying.

- Successfully dried nano-grained green bodies by exchanging entrained water with acetone containing an acryloid binder.
- Sintered nano-grained green bodies to 100% theoretical density while maintaining grain sizes below 100 nm.

Future Direction

- Continue to produce nano-grained green bodies with constant-rate filter pressing.
- Compare constant-rate filter pressing to constant-pressure filter pressing.
- Optimize solvent exchange drying procedure to optimize green densities.
- Produce larger-diameter green bodies for sintering and mechanical testing.

Introduction

The main objective of this research was to manufacture bulk, dense ceramics with grain sizes of less than 100 nm. The material chosen for this purpose was ZrO_2 and Y_2O_3-stabilized ZrO_2 because of its mechanical properties and its ease of production in the appropriate size scale.

Previously, nanoscale ZrO_2 and Y_2O_3-stabilized ZrO_2 have been synthesized using a protocol developed by Kimel and Adair [2–4] in which zirconyl nitrate (and yttrium nitrate) is complexed with bicine in aqueous solution through alkaline pH adjustment. Hydrothermal treatment at 200°C for 8 hours allowed particles of the tetragonal phase with sizes of between 8 and 15 nm to precipitate. The product suspension was then washed with an aqueous solution of oxalic acid to remove any remaining bicine and disperse the suspended particles. However, solid yield was only about 25 g/L using this method.

By increasing the concentration of reagents, yield was increased to about 50 g/L. The limiting factor in this protocol became the solubility of both bicine and the organic base used to adjust pH (tetraethylammonium hydroxide, TEAOH). To address this issue, dry zirconyl nitrate and bicine were mixed with an appropriate amount of solid organic base, tetramethylammonium hydroxide pentahydrate (TMAOH). Because of the water content of both the zirconyl nitrate and TMAOH, the mixture became an aqueous solution, which was hydrothermally treated to produce 10–30 nm ZrO_2. Using this method, ZrO_2 yield was increased to 100 g/L.

Approach

The current task in this research has been the production of green bodies for sintering studies. This was accomplished with constant rate filter pressing, in which plungers moving at a constant rate apply a load to a concentrated suspension. Solution is then removed through filters at the bottom of the solution chamber (see Figure 1).

Once the wet pellets are removed from the filter press die, they must be carefully dried to avoid cracking within the body. This can be done either with controlled humidity or by exchanging water within the pellet with another liquid of lower surface tension (solvent exchange).

Results

With the current filter pressing protocol, pellet production has been increased to about four pellets per 4 hours (from four pellets per 12–18 hours). Humidity drying, the previously preferred method, has been limited as a result of difficulties with equipment. Therefore, solvent exchange drying has been investigated.

Initially, four solvents were chosen: methylethylketone (MEK), 40% MEK–60% ethanol (by weight), acetone, and isopropanol. Each of these solvents was pushed through a filter-pressed pellet immediately after pressing concluded. Upon removal from the die, the solvent-exchanged pellets were all cracked but dry. Density measurements by the Archimedes method revealed a marked increase in density (see Table 1). However, the dry pellets maintained little green strength.

Table 1. Archimedes density measurement results of solvent-exchange–dried ZrO2 pellets

Solvent	Density (g/cm3)	Theoretical density (%)
Methylethylketone (MEK)	3.99	66
40% Methylethylketone – 60% Ethanol (by weight)	4.01	68
Isopropanol	3.07	51
Acetone	3.61	60

It was then proposed that a binder be added to the solvent to add green strength to the dry body. An acetone-soluble acryloid binder (Rohm and Haas), which is typically used in dry pressing, was chosen. When the acetone-binder solution was pressed through wet filter-pressed pellets, cracks were still present, but to a smaller degree. Cracking was reduced further by introducing the acetone-binder solution to pellets that were not fully consolidated. Archimedes density determination on fragments of these pellets reveals, again, that pellets are achieving a high density after drying with the solvent exchange process (Table 2). Also, the high densities achieved with acryloid binder present require recalculation once the actual concentration of binder is determined by controlled thermolysis. It is likely that the very large values (in some cases greater than 70% theoretical density) will be in the 60% theoretical density range when the concentration of binder is known and accounted for in the density calculation. Whether cracking can be eliminated completely by beginning the solvent exchange drying process earlier in the filter pressing procedure is currently under investigation.

Conclusions

The research focus has centered recently on increasing yield during synthesis and producing green bodies for sintering studies. By modifying the previous synthesis procedure, ZrO_2 yield was increased fourfold. Pellet pressing times have also been decreased significantly. Solvent exchange drying was demonstrated to be an effective method of drying filter-pressed green bodies to a high density. Efforts are continuing to eliminate cracks after drying with the solvent exchange procedure.

Table 2. Archimedes density measurement results of solvent-exchange–dried ZrO2 pellets (dried with a solution of acetone and an acryloid binder)

Sample number	Binder concentration	Density (g/cm3)*	Theoretical density* (%)
a3	0%	4.32	72
a1	2% (relative to weight of solids)	4.48	74
a2	3% (relative to weight of solids)	4.17	69
b1	0%	4.71 (very small sample)	78
b2	1% (relative to weight of solution)	4.65	77
b3	2% (relative to weight of solution)	4.45	74
b4	5% (relative to weight of solution)	4.13	69
c1	1% (relative to weight of solution)	4.30	71
c2	2% (relative to weight of solution)	4.48	75
c3	5% (relative to weight of solution)	3.95	66

References

1. I. W. Chen and X. H. Wang, “Sintering Dense Nanocrystalline Ceramics without Final-Stage Grain Growth,” *Nature* **404,** 168–171 (2000).

2. R. K. Kimel, *Aqueous Synthesis and Processing of Nanosized Yttria Tetragonally Stabilized Zirconia,* Ph.D. Thesis, The Pennsylvania State University, August 2002.

3. R. K. Kimel and J. H. Adair, “Aqueous Synthesis of Well-Dispersed Less than 10 nm Yttira Tetragonally Stabilized Zirconia at 200°C by Precipitation from Homogeneous Solution Using Complexation Chemistry,” submitted to *J. Am. Ceram. Soc*.

4. R. K. Kimel and J. H. Adair, “Recovery and Dispersion of 8 nm Y-TZP Utilizing a Nanoscale Analog to the Protective Colloid Approach,” submitted to *J. Am. Ceram. Soc*.

T. Development of Titanium Component Applications in Heavy Duty Diesel Engines

Jesus Chapa-Cabrera, Principal Investigator
John Grassi, Co-Investigator
Caterpillar Inc.
Tech Center 854-80 TC-E
14009 Old Galena Rd.
Mossville IL, 61552
(309) 578-8347; fax: (309) 578-2953; e-mail:chapa-cabrera_jesus_g@cat.com

DOE Technology Development Area Specialist: Dr. Sidney Diamond
(202) 586-8032; fax: (202) 586-1600; e-mail: sid.diamond@ee.doe.gov
ORNL Technical Advisor: D. Ray Johnson
(865) 576-6832; fax: (865) 574-6098; e-mail: johnsondr@ornl.gov

---

Contractor: Oak Ridge National Laboratory, Oak Ridge, Tennessee
Prime Contract No: DE-AC05-00OR22725
Subcontractor: Caterpillar Inc., Peoria, Illinois

Objectives

- Design and fabricate a cost-competitive diesel engine turbocharger using lightweight titanium materials that reduces both fuel consumption and transient emissions.

Approach

- Design a series turbocharger for use on multiple engine platforms. The turbocharger consists of one turbo wheel and two compressor wheels that are attached to a single rotating drive shaft.
- Use this compact design to simplify complex multi-turbocharger systems presently installed in different engine platforms.
- Use titanium aluminide (TiAl) for the turbine wheel and a titanium alloy for one of the compressor wheels.

Accomplishments

- Procured cast TiAl turbine wheels and test materials from two suppliers.
- Finalized subcontracts with two vendors.
- Completed three iterations of simulation and friction welding experiments to produce turbine-to-shaft joints. Produced welds with higher joint strength than the base TiAl turbine wheel.
- Established a nondestructive inspection methodology to assess robustness of the joints.
- Conducted preliminary turbocharger bench tests using base nickel alloy and TiAl turbines.

Future Direction

- Conduct a complete redesign of the wheel to increase the overall strength and create a robust joint.
- Complete detailed material characterization of two TiAl alloys processed by counter-gravity and gravity casting.

- Perform turbocharger bench tests and engine tests.
- Assess the commercial viability of using titanium alloys for turbocharger applications for heavy-duty diesel engines.

Introduction

Turbochargers on diesel engines play an integral role in meeting emission regulations and controlling fuel economy. A recently designed series turbocharger by Caterpillar will use TiAl and titanium alloys for the turbo wheel and compressor wheel, respectively. The dual turbocharger has two complete systems that are connected in series, as shown in an ACERT® engine in Figure 1, while the proposed turbocharger design is one system with two compressor wheels attached to a single drive shaft. Lightweight titanium materials are important technologies for this turbocharger design and are anticipated to provide faster response time (reduced transient emissions) and better fuel economy.

Figure 1. ACERT® engine. The two turbochargers in series are circled.

Approach

Caterpillar has selected candidate TiAl alloys for a series of characterization tests and development of a joining process. These tests will examine mechanical and physical properties of selected TiAl alloys. Friction weld trials will determine the optimal parameters for joining the TiAl wheel to the drive shaft. Based on the turbocharger validation tests, modifications to the turbo wheel will be modeled and the performance will be assessed. Bench tests will be completed before engine tests are scheduled.

Results

Two of the three parties that were initially identified as potential subcontractors for the project have completed contract agreements with Caterpillar. After further consideration, it was determined that the third vendor would participate in the program solely as a materials supplier.

Finite element modeling of the existing HEAT® turbocharger design was completed. The objective of this analysis was to evaluate the critical stresses that develop during an extreme operating cycle and compare the results for TiAl with the nickel-based alloy Inconel 713, which is typically used in similar applications. The modeled cycle consisted of going from a cold start to peak torque, followed by low idle conditions. Identical operating conditions and wheel design were used in both analyses; thus the different results can be attributed only to differences between the two materials. The code ABAQUS® was used for the analysis, using loads and boundary conditions obtained from aerodynamic simulations. Only an angular portion of the wheel and shaft was modeled, owing to symmetry, as shown by the mesh in Figure 2. This wedge consists of a blade, a section of the wheel hub, and a section of the shaft. Temperatures and stresses were obtained from the analyses, and the results showed that transient peak stresses on the wheel are reduced by approximately 50% by replacing the Inconel 713 with TiAl. Critical stresses result from superimposing centrifugal and thermal effects, and the significant reduction in operating stresses corresponds to the lower density and higher thermal diffusivity of TiAl relative to Inconel 713.

Thirty TiAl wheels produced by the countergravity casting method were procured, in addition to more than 30 wheels produced by a second supplier using a gravity investment casting process. Analysis of the castings produced with these two techniques is ongoing to determine the optimum and most cost-efficient process for the application. Test bars for

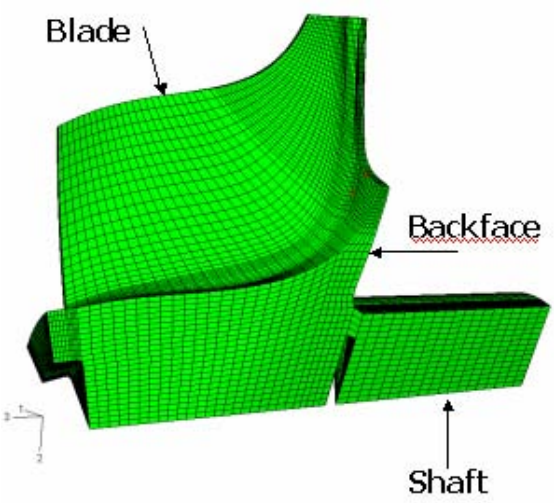

Figure 2. Mesh of an angular section of the wheel modeled in ABAQUS®. Using TiAl reduces the operating stresses by approximately 50% relative to Inconel 713.

welding experiments and material characterization were procured in addition to the wheel castings.

Test bars were machined from the wheel and shaft materials. The surfaces of the TiAl wheels were conditioned for friction welding trials. The cross section of the TiAl bars used for welding experiments was identical to that of the wheels. Joints were produced between the TiAl and the shaft material using bar-to-bar and shaft-to-wheel configurations. The friction welding process parameters were varied to produce the joints, and the resulting bar-to-bar jointed specimens were tested to failure in bending. A combination of parameters was established that produced bar-to-bar joints with a strength higher than that of the TiAl base material. Friction welding experiments showed a large dependency of the quality of the weld on the different process parameters. In addition, mass changes were shown to have a significant impact on the strength of the welds. This effect was evident after TiAl bars were welded to bars of the shaft material, producing joints with strength higher than that of the base TiAl. The conditions that produced strong bar-to-bar welds were used to make two prototype shafted wheels. Weak, flawed joints with a strength of approximately 50 MPa resulted; this was attributed to the higher heat dissipation from the weld area due to the increase in thermal inertia and resulting sharper temperature gradients.

Simulation was conducted to increase understanding of the sensitivity of the joint strength to the different process parameters. Modeling of the friction welding process was conducted using commercial simulation tools and customized user subroutines. Analyses were conducted using systematic combinations of rotational speed, frictional and forge loads, and frictional time and evaluating the effect of these factors on the resulting temperatures and thermal stresses. A proportional relation between the severity of the temperature gradients and the thermal inertia was observed. A higher thermal inertia increases the severity of the temperature gradients, which leads to higher thermal stresses and cracking. This correlates with cracking observed on the heat-affected zone of the shafted wheels.

Simulation results were used to define improved processing conditions for an additional round of welding experiments; and 16 additional joints, including bar-to-bar and shaft-to-wheel joints, were produced. The jointed specimens were heat-treated to relieve stresses, machined to remove the flash, and subjected to non-destructive evaluation (NDE). After NDE, the specimens were tested to failure in tension, and the tensile strengths were recorded. Subsequently, fractography was conducted to determine the nature of the failures and to correlate with features observed with NDE. The strength of the joints was increased in this round of tests, producing shafted wheels that, when tested in tension, failed away from the weld on the base TiAl material. However, the strength recorded was lower than expected for TiAl because of stress concentration. A parametric study is being conducted to modify the back face geometry of the turbine, with the purpose of increasing the overall strength of the component by reducing stress concentrations and thermal stresses. The results of the parametric study will be used for another iteration of welding experiments with the objective of completing the development of the joint.

Two different NDE techniques were used to identify subsurface defects on the weld and the heat-affected zone. A specimen with a poor weld was selected for initial evaluation to establish a baseline by identifying and characterizing features that are not desirable in sound welds, such as incomplete bonding and radial cracking. The first technique employed was eddy current, using a setup for automatic scanning by attaching the specimen to a turntable and controlling the vertical position of the probe. A prototype TiAl wheel shaft undergoing eddy current inspection is shown in Figure 3. The second

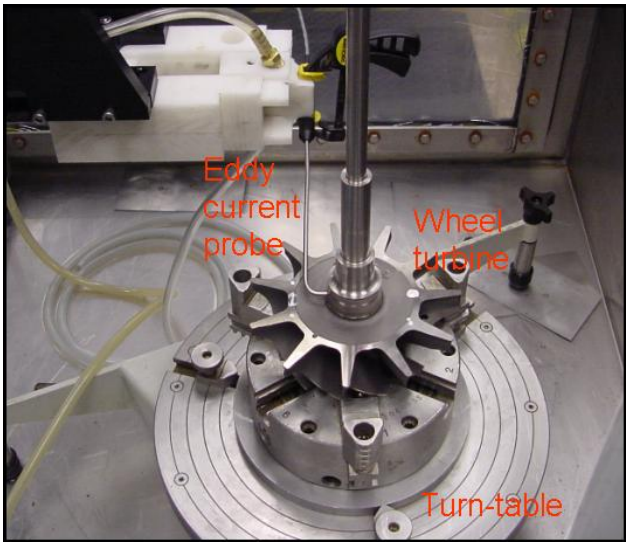

Figure 3. Shafted TiAl turbine wheel during NDE inspection.

technique was immersed ultrasound inspection, setting the specimen up in a similar automated configuration. Ultrasound inspection, with its finer resolution, showed not only the features observed with the eddy current but also smaller cracks. Features observed with both techniques were correlated with features observed on fractographic analysis, positively identifying defects on the weld plane as well as radial cracks.

A prototype HEAT® turbocharger was built using an Inconel 713 turbo wheel and tested on an internally designed Caterpillar gas stand as well as on an engine. The purpose of these prototype tests was to validate the compression capacity of the HEAT® turbocharger design and to obtain baseline data for comparison with a HEAT® turbocharger to be built using a TiAl turbo wheel. Steady and transient test results indicate that the HEAT® turbocharger likely has the potential to meet the performance and emission requirements of the engine after redesign of the wheel.

The decision was made to use one of the prototype TiAl wheel shafts produced during the second round of experiments to assemble a HEAT® turbocharger unit and to obtain all performance information possible in gas stand testing, knowing of the limited strength of its weld. This test was intended as a proof of concept and in no way intended to be a reliability or durability checkpoint. This HEAT® turbocharger unit was tested in the gas bench, and data were collected at two speed lines above 60,000 RPM. The weld failed at 330°C after 9 hours of operation and immediately following an engine surge. After failure, the loose wheel continued rotating inside the housing, impacting the leading edges with the housing, and four blade tips fractured. The wheel did not burst, even though it failed below its brittle-to-ductile transition temperature. Post-test inspection of the wheel revealed that the damage on the TiAl wheel blades was similar to that observed on Inconel wheels after a weld failure, even with the severity of impacts it received. These results strengthened the position of the entire team that TiAl has great potential for this application. Joints with strengths close to three times the strength of the specimen tested in the gas stand have been produced after iterations of experiments and simulation. Further gas stand testing will be conducted after fully optimizing these joints.

Joined by a representative from a turbocharger manufacturer, the Advanced Materials Technology and Air Systems team conducted on-site initial assessments of the TiAl casting processes of two suppliers. Test materials, including wheels and bars, have been procured from both suppliers and are under evaluation.

Conclusions

Titanium aluminide is an important material for less complex and more efficient air systems for Caterpillar engines. The lightweight nature of the material reduces the inertia of rotating components, enabling more compact and reliable turbocharger designs that will potentially lead to increased fuel efficiency and reduced transient emissions. An additional benefit of TiAl, demonstrated with finite element analyses, is the reduction of stresses during operation by 50% relative to Inconel 713, as a result of lower centrifugal loads and higher thermal diffusivity.

Initial assessment of two foundries was completed, and TiAl wheel castings and test bars were procured from both suppliers. Materials obtained from these suppliers have been used to develop a process to join the TiAl wheel to shaft materials. An iterative approach for this development has been applied, conducting welding experiments and simulation. Optimization of the geometry of the wheel and shaft and of friction welding parameters is ongoing to increase the overall strength of the component.

A methodology for conducting NDE of the wheel-shaft joints has been developed using eddy current and automated immersed ultrasound. Features observed on fractographic examination of specimens tested in tension have been positively correlated to features observed with the NDE techniques used.

A shafted TiAl turbine wheel was assembled into a turbocharger and tested on a gas stand rig. This test was intended as a proof of concept and not as a reliability or durability checkpoint. Damage on the wheel was similar to that observed on failures of Inconel 713 wheels. These results strengthened the position of the team that TiAl has great potential for this application. Joints with strength close to three times the strength of the specimen tested in the gas stand have already been produced after iterations of experiments and simulation. Further gas stand testing will be conducted after fully optimizing these joints.

5. TEST AND MATERIALS STANDARDS

A. Rolling Contact Fatigue

Andrew A. Wereszczak
Ceramic Science and Technology Group (CerSaT)
Oak Ridge National Laboratory
PO Box 2008, MS 6068,
Oak Ridge, TN 37831-6068
(865) 576-1169; fax: (865) 574-6098; e-mail: wereszczakaa@ornl.gov

DOE Technology Development Area Specialist: Dr. Sidney Diamond
(202) 586-8032; fax: (202) 586-1600; e-mail: sid.diamond@ee.doe.gov
ORNL Technical Advisor: D. Ray Johnson
(865) 576-6832; fax: (865) 574-6098; e-mail: johnsondr@ornl.gov

---

Contractor: Oak Ridge National Laboratory, Oak Ridge, Tennessee
Prime Contract No.: DE-AC05-00OR22725

Objective

- Characterize the rolling contact fatigue (RCF) performance of ceramics and tribological coatings that are under consideration for use in rolling element components (e.g., hybrid bearings)
- Determine the effects of subsurface damage, properties such as (static and dynamic) hardness and fracture toughness, and the stress state from Hertzian contact on RCF performance.
- Model hypothetical microstructures that will promote improved RCF performance.
- Link RCF performances measured by different internationally used RCF test techniques.

Approach

- Establish three-ball-on-rod (3BOR) RCF test facilities and collaborations with domestic and international institutions that employ different RCF test techniques. Correlate test results.
- Vary machining-induced subsurface damage in a silicon nitride (Si_3N_4) and correlate that to measured RCF performance.
- Provide new understanding of RCF performance/microstructure relationship to ceramic manufacturers that will serve to promote microstructure engineering and improved RCF performance.

Accomplishments

- Established 3BOR RCF facility.
- Initiated formal collaboration with Bournemouth University (BU) in the United Kingdom to relate performances measured with 3BOR and three-ball-on-ball (3BOB) RCF test techniques.
- Defined machining conditions and designed and procured test coupons. Initiated testing.

Future Direction

- Conduct domestic interlaboratory study to compare 3BOR performances of a selected Si_3N_4.
- Compare RCF damage on rods and balls of a selected Si_3N_4 with the same coarse and fine grinding.
- Conduct international interlaboratory study to compare performances measured with different RCF test methods.

Introduction

The use of ceramics in rolling elements shows many practical advantages over traditional hard and bearing-grade steels. Current demands on load-bearing contacts in all kinds of machinery are leading to developments aimed at running them at high speeds with minimum vibration, hostile environments, increased unit loads, and restricted lubrication. The design and manufacture of such contacts are at the limit of established technology; hence the need for ceramic contacts.

Si_3N_4 is one class of ceramic that has combined properties that are most suited for rolling contact conditions. Experimental programs with Si_3N_4 contacts using full-scale and bench tests have produced some understanding of RCF modes failure and durability; however, the effects of grinding or finishing rate on the subsurface integrity and hence RCF durability and failure modes are poorly understood.

To address these issues, this project is characterizing the RCF performance of Si_3N_4 compositions that are under consideration for use (or that are presently used) in rolling element components (e.g., hybrid bearings, cam roller followers) (see Figure 1). There are several different test methods to measure RCF performance, so this project also works toward reconciling their measured differences so that their results can be validly pooled. The study of the effects of subsurface damage, properties such as (static and dynamic) hardness and fracture toughness, and the stress state from Hertzian contact on RCF performance is a natural outcome. Based on those findings, hypothetical microstructures that will promote improved RCF performance will be identified and shared with ceramic manufacturers.

Approach

There are three primary aspects to the project—measure RCF performance and reconcile results that were generated using different RCF test techniques; examine the effects that subsurface damage and microstructure have on RCF performance; and iteratively work with ceramic manufacturers and communicate RCF results and interpretations those manufacturers can then use to develop lower-cost Si_3N_4 compositions, improve Si_3N_4 machinability, improve RCF performance, or combinations thereof.

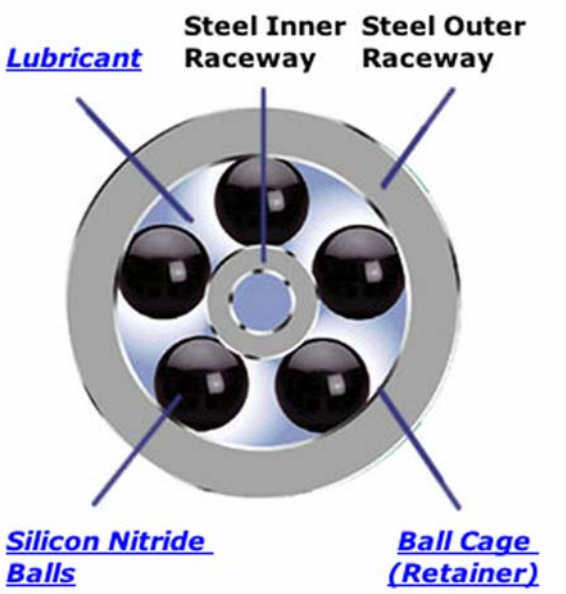

Figure 1. Schematic of a hybrid bearing system that includes silicon nitride balls. *Source: www.cerbec.com.*

A multi-task, 3-year project involving BU and the Oak Ridge National Laboratory (ORNL) was initiated in the last quarter of FY 2004; this collaboration will serve as a key component of the project. A BU Ph.D. student will be a primary performer of these tasks and will alternate on-site research at BU and ORNL over the life of the project, spending about half of the time at each institution. This student will work under the supervision of Prof. Mark Hadfield at BU and the project principal investigator at ORNL.

RCF performance of Si_3N_4 will be interrogated using 3BOB and 3BOR (NTN–Bower) RCF test methods conducted at BU and ORNL, respectively; and RCF performance measured with each technique will be linked. Additionally, the generated subsurface damage in cylindrical rods and spheres machined under the "same" machining conditions will be compared to assess/verify the sought equivalence. Ceradyne's Ceralloy 147-31N will serve as the model Si_3N_4. A critical element of this project will be the identification, characterization, and interpretation of subsurface damage; these will be accomplished through a variety of inspection means and test techniques. Rotating flexure testing, optical and scanning electron microscope fractographies, dye penetration, optical coherent tomography, scanning acoustic microscopy, and residual stress analysis will be used. Machining damage in Ceralloy 147-31N, which was systematically characterized and exploited by uniaxial flexure testing in a recent study,[1,2] will provide a useful guide to RCF sample preparation. Indentation and scratch testing and finite element analysis (FEA) will also be used to supplement the characterization and interpretation of results. Finally, the student, project principal investigator, and Hadfield will integrate the results and interpret the effect of subsurface damage on RCF in Si_3N_4.

Results

RCF performance is being interrogated as a function of pre-existing subsurface damage in Ceralloy 147-31N Si_3N_4. Specimens were ground in one of three ways: 100-grit roughing and 600-grit finishing; 180-grit roughing and 600-grit finishing; and the conventional method for machining RCF specimens (1200-grit finish). Table 1 provides additional details of the machining.

The effects of subsurface damage in monolithic ceramics are critical to RCF performance, but that relationship has largely been taken for granted and is little understood. To help resolve the issue, numerous test coupons were prepared or designed to facilitate the quantification of a critical independent parameter in this project: depth of machining damage. Ceralloy 147-31N RCF (Figure 2), half-RCF (Figure 3), rotary bend strength (RBS) (Figure 4), half-RBS (Figure 5), and ASTM C1161B test specimens have been prepared and are undergoing testing. All five of those specimen geometries were machined according to the conditions outlined in Table 1. The RBS, half-RCF, half-RBS, and ASTM C1161B (uniaxial 4-point-bend flexure) specimens are being tested in parallel with the RCF specimens because flexure tests are efficient at quantifying the depth of subsurface damage (via companion fractography) and at exploiting the effects of sub-surface damage (on strength in this case). The RBS specimen rotates during its monotonic loading to fracture, so its entire gage section is subjected to outer-fiber tensile stresses. This will enable the study of strength-size scaling effects. The half-RCF and half-RBS specimens were strength-tested in four-point-flexure (Figure 6). The strength calculation for the half-RCF (i.e., half-cylinder) geometry is straightforward; however, the calculation of fracture stress for the half-RBS geometry from the fracture load is not. FEA of the half-RBS specimen (Figure 7) was used, and failure load was linked to maximum outer fiber tensile stress in the specimen's gage section. Weibull strength statistics for the half-RBS specimen are listed in Table 2. Strengths among the three sets were not appreciably different.

Table 1. Ceralloy specimens were prepared by one of three finishing conditions

Finish	Step	Wheel	Removal (in.)	Removal per pass (in.)
Coarse	1. Roughing 2. Induce damage 3. Finishing	Accepted practice 100 grit 600 grit	 0.004 0.0005	0.001 0.001 0.0001
Fine	1. Roughing 2. Induce damage 3. Finishing	Accepted practice 180 grit 600 grit	 0.004 0.0005	0.001 0.001 0.0001
RCF-conventional	Use the "accepted" practice for RCF test bar finishing (Ref PO# SB 1341-02-N-1669). Fine grinding using 1200-grit diamond, per Siddiqui e-mail of February 18, 2004			

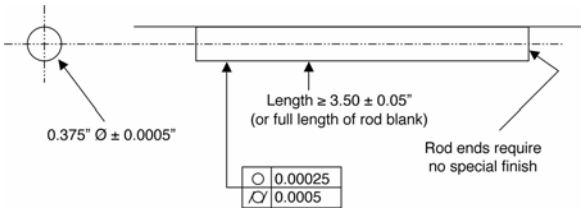

Figure 2. Schematic of RCF specimen geometry. This specimen is used in 3BOR RCF tests.

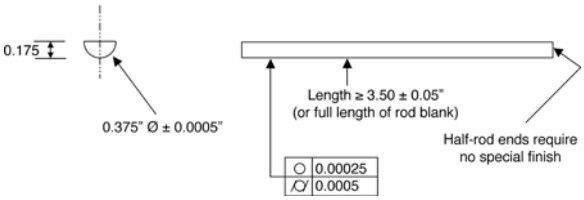

Figure 3. Schematic of half-RCF specimen geometry. The four-point-flexure flexure strength distribution and depth of machining-induced subsurface damage were measured.

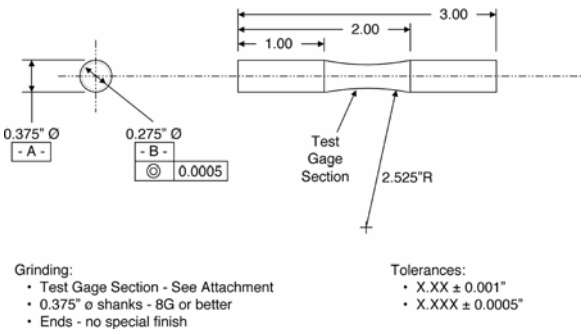

Figure 4. Schematic of RBS specimen geometry. This specimen is being subjected to rotary bending and monotonically loaded to fracture—a new test method developed in this program.

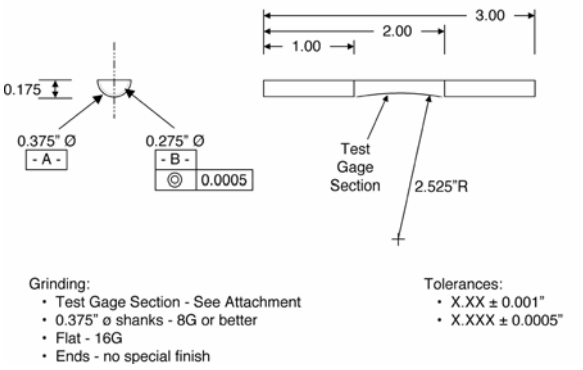

Figure 5. Schematic of half-RBS specimen geometry. The four-point-flexure flexure strength distribution and depth of machining-induced subsurface damage were measured.

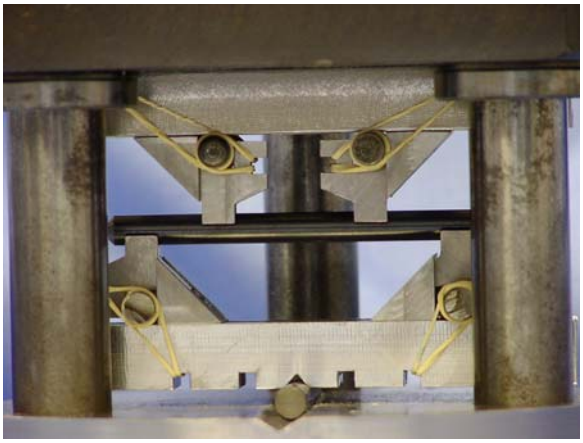

Figure 6. Four-point-bend fixture used to flexure-strength-test cylindrical or half-RCF or half-RBS specimens.

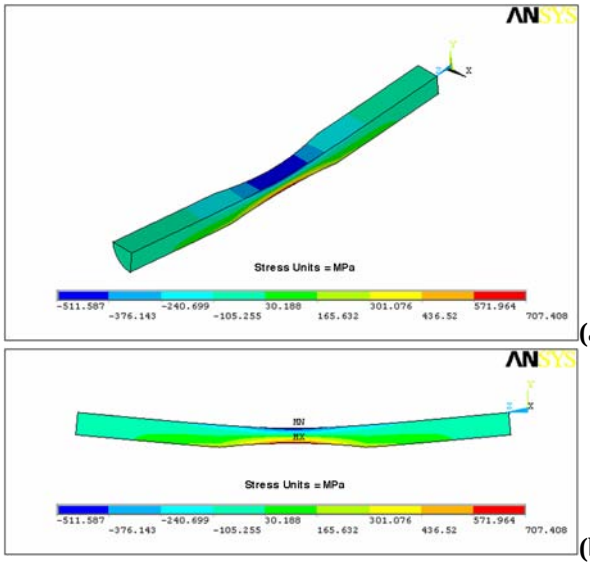

Figure 7. Oblique view (a) of FEA stress analysis of half-RBS specimen. Symmetry was used to simplify the model, so only one-half of the half-RBS specimen was analyzed. Four-point-flexure failure load was used to calculate the outer fiber tensile stress (b) that existed at fracture.

Fractography of these specimens (and all the other flexure specimens) is presently under way to examine the depth of machining-induced subsurface damage.

To better understand RCF damage and its link to material microstructure, several supplemental characterization test methods are used. For example, instrumented static and dynamic indentation testing and instrumented scratch testing of the Ceralloy

Table 2. Half-RBS flexure strength results

Finish	Number of test specimens	Average strength (MPa)	Standard deviation (MPa)	Characteristic strength (MPa)	Weibull modulus
Coarse	10	715.6	99.1	753.6	8.1
Fine	10	756.4	51.9	775.2	15.1
RCF-Conv.	10	732.0	79.6	765.1	11.3

147-31N are used to explore how contact loading damage (as a function of loading rate) is affected by sub-surface damage. The competition of quasi-plastic damage and cracking processes in Ceralloy 147-31N is being interrogated as a function of the depth of the sub-surface damage and compared with polished material as well. NBD200 Si_3N_4 (NIST standard reference material for Knoop hardness) and NC132 Si_3N_4 (NIST standard reference material for fracture toughness) are also being tested; specimens of those materials are presently undergoing indentation and scratch testing, the results of which will serve as a performance reference for comparing the performance of Ceralloy 147-31N and whatever additional ceramics are ultimately tested in this program. SN101C and TSN-03NH (both bearing grades of Si_3N_4) are undergoing instrumented indentation and scratch testing as well, and their performance will be compared with that of the other listed silicon nitride compositions. Raman spectroscopy, which can measure residual stresses, is being used. Preliminary results suggest that residual stresses (manifested by changes in wave number peak location in Figure 8) can indeed be quantified.

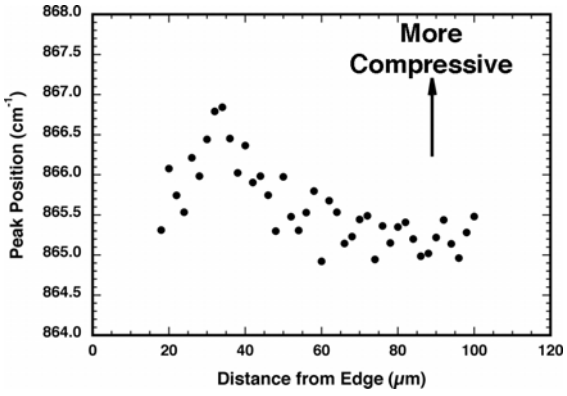

Figure 8. PiezoRaman spectroscopy profile of Raman peak position as a function of distance from the edge in a SN101C ball. Higher peak position is proportional to residual compressive stress, so this measurement shows that a gradient in compressive stress exists as a function of depth.

An interlaboratory study of research institutions and universities within the United States is being organized whereby RCF testing will be performed on samples of Si_3N_4 and the results combined and compared. Colorado State University and the Air Force Research Laboratory have so far given verbal commitments of participation.

In addition to the collaboration with BU, interactions exist with Germany's Bundesanstalt für Materilforschung und–prüfung, Japan's National Institute of Advanced Industrial Science and Technology, and the United Kingdom's National Physics Laboratory to compare RCF performance. These interactions exist under the auspices of the International Energy Agency Annex III. Working group participants met in January in Cocoa Beach, FL; the next meeting is tentatively set for June 2005 in Kobe, Japan, coincident with the International Tribology Conference.

Dialogue with ceramic bearing manufacturers is critical to maintaining relevance in this program. Frequent communication occurs between the principal investigator and chief scientists at several domestic manufacturers (Cerbec/Saint-Gobain, Ceradyne, Enceratec, Kennametal, and Cercom) regarding this project's test matrix, plans, and progress.

Conclusions

A 3BOR RCF test facility was established at ORNL, and the evaluation of ceramic RCF performance is now under way. A formal collaboration was initiated with BU for 3BOB RCF testing of ceramics; it will enable the eventual reconciliation of RCF performance measured with those two techniques. The effects of subsurface damage on RCF performance are being scrutinized. Several supplemental characterization routes (e.g., flexure strength testing and subsurface damage interrogation, damage evaluation from Hertzian indentation, piezoRaman spectroscopy) are used to assist in the interpretation of RCF performance. Domestic and international interlaboratory RCF studies are planned to compare

and verify ORNL measurements with those generated at other laboratories and institutes. Finally, new under-standing of the RCF performance/microstructure relationship will be provided to ceramic manufacturers that will serve to promote microstructure engineering and improved RCF performance.

References

1. J. Kang, R. T. Cundill, and M. Hadfield, "The Consequences of Aggressive Lapping Processes on the Surface Integrity of HIPed Silicon Nitride Bearing Balls," *Tribology in Environmental Design 2000*, Professional Engineering Publishing, London.

2. G. D. Quinn, L. K. Ives, and S. Jahanmar, "On the Fractographic Analysis of Machining Cracks in Ground Ceramics: A Case Study on Silicon Nitride," NIST Special Publication 996, National Institute of Standards and Technology, U.S. Department of Commerce, May 2003.

Presentations

A. A. Wereszczak, "IEA Annex III Working Group Meeting on Rolling Contact Fatigue," presented at the 28th International Cocoa Beach Conference on Advanced Ceramics and Composites, Cocoa Beach Hilton, Cocoa Beach, FL, January 27, 2004.

A. A. Wereszczak, "ORNL Characterization of Ceramics for Armor, Transportation, and Energy Applications," presented at Cercom, Inc, Vista, CA, February 25, 2004.

A. A. Wereszczak, "ORNL Characterization of Ceramics for Armor, Transportation, and Energy Applications," presented at Ceradyne Inc, Costa Mesa, CA, February 26, 2004.

A. A. Wereszczak, "Evaluation of Ceramic Deformation Processes Through Hertzian Indentation," presented at Saint-Gobain, Worcester, MA, August 3, 2004.

B. Implementing Agreement for a Programme of Research And Development on Advanced Materials for Transportation Applications

M. K. Ferber
Ceramic Science and Technology Group
Oak Ridge National Laboratory
P.O. Box 2008, MS: 6068
Oak Ridge, TN 37831-6068
(865) 576-0818; fax: (865) 574-6098; e-mail: ferbermk@ornl.gov

DOE Technology Development Area Specialist: Dr. Sidney Diamond
(202) 586-8032; fax: (202) 586-1600; e-mail: sid.diamond@ee.doe.gov
ORNL Technical Advisor: D. Ray Johnson
(865) 576-6832; fax: (865) 574-6098; e-mail: johnsondr@ornl.gov

Contractor: Oak Ridge National Laboratory, Oak Ridge, TN
Prime DOE Contract Number: DE-AC05-00OR22725

Objectives

- Facilitate the integration of new technologies into the transportation sector by implementing research that validates the applicability of these technologies to improve material properties while maintaining acceptable life-cycle costs.
- Promote commercialization of new materials technologies by developing standard testing and characterization methods in conjunction with national and international standards communities.

Approach

- Define and implement research under the International Energy Agency (IEA) Implementing Agreement (IA) entitled *Implementing Agreement for a Programme of Research and Development on Advanced Materials for Transportation Applications* (IA–AMT).
- Conduct major research themes as annexes under the current IA:
  - Annex II: Co-Operative Program on Ceramics for Advanced Engines and Other Conservation Applications
  - Annex III: Co-operative Program on Contact Reliability of Advanced Engine Materials

Accomplishments

- Created a web site that provides the international technical community with information about (1) the mission and strategy of the IA, (2) details of the various annexes, and (3) a number of technical reports generated by collaborative research tasks conducted under Annex II. The site is at http://ia-amt.ornl.gov/index.html.
- Initiated Annex IV, A Cooperative Program on Integrated Engineered Surface Technology. Technical efforts associated with this annex are under way.
- Initiated Annex V, Light-Weighting of Materials. Planning efforts are under way.
- Canada and the United Kingdom joined the IA. Canada will participate in the lightweighting materials activity, while the United Kingdom will participate in Annex III.

Future Direction

- Develop plan for lightweighting materials annex and present to the Executive Committee for approval.
- Initiate test plan for Annex V.

Introduction

The current mission of the IA–AMT is to investigate promising new technologies for evaluating and ultimately improving the performance of materials for transportation systems. The primary motivation for this activity is the fact that new materials technologies are required to increase efficiency and reduce harmful emissions in these systems. Examples of these technologies include (1) lightweighting to improve fuel efficiency; (2) surface engineering to improve the resistance to wear and contact damage; (3) development of durable coating systems for thermal, wear, and environmental management; and (4) development of revolutionary materials (structural ceramics and ceramic matrix composites) for operation at much higher temperatures and pressures. As discussed in this report, the research activities within the IA–AMT focus specifically on (1) the identification of promising new technologies for improving materials performance and (2) the development of specialized characterization techniques for validating the applicability of this technology to improve material properties while maintaining acceptable life cycle costs.

At present the active contracting parties for the IA-AMT are

- Germany—Bundesanstalt für Materialforschung und –prüfung (BAM)
- Canada—Materials Technology Laboratory, CANMET
- United Kingdom—Department of Trade and Industry
- United States—U.S. Department of Energy

Approach

In the area of performance improvement, the current emphasis is on integrated engineered surface technology (IEST) and lightweighting of materials. IEST encompasses the synthesis, processing, characterization, and application of technologies that enhance the functionality of surfaces in contact with the environment or with the surfaces of other solids. Activities on lightweighting of materials focus on aluminum, high-strength steels, magnesium, metal and polymer composites, titanium, intermetallic alloys, and other advanced materials. Current topics under consideration include (1) data on production and resource availability; (2) life cycle data on environmental impacts associated with production, processing, and use of lightweight materials; (3) recycling information including regulatory frameworks; (4) data on crashworthiness, design, and testing methodologies; (5) data on base material cost; (6) data on energy impacts of lightweight materials; and (7) shared information on research programs on lightweight materials.

In terms of performance evaluation, the primary focus is on techniques for (1) assessing environmental degradation of structural (non-oxide) ceramics; (2) evaluating time-dependent degradation of the mechanical performance of structural ceramics; (3) quantifying key properties of coatings for wear, thermal, and environmental protection of current transportation materials; and (4) developing techniques for measuring key properties (topography, chemistry, subsurface damage) of engineered surfaces. Items 1 and 2 are motivated by the need to address key barriers to the use of this important class on material. For example, given the recent concern over environmental degradation of non-oxide ceramics in combustion environments, cost effective techniques are required to simulate these effects as well as to assess the effectiveness of environmental barrier coatings. The IA–AMT is currently evaluating a variety of techniques ranging from complex high-pressure burner rig tests to a simple cost-effective steam injection system. Ceramic coatings hold considerable promise for (1) improving wear resistance, (2) providing thermal protection, and (3) reducing environmental degradation of critical metallic components used in internal combustion engines. Unfortunately, techniques for assessing key properties, particularly with respect to the interface, are unproven. Item 3 addresses this limitation. In a similar fashion, as surface modification technologies mature, proven characterization techniques will be required to validate their performance (Item 4).

Results

The activities related to performance improvement and performance evaluation are covered in 4 annexes. Annex II focuses on pre-standardization (i.e., performance evaluation) issues related to the deployment of structural ceramics in transportation activities. Specific applications include ceramic diesel exhaust values, cam roller followers, timing plungers, etc. Results from these subtasks have led to the optimization of techniques for (1) characterization of powder properties, (2) quantification of the green-state characteristics, and (3) evaluation of mechanical performance. This extensive set of results generated in Annex II has been used in the establishment of standards [via the American Society for Testing and Materials (ASTM), Japan Industrial Standards (JIS), the Committee for European Normalization (CEN), the International Organization for Standards (ISO)] and National Institute of Standards and Technology (NIST) guidelines (see the publications list), which in turn have benefited the entire ceramics community.

Table 1 summarizes some of the existing standards that have benefited from the work conducted in this IA. In the case of room-temperature flexural strength, the test standard, ASTM C1161, was revised to reflect lessons learned about fixturing and test specimen configurations. ISO 14704 evolved from several standards (ASTM C1161, CEN EN843-1, and JIS R1601) and lessons learned from the IA–AMT work. The high-temperature flexural strength standard, ASTM C1211, evolved about the time of the IA–AMT round robin (Subtask 5–Annex II) and included lessons learned from C1161 and the IEA work. ISO DIS 17565 (not yet a standard) has evolved from several standards (ASTM C1211, CEN prEN820-1, and JIS R1604) and lessons learned from the IA–AMT subtask. The room temperature tensile strength standard, ASTM C1273, was developed as the IA–AMT results were being reviewed and analyzed and included many lessons learned. ISO 15490 evolved from two standards (ASTM C1273 and JIS 1606); and the IA–AMT round robin results were instrumental in establishing test specimen configurations, gripping arrangements, allowable bending, and test rates. The thermal shock standard, ASTM C1525, was developed after the IA–AMT subtask on thermal shock was completed. Although this standard follows a more conventional approach to thermal shock by using water quenching and standard MOR bars, insights garnered from the IA–AMT work are used in providing guidance to users in notes and discussions.

Current activities are focused on the evaluation and consolidation of nanocrystalline ceramics. Participants include the United States and Germany.

Table 1. Standards that have benefited from the IA subtasks

Property	JIS	ASTM	CEN	ISO
Flexural strength: RT	R1601-95	C1161-02	EN 843-1:95	14704:2000
Flexural strength: HT	R1604-95	C1211-98	prEN 820-1	DIS 17565
Statistical analysis	R1625-96	C1239-00	ENV 843-5:97	CD 20501
Fractography		C1322-02	prENV843-6	
Tensile strength	R1606-95	C1273-00		15490:2000
Sample preparation for the determination of particle size distribution of ceramic powders	R1619:95	C1282-00	EN 725-5:96	14703:2000
Surface area	R1626-96	C1274-00	EN 725-6:96	DIS 18757
Particle size distribution of powder by laser diffraction method	R1629:97			TC206 NP02
Thermal shock	R1615-93	C1100-98	prEN 820-3	
Flowability	R1639-4:99			TC206 WI93
Size distribution of granules	R1639-1:99			
Binder content of granules				
Drying loss of granules	R1639-3:99			
Bending fatigue: RT	R1621:95	C1368-00		TC206 PWI 07
Bending fatigue: HT	R16xx:01			

RT = room temperature; HT = high-temperature

Annex III also focuses on performance evaluation with emphasis on the evaluation of contact damage. International activities include a formal collaboration between Mark Hadfield of Bournemouth University (BU) in the United Kingdom and Oak Ridge National Laboratory (ORNL) in the United States. The study of the effects of subsurface damage (e.g., that results from component machining) on the rolling contact fatigue (RCF) performance of silicon nitride (Si_3N_4) is the primary theme. A BU Ph.D. candidate will serve as the cornerstone of the collaboration and alternate on-site research at BU and ORNL over the life of the project. The RCF performance of Si_3N_4 will be interrogated using ball-on-three-ball (Plint TE92) and three-ball-on-rod (NTN) RCF tests conducted at BU and ORNL, respectively. The Ph.D. candidate will attempt to link RCF performances measured with each technique. Additionally, the generated subsurface damage in cylindrical rods and spheres machined under the "same" mching conditions will be compared to assess/verify the sought equivalence.

A second international activity involves the preparation of a written report detailing techniques on RCF testing in each of the participating countries. Participants include Japan (AIST, KOYO-Seiko, and NSK), Germany (BAM), United Kingdom (NPL), and the United States (ORNL). The report will be completed at the end of 2004.

In 2005 and 2006, RCF studies involving both international and domestic participants will be implemented. Details of this international activity will be developed at the next IEA Annex III RCF Working Group meeting, tentatively set for June 2005 in Kobe, Japan—coinciding with the International Tribology Conference. Attendance of participants from Japan and the United Kingdom has been confirmed. The primary goal is to reconcile differences in the various test techniques and hardware. Results, including recommendations, will be forwarded to the appropriate standards setting organizations.

The effort conducted within the United States consists of an interlaboratory study of RCF testing involving research institutions and universities. Colorado State University and the U.S. Air Force Research Laboratory have so far given verbal commitments of participation.

Annex IV, A Cooperative Program on Integrated Engineered Surface Technology, focuses on the implementation of a vertically integrated engineered surface concept: combining surface texturing, thin films, and lubrication to create an engineered surface appropriate for different applications, with an overall objective of reducing friction and increasing durability. Although engineered surfaces can play a dominant role in energy conservation and utilization, several technical challenges must be addressed before such technology can be fully utilized. One broad area of crucial importance and mutual benefit is the development of international standards and practices for textured surfaces under different application conditions. Characterization and mechanical properties of an integrated engineered surface in terms of friction reduction, load-bearing capability, fatigue mechanisms, and life prediction are important issues that need to be addressed. Activities under Annex IV shall include various forms of characterization, evaluation methods, modeling, bench-scale testing, and demonstration field trials.

The implementation of lightweighting strategies in the transportation sector represents a major approach to increasing fuel efficiency and reducing emissions of greenhouse gases. Accordingly, a number of countries (see Table 2) are involved in extensive research activities to develop and validate advanced materials and manufacturing technologies for significantly reducing vehicle body and chassis weight. Materials under consideration include high-strength steels, magnesium, aluminum, titanium, metal-matrix composites, plastics, and ceramics, where applicable. Annex V, Light-Weighting of Materials, focuses on methods required for both performance improvement and evaluation, which are of interest to the participants. Current topics under consideration include (1) data on production and resource availability; (2) life cycle data on environmental impacts associated with production, processing, and use of lightweight materials; (3) recycling information, including regulatory frameworks; (4) data on crashworthiness, design, and testing methodologies; (5) data on base material cost; (6) data on energy impacts of lightweight materials; and (7) shared information on research programs on lightweight materials. In terms of recent achievements a draft plan outlining the scope of work, which covers areas of mutual interest, was prepared for discussion at the executive committee meeting in October 2004. Participants included the United States, Canada, and Australia (membership pending).

Table 2. Summary of lightweighting materials programs

Country	Program
United States	FreedomCAR and Vehicle Technologies Program *http://www.eere.energy.gov/vehiclesandfuels/technologies/materials/index.shtml*
Canada	AUTO21 Network of Centres of Excellence *http://www.auto21.ca/materials_e.html* Canadian Lightweight Materials Research Initiative (CLiMRI) *http://climri.nrcan.gc.ca/default_e.htm*
Australia	Light Metals Action Agenda *http://www.industry.gov.au/content/itrinternet/cmsindexpage.cfm* Cooperative Research Centre for Cast Metals Manufacturing (CAST) *http://www.cast.crc.org.au/*

Conclusions

The IA–AMT has made significant progress in expanding its scope, as evidenced by the addition of two new annex (IV and V). Both annexes are expected to generate new members. Given this progress, a formal request has been made to the IEA to extend the IA–AMT for a period of 3–5 years.

Publications/Presentations

Implementing Agreement for a Programme of Research and Development on Advanced Materials for Transportation Applications (IA-AMT), Strategic Plan, March 2004 (available at http://ia-amt.ornl.gov/.

International Energy Agency Implementing Agreement for a Programme of Research and Development on Advanced Materials for Transportation Applications, Annual Report 2003, February 2004 (available at http://ia-amt.ornl.gov).

C. Testing Standards

George Quinn
National Institute of Standards and Technology
Ceramics Division, Stop 8529
Gaithersburg, MD 20899
(201) 975-5765; fax (301) 975-5334; e-mail; geoq@nist.gov

DOE Technology Development Area Specialist: Dr. Sidney Diamond
(202) 586-8032; fax: (202) 586-1600; e-mail: sid.diamond@ee.doe.gov
ORNL Technical Advisor: D. Ray Johnson
(865) 576-6832; fax: (865) 574-6098; e-mail: johnsondr@ornl.gov

---

Contractor: Oak Ridge National Laboratory, Oak Ridge, Tennessee
Prime Contract No: DE-AC05-00OR22725
Subcontractor: National Institute of Standards and Technology, Gaithersburg, Maryland

---

Objective

- Develop mechanical test method standards in support of the Propulsion Systems Materials Program. New methods and sound engineering data will facilitate adoption of new materials in heavy vehicle propulsion systems.

Approach

- Conduct pre-standardization research on test methods that need refinement, or develop new test methods.
- Develop draft recommendations for practices or procedures based upon the needs identified by the research.
- Conduct round robins as necessary.
- Standardize procedures in the American Society for Testing and Materials (ASTM) and/or the International Organization for Standards (ISO).

Accomplishments

- Completed pre-standardization work on the flexural strength testing of split cylinders. A report is in preparation. Completed and fully documented all work on the fractographic characterization of grinding damage cracks.
- Completed a series of papers and made presentations.
- Completed about half of a NIST *Guide to Practice on Fractographic Analysis of Brittle Materials*.
- Revised, refined, and improved a variety of current ASTM and ISO standards.
- Helped found a new ASTM subcommittee on applications standards.
- Worked to correct and refine an ASTM standard specification for silicon nitride bearing balls.

Future Direction

- Write up the split cylinder test method and present the results to ASTM Committee C-28, Advanced Ceramics, for review. The error analyses for flexural strength testing of cylindrical rod specimens will be completed and a draft standard prepared for ASTM.

- Complete *the Guide to Practice on Fractographic Analysis*.
- Resume pre-standardization testing on the diametral compression strength test with the goal of standardization.

Introduction

This project creates new test methods that will facilitate the use of advanced materials in heavy-duty propulsion systems. Much of the work is for brittle materials such as ceramics, for which classical mechanical test methods developed for metals are not suitable. For example, tension-strength test specimens of many ceramic materials made in short, stubby cylindrical shapes (e.g., diesel engine fuel injector pins, timing plungers, valves) and classical dog bone shapes are impractical (Figure 1). Our goal is to adapt or refine existing test methods or invent new ones that will allow engineers and researchers to measure mechanical properties with good accuracy and precision. Formal test method standards are our primary objective. Sound test methods and high-quality databases will enhance the credibility of new materials and encourage engineers to use them in advanced heat engines.

Figure 1. Silicon nitride bearings.

Approach

Over the course of this program, we have formulated or contributed to the development of 17 ASTM and ISO standards. These have covered a range of topics including hardness, flexural strength, fracture toughness, fractography, elastic modulus, and Weibull strength distribution parameter determination. We have even contributed to a ceramic material specification for silicon nitride ball bearing materials. A spin-off benefit of this work has been that the generic test method standards have been used to create several biological ceramic materials specifications for dental and hip joint implant ceramics. Work continues on new alternative test methods.

A major element of this program has been the refinement of fractographic techniques to facilitate the detection and characterization of strength-limiting flaws in both laboratory-scale test specimens and components. The strength of ceramic components or parts is controlled by microscopic flaws, which may either be intrinsic to the manufacture or be introduced during grinding and finishing.

We also continued our work on several new mechanical test methods that are designed to measure mechanical properties of cylindrically shaped components or test coupons. Formal standard test methods are on the books for rectangular bend bars or tension-strength specimens, but these are not suitable for cylindrical parts (Figure 2). Simple methods for cylindrical parts are needed. Three methods we are working on are split cylinder flexural strength tests, rod flexural strength tests, and diametral compression strength tests.

Figure 2. Round specimens.

Important refinements and corrections were made to several existing standards during the past year. Thus “standards maintenance” activity is necessary to incorporate improvements and lessons learned from this and other projects.

Results

A major task was completed that involved fractographic characterization of grinding-induced cracks on the surface of finished ceramics. Figure 3 shows an example of a grinding crack in a rod

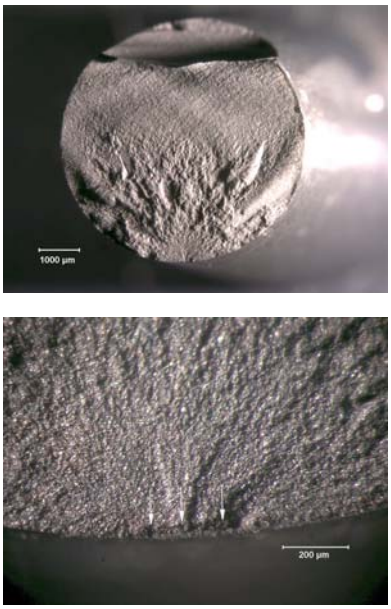

Figure 3. Fracture surface of a broken ceramic rod test specimen. The fracture origin is in the smooth semicircular region on the bottom of the figures. The origin is a "V-machining" crack (arrows in the lower figure) created when the rod was ground to final dimensions. Similar cracks can limit strength in components

strength test specimen. Several major reports and technical papers were prepared and presented to distribute this important information about grinding-induced damage. Lessons learned were incorporated into several ASTM standards.

An ASTM standard for fractographic analysis, C 1322, has already been adopted; but a more user-friendly *Guide to Practice for Fractographic Analysis* is also in preparation. The formal standard outlines the optimum procedures that engineers and fractographers should follow in performing fractography, but it assumes the analyst has moderate experience. The *Guide to Practice* will be a tutorial that will help the lay engineer learn the art of fractographic analysis of brittle materials and help transform what may seem to be a mysterious art into a routine engineering practice. It will have hundreds of example fractographs. Figure 4 is an example illustration showing how grazing incident angle lighting can help bring out fracture markings on fracture surfaces. The new *Guide to Practice* will include a set of recommendations for measuring

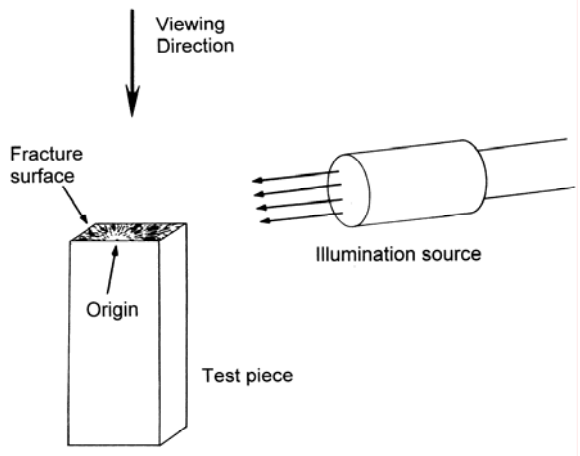

Figure 4. An example illustration from the *Guide to Practice for Fractographic Analysis of Brittle Materials*. This schematic shows vicinal, or low angle grazing illumination, which can create shadows that highlight features on the rough fracture surface of a broken test piece such as shown in the previous figure. Fractography can be effectively applied to understand the causes of fracture in the laboratory and in service components.

fracture mirror sizes. Fracture mirrors are relatively smooth zones surrounding fracture origins in ceramics, and their size can be directly correlated to the stress in the specimen or component at the instant of fracture. Fracture mirror analysis is powerful tool for forensic analysis since it can calculate the fracture stress even if the mode of loading is unclear or unknown.

Substantial progress was made this year on pre-standardization for the split cylinder strength test method. Short, stubby cylindrical parts are difficult to test for strength. A simple solution is to split the cylinder lengthwise and test the halves in a modified common flexural strength test fixture, as shown in Figures 5 through 7. Figure 8 shows a fracture surface of one of the rods. We had difficulty identifying the precise nature of the flaws in this material, but we eventually deciphered several fracture origins. A paper is in preparation on our findings. The Weibull strength distribution for one particular batch of material is shown in Figure 9. The findings of this work will be presented to ASTM Committee C-28, Advanced Ceramics, for review for suitability as a standard test method. Results will also be coordinated with the appropriate ceramic part manufacturers and engine companies.

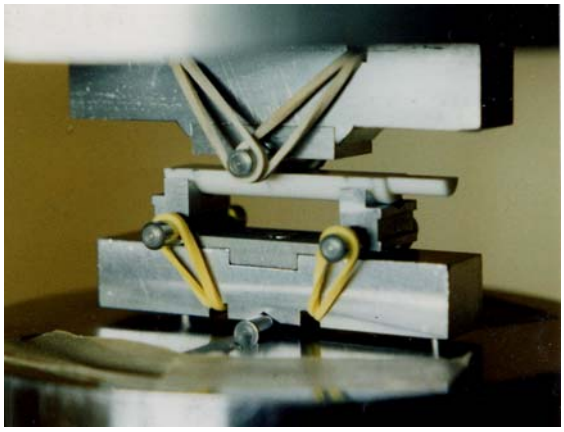

Figure 5. A ceramic split cylinder specimen (white) in a common three-point flexure strength fixture. This is a simple way to measure the strength of the ceramic part, which would be difficult to do for the intact part due to the high forces that would be necessary to break it. The finished round outer part surface is tested, and the cut surface which is on the top (compression side) of the bending loading, does not affect the results.

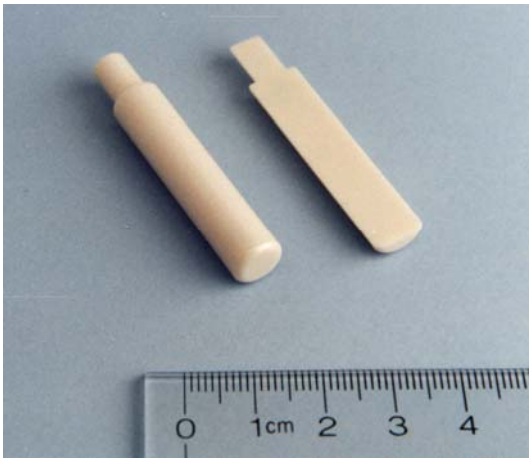

Figure 6. A cylindrical zirconia ceramic engine part. The part is a fuel injector pin for a heavy duty diesel engine. The left shows the intact part and the right shows a part cut in half. The latter is easier to test for strength.

Figure 7. Expanded view of the bend fixtures for a split cylinder (white specimen). Cradles hold the bottom of the specimen and distribute the load evenly. Load is applied to the specimen top (the cut surface) by the middle roller which is shown held in place by rubber bands on the subassembly on the top right of the photo. The middle roller is free to articulate or rock to match the specimen surface. Extra parts are shown in the fore and background.

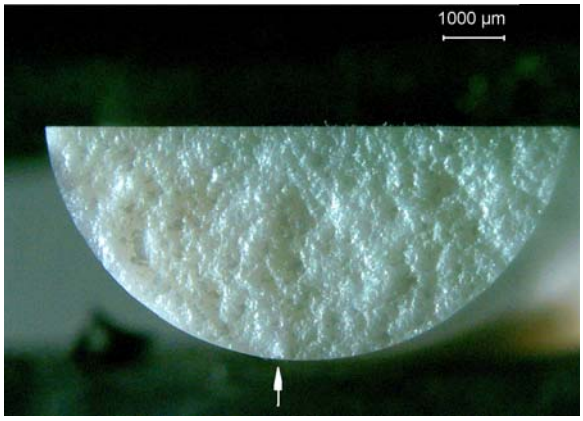

Figure 8. Optical fractograph showing the fracture surface of a broken split cylinder zirconia specimen. The arrow marks the fracture origin. Fractographic analyses was difficult in this material which had very rough fracture surfaces.

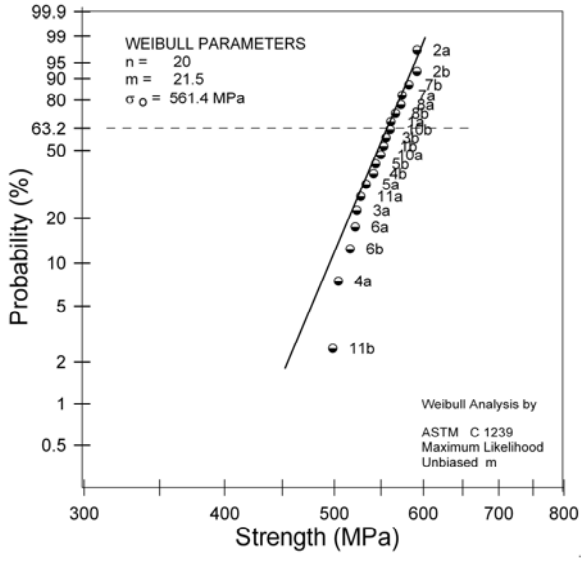

Figure 9. Weibull plot for split zirconia fuel injector pin parts.

We have made substantial progress in refining testing methods for measuring the flexural strength of full cylindrical rod specimens. Figure 10 shows a full-size rod specimen which, unlike the parts shown in earlier figures, is longer and therefore can be tested more easily. Cradles must be used to apply the forces evenly to the specimen. In FY 2004, we made progress on the analytical error analysis for this configuration. We expect to finish this work in the upcoming year, paving the way for standardization.

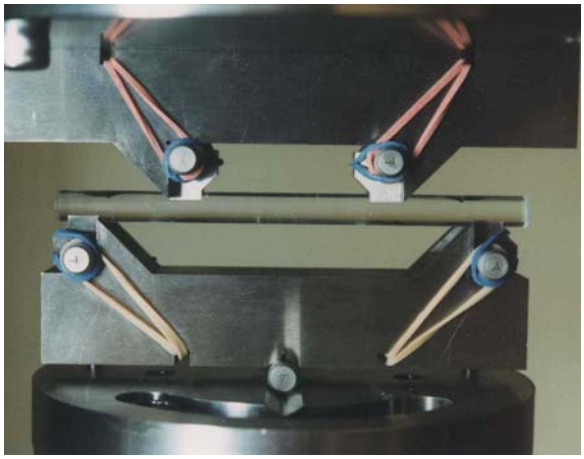

Figure 10. Flexural strength test fixture for a rod specimen.

Pre-standardization work on the diametral compression strength test specimen is planned for the upcoming year (Figure 11). Small pill-shaped specimens are loaded on their rims and split by tensile stresses. This is a convenient testing configuration, which in principle is ideally suited for small cylindrical parts; but there are some unsolved problems. We have completed some preliminary work and a review of the literature, which has revealed some of the problems with the method.

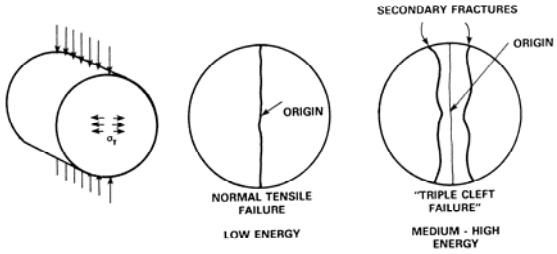

Figure 11. Diametral compression strength test.

Finally, we refined and updated a number of the standards created earlier in this program, including ASTM hardness, C 1326 and C 1327; ASTM fracture toughness, C 1421; ASTM fractographic analysis, C 1322; ASTM silicon nitride bearing specification, F 2094; and ISO 14704 and ISO 17565 on flexural strength at room temperature and high temperatures, respectively. As new information becomes available or shortcomings are revealed, it is prudent to update and correct these formal standards.

Conclusions

We have made progress in expanding the suite of test methods available for evaluating the properties of brittle ceramic materials. Our goal is to improve the test method and data base infrastructure that facilitates the incorporation of new advanced materials in heavy-duty diesel engines. Substantial progress was made in improving fractographic methods for detecting grinding-induced cracking and in developing test methods for measuring the strength of cylindrical parts. ASTM and ISO standards have been adopted, refined, and updated.

Publications/Presentations

G. D. Quinn, L. K. Ives, and S. Jahanmir, "Fractography Reveals Machining Cracks," *Bul. Amer. Ceram. Soc*. **82(**7) 11 (2003).

G. D. Quinn, L. K. Ives, and S. Jahanmir, "Machining Cracks in Finished Ceramics," to be published in *Fractography of Advanced Ceramics, II*, ed. J. Dusza, TransTech Publishing, Zurich, 2005.

G. D. Quinn, L. K, Ives, and S. Jahanmir, "Machining Damage Cracks: How to Find and Characterize Them by Fractography," pp. 383–394 in *Ceram. Eng. Sci Proc*. **24**(4), 2003.

G. D. Quinn, R. J. Gettings, and L. K. Ives, "A Standard Reference Materials for Vickers Hardness of Ceramics and Hardmetals," to be presented at the IMEKO Hardness Conference, National Institute of Standards and Technology, November 11–12, 2004.

G. D. Quinn, J. Eichler, U. Eisele, and J. Rödel, "Fracture Mirrors in a Nanoscale 3Y-TZP," *J. Amer. Ceram. Soc*. **87(**3) 513–516 (2004).

A. B. Kounga Njiwa, T. Fett, J. Rödel, and G. D. Quinn, "Crack Tip Toughness Measurements on Sintered Reaction-Bonded Si_3N_4," *J. Amer. Ceram. Soc*. **87(**8) 1502–1508 (2004).

D. Surface Modification of Engineering Materials for Heavy Vehicle Applications

Stephen Hsu
National Institute of Standards and Technology
100 Bureau Drive, Gaithersburg, MD 20899
(301) 975-6120; fax:(301) 975-5995 ; e-mail: stephen.hsu@nist.gov

DOE Technology Development Area Specialist: Dr. Sidney Diamond
(202) 586-8032; Fax: (202) 586-1600; e-mail: sid.diamond@ee.doe.gov
ORNL Technical Advisor: D. Ray Johnson
(865) 576-6832; fax (865) 574-6098; e-mail: johnsondr@ornl.gov

---

Contractor: Oak Ridge National Laboratory, Oak Ridge, Tennessee
Prime Contract No: DE-AC05-00OR22725
Subcontractor: National Institute of Standards and Technology, Gaithersburg, Maryland

---

Objectives

- Organize an international cooperative research program on integrated surface modification technology under the auspices of the International Energy Agency (IEA).
- Design and identify surface features and patterns that can achieve friction reduction and enhanced durability for heavy duty diesel engine components.
- Develop the understanding and appropriate models to explain the texturing effects on frictional characteristics. Develop appropriate thin films and coatings to achieve a synergistic and complementary relationship with texturing to enhance performance.
- Discover and develop a surface chemistry for protective films and coatings that works in synergy with the coatings.

Approach

- Determine the effect of size, shape, pitch, and patterns of surface textural features on friction under (1) a high-speed, low-load regime; (2) a high-load, high-speed regime; and (3) a high-load, low-speed regime.
- Develop cost-effective fabrication technologies for creating surface textural features on various surfaces including metals, ceramics, and coatings.
- Develop a test methodology to measure the effects of the textures on friction.
- Conduct research to develop an integrated system approach to combine the best practices in thin films, coatings, and surface chemistry for performances unrealizable by an individual approach alone.
- Concurrently, organize an international cooperative research program under the auspices of the IEA to pool resources and share this energy conservation technology worldwide.

Accomplishments

- Developed a new design principle for surface texture design to enable friction reduction under boundary lubrication conditions.
- Developed in situ instrumentation to allow direct observation of interface flow patterns with and without surface textural features.

- Visited several countries to establish agreement to join the IEA cooperative research activity.
- Visited various domestic companies and universities to organize a U.S. working group on integrated surface technology.
- Obtained final approval from the IEA Executive Committee on a new Annex on integrated surface technology in March 2004.

Future Direction

- Organize a U.S. national working group under the IEA banner to conduct joint research and provide information for international exchange.
- Organize an international working group and arrange a meeting at a location and time convenient to all participants.
- Add a modeling component to determine why some textural features function and some do not. The results will lead to design guidelines.
- Initiate the synergistic effect of thin films and coatings to protect textures.
- Explore the tribochemistry of various thin films and coatings.

Introduction

Frictional losses are inherent in all mechanical components in relative motion. The ability to control friction enables many technologies. Over the years, materials, lubricants, and surface modifications have provided the means to control and reduce friction to enhance energy efficiency in automotive and truck applications. A new avenue is needed to continue to increase the efficiency of energy utilization. Recently, dimples have been demonstrated to achieve friction reduction and durability enhancement in conformal contacts such as seals. The effect of dimples depends strongly on pattern design, contacting materials, and lubricant properties. A full understanding of these dependencies has yet to be developed. This research opens up a new avenue for increasing energy efficiency by combining surface textures, thin films and coatings, and the associated chemistry to protect surface textures. The objective of this project is to identify critical pattern features that control friction under a broad range of contact conditions and to develop models to explain these relationships.

Concomitant to this research, international cooperative research under the auspices of the IEA is planned to pool resources worldwide to accelerate this technology development. The results of this cooperative research will impact energy conservation efforts worldwide. Toward this end, the United Kingdom, Germany, Finland, Sweden, Israel, and Japan have agreed to participate in this activity under IEA Annex IV.

Approach

During FY 2004, experiments were conducted to examine various surface textures on steel surfaces using photolithography and chemical etching. Using the same area coverage (% of area occupied by the surface textural features), surface features such as grooves, triangles, ellipses, and circles were compared under high-speed, low-load conditions similar to those experienced by surface seals. Results indicated that (1) surface feature shape had great influence on friction reduction, and (2) friction reduction also depended strongly on the orientation of the surface features with respect to the direction of sliding. The results suggested that the conventional theory of hydrodynamic lift is not adequate to explain these observations, and a new theory is needed. Therefore, an in situ observation of the lubricant flow pattern will be developed to observe how a specific feature would affect the friction. A modeling effort will also be initiated in FY 2005.

To achieve energy savings, friction reduction needs to be achieved over a wide range of contact conditions existing in gears, transmissions, and engines. Therefore, the approach was to move into higher and higher loads and slower and slower speeds. New instrumentation and methods needed to measure the effect of textures will be developed.

New design principles for textural features will need to be developed to meet the load and speed requirements.

Results

Circular dimples were used to conduct high-load experiments using stainless steel specimens. The load was raised to 93 N on a smaller sample pin so that the apparent contact pressure was approximately 15–20 MPa. To prevent wear of the dimples, a fully formulated synthetic lubricant was used. Baseline specimens with and without dimples were compared. In each case, the dimples caused high friction. Grooves also exhibited higher friction when the contact pressure was increased or the speed reduced. These results tended to confirm the fluid mechanics models. A new design principle was needed to move into GPa contact pressure range.

Considering the basic principles of hydrodynamic lift, we designed a surface feature with a sloped bottom to provide an artificial hydrodynamic wedge. The idea was that if sufficient contact pressure were exerted, the surface would undergo elastic and plastic deformation and the liquid inside the feature would be squeezed, producing reactionary pressure to support the load. Since the pin-on-disk apparatus was limited by load, a four-ball wear tester with a configuration of ball-on-three-flat was used to generate high contact pressures. A 2.4-mm-diam 52100 steel ball bearing was used to slide on top of three 6-mm-diam disks. The testing conditions were 0.19–1.9 m/s speed and 2-, 5-, and 8-Kg loads lubricated by a fully formulated engine oil. The disks were also 52100 steel without case hardening. The surface texture was fabricated using mechanical scribing and electrochemical etching to create various sizes and shapes and slopes at the bottoms of the features. Since earlier work suggested that orientation with respect to the flow direction was a factor, the disks were carefully marked along the major axis of the features and mounted in the test apparatus. Figures 1 and 3 display the data in a 3-dimensional plot showing friction as a function of speed and load for steel on copper.

Figure 1 shows the baseline friction as a function of load and speed. Figure 2 shows the sliding direction in a typical hydrodynamic wedge shape; the friction coefficients across the speed and load range were lower than in the untextured case.

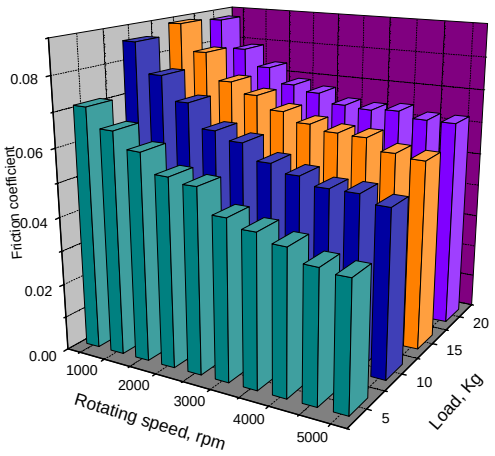

Figure 1. Untextured surface showing friction as a function of load and speed.

Figure 3 shows the sliding direction from shallow to deeper slope; the friction showed uniform improvement across the ranges. This finding was surprising, but it suggested other mechanisms might be in involved in addition to the classical hydrodynamic wedge theory. For these experiments, the contact pressure was approaching the GPa range. Instead of increasing friction, the hidden wedge geometry was able to reduce friction compared with the base case under boundary lubrication conditions. The dependence of the orientation direction was also surprising. If the major mechanism was to squeeze the fluid film along the wedge, then we would expect that flow direction along the long axis of the feature would give lower friction. For that matter, the cavitation mechanism would also suggest that this geometry would be better. The fact that flow along the short axis gives better friction control would seem to suggest that back-flow within the feature might play a more significant role than previously suspected.

Conclusions

We have demonstrated a new design principle that can reduce friction under boundary lubrication conditions. Additional tests on softer materials, in which we had more control over shaping the features, showed experimentally that a friction reduction of an order of magnitude was achievable.

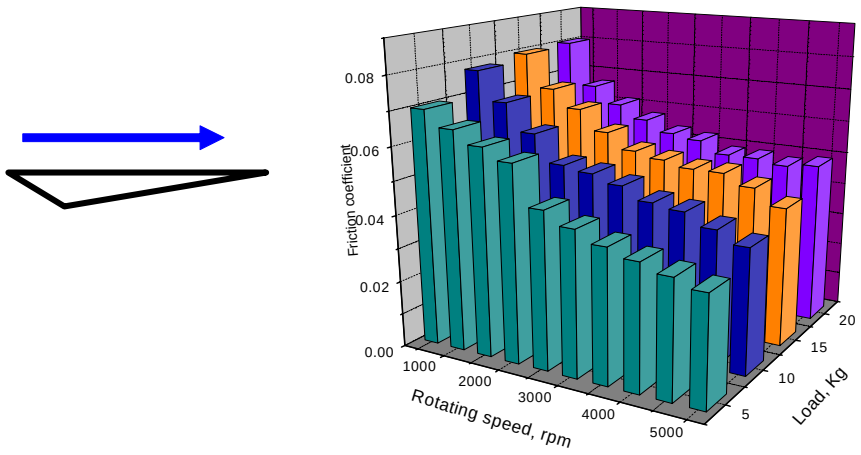

Figure 2. Textured surface with the flow toward the long axis of the feature.

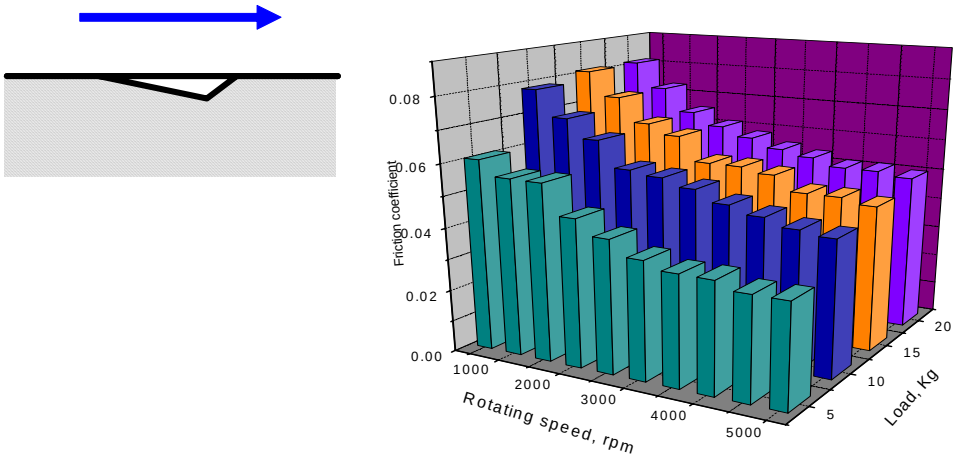

Figure 3. Textured surface with the flow toward the short axis of the feature.

This opens up a whole new avenue—the use of surface texturing in energy-intensive applications. The lack of an existing theory to adequately explain these observations suggests a new theory is needed. Therefore, in FY 2005, we will initiate a new modeling effort to increase understanding of the fundamental mechanisms.

Presentations

S. M. Hsu, "An Integrated Approach to Design Intelligent Surfaces for Heavily Loaded Contacts," presented at the International Joint Tribology Conference, Ponte Vedra, FL, October 27–29, 2003.

S. M. Hsu, "An Integrated Surface Texture Design with Surface Modification Techniques and Thin Lubricating Films," presented at the Smart Surfaces in Tribology: Advanced Additives and Structured Coatings Conference, Zurich, Switzerland, September 10–12, 2003.

S. M. Hsu, "An Integrated Surface Technology International Program under IEA," presented at the International Energy Agency Executive Committee meeting, Oakland, CA, October 20–23, 2003.

S. M. Hsu, "Surface Texturing under Boundary Lubrication for Friction Control," presented at the STLE annual meeting, Toronto, Canada, May 17–20, 2004.

Jorn Larson Basse, X. Wang, L. Ives, and S. M. Hsu, "Some Friction Experiments with Textured Surfaces," presented at the Nordic Symposium on Tribology, Troms, Norway, June 2004.

Jorn Larson Basse, X. Wang, L. Ives, and S. M. Hsu, "Some Friction Experiments with Dimpled Surface Texture," presented at the Fourth China International Symposium on Tribology, Xian, China, November 8–11, 2004.

S. M. Hsu, "An Integrated Surface Modification Technique to Control Friction: A New Paradigm," keynote speech at the Fourth China International Symposium on Tribology, Xian, China, November 8–11, 2004.

Y. Chae, X. Wang, and S. M. Hsu, "The Size Effect of Surface Texture on Lubricated Friction," presented at the First International Conference on Advanced Tribology, Singapore, December 1–3, 2004.

Publications

Jorn Larson Basse, X. Wang, L. Ives, and S. M. Hsu, "Some Friction Experiments with Textured Surfaces," in *Proceedings of Nordic Symposium on Tribology*, Troms, Norway, June 2004.

X. Wang and S. M. Hsu, "An Integrated Surface Modification Technique to Control Friction: A New Paradigm," keynote paper, in *Proceeding of the Fourth China International Symposium on Tribology*, Xian, China, November 8–11, 2004.

Appendix A. ACRONYMS AND ABBREVIATIONS

2D	two-dimensional
3D	three-dimensional
3BOB	three-ball-on-ball
3BOR	three-ball-on-rod
ACEM	aberration-corrected electron microscope
ADF	annular dark-field
AE	acoustic emission
AFM	atomic force microscope
Al	aluminum
AMCL	Advanced Materials Characterization Laboratory
ANL	Argonne National Laboratory
ASM	American Society for Metals
ASME	American Society of Mechanical Engineers
ASTM	American Society for Testing and Materials
Ba	barium
BET	Brunauer-Emmett-Teller theory
BMO	base metal oxides
BU	Bournemouth University
CARES	Ceramic Analysis and Reliability Evaluation of Structures
CC	current collector
CCVD	combustion chemical vapor deposition
CDF	cumulative distribution function
CEN	Committee for European Normalization
CERT	Committee on Energy Research and Technology
CHIP	cold + hot isostatic pressing
CIM	chemically interactive material
CP	commercially pure
CVD	chemical vapor deposition
CF8C	an Fe-19Cr-12NiCNb austenitic stainless steel
CN-12	an Fe-25Cr-13NiCNNb austenitic stainless steel
CRADA	cooperative research and development agreement
CRT	continuously regenerating technology
CWRU	Case Western Reserve University
DDC	Detroit Diesel Corporation
DISI	direct-injection spark-ignition
DITS	dynamic indentation test system
DOE	U.S. Department of Energy
DPF	diesel particulate filter
DRIFT	diffuse reflectance infrared Fourier transform spectroscopy
DSC	dispersion-strengthened composite
DT	deformation twin
DTA	differential thermal analyzer
EDM	electro-discharge machining

EDS	energy-dispersive spectroscopy
EERE	Office of Energy Efficiency and Renewable Energy
EGR	engine gas recirculation
EPA	U.S. Environmental Protection Agency
EPMA	electron probe microanalysis
EVD	electrochemical vapor deposition
FCVT	FreedomCAR and Vehicle Technologies
FEA	finite element analysis
FEM	finite element method/finite element modeling
FTIR	Fourier transform infrared spectroscopy
GPa	gigapascals
HA-ADG	high-angle annular dark field
HC	hydrocarbons
HDI	high-density infrared
HFIR	High Flux Isotope Reactor
HIP	hot isostatic pressing
HS	high stress
HSWR	High-Strength Weight-Reduction Materials Program
HTML	High Temperature Materials Laboratory
HVOF	high velocity oxygen-fuel
IA	implementing agreement
IA-AMT	Implementing Agreement for a Programme of Research and Development on Advanced Materials for Transportation Applications
IITS	instrumented indentation test system
IEA	International Energy Agency
IEST	integrated engineered surface technology
INEEL	Idaho National Engineering and Environmental Laboratory
ISO	International Organization for Standards
JIS	Japan Industrial Standards
LANL	Los Alamos National Laboratory
LBNL	Lawrence Berkeley National Laboratory
LNT	lean No_x trap
LS	low stress
LSCF	$La_{0.6}Sr_{0.4}Co_{0.8}Fe_{0.2}O_3$
LST	laser surface texturing
Mg	magnesium
MMC	metal matrix composite
NASA	National Aeronautics and Space Administration
NDE	nondestructive evaluation
NiAl	nickel aluminide
NiCr	nickel chromium
NiCrFe	nickel chromium iron
NIST	National Institute of Standards and Technology
NO_x	oxides of nitrogen; nitrites/nitrates species

NPD	neutron powder diffraction
NSF	National Science Foundation
NSR	NO_x stoichiometric ratio
NTRC	National Transportation Research Center
OBD	on-board diagnostic
OFCVT	Office of FreedomCAR and Vehicle Technologies
OFHC	oxygen-free high-conductivity
OM	optical microscopy
ORNL	Oak Ridge National Laboratory
PBC	phosphate-bonded composite
PCA	principal component analysis
PM	particulate matter
PM	parts per million
PMT	photomultiplier tube
PNNL	Pacific Northwest National Laboratory
PoT	pin-on-twin oscillating wear test
Pt	platinum
PZT	lead zirconate titanate
RBS	rotary bend strength
RCF	rolling contact fatigue
RE	reference electrode
SAcM	scanning acoustic microscopy
SAM	scanning auger microprobe
SAXS	small angel x-ray scattering
SCG	slow crack growth
SCR	selective catalytic reduction
SE	sensing electrode
SEM	scanning electron microscopy
SiC	silicon carbide
SIDI	spark-ignition direct-injection
SIUC	Southern Illinois University–Carbondale
SMPS	scanning mobility particle sizer
SOFC	solid oxide fuel cell
SO_x	oxy-sulfur species
SpaciMS	spacially resolved mass Spectrometer
SRBSN	sintered reaction-bonded silicon nitride
SRM	Standard Reference Material
SS	stainless steel
STEM	scanning transmission electron microscopy
TBCs	thermal barrier coatings
TEM	transmission electron microscopy
TFS	thru focal series
TGA	thermal gravimetric analysis (or analyzer)
Ti	titanium
TiAl	titanium aluminide

TiC	titanium carbide
TTBCs	thick thermal barrier coatings
TTZ	transformation-toughened zirconia
TWC	three-way catalyst
TWS	Third-Wave Systems
UHR-TEM	ultra-high resolution TEM
UHMW-PE	ultra-high molecular weight polyethylene
UTBM	University of Technology at Belfort-Montbeliard
WBDF	weak beam dark field
WC	tungsten carbide
XPS	X-ray photoelectron spectroscopy
XRD	X-ray diffraction/X-ray powder diffraction
YSZ	yttria-stabilized zirconia

A Strong Energy Portfolio for a Strong America

Energy efficiency and clean, renewable energy will mean a stronger economy, a cleaner environment, and greater energy independence for America. Working with a wide array of state, community, industry, and university partners, the U.S. Department of Energy's Office of Energy Efficiency and Renewable Energy invests in a diverse portfolio of energy technologies.

For more information contact:
EERE Information Center
1-877-EERE-INF (1-877-337-3463)
www.eere.energy.gov